2012

Evaluation of High-Level Lighting Poles Subjected to Fatigue Loading

Reilly William Thompson
Lehigh University

Evaluation of High-Level Lighting Poles Subjected to Fatigue Loading

by

Reilly W. Thompson

A Thesis
Presented to the Graduate and Research Committee
of Lehigh University
in Candidacy for the Degree of
Master of Science

in
Civil and Environmental Engineering

Lehigh University

December, 2011

This thesis is accepted and approved in partial fulfillment of the requirements for the Master of Science.

_____

Date

_____

Dr. Sougata Roy
Thesis Advisor
ATLSS Engineering Research Center,
Lehigh University

_____

Dr. Richard Sause
Thesis Advisor
Department of Civil and Environmental
Engineering, Lehigh University

_____

Dr. Sibel Pamukcu
Chairperson
Department of Civil and Environmental
Engineering, Lehigh University

ACKNOWLEDGEMENTS

This thesis is based on part of the research conducted under the National Cooperative Highway Research Program (NCHRP) Project 10-70: Cost-effective Connection Details for Highway Sign, Luminaire and Traffic Signal Structures. The research project was sponsored by the American Association of State Highway and Transportation Officials, in cooperation with the Federal Highway Administration, and was conducted in the National Cooperative Highway Research Program, which is administered by the Transportation Research Board of the National Research Council. Additional funding for the project was provided by the Pennsylvania Infrastructure Transportation Alliance, Department of Community and Economic Development, Commonwealth of Pennsylvania.

The author wishes to thank Dr. Sougata Roy for his guidance and supervision during the research and writing processes. Dr. Richard Sause also receives gratitude for his assistance in the writing process. Additional expert advice and input during the research was provided by Dr. John Fisher, Dr. Eric Kaufmann, and Dr. Ben Yen.

Finite element analysis and assistance in every aspect of fatigue testing was provided by project team member Mr. Yeun Chul Park. Additional data support was provided by Mr. Nirab Manandhar, who joined as a research assistant following the author's departure from the project.

This would not have been possible without the support of my wife Amy and the support of my parents, William and Jodi Thompson.

CONTENTS

LIST OF TABLES x

LIST OF FIGURES xii

ABSTRACT 1

1. INTRODUCTION 3

1.1 Background 3

1.1.1 High-level Lighting Poles 3

1.1.2 In-Service Cracking 6

1.1.3 Fatigue of High-Level Lighting Poles 8

1.2 Motivation for Current Research 11

1.3 NCHRP Project 10-70 13

1.4 Literature Review 14

1.4.1 TPF-5(116) Phase I (2007) 15

1.4.2 TPF-5(116) Phase II (2009) 19

1.5 Scope 25

1.6 Methodology 26

1.7 Outline 26

2. DETAILS OF EXPERIMENTS 29

2.1 Description of High-Level Lighting Pole Specimens 29

2.1.1 Type X Specimens 30

2.1.2 Type XI Specimens 31
2.1.3 Type XII Specimens 33
2.2 Test Setups 35
2.2.1 Loading Arrangement 35
2.2.2 Specimen Installation 36
2.2.3 Loading Fixture 37
2.3 Instrumentation 39
2.3.1 Displacements and Load Sensors 39
2.3.2 Strain Gages 39
2.4 Strain Gaging Plans 40
2.4.1 Type X Specimen 41
2.4.2 Type XI Specimen 42
2.4.3 Type XII Specimen 44
2.5 Data Collection 46
2.6 Static Testing 47
2.7 Fatigue Testing 48
3. STATIC TEST RESULTS 51
3.1 Type X Specimen 51
3.2 Type XI Specimen Static Test Results 55
3.3 Type XII Specimen Static Test Results 61
3.3.1 Stiffener-on-Center Testing 61

3.3.2 Bolt-on-Center Testing 66

4. FATIGUE TEST RESULTS AND PERFORMANCE ASSESSMENT 70

4.1 Type X Specimen 70

4.1.1 Fatigue Test Results 70

4.1.2 Cracking Modes 71

4.1.3 Origin and Growth of Fatigue Cracks 73

4.1.4 Assessment of Fatigue Resistance 74

4.2 Type XI Specimen 75

4.2.1 Fatigue Test Results 75

4.2.2 Cracking Modes 76

4.2.3 Origin and Growth of Fatigue Cracks 80

4.2.4 Assessment of Fatigue Resistance 81

4.3 Type XII Specimen 81

4.3.1 Fatigue Test Results 81

4.3.2 Cracking Modes 82

4.3.3 Origin and Growth of Fatigue Cracks 85

4.3.4 Assessment of Fatigue Resistance 87

5. ASSESSMENT OF VARIABILITY IN FATIGUE TEST RESULTS 89

5.1 Observed Scatter 89

5.2 Determination of Weld Geometry 92

5.3 Idealization of Weld Geometry 93

5.4 Evaluation of Scatter Due to Weld Geometry 95

5.5 Explanation of Scatter 98

6. FRACTURE SURFACE ANALYSIS 102

6.1 Assessment of Crack Shape 102

6.2 Approaches of Crack Growth Prediction 103

6.2.1 Method 1 103

6.2.2 Method 2 109

6.3 Results of Crack Progression Analysis 111

6.3.1 Specimen X-2 111

6.3.2 Specimen XII-2 112

7. RETROFITTING OF HIGH-LEVEL LIGHTING POLES 114

7.1 Impetus for Retrofitting 114

7.2 Previous Retrofitting of High-Level Lighting Poles 115

7.3 Retrofit Jacket for NCHRP Project 10-70 117

7.4 Finite Element Analysis of the Jacket Retrofit 119

7.4.1 3D Model 1 120

7.4.2 3D Model 2 123

7.4.3 Notch Stress Models 125

7.5 Assessment of Fatigue Resistance of Jacket Wall-to-Base Plate Connection126

7.6 Laboratory Testing 129

7.7 Retrofitting Conclusions 131

8. CONCLUSIONS 133

8.1 Behavior of Pole-to-Base Plate Connections 134

8.2 Fatigue Testing 136

8.3 Effect of Weld Geometry on Fatigue Performance 138

8.4 Origin and Propagation of Fatigue Cracks 139

8.5 Jacket Retrofitting 139

8.6 Recommendations for Further Research 140

TABLES 142

FIGURES 155

REFERENCES 240

APPENDIX A OBSERVED CRACK LENGTHS DURING FATIGUE TESTING 243

APPENDIX B 3D-ICP BACKGROUND 259

B.1 Equipment 260

B.2 Calibration 260

B.3 Stochastic Pattern 261

B.4 Facets 261

B.5 Measurement 262

B.6 Filtering 263

B.7 Masking 266

B.8 Boundary Effects 267

VITA 277

LIST OF TABLES

Table 1. AASHTO detail categories and corresponding constant amplitude fatigue limits 142

Table 2. Test Results Type X Specimen 143

Table 3. Test Results Type XI Specimen 144

Table 4. Test Results Type XII Specimen 147

Table 5. Type XI specimen weld profile measurements 150

Table 6. Weld profile geometry measurement results 151

Table 7. Specimen X-2 crack propagation estimate, Method 1 152

Table 8. Specimen X-2 crack propagation estimate, Method 2 153

Table 9. Specimen XII-2 crack propagation estimate, Method 1 154

Table 10. Specimen XII-2 crack propagation estimate, Method 2 154

Table A-1 Crack length observations specimen X-1 244

Table A-2. Crack length observations specimen X-2 245

Table A-3. Crack length observations specimen X-3 246

Table A-4. Crack length observations specimen XI-1 246

Table A-5. Crack length observations specimen XI-2 247

Table A-6. Crack length observations specimen XI-3 248

Table A-7. Crack length observations specimen XI-4 248

Table A-8. Crack length observations specimen XI-5 249

Table A-9. Crack length observations specimen XI-6 250

Table A-10. Crack length observations specimen XI-7 251

Table A-11. Crack length observations specimen XI-8 251

Table A-12. Crack length observations specimen XI-9 252

Table A-13. Crack length observations specimen XI-10 252

Table A-14. Crack length observations specimen XII-1 253

Table A-15. Crack length observations specimen XII-2 253

Table A-16. Crack length observations specimen XII-3 254

Table A-17. Crack length observations specimen XII-4 255

Table A-18. Crack length observations specimen XII-5 256

Table A-19. Crack length observations specimen XII-6 256

Table A-20. Crack length observations specimen XII-7 257

Table A-21. Crack length observations specimen XII-8 257

Table A-22. Crack length observations specimen XII-9 258

Table A-23. Crack length observations specimen XII-10 258

LIST OF FIGURES

Figure 1. Example of a high-level lighting pole in service 155

Figure 2. Tube-to-base plate connections: *a*, fillet-welded connection; *b*, full-penetration welded connection; *c*, stiffened fillet-welded connection. 155

Figure 3. Example of a handhole on an in-service structure 156

Figure 4. Close-up of collapsed tower *(reprinted from Dexter, 2004)* 156

Figure 5. Handhole crack at corner *(reprinted from Koob, 2006)* 157

Figure 6. Stool base connection detail *(reprinted from Dexter, 2004)* 157

Figure 7. Schematic of a von Karman vortex street in the wake of a cylinder *(reprinted from Kaczinski et al., 1998)* 158

Figure 8. AASHTO Bridge Specification stress-life design curves 158

Figure 9. University of Texas at Austin test results, first phase 159

Figure 10. University of Texas at Austin test results, second phase 159

Figure 11. Type X specimen dimensions, part 1 of 2 160

Figure 12. Type X specimen dimensions, part 2 of 2 161

Figure 13. Type XI specimen dimensions, part 1 of 2 162

Figure 14. Type XI specimen dimensions, part 2 of 2 163

Figure 15. Type XII specimen dimensions, part 1 of 3 164

Figure 16. Type XII specimen dimensions, part 2 of 3 165

Figure 17. Type XII specimen dimensions, part 3 of 3 166

Figure 18. Fatigue testing setup at ATLSS 167

Figure 19. Elevation schematic of testing setup 168

Figure 20. Comparison between boundary conditions: *a*, in-service; *b*, laboratory. 169

Figure 21. Loading rod connection schematic 170

Figure 22. Loading collar connection schematic 170

Figure 23. Loading collar plan view 171

Figure 24. Fully pretensioned connection schematic 172

Figure 25. Type X specimen elaborately instrumented specimen strain gaging plan172

Figure 26. Type X specimen extensively instrumented specimen strain gage plan, interior 173

Figure 27. Type XI specimen elaborately instrumented specimen strain gaging plan, handhole side 173

Figure 28. Type XI specimen elaborately instrumented specimen strain gaging plan, opposite side 174

Figure 29. Type XI specimen elaborately instrumented specimen strain gaging plan, tube inside surface 174

Figure 30. Type XII specimen elaborately instrumented specimen strain gaging plan 175

Figure 31. Type XII specimen elaborately instrumented stiffener, view A-A 175

Figure 32. Dynamic testing run-out values 176

Figure 33. Type X control gage comparison of nominal stress, FEA result, and measured values from static test 176

Figure 34. Type X FEA model: *a*, global view; *b*, close-up of loading area; *c*, top view of deformed shape. 177

Figure 35. Type X strain gage comparison of nominal stress, FEA result, and measured values from static test. Gage abutting weld toe at pole base. 177

Figure 36. Type X comparison of FEA result, strain gage values, and nominal stress 178

Figure 37. Cross-section of Type X FEA, showing displaced shape 178

Figure 38. Stress profile in specimen X-2 above pole base on handhole side, in the loading plane 179

Figure 39. Differences in weld shape: *a*, FEA model; *b*, 3D-ICP section of weld profile; *c*, enlarged view of 3D-ICP. 179

Figure 40. Type XI control gage comparison of nominal stress, FEA result, and measured values from static test 180

Figure 41. Type XI strain gage comparison of nominal stress, FEA result, and measured values from static test. Gage abutting weld toe at pole base. 180

Figure 42. Type XI comparison of FEA result, strain gage values, and nominal stress 181

Figure 43. Stress profile in specimen XI-6 above pole base opposite to the handhole, in the loading plane 181

Figure 44. Enlarged view of stress profile in specimen XI-6 abutting pole-to-base plate weld toe 182

Figure 45. Non-uniform contact between backing ring and pole wall in Specimen XI-7 182

Figure 46. 3D-ICP camera image of Type XI pole base opposite actuator 183

Figure 47. Type XI strain comparison at pole base centerline opposite actuator (arrows indicate strain direction): *a*, 3D-ICP contour plot; *b*, FEA contour plot; *c*, global view with comparison area highlighted. 184

Figure 48. Specimen XI-6 comparison of FEA result, 3D-ICP result, and strain gage values above pole base on actuator side 185

Figure 49. Enlarged view of Specimen XI-6 comparison of finite element analysis result, 3D-ICP result, and strain gage values at pole base weld toe on actuator side 185

Figure 50. 3D-ICP camera image of Type XI pole base centerline on actuator side 186

Figure 51. Enlarged view of 3D-ICP camera image of Type XI pole base centerline on actuator side 187

Figure 52. Type XI 3D-ICP strain contour plot at pole base centerline on actuator side using mean filter (arrow indicates strain direction). Inset shows location on structure. 187

Figure 53. Type XI strain comparison at pole base centerline on actuator side (arrows indicate strain direction): *a*, 3D-ICP contour plot using median filter; *b*, FEA contour plot; *c*, global view with comparison area highlighted. 188

Figure 54. Type XII control gage comparison of nominal stress, FEA result, and measured values from static test 189

Figure 55. Type XII strain gage comparison of nominal stress, FEA result, and measured values from static test. Gage abutting weld toe at stiffener termination. 189

Figure 56. Stress profile in specimen XII-3 above stiffener termination, in the loading plane 190

Figure 57. Enlarged view of stress profile in specimen XII-3 abutting stiffener weld toe 190

Figure 58. 3D-ICP camera image of Type XII at stiffener termination 191

Figure 59. Type XII strain comparison at stiffener termination opposite actuator (arrows indicate strain direction): *a*, 3D-ICP contour plot; *b*, FEA contour plot; *c*, global view with comparison area highlighted. 192

Figure 60. Stress profile in specimen XII-3 at pole-to-base plate weld, in the loading plane 193

Figure 61. Enlarged view of stress profile in specimen XII-3 abutting pole-to-base plate weld 193

Figure 62. 3D-ICP camera image of Type XII at pole base bend opposite actuator 194

Figure 63. Type XII strain comparison at pole base bend opposite actuator (arrows indicate strain direction): *a*, 3D-ICP contour plot; *b*, FEA contour plot; *c*, global view with comparison area highlighted. 195

Figure 64. Stress profile in specimen XII-3 above stiffener termination, in the loading plane, bolt-on-center 196

Figure 65. Enlarged view of stress profile in specimen XII-3 abutting stiffener weld toe, bolt-on-center 196

Figure 66. 3D-ICP camera image of Type XII at stiffener termination 197

Figure 67. Type XII strain comparison at stiffener termination opposite actuator (arrows indicate strain direction): *a*, 3D-ICP contour plot; *b*, FEA contour plot; *c*, global view with comparison area highlighted. 198

Figure 68. Stress profile in specimen XII-3 at pole-to-base plate weld, in the loading plane, bolt-on-center 199

Figure 69. Enlarged view of stress profile in specimen XII-3 at pole-to-base plate weld, in the loading plane, bolt-on-center 199

Figure 70. Crack initiation points in Type X specimens 200

Figure 71. Crack of specimen X-1 at first observation 200

Figure 72. Final crack at termination of fatigue testing of specimen X-2 201

Figure 73. Crack growth versus number of cycles for Type X specimen 201

Figure 74. Specimen X-2 fracture surfaces 202

Figure 75. Enlarged view of specimen X-2 fracture surfaces (refer Figure 74) 202

Figure 76. Scanning electron micrograph of typical crack initiation site for specimen X-2 (refer Figure 75) 203

Figure 77. Test results of Type X specimen 203

Figure 78. Crack of specimen XI-3 at first observation 204

Figure 79. Measured strain range at center of backing ring for Specimen XI-6 204

Figure 80. Final crack at termination of fatigue testing of specimen XI-6 205

Figure 81. Fatigue cracks in specimen XI-8 205

Figure 82. Crack growth in specimen XI-4 206

Figure 83. Crack growth versus number of cycles for Type XI specimen 206

Figure 84. Specimen XI-3 fracture surfaces 207

Figure 85. Scanning electron micrograph of typical crack initiation site for specimen XI-3, image 1 (refer Figure 84) 207

Figure 86. Scanning electron micrograph of typical crack initiation site for specimen XI-3, image 2 (refer Figure 84) 208

Figure 87. Test results of Type XI specimens 208

Figure 88. Crack of specimen XII-6 at first observation 209

Figure 89. Fatigue cracking from lack of fusion defect in specimen XII-6 209

Figure 90. Crack of specimen XII-4 at first observation 210

Figure 91. Final crack at termination of fatigue testing of specimen XII-2 210

Figure 92. Final crack at termination of fatigue testing of specimen XII-4 211

Figure 93. Crack growth versus number of cycles for Type XII specimen 211

Figure 94. Specimen XII-1 fracture surfaces 212

Figure 95. Scanning electron micrograph of typical crack initiation site for specimen XII-1 (refer Figure 94) 212

Figure 96. Specimen XII-1 fracture surfaces at pole base 213

Figure 97. Scanning electron micrograph of typical crack initiation sites for specimen XII-1 at pole base (refer Figure 96) 213

Figure 98. Specimen XII-9 fracture surface 214

Figure 99. Scanning electron micrograph of crack initiation site for specimen XII-9 (refer Figure 98) 214

Figure 100. Test results of Type XII specimens 215

Figure 101. Analysis of fatigue test results of Type XI specimens 215

Figure 102. Category E upper and lower bounds plotted with Type XI test results 216

Figure 103. Test results, select Type I specimens 216

Figure 104. Type I specimen mast arm weld profiles: *a*, Specimen I-1; *b*, Specimen I-2; *c*, Specimen I-3. 217

Figure 105. Effect of weld angle, Type I specimens 217

Figure 106. 3D-ICP weld profile over a cross section of same location captured through visual microscopy 218

Figure 107. Specimen XI-1 weld profile obtained through 3D-ICP 219

Figure 108. Weld dimension parameters. Inset shows weld idealization over typical weld profile. 219

Figure 109. Submodeling: *a*, Region shown on global FEA model; *b*, Submodel dimensions (inches). 220

Figure 110. Submodel finite element mesh for geometric stress method 220

Figure 111. Geometric stress result for worst-considered weld geometry 221

Figure 112. Geometric stress result for best-considered weld geometry 221

Figure 113. Upper and lower bound estimates of fatigue life based on weld geometry plotted with Type XI test results 222

Figure 114. Comparison of Type XI welded connection and Category E cover plate connection. 222

Figure 115. Category E scatter attributed to weld toe notch effects added to scatter attributed to variation in weld geometry, plotted with Type XI test results 223

Figure 116. Variables used to calculate the complete elliptic integral of the second kind 223

Figure 117. Labels used within crack propagation calculations 224

Figure 118. Flowchart of crack progression analysis 225

Figure 119. Type XII specimen stress concentration factor through thickness. *From analysis by Mr. Yeun Chul Park.* 226

Figure 120. Variables used for calculating the geometry correction factor using Method 2 226

Figure 121. Specimen X-2 fracture surface with observed beach marks 227

Figure 122. Specimen X-2 observed crack growth and estimated crack growth 227

Figure 123. Specimen XII-2 fracture surface with observed beach marks 228

Figure 124. Specimen XII-2 observed crack growth and estimated crack growth 228

Figure 125. Iowa DOT retrofit jacket: *a*, side view; *b*, front view. *(reprinted from Koob, 2006)* 229

Figure 126. Retrofit jacket for use with cracked test specimens 230

Figure 127. Front side exploded view of Model 1: *a*, splice plates; *b*, retrofitted pole; *c*, retrofit jacket. 231

Figure 128. Back side exploded view of Model 2: *a*, splice plates; *b*, retrofitted pole; *c*, retrofit jacket. 232

Figure 129. Model 1 interior surface of jacket 233

Figure 130. Retrofit jacket FEA comparison, handhole side: *a*, cracked pole without jacket; *b*, retrofitted pole; *c*, retrofit jacket. 233

Figure 131. Model 1 FEA results 234

Figure 132. Model 2 dimensions 234

Figure 133. Model 2 results: *a*, exploded at centerline; *b*, stress profile through thickness. 235

Figure 134. Model 3 dimensions. Extents of Model 4 highlighted on surface. 236

Figure 135. Cross-section of Model 4 showing salient dimensions and mesh 237

Figure 136. Cross-section of Model 4 results showing contour of maximum principal stress 237

Figure 137. Retrofit jacket ready for connection to Specimen XI-9 238

Figure 138. Stress profile in specimen JRXI above jacket base opposite to the handhole, in the loading plane 239

Figure B-1. Three-dimensional image correlation equipment used 269

Figure B-2. Schematic of 3D-ICP facet parameters 269

Figure B-3. Type XII stiffener termination weld 3D-ICP strain results: *a*, unfiltered results; *b*, filtered results. 270

Figure B-4. 3D-ICP results after one filter pass 271

Figure B-5. 3D-ICP results after two filter passes 271

Figure B-6. 3D-ICP results after three filter passes 272

Figure B-7. 3D-ICP results using a size 7 median filter 272

Figure B-8. 3D-ICP results using a size 9 median filter 273

Figure B-9. 3D-ICP results using a size 11 median filter 273

Figure B-10. 3D-ICP results using a size 7 mean filter 274

Figure B-11. 3D-ICP results using a size 9 mean filter 274

Figure B-12. 3D-ICP results using a size 11 mean filter 275

Figure B-13. Finite element analysis predicted stresses for Type XII at stiffener termination weld toe 275

Figure B-14. Comparison of 3D-ICP data for Type XII at stiffener termination with strain masking and without strain masking of weld surface 276

ABSTRACT

The fatigue resistance of common welded details used in high-level lighting poles was evaluated through full-scale fatigue testing. Test specimens included three specimens with fillet-welded pole-to-base plate connections, ten specimens with full-penetration groove-welded pole-to-base plate connections, and ten specimens with stiffened fillet-welded connections. Additional fatigue testing was conducted on a retrofit jacket, intended for retrofitting a fatigue cracked structure in-service. Static testing was conducted to characterize the behavior of the structures under load and to identify the critically stressed regions. The strain measurements from conventional strain gages as well as three-dimensional image correlation photogrammetry were compared to finite element analysis results. Fatigue testing was conducted to establish both the finite life and infinite life resistances of the connection details.

The fatigue test results indicated that the constant amplitude fatigue limit of the fillet-welded connection in the test geometry was likely above 4.5 ksi (31 MPa), corresponding to an AASHTO Category E detail. The finite life performance of this connection was characterized as AASHTO Category E′. The constant amplitude fatigue limit of the full-penetration groove-welded connection of the test geometry was 7 ksi (48 MPa), corresponding to an AASHTO Category D detail. This connection was characterized as Category E in the finite life region. The constant amplitude fatigue limit of the stiffened fillet-welded connection for the test geometry was defined as 7 ksi (48 MPa), corresponding to an AASHTO Category D detail, for both fatigue cracking at the stiffener termination on the pole and at the fillet weld toe

on the pole. The finite life fatigue resistance of this connection was defined as Category E′.

The scatter observed in the fatigue test results was primarily due to the inherent variability in macro and micro-discontinuities at the weld toe. Unusual scatter was observed in some test results, which were found to be due to the variability in the weld geometry in addition to the inherent scatter in fatigue resistance of welded connections. The observed crack propagation during fatigue testing was assessed by two fracture mechanics models based on visible macro features on the fatigue fracture surface. An optimized retrofit jacket was designed using finite element analysis, whose infinite life fatigue resistance was established as 10 ksi (69 MPa), the constant amplitude fatigue limit of AASHTO Category C details.

1. INTRODUCTION

1.1 Background

1.1.1 High-level Lighting Poles

High-level lighting is commonly used at highway interchanges and in open parking facilities for illuminating a large area. To maximize the coverage, luminaires are elevated above the ground by high-level lighting poles with heights typically between 55 ft (17 m) and 180 ft (55 m); although taller structures are increasingly being used. These structures support between four and twelve luminaires at the top. An example of a high-level lighting pole is shown in Figure 1.

High-level lighting poles are comprised of a vertical pole welded to a horizontal base plate. The pole is a thin-walled hollow shape of circular or multi-sided cross-section, with a diameter usually between 16 in (406 mm) and 36 in (914 mm). Multi-sided cross-sections are typically 12-sided or 16-sided, approximating a circular section. The base plate transfers the loads applied on the pole to the foundation. The pole-to-base plate connections are either fillet-welded or full-penetration groove welded. In a fillet-welded connection (also called a socket connection), the pole passes through a matching opening cut into the base plate and is fillet welded to the base plate at the top. An example of a fillet-welded connection is shown in Figure 2(a). Another fillet weld is deposited between the bottom edge of the pole and the inside face of the base plate opening, primarily in galvanized structures, to seal the gap between the pole and the base plate. In a full-penetration groove welded connection,

the pole is welded to the top of the base plate. Usually, a backing ring fillet-welded to the base plate at the bottom is provided to achieve a full penetration weld of adequate quality at the root. In a galvanized structure, the backing ring may also be welded to the pole at the top for sealing the gap between the backing ring and the pole, for preventing acids used in the galvanizing process from becoming trapped, which may lead to crevice corrosion when exposed to moisture. An example of a full-penetration groove welded connection is shown in Figure 2(b). Another variation of the pole-to-base plate fillet-welded connection is sometimes employed, where discrete longitudinal stiffeners are fillet-welded to the pole and the base plate, as shown in Figure 2(c). The stiffeners are intended to "protect" the fillet-welded connection by inhibiting cracking at the fillet weld.

The base plate is discretely fastened to a concrete foundation by eight to sixteen anchor rods along the perimeter, which pass through holes in the base plate and are anchored down in the foundation. Leveling nuts are provided on the anchor rods to support the pole and level it during installation. The base plate is secured in position using a nut on the top of the base plate and an additional locknut. The gap between the base plate and the foundation is left as-is, and as a result the pole is supported discretely on the leveling nuts at the anchor rod locations. This installation is preferred for ease of ensuring verticality of the pole and for preventing corrosion by allowing easy drainage through the gap.

A cutout, referred to as a handhole, is provided in the pole wall for accessing the internals, including the mechanism to lower and raise the luminaires. A stiffening

frame is provided around the perimeter of the handhole to replace the section lost due to the opening, as shown in Figure 3. This frame is welded to the pole wall from the outside using a fillet or partial-joint penetration weld.

High-level lighting poles are typically constructed of multiple sections to reach the required height, for ease of fabrication and transport. With the exception of longitudinal seam welds, all welded details are contained in the lower section of the pole. A taper is provided to lessen the height range over which the aero-elastic phenomenon of vortex shedding, discussed in Section 1.1.3, will apply cyclic load to the structure. This taper allows for slip-fit connections between the pole sections with no other means of attachment necessary.

High-level lighting poles are typically galvanized for corrosion protection. A survey of state departments of transportation found that 93% of the respondent states had galvanized poles in their inventory (Roy et al. 2006). A total of 18% of the respondent states had poles constructed of weathering steel. Finally, a total of 13% of the respondent states had poles that were painted for corrosion protection (with some states having a mix of corrosion protection methods used). Up until the late 1990s, the only known failure of high-level lighting poles in service was a structure around Philadelphia, Pennsylvania that was made of weathering steel. This structure experienced severe corrosion at the slip-fit joints that remained wet from trapped water, which was contrary to the condition required for the desired performance of weathering steel. Additionally, the presence of road salts increases corrosion of

weathering steel structures close to the ground. Subsequently, the owners preferred galvanized structures for high-level lighting poles.

1.1.2 In-Service Cracking

In November, 2003 a 140 ft (43 m) high-level lighting pole collapsed in-service near Sioux City, Iowa. The results of the ensuing investigation were reported in Dexter (2004). Figure 4 is a close-up photograph of the base of the collapsed tower. As is evident, the structure employed a fillet-welded pole-to-base plate connection. The base plate and the top fillet-welded connection of the pole remained in place on the foundation. The investigators concluded that the collapse was due to fatigue cracking at the pole-to-base plate connection. The primary fatigue loading for the high-level lighting pole was identified as wind-induced vibration, which is discussed further in Section 1.1.3.

After the collapse, the remaining inventory of 232 high-level lighting poles in Iowa was inspected. Cracking at the pole-to-base plate connection was observed in all 17 high-level lighting poles that were similar in design to the collapsed pole, referred to as the I-29 towers. These poles installed around 2000 had a fillet-welded pole-to-base plate connection, and were galvanized for corrosion resistance. Another 18 structures installed around the same time were of similar geometry and also galvanized, but used a full-penetration groove welded pole-to-base plate connection. These structures will be referred to as the US75 towers, though their location varied. These structures did not exhibit any cracking. Both groups were 140 ft (43 m) tall, were 16-sided, had a diameter of 24 $^{3}/_{4}$ in (629 mm) at the pole-to-base plate

connection, had a wall thickness of 0.188 in (5 mm), and had a 1 $^{1}/_{4}$ in (32 mm) thick base plate.

A total of 107 high-level lighting poles were installed in Iowa during the 1980s and 1990s that were constructed of weathering steel. Cracking was observed at the pole-to-base plate connection in three of the structures and at the handhole frame-to-pole weld in one of the structures, shown in Figure 5. These cracked structures will be referred to as the I-35 towers. The I-35 towers employed a full-penetration groove welded pole-to-base plate connection, were 148 ft (45 m) tall, were 12-sided, had a diameter of 28 $^{1}/_{2}$ in (724 mm) at the pole-to-base plate connection, had a wall thickness of $^{5}/_{16}$ in (8 mm), and had a 1 $^{3}/_{4}$ in (44 mm) thick base plate.

A total of 90 structures with a stiffened stool connection at the pole base were installed during the 1970s and 1980s and were constructed of weathering steel as shown in Figure 6. No cracking was observed in these structures, which will be referred to as the stool connection towers. Amongst the stool connection towers, the pole height varied between 100 ft (30 m) and 180 ft (55 m), the diameter at the pole-to-base plate connection varied between 24 in (610 mm) and 33.3 in (846 mm), and the wall thickness varied between $^{5}/_{16}$ in (8 mm) and 0.688 in (17 mm).

A lack of observed cracking in the US75 towers suggests greater fatigue resistance of the full-penetration groove welded connection compared to the fillet-welded connection of the otherwise similar I-29 towers. The survival of a larger percentage of the I-35 towers over a longer period of time suggests that the increased diameter, the increased wall thickness, or the increased base plate thickness could

have increased fatigue resistance. For the stool connection towers, possible reasons for the long service life are the pole-to-base plate connection detail and a more conservative design approach. The thicker section used for the stool connection towers and the occurrence of fatigue cracking in the I-29 towers after only three years both indicate changes in the design approach that affected fatigue resistance.

Additional instances of failures of high-level lighting structures were reported by Rios (2007). Two separate failures at the same site occurred in South Dakota in 2005 and 2006. A third failure occurred in Colorado in 2007. It was noted that all collapsed structures were designed with a relatively thin base plate; less than 2 in (51 mm) thick.

1.1.3 Fatigue of High-Level Lighting Poles

Fatigue is the progressive, localized, and permanent structural damage that occurs in a material subjected to repeated or fluctuating tensile stress at nominal stresses with maximum values often much less than the static yield strength of the material. Fatigue is the mechanism of crack initiation and propagation, and requires simultaneous actions of fluctuating load or load range, tensile stress, and plastic strain. Dynamically loaded welded structures are particularly susceptible to fatigue cracking as all conditions responsible for fatigue damage are inherent in them. Weld geometry introduces stress concentrations at the weld toe and the weld root, increasing the effect of the applied stress range. A stress concentration due to the global geometry and behavior of the structure is referred to as a geometric stress concentration, with the stress value referred to as the geometric stress. A stress concentration due to the

abrupt change in direction at a weld toe is referred to as a notch stress concentration, with the stress value referred to as the notch stress. Within the weld, non-metallic inclusions in the form of trapped slag exist at the fusion boundary of weld and base material and serve as initial cracks; micro-discontinuities with theoretically infinite stress concentration that introduce plastic straining in the material around the crack tips. In addition, shrinkage of the deposited weld metal during cooling results in residual tensile stresses to the order of yield strength of the material at the weld toe and the weld root. This residual stress causes a net tensile stress even under load reversal.

Fatigue of high-level lighting poles is caused by wind-induced oscillations due to the aero-elastic phenomenon of vortex shedding and the aerodynamic vibrations of natural wind gust. Vortex shedding is the most common cause of large-amplitude, long-duration oscillations of these poles, imparting most of the fatigue damage to the welded connections in the structures. The mechanism of vortex shedding induced oscillation is as follows. A cylindrical body, such as a high-level lighting pole, subjected to a steady, uniform wind flow will shed vortices in the wake, commonly known as a von Karmen vortex street. Figure 7 shows a schematic of a von Karmen vortex street formed in the wake of a cylinder, with vortices emanating from alternating sides. These vortices are shed at a frequency proportional to the flow velocity (Kaczinski, 1998).

The shedding of a vortex develops a negative pressure, which results in a pressure differential between the sides of the cylinder (the side on which the vortex is

shed and the opposite side) perpendicular to the wind direction. The differential pressure oscillates the structure. When the frequency of vortex shedding approaches one of the natural frequencies of the high-level lighting pole, typically the frequency associated with the second or third mode shape, resonance occurs. Vortices shed at the frequency associated with the first mode shape lack the energy density to produce cyclic motion in the structure. At wind speeds that would generate vortices at the frequency associated with the fourth mode shape, there is sufficient natural turbulence prevent the formation of vortices. The low damping in high-level lighting poles, less than 1% of critical, leads to dynamic amplification and displacements on the order of 1.5 times the width of the structure. Resonant vibration of the high-level lighting pole slightly alters the emanation of vortices, with the vortex shedding frequency aligning with the natural frequency of the structure. As a result, the frequency of vortex shedding remains constant even with changes in the wind velocity, a condition known as "lock-in." Due to "lock-in" and low damping, the structure once excited experiences a large number of oscillations over a short period of time, imparting fatigue damage to the welded connections in the structure (Kaczinski et al. 1998).

Over the height of the structure, the bending moment due to wind induced oscillation introduces in-plane membrane stresses in the pole wall and the pole cross-section deforms into a "pear" shape. Near the base, these stresses are intensified by the interaction of the pole cross-section and the base plate. To maintain compatibility, the pole wall deforms in reverse bending introducing out-of-plane bending stresses through the pole wall. The flexibility of the base plate allows rotation of the

connection, increasing the out-of-plane bending stresses in the pole wall further. Superposition of the out-of-plane bending stress on the in-plane membrane stress magnifies the surface stress on the pole wall in the vicinity of the weld toe, which precipitates fatigue damage of the connection. The severity of the out-of-plane bending is dependent on the relative stiffness of the base plate and the pole, i.e., the geometry of the connection, with the pole diameter, the pole wall thickness, the base plate thickness, the opening in the base plate, and the number of anchor rods affecting the relative stiffness (Roy et al. 2008, Roy et al. 2010).

1.2 Motivation for Current Research

The current design specification for high-level lighting poles is the American Association of State Highway and Transportation Officials (AASHTO) *Standard Specifications for Structural Supports for Highway Signs, Luminaires and Traffic Signals, 5th Edition 2009*, hereafter referred to as the AASHTO Specification. The AASHTO Specification recommends a 25-year design life for the subject structures. Recognizing the impossibility of accurately determining the number of stress cycles that the structures may experience during their design life, which can exceed 100 million stress cycles, AASHTO recommends designing the structures for infinite life.

Despite this recommendation, the detail categories for high-level lighting pole welded details in the AASHTO Specification were created without the support of experimental results. The constant amplitude fatigue limit (CAFL) values were taken from the stress-life design curves of the AASHTO Standard Specifications for Highway Bridges, hereafter referred to as the AASHTO Bridge Specification. The

design curves are plotted in Figure 8, with the solid lines representing the finite life curves and the dashed lines representing the CAFL values. These curves were created from test data for welded bridge details, as described in National Cooperative Highway Research Program (NCHRP) Reports 102 and 286.

Research conducted after publishing of the 2001 version of the AASHTO Specification by Koenigs (2003) and Ocel (2006) found discrepancies between detail category and fatigue performance of mast-arms for cantilevered sign/signal structures. Koenigs' test results included a specimen design with a full-penetration groove welded pole-to-end plate connection. The two specimens tested had a round cross-section, 10 in (254 mm) outer diameter, 0.179 in (4.6 mm) thick pole, and 1 $^{1}/_{2}$ in (38 mm) thick base plate. These specimens exhibited Category D resistance, whereas the current AASHTO Specification predicts Category E resistance. Conversely, Ocel's test results included a specimen design with a fillet-welded pole-to-end plate connection that failed to meet the predicted resistance. The eight specimens tested had an octagonal cross-section, 11.6 in (295 mm) corner-to-corner diameter, 0.31 in (7.9 mm) thick pole, and 1 $^{1}/_{4}$ in (32 mm) thick base plate. The maximum resistance exhibited was on the Category E line, with half of the specimens exhibiting Category ET resistance, whereas the current AASHTO Specification predicts Category E resistance. Additionally, the specimens tended to crack at the corners of the cross-section farthest from the neutral axis on the tension side, rather than the flat between them. This indicated that the stress concentration formed by the corner affected the crack location. The AASHTO Specification makes no distinction between round and multi-sided

cross-sections, apart from recommending that square cross-sections not be used. This approximation of connections in high-level lighting pole details to their bridge counterparts does not consider the behavior of thin tubular structures, causing inaccurate predictions of fatigue resistance that can be both conservative and nonconservative.

The AASHTO Specification does not include the connection geometry as a parameter for determining fatigue resistance. Koenigs (2003) and Ocel (2006) both observed improved fatigue performance when the base plate of their mast-arm specimens was thicker, which decreased base plate flexibility. In subsequent tests, Rios (2007) observed improved fatigue performance in high-level lighting pole specimens when the number of anchor rods was increased, increasing base plate fixity. The current AASHTO Specification only recommends a base plate thickness on the order of 3 in (76 mm), without considering the change in behavior as the relative stiffness of the base plate to the pole wall is altered. As discussed in Section 1.4.1, there was a significant difference in the performance of test specimens when geometric parameters were altered, though the AASHTO Specification considered them all to be of the same detail category.

1.3 NCHRP Project 10-70

To address the deficiencies in the AASHTO Specification, the National Cooperative Highway Research Program (NCHRP) in 2006 initiated Project 10-70: Cost-effective Connection Details for Highway Sign, Luminaire and Traffic Signal Structures. The objectives of this research project were: to establish the fatigue

resistance of existing, retrofitted, and new cost-effective connection details; to develop fatigue design guidelines for the connection details; and to recommend revisions to the existing specification. The project objectives were accomplished through a combination of three-dimensional parametric finite element analyses (FEA) and fatigue testing of full-size specimens of the subject structure incorporating the various connection details of interest. As part of the project, 80 full scale specimens distributed over 11 types were tested, including seven types of cantilever sign and traffic signal structures (47 specimens) and four types of high-level lighting poles (33 specimens). Each specimen type contained welded connection details that were optimized through parametric FEA. The specimens were evaluated for both finite life and infinite life performance. The project also investigated a steel jacket retrofit for high-level lighting poles cracked at the pole-to-base plate connection.

1.4 Literature Review

Prior to the initiation of NCHRP Project 10-70, little research was conducted on high-level lighting poles. The available research centered on the collapse in Iowa, discussed in Section 1.1.2. In addition to the investigation by Dexter (2004), field research and FEA were conducted to determine the dynamic characteristics of in-service high-level lighting poles and the effect of the connection geometry on the stress concentration at the pole-to-base plate connection (Warpinski 2006). This research discovered that the damping ratio decreased in higher modes, therefore the damping ratio given in the AASHTO Specification was not necessarily conservative. Additionally, the FEA aspect of the research found a correlation between base plate

thickness and fatigue resistance, supporting Koenigs (2003). Based on the results, a minimum base plate thickness of 3 in (76 mm) with a $^{1}/_{2}$ in (13 mm) thick pole wall and eight anchor rods was recommended for the pole-to-base plate connection. No experimental work was conducted to verify the FEA result.

Concurrent with NCHRP Project 10-70, fatigue performance of welded tube-to-transverse plate connections in mast-arms of sign/signal structures and high-level lighting poles was investigated by the University of Texas at Austin under the Federal Highway Administration Transportation Pooled Fund Program, hereafter referred to by its project number of TPF-5(116) as the TPF-5(116).

TPF-5(116) was performed in two phases. The research on connections in high-level lighting poles was reported by Rios and Stam as part of their Masters theses, which became available in May, 2007 and May, 2009 respectively. The outcome of this test program had no impact on the NCHRP Project 10-70, which was conducted independently and adopted a different research approach, as will be discussed further. The research under TPF-5(116) has been discussed here for completeness.

1.4.1 TPF-5(116) Phase I (2007)

Rios (2007) reported on a subset of the test program consisting of 16 full scale specimens that were representative of high-level lighting poles in service. These tests investigated the effects of the base plate thickness, the effect of the number of anchor rods, and the variation in fatigue resistance for fillet-welded, full-penetration groove welded, and stool base details at the pole-to-base plate connection. Eight connection

details with two replicates each were tested. All specimens were 16-sided, with a 24 in (610 mm) diameter (corner-to-corner) tapered pole with a wall thickness of $^{5}/_{16}$ in (8 mm). The base plates were of 36 in (914 mm) diameter with eight or twelve 1 $^{3}/_{4}$ in (44 mm) diameter anchor rods equally spaced in a 30 in (762 mm) diameter pattern. All test specimens were galvanized.

A total of 10 specimens were constructed with a fillet-welded pole-to-base plate connection. Four specimens were constructed with a 1 $^{1}/_{2}$ in (38 mm) thick base plate; two with eight anchor rods and two with 12 anchor rods. Four specimens were constructed with a 2 in (51 mm) thick base plate; two with eight anchor rods and two with 12 anchor rods. Two specimens were constructed with a 3 in (76 mm) thick base plate and eight anchor rods. In the pattern with eight anchor rods, the rods were aligned with alternate bend corners of the pole. In the pattern with 12 anchor rods, the rods aligned with the bend corners at 90° intervals, with two anchor rods equally spaced on the arcs in between. Specimens with a full-penetration groove welded pole-to-base plate connection with a backing ring were tested, having a 2 in (51 mm) thick base plate and eight anchor rods. Specimens with a full-penetration groove welded pole-to-base plate connection without a backing ring were also tested, having a 3 in (76 mm) thick base plate and 12 anchor rods. Finally, specimens with a stool stiffened connection with eight stools, at alternating bend corners of the pole, were tested with a 2 in (51 mm) thick base plate.

The specimens were tested in pairs in a horizontal configuration, with the base plates of two specimens affixed to a central loading box connected to a vertical

hydraulic actuator. The other ends of the specimens were supported with a pinned/roller connection such that the pair of specimens resembled a simply supported beam loaded at the mid span. For both anchor rod patterns, the specimens were oriented such that a corner aligned with an anchor rod was placed at the extreme tension fiber. Testing was conducted under tension-tension sinusoidal loading at 1.75 Hz and was displacement controlled. Koenigs (2003) had previously noted that the inertial effects of the loading box for a similar test setup altered the load/displacement relationship when comparing static test results to dynamic test results. As such, the displacement limits were determined from static testing of the pair of specimens being tested. Failure of a specimen was defined by a 10% overall reduction in the loads required to meet the minimum and maximum displacements. This corresponded to a drop in stiffness, due to the presence of fatigue cracking. The fatigue tests were conducted under a nominal ($^{Mc}/_{I}$) stress range of 12 ksi (83 MPa) at the pole-to-base plate connection for all test specimens. The section properties were determined through measurements of the two specimens to be tested, with the mean inside flat-to-flat diameter and mean wall thickness used to create a mean section. The required moment to produce the nominal stress was calculated using the properties of the mean section.

Fatigue cracking in the fillet-welded connection occurred at the fillet weld toe, on the pole. Fatigue cracking in the full-penetration welded connections occurred at the toe of the fillet reinforcement on the pole wall. In all specimens, cracking initiated at the extreme tension fiber and typically propagated between 15 in (381 mm) and 30

in (508 mm) at the conclusion of testing. Fatigue cracking in the stool stiffened connection occurred at the weld toe of the fillet weld between the top plate and the pole, on the pole wall.

Results of Phase I tests are shown in Figure 9. The results indicated that increasing the base plate thickness and the number of anchor rods improved the fatigue performance of the pole-to-base plate connections. The fillet-welded connections demonstrated the least fatigue resistance, lower than the Category E′ recommendation of the AASHTO Specification. For the same base plate thickness and number of anchor rods, the full-penetration groove welded connection demonstrated improved performance over the fillet-welded connection. The fillet-welded connection with 2 in (51 mm) base plate and 12 anchor rods, the fillet-welded connection with 3 in (76 mm) base plate and eight anchor rods, and the groove welded connection with 2 in (51 mm) base plate and eight anchor rods exhibited the same fatigue resistance, although less than Category E′. The groove welded connection with 3 in (76 mm) base plate and 12 anchor rods exceeded the fatigue resistance of Category E′. The stool stiffened connection demonstrated a fatigue resistance slightly less than Category E, the best among all test specimens. While the stool stiffened connection did protect the fillet weld at the pole base, the out-of-plane bending was merely shifted to the area above the stool detail, and cracking still occurred. Overall, these test results demonstrated the effect of base plate flexibility on the fatigue resistance of the pole-to-base plate connection. The connection with a $1\ ^{1}/_{2}$ in (38 mm) base plate and eight anchor rods had the most flexible base plate and exhibited the

worst fatigue performance (well below AASHTO Category E′). As the base plate flexibility was reduced with increased plate thickness and number of anchor rods, the fatigue resistance of the connection improved. As mentioned in Section 1.2, neither the base plate thickness nor the numbers of anchor rods are considered as variables for fatigue resistance in the current AASHTO Specification.

While the test program exhibited general trends of the effects of various connection parameters, the effectiveness of the program establishing design recommendations for the connections tested is questioned. Since two replicates of each connection were tested, only one data point could be obtained for each pair when fatigue cracking of one specimen terminated the tests. This was the case for six of the eight connection details, which was insufficient for a statistical comparison to determine if the difference in fatigue performance between connection types were significant or within the normal variability in fatigue test data. Additionally, all tests provided finite life performance of the connection details, and their CAFLs were not determined experimentally.

1.4.2 TPF-5(116) Phase II (2009)

Stam (2009) reported on a subset of the Phase II test program consisting of 18 full scale specimens, with connection details modified based upon the test results from Phase I. The test program investigated the effects of: external stiffening on details tested in Phase I; the pole wall thickness; the base plate thickness; the number of anchor rods; and the size of base plate opening in full-penetration groove welded

connections. In addition, the tests investigated the difference in performance of poles produced by Valmont Industries and Pelco Structural.

To investigate the effects of external stiffening, an external collar was added to the pole specimens with fillet-welded and full-penetration groove welded connections tested in Phase I. These specimens had a $^{5}/_{16}$ in (8 mm) thick pole and a 3 in (76 mm) thick base plate with 12 anchor rods. The specimen employing a full-penetration groove welded connection without a backing ring had a base plate opening diameter of 20 $^{1}/_{2}$ in (521 mm), which was 85.4% of the pole diameter. The diameter of base plate opening in the specimen employing a groove welded connection with a 3 in (76 mm) high backing ring was 12 $^{1}/_{2}$ in (318 mm), which was 52.1% of the pole diameter. Decreasing the base plate opening was intended to improve fatigue performance by increasing base plate stiffness. Two replicates each were tested of the external collar fitted to a fillet-welded connection, full-penetration groove welded connection with a backing ring, and full-penetration groove welded connection without a backing ring.

To investigate the effect of pole wall thickness, the thickness was increased to $^{1}/_{2}$ in (13 mm) for the full-penetration groove welded connection with an internal backing ring. These specimens maintained the 24 in (610 mm) outer corner-to-corner diameter, and had 12 anchor rods, a 3 in (76 mm) thick base plate, and a 12 $^{1}/_{2}$ in (318 mm) diameter opening in the base plate. This specimen did not have an external collar. Two replicates were tested.

A variation of the stool stiffened connection detail was tested in three configurations. The connection was a variation of the one shown in Figure 6. The top

plates of the individual stools were joined into a single annular plate, and welded to the pole wall with a fillet weld at the top. The connection was investigated with both eight and 12 anchor rods arrangements. One version with 12 anchor rods used the orientation previously discussed for Phase I. The second version was altered, with the anchor rods previously aligned with corners instead aligned with the flats on the pole wall. The base plate for these specimens was 2 in (51 mm) thick; the top plate on the stiffeners was 1 $^{1}/_{4}$ in (32 mm) thick. Two replicates of each configuration of the continuous stool stiffened connection were tested.

To investigate the influence of manufacturing on the fatigue performance of the pole-to-base plate connections, specimens with a fillet-welded connection and two types of full-penetration groove welded connections were fabricated by Pelco Structural. The specimens with a fillet-welded connection were fitted with an external collar and had 16 anchor rods and a 3 in (76 mm) thick base plate. Two replicates of this specimen type were tested. Two specimens with a full-penetration groove welded connection were tested, one with a backing ring and one without. Both had a 3 in (76 mm) thick base plate with 16 anchor rods and a 12 $^{1}/_{2}$ in (318 mm) diameter opening in the base plate.

The Phase II testing was conducted using the same test setup and methodology of Phase I. The reported stress range assumed that stiffeners and collars did not participate in bending, and section properties were based on the pole wall where it intersects the base plate. This is the same location at which the stress range was calculated, regardless of the location of other welds in the connection. This method

for determining the nominal stress causes the test results to be questionable. By neglecting the stiffeners and collars in determining the section properties, the fatigue results are only valid for the specific geometry of stiffener or collar tested. Section 3.3 discusses the static test results for stiffened specimens, in which the stiffeners were found to participate in bending. The stress ranges reported here for TPF-5(116) are the calculated values provided by Stam (2009). All stress ranges are for the weld toe on the pole wall at the pole-to-base plate weld.

The specimens constructed with the stool connection were tested at 12 ksi (83 MPa) nominal stress range. The poles constructed with a thicker pole were tested at the same load range as the specimens with the same weld detail, thinner wall, and external collar. The corresponding nominal stress range was 11.4 ksi (79 MPa) at the pole-to-base plate connection. The specimens with a full-penetration groove welded connection without a backing ring were tested at 12 ksi (83 MPa) nominal stress range at the pole-to-base plate connection. All other specimens were tested at 18 ksi (124 MPa) nominal stress range.

Fatigue cracking in the fillet-welded connections with an external collar occurred at the fillet weld toe on the pole for specimens with 12 anchor rods and at the collar termination weld toe on the pole for specimens with 16 anchor rods. Fatigue cracking in the full-penetration groove welded specimens with a backing ring and external collar occurred at the collar termination weld toe, on the pole. Fatigue cracking in the full-penetration groove welded specimens with an external collar and without a backing ring occurred at the pole-to-base plate fillet weld reinforcement, on

the collar wall. Fatigue cracking in the full-penetration groove welded specimens without an external collar occurred at the weld toe of the fillet weld reinforcement, on the pole. Fatigue cracking in the stool connection occurred above the top plate at the fillet weld toe, on the pole. Crack lengths and the location of crack initiation along the perimeter were not reported for Phase II.

Results of Phase II tests are shown in Figure 10. The fillet-welded connection with an external collar from Pelco Structural exhibited a fatigue resistance of Category E′, the least among all. The full-penetration groove welded connection with a $^1/_2$ in (13 mm) wall also demonstrated Category E′ resistance. The stool connections demonstrated similar fatigue resistance for all variations, ranging from just below Category D to just below Category C. The fillet-welded connection with an external collar from Valmont Industries demonstrated fatigue resistance just below Category D as well. Both full-penetration groove welded connections with an external collar from the Valmont Industries demonstrated Category C resistance.

The multitude of variables tested within Phase II limits conclusions regarding the effect of each variable in altering fatigue performance. For the same number of anchor rods and base plate thickness, the stiffening collar improved the fatigue resistance of the full-penetration groove welded connection without a backing ring from Category E' resistance to Category B'. For the same geometry and with both specimens fabricated by Pelco Structural, the full-penetration groove welded connection with a backing ring demonstrated improved fatigue resistance over the same connection without a backing ring. The specimen with a backing ring was just

below Category D, while the specimen without was just above Category E resistance. The stool connection demonstrated improved fatigue resistance over the version tested in Phase I without a continuous top plate, increasing the fatigue resistance from Category E to Category D. Additionally, rotating the location of the anchor rods on the stool connection caused little difference in fatigue resistance, with both details demonstrating Category D resistance.

By testing many variables with a limited number of replicates, the data were of little value for statistical analysis. As with Phase I, it is impossible to determine if the difference in fatigue performance is within the normal variability in fatigue test data. The specimen design methodology also makes it difficult to determine the effect of a particular variable. For example, in Phase II, two specimens were constructed with a $^{1}/_{2}$ in (13 mm) thick pole to determine the effect of the pole wall thickness. These specimens has a 3 in (76 mm) thick base plate, 12 anchor rods, and a 12 $^{1}/_{2}$ in (318 mm) diameter opening in the base plate. The most similar specimens with a $^{5}/_{16}$ in (8 mm) thick pole were tested in Phase I. These specimens had a 2 in (51 mm) thick base plate, eight anchor rods, and a 20 $^{1}/_{2}$ in (521 mm) diameter opening in the base plate. The fatigue resistance of the Phase I specimens was below Category E′. The fatigue resistance of the Phase II specimens was just below Category E. With four variables altered, it is difficult to determine the effect of wall thickness on fatigue resistance from these results. By changing multiple variables between specimen types, the test program limited the conclusions that can be drawn from the results.

Fatigue testing in both Phase I and Phase II was finite life, with no attempt made to determine the CAFL of the details used. The AASHTO Specification recommends that all high-level lighting poles be designed for infinite life. Furthermore, the research did not determine if the correlations between finite life performance and CAFL developed for the AASHTO Bridge Specification are valid for high-level lighting poles. These test results are accordingly of limited use for designing new high-level lighting pole structures.

1.5 Scope

The scope of this thesis is limited to the experimental of behavior and fatigue performance of cost-effective connection details developed under NCHRP Project 10-70, as well as the design and experimental studies of a possible jacket retrofit of cracked poles. The discussion is limited to 23 of the total 80 specimens tested under the research program. The three specimen types were identified by Roman numerals as Type X, Type XI and Type XII. A total of three Type X specimens were tested. These specimens were constructed with a fillet-welded pole-to-base plate connection and a frame-reinforced handhole. A total of 10 Type XI specimens were tested. These specimens were constructed with a full-penetration groove welded pole-to-base plate connection and a frame-reinforced handhole. A total of 10 Type XII specimens were tested. These specimens were constructed with a stiffened fillet-welded connection. A single jacket retrofit specimen was designed and its fatigue performance was evaluated to determine if it provided a cost-effective alternative to replacement of fatigue-damaged high-level lighting poles.

1.6 Methodology

Specimens were designed based on FEA results. The specimen design and FEA are outside the scope of this thesis. Static testing was conducted on a specimen of each type, which was elaborately gaged with conventional strain gages to understand behavior and determine fatigue critical detail. These measurements were guided by FEA results and were conducted to corroborate the findings. Measurements were also conducted by Three-Dimensional Image Correlation Photogrammetry (3D-ICP) to obtain spatial distribution of the stress field and corroborate the findings of FEA and conventional measurements. Fatigue testing was conducted for establishing finite life and infinite life fatigue performance, with particular focus on determining the CAFL. Measurements were made of the Type XI weld profiles and FEA was conducted on extreme-case welds to determine the effects of the variation of weld geometry on the scatter observed in fatigue test results. The jacket retrofit was designed using FEA. The notch-stress approach was employed to estimate the CAFL of the jacket retrofit. The jacket retrofit was fabricated and fatigue tested while attached to cracked specimens to establish the infinite life fatigue performance of the jacket retrofit. Based on the findings of this research, recommendations for fatigue design of new structures and recommendations for further research are proposed.

1.7 Outline

The thesis contains eight chapters and two appendices. The first chapter introduces the background and the problem statement and discusses the issues with designing high-level lighting poles for achieving their required service life.

Motivation for the research presented in this thesis is discussed and the research scope and methodology are provided.

The second chapter describes the high-level lighting pole specimens tested in the experimental program. The chapter provides details of the testing setups and the instrumentation methods. In addition, the test protocols are included in the chapter.

The third chapter discusses the strain results from finite element analyses and compares the results to strain measurements collected by 3D-ICP and strain gages during static testing.

The fourth chapter discusses the fatigue test results including the observed failure modes, fatigue crack growths, and assessment of fatigue resistance.

The fifth chapter investigates the effects of weld geometry on the observed scatter in test data. Measurements of as-built weld profiles in specimens using 3D-ICP are presented and effects of their variability on the fatigue resistance of the pole-to-base plate connections are evaluated using finite element analyses.

The sixth chapter compares two methods of predicting crack propagation in pole based on the observed crack size. Fracture surface photographs and crack size data are used to determine the effectiveness of the methods.

The seventh chapter evaluates the retrofit jacket scheme for fatigue cracked high-level lighting poles. Finite element analysis results for the retrofit are discussed. The results of laboratory testing to establish the constant amplitude fatigue limit for the retrofit jacket are presented.

The final chapter presents the conclusions, recommendations, and requirements for further research.

Appendix A contains the crack propagation records obtained during fatigue testing.

Appendix B presents the background information for 3D-ICP, describing the concepts, terminology, and methodology used in this research. Included are the results of parametric studies to determine a suitable filtering algorithm and settings for 3D-ICP strain results.

2. DETAILS OF EXPERIMENTS

The details of the experimental studies are provided in this chapter. This includes description of specimens, testing setups, instrumentation, and experimental protocols. In the test program the specimen types were identified by Roman numerals. Individual specimens of each type were identified by an Arabic numeral suffixed to the specimen type. Specimens Type X, Type XI, and Type XII were included in the scope of this thesis and are presented in the following.

2.1 Description of High-Level Lighting Pole Specimens

The specimens were designed to represent the lower section of a high-level lighting pole. A total of twenty-three full size specimens were tested. All specimens had a 16-sided cross-section with a 4 in internal bend radius at the corners and $^{5}/_{16}$ in (8 mm) thick wall. The poles were tapered at 0.14 in (3.6 mm) per 1 ft (305 mm). The exterior flat-to-flat distance of the pole section was 24 in at the top of the base plate. For ease of comparison and data assimilation, the pole cross section was chosen to match the high-level pole specimens tested under TPF-5(116) as discussed in Chapter 1. The same pole cross section was also suggested by the Wyoming Department of Transportation (WYDOT). All specimens had a 36 in (914 mm) diameter base plate and a 30 in (762 mm) diameter bolt circle. All specimens were constructed of A572 Gr. 50 steel and were hot-dip galvanized.

The Type X specimens were designed with consideration to standard drawings for high-level lighting poles received from WYDOT during the survey of state

departments of transportation at the onset of the research project. This was the only DOT that had standard drawings for high-level lighting poles at the time the project was initiated in 2006. The drawings specified a minimum 16-sided cross-section, a maximum corner-to-corner distance of 24 $^{1}/_{4}$ in (616 mm), and a full-penetration groove welded pole-to-base plate connection. During the design phase of Type X specimens, the interim test data from Phase I of TPF-5(116) became available. As discussed in Chapter 1, this study indicated that a full-penetration groove welded connection had improved fatigue resistance over a fillet-welded connection with similar geometry. To further the goal of developing cost-effective connection details under NCHRP Project 10-70, it was decided to test more full-penetration groove welded connections than fillet-welded connections. Due to the fact that the test matrix called for three Type X specimens and ten Type XI specimens, Type X was selected to include the fillet-welded pole-to-base plate connection.

2.1.1 Type X Specimens

The Type X specimens were designed to extend the TPF-5(116) specimens to a practical extreme of base plate stiffness. A total of three Type X replicates were tested. The specimens tested under TPF-5(116) Phase I containing fillet-welded pole-to-base plate connections had 2 in (51 mm) and 3 in (76 mm) thick base plates and eight and 12 anchor rods. The study results demonstrated that the thicker base plate with more anchor rods provided better fatigue resistance. Accordingly, to investigate the effect of further increase in base plate stiffness, the Type X specimens were designed with a 3 in (76 mm) thick base plate with 16 anchor rods uniformly spaced

on the bolt circle, with each anchor rod aligned with one corner of the pole. Use of 16 anchor rods also provided symmetry to the arrangement of anchor rods with respect to the corners and flat faces of the pole, which was not possible with 12 anchor rods. Efficacy of this design was evaluated by FEA conducted under NCHRP Project 10-70 (Roy, 2007), where the TPF-5(116) specimens as well as the Type X specimen were analyzed using the proposed analytical protocol. The design drawings for the Type X specimens are shown in Figure 11 and Figure 12. The specimen was provided with a reinforced handhole as per the WYDOT standard drawings. The specimens tested under TPF-5(116) did not include handhole details, which are always provided in the high-level lighting poles and have developed fatigue cracking in service, as discussed in Section 1.1.2. In the design drawings, the clear distance between the handhole frame and the top of the base plate was specified as 14 in (356 mm). In the fabricated specimen, however, this distance was 11 in (279 mm). The specimens were tested as fabricated to prevent a delay in the testing program.

2.1.2 Type XI Specimens

The Type XI specimens were designed to include a full-penetration groove welded pole-to-base plate connection. The detail was based on the WYDOT standard drawing discussed in Section 2.1.1 and was also tested under TPF-5(116) Phase I, the results of which were available at the time of designing this specimen. Figure 13 and Figure 14 are the design drawings for the Type XI specimens. For ease of comparison, the overall sizing of the specimen was maintained the same as the Type X specimens. Only the pole-to-base plate connection and the base plate parameters were

different. The full-penetration groove welded connection used a 2 in (51 mm) by $^1/_4$ in (6 mm) thick backing ring, which was welded to the pole and the base plate at the top and bottom, respectively. The groove weld was provided with a fillet reinforcement that matched the fillet weld in Type X specimens, removing the nominal weld geometry as a potential variable between specimen types.

The base plate of the Type XI specimen was designed as a new cost-effective solution for improving fatigue performance. Test results from Rios (2007) indicated an improvement in fatigue resistance when the base plate stiffness was increased by increasing its thickness or providing more anchor rods. As stated in Roy et al. (2010), the flexibility of the base plate is affected by the base plate thickness, the opening, the number of anchor rods, and the bolt circle ratio, defined as the ratio of the bolt circle diameter to the pole diameter. Due to the fact that the pole sits on top of the base plate rather than passing through it, the full-penetration groove welded connection allows stiffening of the base plate by decreasing the diameter of the opening at the center of the base plate. An opening diameter of 14 in (356 mm) was specified, which was deemed by the fabricator to be the minimum access required to produce a good quality weld between the backing ring and the pole wall. The quality of this "seal" weld, so named because it seals the crevice between the backing ring and pole from corrosive liquids during the galvanizing process, is important because the weld provides an alternate load path and is therefore susceptible to fatigue cracking. The opening in the base plate was provided with two 1 in (25 mm) wide slots, which extended to $^1/_4$ in (6 mm) from the backing ring. These slots facilitated the flow of liquid zinc during the

galvanizing process. The base plate was 2 $^{1}/_{2}$ in (64 mm) thick with 8 anchor rods located at alternating bends in the pole cross-section. These parameters were determined through finite element analyses conducted in the project to maintain the same stress concentration at the weld toe on the pole as that of the Type X specimens.

2.1.3 Type XII Specimens

The Type XII specimens were designed with a stiffened fillet-welded pole-to-base plate connection. Figure 15 and Figure 16 are the design drawings for the Type XII specimen. The stiffened fillet-welded connection was investigated as a way to lower the stresses at the fillet weld toe at the base. As discussed in Roy et al. (2009), stiffeners achieve this effect by acting as an alternate load path and decreasing out-of-plane distortion in the pole wall at the pole-to-base plate connection. While stresses at the fillet weld toe at the base are reduced, the stiffener termination on the pole and on the base plate become additional potential crack initiation sites. For the connection tested, eight triangular stiffeners were provided at alternating corners on the cross-section between the base plate and the pole wall to reduce the flexibility of the base plate and to limit out-of-plane deformation of the pole wall. A 2 in (51 mm) thick base plate was specified as a minimum, based on FEA conducted by others as part of the project (Roy et al. 2011). The rigidity provided by the stiffeners removed the need for a thicker plate. The specimen was fastened using eight anchor rods aligned with corners alternating the stiffeners.

The stiffener thickness, stiffener height, and stiffener termination angle at the pole wall were optimized through parametric finite element analyses conducted under

the project (Roy et al. 2009). Separate analyses were conducted with a stiffener in the loading plane and an anchor rod in the loading plane, as the direction of in-service wind loading is random. It was determined that the possible failure locations were the fillet-welded connection, the stiffener termination on the pole, and at the stiffener termination on the base plate. The optimization criteria were to eliminate the possibility of cracking at the stiffener termination on the base plate, producing the lowest possible stresses at the stiffener termination on the pole and at the fillet-welded connection, and providing comparable magnitudes at the two failure locations. Figure 17 is the design drawing for the finalized stiffener dimensions. The specified stiffener was 18 in (457 mm) high and $^{3}/_{8}$ in (10 mm) thick, with a 15° stiffener termination angle on the pole. These dimensions, and the orientation of the stiffeners in-plane with the loading, were selected to slightly favor failure at the stiffener termination.

No handhole was provided in the Type XII specimens. It was observed in the Type X and Type XI specimens that cracking tended to initiate at the pole-to-base plate weld toe opposite to the handhole. FEA of specimens Type X and Type XI confirmed that the proximity of the handhole to the base plate had a stress relieving effect to the welded connection at the base. It was decided that the thirteen specimens with the handhole detail produced a sufficient number of replicates and the handhole was eliminated from the Type XII specimens to avoid any biasing of fatigue crack growth.

2.2 Test Setups

2.2.1 Loading Arrangement

The specimens were tested in the ATLSS Engineering Research Center at Lehigh University. Figure 18 shows the test setups, where two specimens could be tested simultaneously. The specimens were installed vertically, fixed at the base, and loaded laterally using hydraulic actuators that reacted against the reaction wall in the laboratory. The test setups and loading simulated the in-service condition and the effects of vortex shedding on high-level lighting poles in the first mode shape. Although the second and third modes are the primary modes of vibration in service, the deviation in the test setup had no effect on the fatigue resistance of the tested details as a function of the applied stress range. The test setups were designed for full stress reversal. The actuators used were Vickers TJ actuators with a capacity of 30 kips (133 kN) and MTS 244.22 actuators with a capacity of 22 kips (98 kN). Figure 19 shows a schematic of the test setup. Tests were conducted using a computer controlled closed loop servo-hydraulic system, manufactured by Vickers. For simplicity, the half of the specimen facing the actuator and the reaction wall is hereafter referred to as the front of the specimen. In specimens containing the handhole detail, the frame was oriented at the center of the front side.

The test setups were designed for independent control of each specimen tested. When a specimen showed signs of cracking, it could be shut down for inspection without stopping testing on the other specimen. A large crack in a single specimen did not alter the stress ranges in the other test specimen, as in dual-specimen setups.

Additionally, testing could continue on one specimen while a second specimen was being removed and replaced.

2.2.2 Specimen Installation

The specimens were installed to simulate the in-service condition, with discrete supports at each anchor rod. Figure 20(a) shows the in-service condition at the base, where the structure is installed on leveling nuts on the anchor rods that are built into a concrete foundation. Figure 20(b) shows the boundary condition that was incorporated at the base of the specimens. A 4 in (102 mm) thick plate was set on the laboratory strong floor with a leveling layer of hydrostone, and was held down at the built-in anchor points. This plate served as the foundation for the specimens. Holes were drilled and tapped in the plate for the 1 $^{3}/_{4}$ in (44 mm) diameter anchor rods. The specimens were installed on washers at anchor rods that provided a gap between the foundation plate and the base plate, creating discrete supports. Washers and nuts were fitted on the anchor rods above the specimen base plate and tightened the turn-of-the-nut method with a hydraulic wrench. This configuration allowed for pretensioning of the entire length of the anchor rod between the foundation plate and the top of base plate. This arrangement contrary to field installations, where only the part of the anchor rod between the bottom leveling nut and the top nut is pretensioned. As a result, the anchor rods below the leveling nuts experience the entire stress fluctuation from the supported structures, often leading to fatigue cracking in inadequately designed rods. Combined with oversized anchor rods, the arrangement used in the test program eliminated fatigue cracking of anchor rods. A previous testing program by

Ocel (2006) transitioned to a similar foundation configuration after experiencing repeated anchor rod failures with a foundation using leveling nuts, which interrupted the test program.

2.2.3 Loading Fixture

During fatigue testing, three actuator-to-specimen connection designs were employed. Figure 21 shows the connection used at the beginning of the test program. The actuator was connected to the specimens using four threaded rods, which extended fully through the pole and were separately connected to the opposite faces of the pole to limit ovalization during loading. The connections to the pole were made from plywood spacers and steel plate bolted against both interior and exterior surfaces on both the actuator side and the far side. The spacers allowed for fitting of the flat surface of the actuator clevis plate to the curved specimen surface. This loading arrangement was used for all Type X specimens and all Type XI specimens except XI-3. The drawback to the fixture was that it required a person to crawl inside the specimen while it was laid on its side on the laboratory floor for installing the spacers and bolts within the specimen. This was time consuming and labor intensive. Furthermore, this connection was often loosened during fatigue cycling and cracked the threaded rods.

To save time in changing specimens and to avoid fatigue cracking of the threaded rods, an alternative collar-type connection that could be slipped over the top of the specimen was investigated. Figure 22 shows the collar design fitted to a specimen. Figure 23 is a plan view of the collar. For a uniform fit up, the collar was

constructed using a portion of a pole wall from a specimen that was already tested. Lateral stiffener plates were welded to the two halves of the collar both at the top and bottom, and a connection plate was provided on the half matching the actuator. The collar halves were clamped on the specimen with fully pretensioned threaded rods and the actuator was connected to the connection plate with fully pretensioned bolts. This connection was only employed for specimen XI-3 (refer to the left specimen in Figure 18), and had limited success. While the collar fixture was easy to fit on, incomplete fusion at the welded connection between the collar wall and the top stiffener plates led to early fatigue fracture of the collar. Due to limited project budget and the relatively expensive fabrication of the collar fixture, this fixture was abandoned.

The third fixture was similar to the first one, but the loading rods were pretensioned through the entire specimen against the front and the rear surfaces. Figure 24 shows a section of the connection design. The plywood spacers and the steel clamp plate from the first fixture arrangement were retained on the outside of the tube wall. Inside the pole, however, a spacer was fabricated from four hollow pipes and beveled plates at each end of the pipes to match the contours of the specimen. This spacer was inserted inside the specimen, and the rods were tensioned through the actuator clevis, through the outer clamp and spacer between the clevis and the pole wall, through the pipe spacer inside the specimen, and through the outer clamp spacer on the far side. The arrangement provided a self-equilibrating system that limited ovalization of the pole and allowed pretensioning the rods effectively along their

entire length. As a result, fatigue fracture of the rods due to loss of pretension was reduced. This arrangement also facilitated quicker installation of the specimens.

2.3 Instrumentation

2.3.1 Displacements and Load Sensors

The displacements were measured at the point of and in the direction of load application by MTS Temposonics for the MTS actuators and by internal linear variable displacement transducers (LVDT) for the Vickers actuators. The applied load was measured by in-line fatigue-rated load cells. MTS model 661.20E-03 load cells with a capacity of 22 kip (98 kN) in tension and compression were fitted to the MTS actuators and Lebow model 3156-154 load cells with a capacity of 50 kip (222 kN) in tension and compression were fitted to the Vickers actuators. As the load range during testing never exceeded 20 kip (89 kN), the Lebow load cells were specifically calibrated over a 20 kip (89 kN) range to provide a suitable resolution for testing.

2.3.2 Strain Gages

Bondable strain gages were installed at critical locations on each specimen. Locations of strain gages were determined based on FEA results of the specimens that were performed by others as part of the project. For each specimen type, a single specimen was extensively gaged to determine the distribution of stresses in different regions of the specimen, and to validate the FEA models of the specimens.

Prior to installation of strain gages, the pole surface was ground to remove galvanizing. While installing strain gages adjacent to weld toes, care was taken to

avoid any contact between the weld toe and the die grinder or sanding wheel. Grinding marks parallel to the weld toe were sanded smooth to eliminate potential crack initiation sites. All strain gages were 120 Ω resistance. Tokyo Sokki Kenkyujo (TML) model FLA-1-11-003LE uniaxial strain gages with a gage length of 1 mm (0.04 in), hereafter called 1 mm gages, were used to measure local strain in areas with rapidly varying stresses. Vishay Micromeasurements model CEA-06-250UN-120 uniaxial strain gages with a gage length of $^1/_4$ in (6 mm), hereafter called $^1/_4$ in gages, were used to measure strain in areas away from stress concentrations.

TML model FXV-1-11-002LE uniaxial strip gages, a series of five gages having a 1 mm (0.04 in) gage length on a common backing at 2 mm (0.08 in) centers and oriented in the lengthwise direction of the strip, were used abutting the weld toe to measure the strain gradient in key locations. These gages are hereafter called 1 mm strip gages. TML model FRA-1-11-003LE rosette gages, a series of three strain gages with a 1 mm (0.04 in) gage length arranged circumferentially at 45º intervals, were used to determine principal strains, where the nature and direction of major strains were not known in advance. These gages are hereafter called 1 mm rosette gages.

2.4 Strain Gaging Plans

The following sections detail the placement of strain gages on test specimens. One specimen of each type was extensively gaged to understand behavior under load. Remaining specimens of each type were gaged for fatigue testing control and crack detection purposes. Extensively gaged specimens also included these fatigue testing and crack control gages.

2.4.1 Type X Specimen

Specimen X-2 was elaborately gaged to understand its behavior under load. Figure 25 details the gage arrangement on the exterior face of the specimen. Gage locations denoted by a solid shape were only for the elaborately gaged specimen. Locations denoted by an outline had strain gages on both the elaborately gaged specimen and other specimens. A 1 mm strip gage was installed at the pole centerline at the fillet weld toe at the pole-to-base plate connection and at the fillet weld toe at the bottom of the handhole frame. Measurements from these gages provided a comparison between the decay in the stress field in the actual structure and FEA results. Two 1 mm gages were placed longitudinally in-line, with the gages installed as close as possible to each other, at the center of the first flat and the center of the first bend adjacent to the pole centerline. These gages were to measure the variation of stress along the perimeter of the pole while also measuring the decay in the stress field in the longitudinal direction. In addition, $^1/_4$ in gages were placed 6 in (152 mm) above the 1 mm strip gage and the 1 mm gages for comparison of measured stress and FEA results away from stress concentrations. Figure 26 details the strain gage locations on the interior of the specimen. On the interior, $^1/_4$ in gages were placed on the pole wall opposite the exterior $^1/_4$ in gages to measure the change in stress through the thickness. At the handhole corner, a 1 mm rosette gage was installed on the interior and exterior of the pole to determine the principal strains. A 1 mm gage was located directly below each rosette to provide the strain gradient between the two points.

Four strain gages were provided on specimens X-1 and X-3 as shown in Figure 25. A $^1/_4$ in gage was placed at a distance of 70 in (1778 mm) from the toe of the pole-to-base plate fillet weld on the front face of the pole, aligned with the center of the handhole. Based on FEA the longitudinal stress (along the centerline of the pole) at this location was equal to the nominal stress computed using the section property at this location. At other locations, the stresses were influenced either by the loading arrangement or the handhole. This strain gage was referred to as the control gage, as strains measured at this gage were used to control the tests. A second $^1/_4$ in gage was placed between the base weld toe and the handhole frame to measure the stress in this region for comparison to the finite element analysis results. A 1 mm gage was placed as close as practical to the base weld toe and another was placed at the handhole corner. The purpose of these strain gages was to detect cracking in the specimen through a significant change in the measured strain.

2.4.2 Type XI Specimen

Specimen XI-6 was elaborately gaged to understand its behavior under load. Figure 27 details the gage arrangement on the front exterior face of the specimen. Two 1 mm gages were placed longitudinally in-line, with the gages installed as close as possible to each other, at the centerline to measure the decay in the stress field in the longitudinal direction. At the handhole corner, a 1 mm rosette gage was installed to determine the principal strain. A 1 mm gage was placed directly below the rosette to provide the strain gradient between the two points. The strain gage layout on the back side of the specimen is shown in Figure 28. A 1 mm strip gage was installed at

the pole centerline abutting the base weld toe to provide a comparison between the decay in the stress field in the actual structure and FEA results. Two 1 mm gages were place longitudinally in-line at the adjacent bend in the pole wall. These gages were to measure the variation of stress along the perimeter of the pole while also measuring the decay in the stress field in the longitudinal direction. In addition, $^1/_4$ in gages were placed 6 in (152 mm) above the 1 mm strip gage and the 1 mm gages for comparison of measured stress and FEA results away from stress concentrations. The strain gage layout on the interior of the specimen, opposite the handhole, is shown in Figure 29. The handhole side has been cut away at the neutral axis for clarity. On the interior of the pole, $^1/_4$ in gages were installed on the pole wall opposite the exterior $^1/_4$ in gages to measure the change in stress through the thickness. A strip gage was installed on the pole wall abutting the backing ring seal weld toe, and a pair of 1 mm gages was installed at the center of the adjacent bend. A $^1/_4$ in gage was placed at the center of the backing ring on both front and back centerlines to measure the amount of load sharing between the backing ring and the pole wall.

Six strain gages were provided on specimens XI-1, XI-2, and XI-3. On the front side, $^1/_4$ in gages were installed along the centerline at a distance of 85 in (2159 mm) and 110 in (2794 mm) from the toe of the pole-to-base plate fillet reinforcement weld, aligned with the center of the handhole. On the back side, $^1/_4$ in gages were installed along the centerline at a distance of 55 in (1397 mm) and 110 in (2794 mm) from the toe of the pole-to-base plate fillet reinforcement weld. FEA predicted longitudinal stress equal to the nominal stress computed using the section properties at

these locations. Strains measured at the strain gage 85 in (2159 mm) from the base weld toe were used to control the tests. At the front and back centerlines, a single 1 mm gage was placed 0.2 in (5 mm) from the base weld toe. These gages measured the geometric stress, for verification of the hot-spot stress method, while also detecting cracking through significant changes in the measured strain.

Specimens XI-4 and XI-5 had a pair of $^1/_4$ in gages added to the above gage plan. The gages were installed on the interior of the specimens at the vertical center of the backing ring, at the front and back centerlines. These strain gages measured the change in the stress range in the backing ring as testing progressed and cracks formed on the pole exterior.

Specimens XI-7 through XI-10 had a pair of 1 mm gages added to the gage plan of Specimens XI-4 and XI-5. A 1 mm gage was installed at both the front and back centerlines on the interior of the pole, 0.2 in (5 mm) from the backing ring seal weld toe. These strain gages detected cracks through significant changes in the measured strain.

2.4.3 Type XII Specimen

Specimen XII-3 was elaborately gaged to understand its behavior under load. To examine the effect of the stiffener orientation to the loading plane, the specimen was loaded in-plane with anchor rods then rotated in the setup and loaded in-plane with stiffeners. Figure 30 details the strain gage locations on the back exterior face of the specimen. A total of four 1 mm strip gages were placed, oriented in the longitudinal direction, at two adjacent stiffener terminations and two adjacent bends at

the toe of the pole-to-base plate fillet weld. Measurements from these gages provided a comparison between the decay in the stress field in the actual structure and FEA results. A $^1/_4$ in gage was offset above the strip gages at both loading planes to provide comparison of measured stress and FEA results away from stress concentrations. Additionally, six $^1/_4$ in gages were arrayed on the side of the stiffener on the back face that was in the loading plane, as shown in Figure 31. The stress measured at these gages was used to determine the effectiveness of the stiffener in load sharing.

Ten strain gages were provided on the remaining Type XII Specimens. On the front side, $^1/_4$ in gages were placed at a distance of 36 in (914 mm) and 72 in (1829 mm) from the toe of the pole-to-base plate fillet weld. On the back side, $^1/_4$ in gages were placed at the same locations. Based on FEA the longitudinal stress at these locations was equal to the nominal stress computed using the section properties at these location. Strains measured at the strain gage 72 in (1829 mm) from the toe of the pole-to-base plate fillet weld on the back side were used to control the tests. To reduce the number of channels monitored, this was the only $^1/_4$ in gage from which data was collected during fatigue testing. The other $^1/_4$ in gages were monitored during static testing only. A total of six 1 mm gages were installed on each specimen for crack detection. A single gage was installed on the pole 0.2 in (5 mm) from the weld toe at both stiffener terminations in the loading plane, and 0.2 in (5 mm) from the toe of the pole-to-base plate fillet weld at the bends to either side of the instrumented

stiffeners. These gages measured the geometric stress while also detecting cracking through significant changes in the measured strain.

2.5 Data Collection

Data was collected using Campbell Scientific CR9000 digital data loggers. CR9052DC filter modules, capable of real-time filtering, were used for fatigue testing to reduce the noise levels in the measurements. CR9050 analog modules were used for the elaborately gaged static test, as these modules provided fourteen channels, compared to six for the filter modules, and adequate filter modules were not available. The lack of filtering in the analog cards yielded higher noise in the data, which was taken care of in several ways to maintain the data quality. Since the static tests were conducted at a slow loading rate (see Section 2.6), sufficient time was available for data collection per channel at a slower sampling rate that included a longer settling time and a longer integration time per channel to eliminate noise. Integration and settling times varied with the number of strain gages used. Integration time was on the order of 300 microseconds and settling time was on the order of 100 microseconds for the elaborately gaged static tests. In addition, the collected data was averaged over a 30 second period to remove the noise further. All programming was done using Campbell Scientific PC9000 software. When filter modules were used, the pass band for the filter was set to two-fifths of the sampling frequency, and the sampling rate was set to a minimum of five times the testing frequency to eliminate aliasing in the data. For fatigue tests conducted at 4 Hz and 8 Hz, data were sampled at 20 Hz and 50 Hz, respectively. An excitation of 3 volts was applied to the strain gages by an

external power source. This excitation provided adequate signal strength without causing overheating. An excitation of 10 volts was supplied to the displacement transducers by the Vickers control system. The load cell output was filtered with Vishay Model 2310 signal conditioning amplifiers. An excitation of 10 volts was used for all load cells, supplied by the signal conditioners. Measurement ranges were set at 20 mV for strain gages and 5 volts for load cells and displacement transducers, to maximize the resolution over the respective outputs.

The load and displacement sensors, the data acquisition system, and the signal conditioners were calibrated for this test program. In addition, the load cell outputs and multipliers for the data acquisition system were verified in-place by shunt calibrations according to the manufacturer's instructions. The strain gages were also calibrated in-place to offset the resistance of the wire between the specimen and the data logger. The shunt calibrations provided the correct multiplier for the data acquisition system to convert output voltage to microstrain. The field multipliers were checked against the idealized multipliers calculated from the manufacturer's gage factor for each type of strain gage. The difference was less than five percent for all strain gages.

2.6 Static Testing

A static test was performed for every specimen prior to fatigue testing. The static test verified the stresses at the control gage and was used to "shake down" the residual stress in each specimen due to fabrication. This created an elastic response to the fatigue testing loads. The testing procedure was as follows:

1. Balance all strain gages under zero load and record initial displacement value.
2. Apply tensile load at 1 kip (4.4 kN) intervals. At each interval, record displacement value and collect data for thirty seconds. Continue to maximum tensile load to be reached during fatigue testing.
3. Reduce to zero load. Record displacement value and collect data for thirty seconds. Balance all strain gages.
4. Apply compressive load at 1 kip (4.4 kN) intervals. At each interval, record displacement value and collect data for thirty seconds. Continue to maximum compressive load to be reached during fatigue testing
5. Reduce to zero load. Record displacement value. Collect data for thirty seconds. Balance all strain gages.
6. Repeat steps 1 through 5 for at least three trials. If residual strain recorded in step 5 is not negligible after three trials, repeat for additional trials as necessary.

2.7 Fatigue Testing

The variables considered for fatigue testing were the minimum stress, S_{min}, and the stress range, S_r. The loading caused stress reversal, leading to a compressive minimum stress, with a value equal to half the value of the stress range. Due to the presence of tensile residual stresses on the order of the yield stress of the material, the compressive stress was not enough to overcome the residual stress, and the full stress range was effective in causing fatigue damage.

Infinite life and finite life fatigue testing was conducted. The infinite life testing was designed to determine the constant amplitude fatigue limit for the specimen type. For the Type XI and Type XII specimens, four replicates of each type were allocated for infinite life testing. The infinite life testing procedure was as follows:

1. Constant amplitude fatigue limit for detail of interest was estimated based on finite element analysis results.
2. The AASHTO Bridge Specification detail category CAFL value immediately below the estimated CAFL value was selected as the fatigue testing stress range. Refer to Figure 32 for CAFL values.
3. Infinite life fatigue testing was conducted. Specimens that did not develop detectable fatigue cracks after being subjected to stress cycles in excess of the 95% confidence limit to 95% failure life of the detail category were defined as run-out. Refer to Figure 32 for the number of cycles to run-out for the various detail categories. An upper limit of 20 million cycles was used for time and budget considerations.
4. Run-out specimens were inspected for cracking by magnetic particle and dye-penetrant testing. Specimens were then re-run at a stress range corresponding to the next detail category CAFL value.
5. In the event of a specimen failure during the initial infinite life fatigue test, testing for subsequent specimens was started at the stress range corresponding to a lower detail category CAFL value.

Finite life fatigue tests were conducted at stress ranges above the estimated constant amplitude fatigue limit to determine the finite life fatigue resistance. Stress ranges were based on an analytical assessment of the fatigue performance of the detail. The stress ranges were sufficiently separated to determine the linear regression parameters in the log-log basis. The finite life fatigue tests were run to failure, defined by an observed crack size equal to 12 in (305 mm), or one-half of the tube diameter, at the pole-to-base plate connection.

3. STATIC TEST RESULTS

This chapter discusses the results of static testing. One specimen of each type was selected to be elaborately gaged with strain gages. Measurements of the Type XI and Type XII specimens were conducted using both strain gages and three-dimensional image correlation photogrammetry (3D-ICP).

3.1 Type X Specimen

As detailed in Section 2.4.1, specimen X-2 was extensively gaged to determine the behavior of Type X specimens under load. Figure 33 shows the normal stress in the longitudinal direction measured along the pole surface at the control gage, which was located at 70 in (1778 mm) from the base plate. The stress is plotted against the applied load. During the static test the specimen was loaded between +/− 4.6 kip (20.5 kN). Also plotted on the figure is the same stress obtained from FEA and the computed nominal stress. The nominal stress at the control gage was computed as 1.79 ksi (12.3 MPa) under the maximum load of 4.6 kip (20.5 kN) by dividing the bending moment at the section with the nominal section modulus. Three trials were performed and the measurements from all trials are plotted. The measured stress showed repeatability and excellent agreement to the computed nominal stress, confirming that the measurements at this gage could be used for estimating nominal stresses at other sections on the pole and for controlling the fatigue tests. The FEA result differed from the nominal stress and the strain gage measurements. One of the reasons could be that the load was applied to the model as a concentrated load on the

front surface, which ovalized the pole section due to local distortion under the load. The ovalization of the cross-section at the 4.6 kip (20.5 kN) load is shown in Figure 34, with the displacement scaled to 30 times the actual displacement for clarity. As shown in Figure 21, in the test specimen this local distortion was prevented by the loading fixture. In finite element analyses of specimens Type XI and Type XII, the load was applied in halves at the front and back faces of the pole, which limited ovalization of the pole and produced results that displayed better correlation to the strain measurements. Figure 35 shows the stress in the longitudinal direction along the pole wall measured at a strain gage abutting the weld toe at the pole base against the applied load. The measured stresses were repeatable and varied linearly with the applied load. The values were larger than the estimated nominal stress, which was computed as 4.0 ksi (27.6 MPa), as was expected due to geometric and notch stress concentrations. The measured stress was less than the FEA prediction, which was typically observed at the strain gages abutting a weld toe probably due to the way the weld was modeled for the FEA. This is further elaborated later.

The stresses in the longitudinal direction along the exterior and interior pole surfaces are plotted in Figure 36 on a path extending from the weld toe at the pole base to the underside of the handhole in the loading plane. Both the stresses predicted by FEA and measured at the strain gage are plotted. The FEA results on the exterior and the interior surfaces were almost mirrored about a mean stress, which indicated out-of-plane bending in the tube, as shown in Figure 37. The nature of bending changed over the length of the pole. Near the weld toe, the exterior surface stress was higher than

the interior surface stress indicating presence of a hogging bending moment. At about 1 in (25 mm) from the weld toe, stresses on both faces were equal, indicating a point of contraflexure. Beyond this point, the stress on the interior surface was larger indicating presence of a sagging bending moment. Finally, near the handhole frame a hogging bending moment developed. As discussed earlier, this reverse bending resulted from the requirement to maintain compatibility in deformation between the pole and the base plate, and the pole wall and the handhole frame. The stresses measured on the exterior and interior surfaces at the $^1/_4$ in gages, which were 6 in (152 mm) from the weld toe, exhibited a behavior similar to that predicted by the FEA model. The measured stress matched well with the FEA prediction on the exterior surface, however, on the interior surface the measured stress was less than the predicted value. This indicated that the specimen experienced less local bending than predicted by the FEA results. Near the weld toe, the measured stresses at the strip gage were significantly less than the FEA results. Figure 38 is an enlarged view of the same data in the weld toe region. While the same general decay away from the weld toe was observed in both the FEA prediction and the measured stresses, the stress measured in the gage abutting the weld toe was 46.7% less.

The reason for the difference between the FEA result and the measurements at the weld toe was likely due to the way the weld was modeled. In the FE model, the weld was sized as per the nominal dimension shown in the fabrication drawing with a subtended angle of 30° on the pole. The weld toe was modeled as a sharp (zero radius) notch. Theoretically, the stress at the sharp notch of the modeled weld is

infinite. The magnitude of the stress determined by FEA is highly dependent on the mesh size near a stress singularity such as the weld toe. At the weld toe the stress never converges, and keeps on increasing with decreasing mesh size. In the specimen, however, the weld often subtended an angle less than 30° on the pole wall and a finite radius existed at the weld toe. Figure 39(a) shows the idealized weld that was modeled for FEA. Figure 39(b) shows a typical weld cross-section obtained from 3D-ICP measurements. Figure 39(c) shows an enlarged view of the weld termination on the pole, showing a finite radius. Due to the finite radius, the actual notch stress was not infinite at the weld toe and subsequently the measured stress was less than the FEA predicted stress.

The direction of principal stress measured at the handhole corner was consistent with the FEA results, which showed the maximum principal stress was oriented in a nearly vertical direction. The measured principal stress at the exterior rosette was 37.7% lower than the measured stress at the pole base weld toe. The lower stress at the handhole corner correlates with the lack of cracking observed at the handhole for these specimens, as discussed in Chapter 4. The measured principal stress at the interior rosette was 12.0% lower than the exterior rosette. This is consistent with the FEA model, which displayed minimal out-of-plane bending at this location. Due to the presence of the weld surrounding the handhole frame, the FEA result for the principal stress at the handhole was 19.4% higher than the measured value. These results indicate that the FEA model provided a suitable representation of the actual structure. As with other locations, the difference between the modeled and

the actual weld contributed to the difference between the predicted stress and the measured stress adjacent to the weld.

3.2 Type XI Specimen Static Test Results

As detailed in Section 2.4.2, the pole in specimen XI-6 was extensively gaged to determine the behavior of specimens Type XI under load. Figure 40 shows the normal stress in the longitudinal direction measured along the pole surface at the control gage, which was located at 85 in (2159 mm) from the base plate. The stress is plotted against the applied load. During the static test the specimen was loaded between +/− 6.0 kip (26.7 kN). Also plotted on the figure is the same stress obtained from FEA and the computed nominal stress. The nominal stress at the control gage was computed as 2.72 ksi (18.8 MPa) under the maximum load of 6.0 kip (26.7 kN) by dividing the bending moment at the section with the nominal section modulus. The measured stress showed repeatability and excellent agreement to the computed nominal stress, confirming that the measurements at this gage could be used for estimating nominal stresses at other sections on the pole and for controlling the fatigue tests. Figure 41 shows the stress in the longitudinal direction along the pole wall measured at the strain gage abutting the weld toe at the pole base on the back side of the pole against the applied load. The measured stresses were repeatable and varied linearly with the applied load. The values were larger than the estimated nominal stress, which was 6.3 ksi (43.4 MPa), as was expected due to geometric and notch stress concentrations. The measured stress was less than the FEA prediction. The

reasons discussed in Section 3.1 for similar results at the pole base weld toe in the Type X specimen are also valid for the Type XI specimen.

The stresses in the longitudinal direction along the exterior and interior pole surfaces are plotted in Figure 42 on a path in the loading plane extending from the weld toe at the pole base opposite the handhole. The measured stresses at strain gages, the FEA results, and the nominal stress are provided for comparison. The results are for an applied load of 6.0 kip (26.7 kN), corresponding to a nominal stress of 6.3 ksi (43.4 MPa) at the pole-to-base plate weld toe on the pole. The nominal stress was computed by dividing the bending moment at the section with the nominal section modulus, excluding the effect of the backing ring due to its short longitudinal length. While the same general decay away from the weld toe on the exterior surface was observed in both the FEA prediction and the measured stresses, the stress measured at the gage abutting the weld toe was 19.8% less. On the interior surface, the stress measured at the gage abutting the seal weld toe was 8.7% less than the FEA prediction. This suggests that the singularity in the FEA model at the toe of the smaller seal weld affected a smaller portion of the model than the singularity at the larger groove weld. The measured stress in the backing ring indicates that the backing ring participates in load sharing, though at a measured stress only 17.4% of the magnitude of the stress measured at the same point on the exterior face. At 6 in (152 mm) away from the weld toe, the stress measured at the exterior and interior $^1/_4$ in gages matched the FEA results. As discussed in the static test results for the Type X

specimen, the difference between the measured stresses and the FEA results near the weld toe was expected due to the way in which the weld was modeled.

The stresses measured by 3D-ICP in the longitudinal direction along the exterior pole surface are plotted in Figure 43 on a path in the loading plane extending from the weld toe at the pole base opposite the handhole. Also plotted are the FEA results and the strain gage measurements along the same path on the pole exterior surface. The results are for an applied load of 6.0 kip (26.7 kN), corresponding to a nominal stress of 6.3 ksi (43.4 MPa) at the pole-to-base plate weld toe on the pole. Figure 44 shows an enlarged view of the results shown in Figure 43, in the region abutting the weld toe. The stresses obtained from the 3D-ICP measurements and the 1 mm strip gage measurements differed by a maximum of 12.5% of the strain gage measurements. The measured stresses were less than the FEA results by a maximum of 36.4% of the strain gage measurements. Although the stress profiles obtained from the FEA and the measurements exhibited a general trend of decay away from the weld toe, their local trends did not match well. The stress profiles obtained from the 3D-ICP measurements and the FEA results exhibited a similar slope only for a distance of about 0.2 in (5 mm) from the weld toe. The stress profile from 3D-ICP measurements continued to decrease at the initial slope up to a distance of 0.3 in (8 mm) from the weld toe, where it exhibited a valley and began to increase towards the FEA stress profile, attaining a crest at about 0.6 in (15 mm) from the weld toe. The stress profile obtained from the strain gage measurements did not exhibit the valley, and its local trend agreed more with the FEA results compared to the stress profile obtained from

3D-ICP. While the reasons for the deviations in the trends are not clear, a possible explanation for the difference in the FEA and the 3D-ICP stress profiles is the idealized geometry of the connection modeled for the FEA and the actual geometry of the connection in the specimen. In the FE model a gap of $^{1}/_{16}$ in (1.6 mm) was provided between the backing ring and the tube wall. Sections were cut from specimen XI-7 to investigate the presence of this gap in an actual specimen. The sections revealed a non-uniform contact between the backing ring and the pole wall as shown in Figure 45. Such non-uniform contact could have resulted in load sharing between the pole wall and the backing ring by interface friction, causing the local changes in the stress profiles that were noted in the 3D-ICP measurements.

Figure 46 shows the camera image captured during 3D-ICP, with the strain masked area and the area containing valid computation points identified. Also shown on the image are the outlines of the major features of the specimen such as the base plate, the anchor rod and the lock nut, and the weld surface. The 1 mm strip gage, including its wiring, is visible and is delineated for clarity. The vendor for the 3D-ICP equipment, Trilion Quality Systems, initially recommended removal of strain gages prior to 3D-ICP measurement to improve accuracy of measurements by reducing the noise in the data. This way hypothesized to be the reason for a less than adequate accuracy of measurement in an initial study with 3D-ICP, where the strain gages were installed on the surface for verification. In view of the time and cost involved in removing and replacing the already installed strain gages on specimen XI-6, it was decided to conduct 3D-ICP measurements with the strain gages left in place. The first

trial of data analysis showed that the irregular surface of the strain gage lead wires introduced significant noise in the measurements. To remove the effect of the spurious data, the strain gage wires were strain masked in addition to the weld, as discussed in Appendix B. Due to the position of the anchor rod with respect to the measurement area and the size of the view window, very little of the base plate was available for measurement. As such, and because this area was not of interest, it was also strain masked.

Figure 47 shows the strain contour plots from both 3D-ICP and finite element analysis, with both shown in the same scale. Notably absent from the 3D-ICP measurements in

Figure 47(a) is the elevated strain along the weld toe shown in

Figure 47(b). It is unclear why the measurements disagree. As shown at the very top of

Figure 47(a), the stress field is very irregular towards the boundary of the measured area. Such fluctuations are part of the error at the measurement boundary, as discussed in Appendix B, and the data generated in this region was not included in Figure 43 and Figure 44 due to its inaccuracy.

Measurements were also made at the pole base on the handhole side of the specimen, using both the strain gages detailed in Section 2.4.2 and 3D-ICP. On this side, two 1 mm gages were installed abutting each other to provide the stress gradient between the two gages. Figure 48 plots the stresses from FEA against the stresses obtained from strain gages for the pole wall below the handhole and 3D-ICP for the

pole-to-base plate connection. The measurements were made a test load of 6.0 kip (26.7 kN), corresponding to a nominal stress of 6.3 ksi (43.4 MPa) at the pole-to-base plate weld toe on the pole. Figure 49 is an enlarged view of the plot at the weld toe. For this measurement area, the 3D-ICP results from two different filtering algorithms are shown. The mean filter calculates what seems like an appropriate stress at the weld toe, but shows no correlation to the strain gage measurements. The median filter shows good correlation to the strain gage measurements, however parametric studies revealed a median filter is likely to reduce the maximum value at the weld toe.

Figure 50 shows the camera image captured during 3D-ICP, with the strain masked area and the area containing valid computation points identified. Also shown on the image are the outlines of the major features of the specimen such as the base plate, the anchor rod and the lock nut, and the weld surface. Due to the arrangement of the lead wires in relation to the 1 mm gages, a large portion at the top of the frame required strain masking to remove the noise caused by the wires. Figure 51 is an enlarged view around the weld toe near the centerline of the strain gage. There were several small areas along the weld toe where the measurements could not be performed accurately, shown in the figure shaded blue or yellow instead of green. The blue areas represent interpolated points, meaning that the location of the computation point could not be properly determined and its location was interpolated from the surrounding points. The yellow areas represent computation points with a high intersection error, meaning the out-of-plane coordinate could not be accurately triangulated. Points with high intersection error were removed from further

calculations within the software, and appear as blank spots on contour plots. Both interpolation and intersection error are associated with errors in the pattern. As seen in Figure 51, there are two thick black dashed lines on the surface. This was an attempt to provide the centerline of the strain gage and the location of the weld toe for coordinate transformation in post-processing. Unfortunately, these marks caused errors in the measurement of this location and this technique was modified for further 3D-ICP measurement. Figure 52 is the strain contour plot for the mean filter results. Each of the dash lines at the weld toe introduced discontinuity in the results, and caused spurious data in the contour plot. Figure 53(a) shows the same measurements using a median filter. The filter smoothes over the error caused by the points along the weld toe, but also reduces the value of the measured strain at the weld toe. The FEA result is provided for comparison in Figure 53(b). While the magnitude of the strain away from the weld toe is similar for the two plots, the stress concentration at the weld toe was not captured by 3D-ICP. For this location, neither filtering method was able to remove the noise introduced during the measurement process. The lessons learned from the 3D-ICP measurement of the Type XI specimen were applied to later testing of the Type XII specimen.

3.3 Type XII Specimen Static Test Results

3.3.1 Stiffener-on-Center Testing

As detailed in Section 2.4.3, the pole in specimen XII-3 was extensively gaged to determine the behavior of specimens Type XII under load. Figure 54 shows the

normal stress in the longitudinal direction measured along the pole surface at the control gage, which was located at 72 in (1829 mm) from the base plate. The stress is plotted against the applied load. During the static test the specimen was loaded between +/− 7.0 kip (31.1 kN). Also plotted on the figure is the same stress obtained from FEA and the computed nominal stress. The nominal stress at the control gage was computed as 4.0 ksi (27.6 MPa) under the maximum load of 7.0 kip (31.1 kN) by dividing the bending moment at the section with the nominal section modulus. The measured stress showed repeatability and excellent agreement to the computed nominal stress, confirming that the measurements at this gage could be used for estimating nominal stresses at other sections on the pole and for controlling the fatigue tests. Figure 55 shows the stress in the longitudinal direction along the pole wall measured at the strain gage abutting the weld toe at the stiffener termination. The measured stresses were repeatable and varied linearly with the applied load. The values were larger than the computed nominal stress, which was 6.6 ksi (45.5 MPa), as was expected due to geometric and notch stress concentrations. When scale is considered, Figure 55 shows a similar difference between the strain gage measurement and the FEA result when compared to the other specimen types. The reasons discussed in Section 3.1 for similar results at the pole base weld toe in the Type X specimen are also valid for the Type XII specimen stiffener termination.

The stresses in the longitudinal direction along the pole exterior are plotted in Figure 56 on a path in the loading plane extending from the weld toe at the stiffener termination. Also plotted are the FEA results and the 3D-ICP measurements along the

same path on the pole exterior surface. The applied load was 7.0 kip (31.1 kN), corresponding to a nominal stress of 6.6 ksi (45.5 MPa) at the stiffener termination. The nominal stress was computed by dividing the bending moment at the section with the nominal section modulus. As the stiffeners were below the section of interest, they were not a part of the section modulus calculation. At 3 $^{1}/_{2}$ in (89 mm) away from the weld toe, the stress measured at the ¼ in gage matched the FEA result. Figure 57 is an enlarged view of the same data in the region abutting the weld toe over which 3D-ICP measurements were obtained. The stresses obtained from the 3D-ICP measurements and the 1 mm strip gage measurements differed by a maximum of 9.3% of the strain gage measurements. The measured stresses were less than the FEA results by a maximum 31.1% of the strain gage measurements. The 3D-ICP measurements provide excellent correlation to the strain gage measurements in this region. Potential reasons for this correlation are described below.

Figure 58 shows the camera image captured by 3D-ICP, with the strain masked area and the area containing valid computation points identified. Also shown on the image are the outlines of the major features of the specimen such as the stiffener and stiffener termination weld. The location of the 1mm strip gage, removed in this image, is delineated for clarity. Comparing

Figure 58 to Figure 46, a generally finer pattern was used for the Type XII 3D-ICP measurements. The finer pattern improved the performance of the image correlation algorithm, providing greater accuracy in determining movement along the surface and the corresponding strain field. Additionally, the strain gages were removed before

conducting 3D-ICP on the Type XII specimen. Figure 59 shows the strain contour plots from both 3D-ICP and FEA, with both shown in the same scale. The lack of strain gage wires interfering with 3D-ICP measurement provided a larger area for valid computation points. The 3D-ICP result shows the expected boundary noise, but the noise is suitably far from the area of interest, and does not affect the measurements. The maximum strain at the weld toe for the 3D-ICP plot is 605 microstrain, and the maximum for the finite element analysis is 640 microstrain, a difference of 5.4%. The 3D-ICP contour plot shows the advantage of eliminating as many contributors to noise as possible.

The behavior at the pole base was also of interest. The stresses in the longitudinal direction along the pole exterior are plotted in Figure 60 on a path extending from the weld toe at the pole base corner adjacent to the stiffener in the loading plane. Also plotted are the FEA results, nominal stress, and the 3D-ICP measurements along the same path on the pole exterior surface. The applied load was 7.0 kip (31.1 kN), corresponding to a nominal stress of 3.5 ksi (264.1 MPa) at the pole-to-base plate weld toe on the pole. The nominal stress was computed by dividing the bending moment at the section with the nominal section modulus, which included stiffeners. Due to the changing stiffener width, the nominal stress increases away from the weld toe, contrary to the pattern of unstiffened connections. At 4 $^1/_2$ in (114 mm) away from the weld toe, the stress measured at the $^1/_4$ in gage was higher than the FEA result by 50.1% of the FEA result and lower than the nominal stress by 6.7% of the nominal stress. A possible explanation for this is that the stiffeners were more

effective at preventing out-of-plane distortion in the actual structure than predicted by the FEA results. Due to the lack of a handhole for routing of strain gage wires, the interior of the specimen was not gaged. Therefore, strain gage measurements were not available to determine the distribution of stress through the thickness to support this hypothesis. Figure 61 is an enlarged view of the same data in the region abutting the weld toe over which 3D-ICP measurements were obtained. The stresses obtained from the 3D-ICP measurements and the 1 mm strip gage measurements differed by a maximum of 8.8% of the strain gage measurements. The measured stresses were less than the FEA results by a maximum of 15.0% of the strain gage measurements. This plot shows a good correlation between the strain gage measurements and the 3D-ICP measurements. Away from the weld toe, however, the 3D-ICP measurements show more noise than in other plots, including an upward spike at the end of the plot at a distance of 1.6 in (41 mm) from the weld toe.

Figure 62 shows the surface captured by 3D-ICP, with the strain masked area and the area containing valid computation points identified. Also shown on the image are the outlines of the major features of the specimen such as the base plate, the anchor rod and the lock nut, and the weld surface. The only strain masking required was done at the weld directly below the strain gage centerline. Figure 63 shows the strain contour plots for both 3D-ICP and FEA. At this filter level, the 3D-ICP result shows more noise than the previous Type XII stiffener termination measurement. The irregular green areas interspersed in the contour plot signify noise in what should be a smooth contour. This is a situation in which judgment was required. Over the first $^1/_2$

in (13 mm) of the stress plots the 3D-ICP result is relatively smooth, and begins to show evidence of noise after that point. To use a larger filter size or more filter runs risks losing the maximum stress data closest to the weld toe, which is the region of interest. For this case, the noise in the data was deemed acceptable because the affected portion of the data is sufficiently far from the region of interest. Figure 62 shows how the pattern is significantly finer in the weld toe region than towards the top of the frame. The larger pattern size is the likely cause of the noise observed. This demonstrates one of the greatest difficulties that was faced while conducting 3D-ICP measurements. Below the size where stencils are available, producing a correct pattern size required skill while producing the stochastic pattern. Despite considerable practice, a less than ideal pattern was created for this area.

3.3.2 Bolt-on-Center Testing

After the completion of static testing of the Type XII specimen with the stiffener in the loading plane, the specimen was removed from the test setup and replaced with a bolt in the loading plane to provide comparison between the two loading directions. The stresses in the longitudinal direction along the pole exterior are plotted in Figure 64 on a path in the loading plane extending from the weld toe at the stiffener termination. Also plotted are the FEA results and the 3D-ICP measurements along the same path on the pole exterior surface. The applied load was 7.0 kip (31.1 kN), corresponding to a nominal stress of 6.6 ksi (45.5 MPa) at the stiffener termination. At 3 $^{1}/_{2}$ in (89 mm) away from the weld toe, the stress measured at the ¼ in gage was 9.6% less than the FEA result and 3.9% less than the nominal

stress. This indicated that the gage location in the FEA model was still within the influence of the weld toe stress concentration and that in the actual structure, the in-plane membrane stresses dominated at the gage location. Figure 65 is an enlarged view of the same data in the region abutting the weld toe over which 3D-ICP measurements were obtained. The stresses obtained from the 3D-ICP measurements and the 1 mm strip gage measurements differed by a maximum of 17.2% of the strain gage measurements. The measured stresses were less than the FEA results by a maximum of 42.1% of the strain gage measurements. The 3D-ICP measurements provide excellent correlation to the strain gage measurements at the third, fourth, and fifth gage locations away from the weld toe. Potential reasons for this correlation are described below.

Figure 66 shows the camera image captured by 3D-ICP, with the strain masked area and the area containing valid computation points identified. Also shown on the image are the outlines of the major features of the specimen such as the stiffener and stiffener termination weld. The location of the 1mm strip gage, removed in this image, is delineated for clarity. When compared to Figure 58, it can be seen that the pattern was unchanged between the two loading directions, and only the camera angle was adjusted. Though the strain-masked area over the stiffener termination is larger in Figure 66, the masked points end exactly at the weld toe for both surfaces. Despite this similarity, Figure 65 shows an abrupt drop in the 3D-ICP result as it approaches the weld toe, with the tenth point from the weld toe agreeing with the strain gage measurement. As discussed in Appendix B, this lack of correlation approaching the

weld toe occurs when strain masking is not used on the weld surface. It is unclear as to why this occurred for these 3D-ICP measurements, as strain masking was employed. Figure 67 shows the strain contour plots from both 3D-ICP and FEA, with both shown in the same scale. The maximum strain at the weld toe for the 3D-ICP plot is 457 microstrain, and the maximum for the finite element analysis is 586 microstrain, a difference of 22.0%. As shown in Figure 67(a), the strain contour from 3D-ICP measurements was not smooth, indicating noise in the data. Additionally, the top of the surface was not included in computations due to glare on the surface. 3D-ICP measurement of this surface further illustrated the difficulties in obtaining reliable stress values. Despite a suitable pattern, which had been shown effective in previous measurements, a slight variation in camera angle and lighting yielded results that did not correlate to strain gage measurements.

The stresses in the longitudinal direction along the pole exterior are plotted in Figure 68 on a path extending from the weld toe at the pole base in the loading plane. Also plotted are the FEA results and the nominal stress along the same path on the pole exterior surface. The applied load was 7.0 kip (31.1 kN), corresponding to a nominal stress of 3.8 ksi (26.2 MPa) at the pole-to-base plate weld toe on the pole. The nominal stress was computed by dividing the bending moment at the section with the nominal section modulus, which included stiffeners. Due to the changing stiffener width, the nominal stress increases away from the weld toe, contrary to the pattern of unstiffened connections. At 4 $^{1}/_{2}$ in (114 mm) away from the weld toe, the stress measured at the $^{1}/_{4}$ in gage was lower than the FEA result by 23.2% of the FEA result.

This indicates that the magnitude of out-of-plane bending was greater in the physical structure than predicted by the FEA model. Figure 69 is an enlarged view of the same data in the region abutting the weld toe. The measured stresses were less than the FEA results by a maximum of 38.4% of the strain gage measurements.

Comparing the maximum measured stresses at the strain gages abutting the weld toe at the stiffener termination and pole base, the loading direction most likely to produce fatigue cracking is with the stiffener in the loading plane. For the stiffener-on-center loading, the maximum measured stress was 17.6 ksi (121.3 MPa) at the stiffener termination and 14.0 ksi (96.4 MPa) at the pole base. For the bolt-on-center loading, the maximum measured stress was 15.1 ksi (103.8 MPa) at the stiffener termination and 13.7 ksi (94.7 MPa) at the pole base. These measurements supported the FEA findings, and the stiffener-on-center loading direction was used for fatigue testing as the worst-case loading.

4. FATIGUE TEST RESULTS AND PERFORMANCE ASSESSMENT

This chapter presents the fatigue test results, including cracking modes and assessment of the fatigue resistance of relevant weld details. The observed crack propagation is graphically presented and discussed. Additionally, the post-mortem analysis of fracture surfaces for origin of fatigue cracks and crack growth in each specimen type is presented.

4.1 Type X Specimen

4.1.1 Fatigue Test Results

Three Type X specimens were tested. These specimens employed a fillet-welded tube-to-transverse plate connection at the pole base and included a reinforced handhole. Type X specimens were tested during the phase of the project in which experimental and analytical protocols were developed and refined. The fatigue tests were targeted towards determining finite life performance of the connections. Specimen X-1 was intended to be tested at a stress range of 8.0 ksi (55 MPa), exceeding the CAFL of AASHTO Category D, at the fillet-weld toe on the pole of the pole-to-base plate connection. This stress range was chosen based on the FEA results of the specimen type (performed by Mr. Yeun Chul Park as part of this project) and in view of the less than desired fatigue performance of this connection in structures of similar cross-section in TPF-5(116) that were fatigue tested at a stress range of 10 ksi (69 MPa). Although the Type X specimen had a 3 in (76 mm) base plate and employed 16 bolts compared to the TPF-5(116) specimens that used a 2 in (51 mm)

base plate and 12 bolts as detailed in Section 1.4.1, and was expected to exhibit better fatigue performance, the initial stress range was conservatively chosen as a first guess. However, due to an error in computation of the nominal stress, specimen X-1 was inadvertently tested at a nominal stress range of 5.4 ksi (37 MPa) and was run-out after 17 million cycles. Specimen X-1 was re-run at the intended nominal stress range of 8 ksi (55 MPa), and was again run-out after 13 million cycles. The specimen was then re-run at a nominal stress range of 10 ksi (69 MPa), corresponding to the CAFL of AASHTO Category C, and matching with the test stress range of the specimens tested under the TPF-5(116) study, when it developed fatigue cracking at the filled weld toe on the pole. Fatigue testing of specimens X-2 and X-3 was initiated at the intended nominal stress range of 8 ksi (55 MPa) at the fillet-weld toe on the pole of the pole-to-base plate connection. Both of these specimens developed fatigue cracking at the fillet weld toe on the pole. Including re-runs, a total five fatigue tests were conducted on the Type X specimens. The fatigue test results are shown in Table 2.

4.1.2 Cracking Modes

Fatigue cracking of the Type X specimens occurred at the fillet weld toe on the pole of the fillet-welded pole-to-base plate connection. The cracks in Type X specimens were first observed adjacent to the bend corners of the pole, at the point of tangency between the rounded corner and the flat, as shown in Figure 70. An example of the cracking at first observation is shown in Figure 71 for specimen X-1, where the crack is identified by the darker (red) dye on the lighter (white) background of the developer in a dye penetrant inspection. The crack grew on two fronts around the

perimeter of the pole along the fillet weld toe, with the growth towards the loading plane occurring at an increased rate compared to the growth away from the loading plane. In specimen X-2, multiple cracks initiated at tangent points of the same bend corner. These cracks coalesced within 191,000 cycles. Figure 72 shows the fatigue crack in specimen X-2 at the conclusion of fatigue testing, when the crack length was 20 $^{1}/_{4}$ in (514 mm) along the fillet weld toe on the pole. Specimen X-3 developed fatigue cracks both on the handhole side and the opposite side of the pole. The final crack lengths at the termination of fatigue tests are tabulated in Table 2.

Observed crack length on the pole surface and the corresponding number of cycles for all specimens are tabulated in Appendix A. These crack lengths versus number of cycles for the Type X specimens are plotted in Figure 73. At first observation, the minimum crack length was about 1.0 in (25 mm) on the pole surface (specimen X-1). As discussed in the following section, the fatigue crack had probably grown through the thickness of the pole wall at this crack length. Thus, the crack growth plots presented the growth of a through-thickness crack on two fronts along the fillet weld toe on the pole. As seen in Figure 73, the crack growth for the Type X specimens was generally exponential. Symbols of same shape denote crack growth under the same nominal stress range; different colors are used to identify individual specimens. Specimens X-2 and X-3 were fatigue tested under the same nominal stress range of 8 ksi (55 MPa). However, X-2 exhibited significantly less fatigue life compared to X-3, suggesting a larger stress intensity factor range (ΔK) driving the crack growth in X-2 arising from a larger initial flaw and/or larger stress gradient

through the thickness of the pole wall. Existence of larger initial flaws or multiple crack initiations along the weld toe that quickly coalesced into a longer crack would also explain the relatively larger crack length on the pole surface at first observation. Although the surface crack length at first observation for specimen X-1 was similar to that for specimen X-2, specimen X-1 exhibited faster crack growth since the specimen was fatigue tested under a larger nominal stress range of 10 ksi (69 MPa), resulting in a larger ΔK. The crack growth trends demonstrated that most of the fatigue life was spent in growing small cracks to a detectable size.

4.1.3 Origin and Growth of Fatigue Cracks

After fatigue testing, the fracture surfaces in the cracked specimens were exposed for assessment of origin and growth of fatigue cracks. Sections of the specimen containing the cracks were cut out, cooled in liquid nitrogen, and broken open to reveal the fracture surfaces. The fracture surfaces were ultrasonically cleaned in an acetone bath, photographed and examined by an Amray 1810 Scanning Electron Microscope (SEM) for potential crack origins and characterization of fatigue crack growth.

Figure 74 shows typical (exposed) mating fracture surfaces in specimen X-2. The fracture surface adjacent to the weld is on the bottom of the photograph. A two-stage fatigue crack growth initiating at the fillet weld toe on the pole wall was evident. In the first stage, the crack front propagated in a semi-elliptical shape, as shown in Figure 75, until it broke through the thickness of the pole. The crack then progressed on two fronts around the perimeter of the pole along the fillet weld toe. A scanning

electron micrograph of the fracture surface, identified by the inset in Figure 75, is shown in Figure 76. The crack initiation site on the fracture surface is identified by a faint "thumb nail" shaped impression. No unusual flaws were found on the fracture surface and it was concluded that the fatigue crack grew from typical slag-inclusion micro-discontinuities inherent in all welds.

4.1.4 Assessment of Fatigue Resistance

The fatigue resistance of the fillet-welded tube-to-transverse plate connection in the Type X specimens was evaluated by plotting the number of cycles corresponding to a 12 in (305 mm) crack versus the nominal stress range at the cracked section against the fatigue design curves of the AASHTO Bridge Specification, as presented in Figure 77. Specimens X-1 and X-2 exhibited a fatigue resistance of AASHTO Category E against fatigue cracking at the weld toe on the pole. Specimen X-3 achieved a fatigue resistance of Category E′. Specimen X-1 was run-out twice, when tested at nominal stress ranges of 5.4 ksi (37 MPa) and 8 ksi (55 MPa), respectively. Due to lack of sufficient data, and to be consistent with the performance of details with similar stress concentration, the CAFL of this detail in the connection geometry was proposed as 4.5 ksi (31 MPa), the CAFL of AASHTO Category E.

4.2 Type XI Specimen

4.2.1 Fatigue Test Results

Ten Type XI specimens were tested. These specimens employed a full-penetration groove-welded tube-to-transverse plate connection at the pole base, where a backing ring was fillet-welded to the pole and the plate at top and bottom, respectively. In addition, a reinforced handhole was provided. Specimens XI-1, XI-2, and XI-3 were fatigue tested at a nominal stress range of 12 ksi (83 MPa) at the toe of the fillet weld reinforcement on the pole at the base. All specimens tested at this stress range developed fatigue cracking at the weld toes on the pole of both the tube-to-transverse plate weld and the backing ring top weld. Specimens XI-4, XI-5, XI-6 and XI-7 were fatigue tested to determine the CAFL of the groove-welded tube-to-transverse plate connection at the pole base. All specimens were run-out after 12.7 million cycles when tested at a nominal stress range of 7 ksi (48 MPa), and developed fatigue cracking at the weld toes on the pole of both the tube-to-transverse plate weld and the backing ring top weld when re-run at an elevated nominal stress range of 10 ksi (69 MPa). Specimen XI-8 was inadvertently fatigue tested at a nominal stress range of 14 ksi (97 MPa). Specimens XI-9 and XI-10 were fatigue tested at a nominal stress range of 16 ksi (110 MPa) as planned. All three specimens developed fatigue cracking at the weld toes on the pole of both the tube-to-transverse plate weld and the backing ring top weld. Including re-runs for establishing the CAFL, a total fourteen fatigue tests were conducted on the Type XI specimens. While specimens XI-3 and XI-8 were inadvertently removed before the observation of a 12 in (305 mm) crack at

the backing ring, the observed growth rates suggest this did not significantly impact the fatigue life result. The fatigue test results for the Type XI specimens are tabulated in Table 3. The table identifies the controlling crack that caused the termination of fatigue testing for each specimen.

4.2.2 Cracking Modes

Fatigue cracking of the Type XI specimens was first observed at the weld toe of the fillet reinforcement on the pole at the pole base. An example of the cracking at first observation is shown in Figure 78 for specimen XI-3, where the crack is identified by the darker (red) dye on the lighter (white) background of the developer in a dye penetrant inspection. The crack grew on two fronts around the perimeter of the pole along the weld toe, with the growth towards the loading plane occurring at an increased rate compared to the growth away from the loading plane. The cracks in eight Type XI specimens (except specimens XI-2 and XI-10) were first observed adjacent to the bend corners of the pole, at the point of tangency between the rounded corner and the flat. Fatigue cracking in specimens XI-2 and XI-10 was first observed at the middle of a bend corner.

As the crack increased in length, the backing ring, which was welded to the pole at the top and the base plate at the bottom, allowed an alternate stress path from the pole wall to the base plate around the crack. This is illustrated in Figure 79 by plotting the stress ranges measured during fatigue testing at the center of the backing ring, at the pole wall abutting the exterior weld toe, and at the pole wall abutting the interior seal weld (on the top of the backing ring) opposite the handhole for specimen

XI-6. Refer to Figure 28 and Figure 29 for strain gage location. Though the data was continually recorded at 60 second intervals, the values plotted are those recorded during the regular visual inspections to avoid overcrowding of data points. For ease of identification, the corners of specimens were assigned a number, starting with the corner underneath the handhole and progressing counter-clockwise around the specimen. The faces between corners are identified with the closest corner number first. For further explanation of this naming convention, see Appendix A. The stress range was not immediately affected at the exterior weld toe after initial observation of cracking, since the crack initiated on the Face 8-9, closer to a bend corner away from the strain gage. As the crack propagated and an additional crack initiated on Face 9-10, the two cracks caused stress to deviate around the crack locations and towards the strain gage, causing stress concentration. This stress concentration increased until dropping off as the two cracks coalesced and fractured the pole wall below the strain gage. Meanwhile, the stress range at the interior seal weld and backing ring increased as stress was diverted towards the area around Corner 9. Fatigue cracking was not observed at the seal weld toe (Face 8-9) until after the exterior fatigue crack had fractured the pole wall. Due to the crack location at the seal weld toe, the stress range at the interior seal weld and backing ring continued to increase until the crack at the seal weld toe propagated beyond the strain gage location at Corner 9, causing the observed rapid decrease in stress range. At this point, the fatigue life of the specimen had been expended and testing was terminated.

Due to the diversion of stress through the backing ring, the crack growth at the toe of the groove weld reinforcement slowed. For all specimens except XI-2, multiple cracks appeared along the weld toe, typically at bend tangency points, after the growth of the first crack diminished. This indicated that in addition to diversion of stresses through the backing ring at the cracked section, stresses were increasing at the adjacent bend corners of the pole due to deviation of stresses around the crack, initiating fatigue cracks. Once the individual cracks coalesced, the backing ring carried all of the tensile stress. Subsequently, cracking was observed in the backing ring top weld. The backing ring top welds typically developed fatigue cracking at the toe on the pole. Cracking was observed through the weld throat in specimens XI-7, XI-8, and XI-10. Specimens XI-3, XI-7, XI-8, and XI-10 also developed cracks in the backing ring from the root of the vertical seam weld in the backing ring, which had been fabricated by vertically welding two split ring sections. This cracking progressed horizontally through the backing ring base metal. Figure 80 shows an exterior view of typical cracking at the pole base when the fatigue tests were terminated. The dark (red) dye from the dye penetrant test is visible along the full-penetration weld toe extending over 20 in (508 mm) of the perimeter at the bottom. Above it is the dye from the through-thickness crack at the backing ring top weld. Figure 81 shows an interior view of a segment cut from specimen XI-8, where fatigue cracks developed at the backing ring top weld toe, through the backing ring top weld throat, and from the vertical seam weld of the backing ring.

An example of typical crack progression in specimens Type XI is provided in

Figure 82 for specimen XI-4. Fatigue cracking was first observed at Face 9-8 and Face 9-10 of Corner 9. Compared to Type X specimens, crack propagation continued at a slower pace, with multiple visual checks between recorded changes in crack growth. The location of the vertical seam weld in the pole at Corner 9 likely delayed the coalescence of these two cracks. As fatigue testing progressed, cracking was also observed at Face 10-11. After the coalescence of all three cracks produced a total crack length of 13 in (330 mm) at the full-penetration groove weld toe, crack growth remained slow as the backing ring carried the tensile forces at the connection. Further cracking was observed at the backing ring top weld and this crack propagated until testing was stopped.

Observed crack length on the pole surface and the corresponding number of cycles for all specimens are tabulated in Appendix A. These crack lengths versus number of cycles for the Type XI specimens at the weld toe of the fillet reinforcement on the pole are plotted in Figure 83. The effect of the backing ring as an alternate load path was most noticeable in the specimens tested at 10 ksi (69 MPa), specimens XI-4, XI-5, XI-6, and XI-7. Rather than displaying an exponential growth, the interaction between the available load paths resulted in generally linear crack propagation. In terms of in-service structures, the use of a backing bar welded to the pole and base plate would provide an extended period of time between initial observation of fatigue cracking and a loss of strength due to fatigue cracking, compared to the fillet-welded pole-to-base plate connections. Of particular interest is the crack propagation in specimen XI-2. Despite being tested at a nominal stress range of 12 ksi (83 MPa),

crack initiation occurred at a number of cycles exceeding all other specimens, including those tested at 10 ksi (69 MPa). Crack propagation then occurred at a rate less than that of all other specimens. This suggests that the stress intensity factor range (ΔK) was lower for this specimen than all other Type XI specimens. A possible correlation between the weld geometry of specimen XI-2 and the fatigue life is discussed in Chapter 5.

4.2.3 Origin and Growth of Fatigue Cracks

After fatigue tests, fracture surfaces were exposed and examined as described in Section 4.1.3. The presence of semi-elliptical beach marks, lines that denote periods of crack growth, at multiple locations on the fracture surface corroborated multiple fatigue crack initiations along the weld toe on the pole, observed during the fatigue tests. Individual cracks propagated until either breaking through the thickness of the pole or coalescing with an adjacent crack and progressing on two fronts around the perimeter of the pole along the fillet weld toe. Figure 84 shows a typical (exposed) fracture surface in specimen XI-3. Two crack initiation sites were evident on the fracture surface. The cracks coalesced before breaking through the thickness of the pole. The unified crack then progressed on two fronts around the perimeter of the pole along the weld toe. Scanning electron micrographs, identified by the inset in Figure 84, are shown in Figure 85 and Figure 86. The crack initiation sites on the fracture surface are identified, along with the observed beach marks. No unusual flaws were found on the fracture surface and it was concluded that the fatigue crack grew from typical slag-inclusion micro-discontinuities inherent in all welds.

4.2.4 Assessment of Fatigue Resistance

The fatigue resistance of the full-penetration groove-welded tube-to-transverse plate connection in the Type XI specimen was evaluated by plotting the number of cycles corresponding to a 12 in (305 mm) crack versus the nominal stress range at the cracked section against the fatigue design curves of the AASHTO Bridge Specification, as presented in Figure 87. The groove-welded tube-to-transverse plate connection in the Type XI specimens exhibited a lower bound fatigue resistance exceeding AASHTO Category E′ and approaching Category E, against crack growth at the toe of the fillet reinforcement on the pole. The predicted fatigue resistance of this detail in the finite life region was Category E′. The minimum fatigue resistance of the fillet weld at the tope of the backing ring against cracking at the weld toe on the pole exceeded AASHTO Category E. The predicted fatigue resistance of this detail was slightly less than Category D. None of the groove-welded connections developed fatigue cracking when tested at or below a stress range of 7 ksi (48 MPa). As such, the CAFL for this detail is defined a 7 ksi (48 MPa), the CAFL of AASHTO Category D.

4.3 Type XII Specimen

4.3.1 Fatigue Test Results

A total of ten Type XII specimens were tested. These specimens employed a stiffened fillet-welded tube-to-transverse plate connection at the pole base. Specimens XII-1, XII-2, and XII-3 were fatigue tested at a nominal stress range of 12 ksi (83

MPa) at the toe of the stiffener-to-pole weld on the pole. All specimens tested at this stress range developed fatigue cracking at the weld toes on the pole of the stiffener termination weld. Specimens XII-4, XII-5, XII-6, and XII-7 were fatigue tested to determine the CAFL of the stiffened connection at the pole base. Only specimen XII-6 developed fatigue cracking when tested under a nominal stress range of 7 ksi (48 MPa) at the stiffener termination on the pole. The other three specimens were run-out at 12.7 million cycles. Specimen XII-6 developed a crack through the throat of the fillet weld at the stiffener termination, as shown in Figure 88. This crack originated from the unusually large lack of fusion at the weld root as exhibited by the fracture surface shown in Figure 89. The data from this specimen was not considered representative because this cracking mode occurred only in one specimen. Specimens XII-4, XII-5, and XII-7 developed fatigue cracking at the toe of the stiffener termination weld on the pole when re-run at an elevated nominal stress range of 10 ksi (69 MPa). Specimens XII-8, XII-9, and XII-10 were fatigue tested at a nominal stress range of 16 ksi (110 MPa). All three specimens developed fatigue cracking at the weld toes on the pole of the stiffener termination weld. Including re-runs for establishing the CAFL, a total thirteen tests were conducted on the Type XII specimens. The fatigue test results for the Type XII specimens are tabulated in Table 4.

4.3.2 Cracking Modes

Fatigue cracking of Type XII specimens occurred at the stiffener termination weld toe on the pole of the stiffened fillet-welded pole-to-base plate connection, on

stiffeners that were in the loading plane. Five of the specimens first developed a 12 in (305 mm) long fatigue crack on the side towards the actuator; the remaining five first developed a 12 in (305 mm) long fatigue crack on the side opposite the actuator. Similarly, five of the specimens developed fatigue cracks at multiple stiffeners; the remaining five only developed a fatigue crack at a single stiffener. For specimens with and without multiple cracks, there was no apparent bias towards the actuator side or opposite side. Since the Type XII specimens did not include a handhole, fatigue cracking at both stiffener terminations in the loading plane was equally probably. An example of the cracking at first observation is shown in Figure 90 for specimen XII-4, where the crack is identified by the darker (red) dye on the lighter (white) background of the developer in a dye penetrant inspection. The crack initiated at the top-most point of the wrapped-around weld toe of the stiffener termination on the pole. The crack then progressed along the weld toe before branching into the pole wall along a path normal to the maximum principal stress. Figure 91 shows the fatigue crack in specimen XII-2 at the conclusion of fatigue testing, when the crack length was 13 $^{3}/_{8}$ in (340 mm). In addition to fatigue cracking at the stiffener termination, fatigue cracking was observed at the fillet weld toe on the pole of the fillet-welded pole-to-base plate connection on specimens XII-1, XII-8, and XII-10. These cracks did not propagate to the 12 in (305 mm) length defined as the failure criterion, only reaching a maximum of 8 $^{1}/_{16}$ in (205 mm) in specimen XII-8. The interaction of the stiffeners with the pole reduced the geometric stress concentration at the pole-to-base plate fillet weld toe and prevented fatigue crack growth at this connection approaching the

stiffener locations. Specimens XII-1, XII-2, XII-8, XII-9, and XII-10 experienced cracking at both stiffeners in the loading plane. Of these, XII-8 and XII-10 were tested until the smaller crack reached the defined failure length of 12 in (305 mm). The final crack lengths at the termination of fatigue tests are tabulated in Table 4.

After the fatigue crack at the stiffener termination in specimen XII-4 had propagated more than 12 in (305 mm), testing was continued to observe the progression of fatigue cracking around the pole. To the right of the stiffener in the loading plane, the crack propagated at a slight upward angle and continued through the pole wall above the next two adjacent stiffeners. To the left, the crack propagated at a slight downward angle and through the next two adjacent stiffeners, just below the stiffener termination, as shown in Figure 92. Testing was terminated when the strain range could not be maintained at the control gage. At the termination of testing, the crack length was 40 $^{3}/_{4}$ in (1035 mm).

Observed crack length on the pole surface and the corresponding number of cycles for all specimens are tabulated in Appendix A. These crack lengths versus number of cycles at the stiffener termination for Type XII specimens are plotted in Figure 93. The crack propagation was generally exponential and crack growth rate increased rapidly, as the crack branched into the pole wall, suggesting that little useful fatigue life was left after the crack grew along the weld toe at the stiffener termination. Most of the fatigue life was spent in growing the micro-discontinuities into detectable cracks. For specimens XII-1, XII-2, and XII-3, which were tested at a nominal stress range of 12 ksi (83 MPa), there was little variation in crack growth rate and the fatigue

life. Similar was the case for specimens XII-8, XII-9, and XII-10, which were tested at a nominal stress range of 16 ksi (100 MPa). This suggested that the high stress concentration at the stiffener termination on the pole increased the notch severity of the detail and primarily affected the fatigue crack growth; any variability in the micro- and macro-discontinuities at the weld had insignificant effects. The larger variation in the fatigue performance for specimens XII-4, XII-5, and XII-7 is likely due to the proximity of the 10 ksi (69 MPa) nominal stress range to the CAFL of the connection. As is apparent from the figure, the crack growths were identical for these three specimens, and the variation in fatigue life was due to the initial flaw size (depicted by similar plots but shifted along the abscissa). Since the crack growth is driven by the stress intensity factor range (ΔK), which is itself a function of the flaw size, the geometric boundary conditions, and the stress range, a lower stress range magnified the effect of variation in micro- and macro-discontinuities. As such, the difference in fatigue life for specimens XII-4, XII-5, and XII-7 was not considered abnormal.

4.3.3 Origin and Growth of Fatigue Cracks

After fatigue tests, fracture surfaces were exposed and examined as described in Section 4.1.3. Figure 94 shows a typical (exposed) fracture surface in specimen XII-1. A two-stage fatigue crack growth initiating at the stiffener termination weld toe on the pole was evident. In the first stage, the crack front propagated in a semi-elliptical shape, as shown in Figure 94, until it broke through the thickness of the pole. The crack then progressed on two fronts around the perimeter of the pole. A scanning electron micrograph of the fracture surface, identified by the inset in Figure 94, is

shown in Figure 95. The crack initiation site on the fracture surface is identified by the remnants of a slag inclusion. This flaw was considered to be normal, as similar micro-discontinuities are inherent in all welds. Figure 96 shows a typical (exposed) fracture surface at the pole base in specimen XII-1. A two-stage fatigue crack growth initiating at the fillet weld toe on the pole was evident. In the first stage, the crack front propagated in a semi-elliptical shape, as shown in Figure 96, until it broke through the thickness of the pole. The crack then progressed on two fronts around the perimeter of the pole until propagation was prevented by the presence of adjacent stiffeners. A scanning electron micrograph of the fracture surface, identified by the inset in Figure 96, is shown in Figure 97. While evidence of multiple crack initiation sites was found, none of the flaws were considered unusual and it was concluded that the fatigue crack grew from typical slag-inclusion micro-discontinuities inherent in all welds.

Apart from the lack of fusion defect in specimen XII-6, as discussed in Section 4.3.1, the only observed anomaly was at the fracture surface at the stiffener termination on the back side of specimen XII-9. Figure 98 shows the (exposed) fracture surface. The fracture surface adjacent to the stiffener termination weld toe is at the top of the photograph. A scanning electron micrograph of the fracture surface, identified by the inset in Figure 98, is shown in Figure 99. The micrograph showed evidence of tearing that is not consistent with fatigue cracking. Cracking at this location was first observed after a fatigue crack at the opposite stiffener had propagated to 5 $^{11}/_{16}$ in (144 mm). The combination of high residual stress and

cracking at the opposite stiffener likely exceeded the fracture resistance at this location and caused the crack, however the dynamic fracture toughness was sufficient to arrest the crack outside of the area of residual stress. The tear then propagated as a fatigue crack, reaching a final length of 2.2 in (56 mm) at the termination of testing. As such, the fatigue performance was considered unaffected.

4.3.4 Assessment of Fatigue Resistance

The fatigue resistance of the stiffened fillet-welded tube-to-transverse plate connection in the Type XII specimens was evaluated by plotting the number of cycles corresponding to a 12 in (305 mm) crack versus the nominal stress range at the cracked section against the fatigue design curves of the AASHTO Bridge Specification, as presented in Figure 100. The stiffened fillet-welded tube-to-transverse plate connections in the test geometry exhibited a lower bound fatigue resistance exceeding AASHTO Category E. These specimens developed fatigue cracking at the stiffener-to-pole weld toe on the pole at the termination of the stiffener, where the predicted fatigue resistance was AASHTO Category E′.

The predicted fatigue resistance against crack growth at the tube-to-transverse plate weld toe on the pole at the pole base was greater than AASHTO Category E′. Fatigue cracking developed in this detail in only three specimens, XII-1, XII-8, and XII-10. However, the crack growth was inhibited by the fatigue cracking at the stiffener termination, and none of the cracks grew to the failure criterion of 12 in (305 mm). In specimen XII-8, fatigue cracking was observed early at both the stiffener termination and at the fillet weld toe on the pole at the pole base. However, the

fatigue life corresponding to a crack length of 12 in (305 mm) at the stiffener termination exceeded the AASHTO Category E design life. The maximum crack length at the fillet weld toe at the pole base was 8 $^{1}/_{16}$ in (205 mm) when the test was terminated.

Except for specimen XII-6, none of the stiffener-to-pole weld at the stiffener termination developed fatigue cracking when tested below a stress range of 10 ksi (69 MPa), the CAFL of AASHTO Category C. Ignoring the result of specimen XII-6, was concluded that the CAFL of the stiffener-to-pole weld at the stiffener termination due to fatigue cracking from the weld toe is 7 ksi (48 MPa), the CAFL of AASHTO fatigue Category D.

5. ASSESSMENT OF VARIABILITY IN FATIGUE TEST RESULTS

As presented in Chapter 4, scatter was observed in the fatigue test results of the high-level lighting poles. While scatter is inherent in all fatigue test data, arising from the variation in weld fabrication-related micro- and macro-discontinuities present in any welded detail, it was unclear as to whether the observed scatter was typical. The Type XI specimens were selected for further analysis of this observed scatter in fatigue test results due to the larger number of specimens tested when compared to Type X specimens, and the increased scatter in fatigue test results when compared to Type XII specimens.

5.1 Observed Scatter

The fatigue test results of the full-penetration groove welded pole-to-base plate connection of the Type XI specimens are shown in Figure 101. Also plotted are the mean life curve and the upper and lower bounds for the finite life data set, obtained by shifting the mean life by two standard deviations. These upper and lower bounds correspond to 95% confidence limit on the 95% probability of failure and survival, respectively. In Chapter 4, the (population) fatigue resistance of the pole-to-base plate connection was defined as Category E, however, the lower bound to the data set indicated a lower bound fatigue resistance of Category E′. Recognizing that a small data set (only 10 samples) tends to show a larger spread in the bounds, and to compare with the spread of Category E detail population, the fatigue test results of the Type XI specimens are plotted in Figure 102 with the AASHTO Bridge Specification Category

E bounds, created from statistical parameters presented in NCHRP Report 286 (Keating and Fisher 1986). The statistical parameters for Category E details were determined based on fatigue test results of 206 details including a wide variety of cover plate attachments in bridge beams. The scatter of Category E bounds is due to inherent variability in fatigue test results primarily from the uncontrolled variables such as the weld toe macro- and micro-discontinuities within the acceptable fabrication practice.

The plot in Figure 102 shows the test results for specimens XI-8 and XI-10 fell slightly below the Category E lower bound, and the test result for specimen XI-2 fell way above the Category E upper bound. Considering the closeness of the data points for specimens XI-8 and XI-10 to the lower bound curve for Category E, it is likely that these data belong to the same detail population. However, the result for specimen XI-2 is certainly an outlier.

It was hypothesized that the weld geometry of specimen XI-2 could have been the cause of this aberration, as welds tend to act as stiffeners to these thin tubes. Previous work within the research project attributed scatter in test results of fillet-welded tube-to-transverse plate connections in cantilevered mast arms to variation in the global weld geometry. The fatigue test results for these specimens, labeled as Type I, are shown in Figure 103. Figure 104 shows the polished and etched sections of the tube-to-transverse plate welded connections in these specimens through the fatigue cracks at the weld toe. As is evident from Figure 103 and Figure 104, specimen I-1 had the least fatigue life and the highest weld angle, whereas specimen I-

3 had the greatest fatigue life and the lowest weld angle. The lower bound fatigue life was determined for the weld angles of 20°, 26°, and 42° (for specimens I-3, I-2, and I-1, respectively) according to the geometric stress method as described in Section 5.5. Figure 105 shows the bounding estimated life including this variation in weld angle and the inherent scatter for Category E detail population. The lower bound estimated life was calculated based on the geometric stress method for the 42° weld, which plots the geometric stress against the Category C lower bound curve. The upper bound estimated life was calculated by including the variability associated with the weld toe for a Category E detail to the geometric stress method result for the 20° weld. Intermediary combinations of weld angle and variability are not shown for clarity. As is evident, the spread in the lower and upper bound estimates compared with the observed scatter in the test data for these three details, although the estimated lives were less than the test results.

The exterior welds of the Type XI specimens were measured as discussed in Section 5.2, and the weld angle was calculated from the overall weld height and weld base thickness. Though an approximation, this revealed that the weld angle of specimen XI-2 was 19.8°, compared to a mean value of 23.3°. It is likely that this contributed to the increased fatigue resistance of this specimen. This effect of variation in the weld geometry is further investigated in the following, where multiple parameters of the full-penetration groove with weld fillet reinforcement for Type XI specimens were considered.

5.2 Determination of Weld Geometry

A novel approach was adopted for determining the weld geometry using 3D-ICP measurements. Initially the weld geometries were obtained from polished and etched sections of the welds, which involved sectioning parts of pole-to-base plate welds, polishing the sections, capturing photo-micrographs, and making measurements on the photo-micrographs. Dozens of individual photo-micrographs obtained at high magnifications through the optical microscopes were digitally overlapped to form an image of the entire weld. The process required significant effort and time. Recognizing that the 3D-ICP method captured a 3D image of the measured surface, it was devised that a weld profile could be easily obtained by discretely sectioning the 3D surface at the pole-to-base plate connection. The ARAMIS software, discussed in Appendix B, included the tools required to section the 3D point clouds depicting the surface and to provide a set of points along the desired section to produce the weld profile. This approach provided an accurate measurement of the weld geometry at discrete sections with minimal effort compared to the earlier adopted destructive evaluation process. Details of the 3D-ICP measurements are provided in Appendix B. The field of view was decreased to improve accuracy over a smaller target area, which consisted of the weld surface and small portions of the pole wall above and the base plate below. In these multi-sided specimens, measurements were made primarily at the bend corners, as cracks typically initiated near corners. On the 3D view of the mapped surface, a plane was aligned perpendicular to both the base plate top surface

and the pole wall at the section of interest. The coordinates on the weld surface that intersected the plane formed a two-dimensional profile of the weld section.

Prior to implementing use of 3D-ICP images for determining weld profiles, the process was verified against the earlier adopted destructive method of determining a weld profile. A typical section of a pole-to-base plate welded connection was identified. The weld profile was determined using 3D-ICP, and the location of the section was identified (marked) on the base plate and the pole. The welded connection was then cut adjacent to this section. The section was polished and etched and photo-micrographs were taken of the etched section. Figure 106 shows the comparison of this weld profile as measured by 3D-ICP and metallographic techniques. The jagged edges represent the limits of individual digital micrographs, which were merged into a composite picture of the entire weld profile, including part of the pole wall at the top and the base plate at the bottom. The weld profile obtained from the 3D-ICP images matched well with the destructively obtained weld profile, except for a deviation of less than $^{1}/_{20}$ of an inch (1.3 mm) towards the bottom of the weld. The reason for this variation is likely due to the difficulty in obtaining the exact cross-section from 3D-ICP image and the metallographic measurements. The small variation between the results was plausible over a small distance along the weld perimeter. The effect of this variation was negligible for the purpose.

5.3 Idealization of Weld Geometry

A total 51 weld sections were measured from the ten Type XI specimens using the 3D-ICP images. A typical weld profile is shown in Figure 107. Based on the

observed weld geometry, the weld profile was idealized by four linear segments. Figure 108 presents this idealized quadrilinear weld profile showing the different measurements (or parameters) considered for describing the weld geometry; along with the idealized quadrilinear weld profile impose on a typical weld profile for comparison. The locations of the vertices for the quadrilinear idealization were determined by the slope and the change in slope between successive points on the weld surface, starting from the uppermost measurement along the pole wall. Between the points on the pole wall the slope, $^{\Delta Z}/_{\Delta X}$, was on the order of 100, using the coordinate system of Figure 108. The weld toe was defined as the point at which the slope between the current point and the next point (in the decreasing Z direction) was below 10.0. This value was selected based on comparison of weld sections with a well-defined toe. To define the weld toe notch, a line was fit through the point at the weld toe and the next three successive points along the weld surface based on minimization of the square of the deviations from the line. The angle between this line and the pole wall was defined as the weld toe angle. This regression line was extended from the weld toe to the horizontal (X-axis) value (vertical projection) of the next (fourth) point on the weld surface. The end of this regression line was the first vertex of the quadrilinear idealization. The second and third vertices were identified as the local maxima in the change in slope between successive points, which were the re-entrant corners in the weld profile that occurred between weld passes. To determine the coordinates of the fourth vertex, a line was fit through the third vertex and the remaining points on the weld surface, based on minimization of the square of

the deviations from the line (i.e., regression with known intercept). This line was extended up to the base plate level, which was determined by visual inspection. As is evident in Figure 108, the fabrication techniques had produced a rounded transition from base metal to weld metal at the base plate. A straight line between the third vertex and the end of the weld (shown in the figure as a dashed line) would have included a significant area, where no weld was present, adding to the stiffness contribution by the weld. Using the regressed line over the bottom of the weld produced a rational idealization.

The measurements of the idealized sections, as shown in Figure 108, are tabulated in Table 5. The mean, standard deviation, maximum, and minimum for each dimension parameter are tabulated in Table 6. All measurements, except the weld toe angle, are in inches. The preliminary study, discussed earlier, demonstrated that the weld toe angle had a significant effect on the fatigue life. To separate the effects of the weld toe angle and stiffening effects caused by a larger weld, the weld toe angle, shown as θ in Figure 108, and the combined remaining weld size parameters (L, H_1, H_2, V_1, V_2, and V_3) were each varied by two standard deviations above and below their respective means. Pairing all combinations of extreme values for the weld toe angle and weld size produced four weld profiles.

5.4 Evaluation of Scatter Due to Weld Geometry

To evaluate the effects of variation in weld geometries, FEA of Type XI pole-to-base plate connections were performed, in which the four weld profiles were incorporated. These models were developed as submodels of an existing global model

of the Type XI specimen created by Mr. Yeun Chul Park as part of the project. In the global model, the maximum stress concentration occurred at the weld toe on the pole, at the centerline of the bend opposite the handhole, in the loading plane. Submodeling was employed to allow for a mesh size appropriate for the geometric stress approach, as detailed in Section 5.5, without exceeding practical limits for computation time. The size of the submodel was selected such that the region of interest was not influence by the discontinuities at the global model and the submodel interface caused by the difference in weld profile between the models. Figure 109 shows the location and the dimensions of the submodel. The length of the pole wall above the weld was chosen to include the portion in which the secondary out-of-plane bending occurred. The base plate was trimmed to remove the interactions with the anchor bolts, and to reduce the modeled plate thickness, which significantly reduced the time for computation.

The submodel was created using 20-node solid hexahedron elements C3D20R (Simulia 2008). The elements were second-order serendipity-type, incorporating isoparametric formulation with reduced integration. This element was chosen because of its capability of producing accurate stress analyses (Simulia 2008). Figure 110 shows the finite element mesh. The mesh size in the submodel was about $^{5}/_{16}$ in (8 mm), equal to the pole thickness. Two layers of elements were provided through the pole thickness to determine the through-thickness stress profile. Two C3D20R elements provided five points across the thickness, allowing up to a fourth-order equation to be fit to the results.

A displacement-based submodeling technique was used, as the slight change in weld profile was expected to alter the stress patterns immediately adjacent to the weld, but not the stiffness of the structure as a whole. The weld cross-section at the edge of the submodel was not included in the definition of submodel boundaries for interfacing with the global model, as the difference between the weld in the submodel and the nominal ($^5/_8$ in (16 mm) high by $^3/_8$ in (10 mm) wide) triangular weld in the global model would have caused discontinuities in the stress pattern. The submodel was extended along the perimeter to the point of tangency between the bend corner and flat at the outside of the adjacent bends (corners 8 and 10), yielding a radial distance of 52.4°. This offset was found to be adequate in preventing the approximations in boundary definition from affecting the stress pattern along the middle plane of the submodel (the loading plane in the global model). The applied load in the global model corresponded to a 5 ksi (34 MPa) nominal ($^{Mc}/_I$) stress at the fillet reinforcement weld toe of the full-penetration groove weld.

The FEA results for the weld profiles with the highest maximum principal stress and the lowest maximum principal stress are presented in Figure 111 and Figure 112, respectively. Both figures are scaled to the geometric stress, explained in Section 5.5. The largest maximum principal stress occurred in the model having the smallest weld angle combined with the largest weld geometry (all size parameters shifted upwards by two standard deviations). The smallest maximum principal stress occurred in the model having the largest weld angle combined with the smallest weld geometry (all size parameters shifted downwards by two standard deviations). These

two weld geometries were considered to predict the bounds of the fatigue resistance of the pole-to-base plate connections due to variation in weld geometry. The weld producing the smallest geometric stress is hereafter referred to as the best-considered weld, and the weld producing the largest maximum principal stress is referred to as the worst-considered weld.

5.5 Explanation of Scatter

The geometric stress approach was used to estimate the lower bound of the fatigue life for the two extreme cases of welds. The geometric stress is determined from the principal stress at $0.1\sqrt{(r\times t)}$ away from the weld toe, where r is the pole radius and t is the pole thickness. As per this method the fatigue life is estimated using the geometric stress with the finite life equation for the AASHTO Category C detail. Further discussion of the method is provided by Roy et al. (2011).

To compare the scatter in test results at the different levels of test stress range, the stress concentration factors for the idealized welds were determined by dividing the geometric stress range from FEA by the nominal stress range simulated in the model. Multiplying the stress concentration factor by the nominal test stress ranges of 10, 12, 14, and 16 ksi (69, 83, 97, and 110 MPa) resulted in the geometric stress range corresponding to each of the nominal test stress ranges. Using these geometric stress ranges along with the AASHTO Category C curve provided the estimated life for the respective nominal stress ranges. It should be noted that this is a lower bound estimate of fatigue life based on the Category C design curve, which corresponds to the 95%

confidence limit to the 95% probability of survival of the Category C detail population.

The AASHTO Bridge Specification stress-life equation was transformed from $N=A\times S_r^{-m}$ to the form:

$$\log(N) = \log(A) - m \times \log(S_r) \qquad (5\text{-}1)$$

Where N is the design fatigue life, log(A) is the intercept of the log-log plot of the S-N curve on the log(N)-axis, and m is the slope of the curve (Keating and Fisher 1986). The values for A and m are provided within the AASHTO Bridge Specification. For Category C using U.S. Customary Units, they are 4.446×10^9 and 3.0, respectively. Following the procedure for the geometric stress method, the geometric stress range was substituted for the nominal stress range. Solving Equation (5-1) for the geometric stress ranges for the best-considered weld and worst-considered weld revealed the scatter in fatigue life caused by variation in weld shape for the Type XI specimen population. Scatter bands were created by solving Equation (5-1) for multiple geometric stress ranges corresponding to multiple nominal testing stress ranges, and by plotting the fatigue lives against the respective nominal stress ranges. The scatter bands are shown in Figure 113. All test results were above the lower bound estimate based on the worst considered weld profile. The upper bound estimate based on the best considered weld profile did not bound the test results because it represented the

lower bound fatigue life for the best-considered weld and did not include inherent scatter due to the weld toe micro-discontinuities.

The full-penetration groove-welded tube-to-transverse plate connection employed in the Type XI specimens is defined by the AASHTO Specification as a Category E connection, a detail category originally designated for transverse welds at the termination of flange cover plates in the AASHTO Bridge Specification. Both the outer fillet-weld reinforcement of the Type XI pole-to-base plate connection and the cover plate termination weld were load-carrying welds with the weld toe transverse to the principal stress direction. Figure 114 shows the Type XI cross-section and a cover plate termination cross-section for comparison. The scatter due to micro-discontinuities in the weld for Category E details was therefore considered applicable to the Type XI connection. This is also consistent with the findings of Chapter 4, where this pole-to-base plate detail is characterized as Category E.

To include the scatter due to weld toe micro-discontinuities, the value of log(A) was calculated for the best-considered weld. Rearranging Equation (5-1):

$$\log(A) = \log(N) + m \times \log(S_r) \qquad (5\text{-}2)$$

Using the nominal stress range and the corresponding estimated fatigue life for the best-considered weld, the value of log(A) representing the best-considered weld profile with the worst effect of weld toe micro-discontinuities was obtained. To calculate fatigue resistance for the most favorable weld toe micro-discontinuities, four

times the standard deviation of log(A) for Category E was added to the lower bound value of the intercept as calculated above. This was done for multiple nominal test stress ranges to produce scatter bands.

The Type XI fatigue test results are plotted with this upper bound in Figure 115. Other than for specimen XI-2, which remains an aberration in the data, the observed scatter was in agreement with the expected scatter for a Category E detail, which matched the AASHTO Specification category for full-penetration groove-welded tube-to-transverse plate connection. Figure 115 therefore illustrates the amount of scatter that can be attributed to variation in weld geometry and the amount of scatter that can be attributed to variation in weld micro-discontinuities. The plot also shows that the welds in the Type XI specimens were mostly represented by the best-considered geometry.

6. FRACTURE SURFACE ANALYSIS

After fatigue testing, the fatigue fracture surfaces were exposed to assess the origins and growth of fatigue cracks and to examine the evolution of crack shapes during propagation. The surfaces were studied for beach marks, distinct lines which represent periods of crack growth. The observed beach marks were used to correlate surface crack length to crack depth, with the goal of using this information to predict the stage of crack progression for a crack discovered during an in-service inspection. It was hypothesized that such predictions could be used to assess the urgency of replacing a high-level lighting pole cracked in service. Two approaches for estimating crack growth based on observed surface crack length were postulated and compared with the crack propagation data recorded during the fatigue tests.

6.1 Assessment of Crack Shape

After completion of fatigue testing, a portion of the specimen (including the pole and the base plate) containing the fatigue crack was cut away from the specimen and the fatigue fracture surface was exposed and photographed. The photographs with visible beach marks on the fracture surface were imported into AutoCAD, a commercially available computer-aided design and drafting software and scaled to actual size, using the $^{5}/_{16}$ in (8 mm) thick pole wall as a reference. From the pattern of beach marks radiating outward from an initial flaw, it was evident that the cracks grew in a semi-elliptical shape until becoming a through-thickness crack, as discussed in Section 4.2.3. The crack then propagated on two fronts (in two directions) along the

pole perimeter. The beach marks observed in the photographs were traced in AutoCAD with idealized ellipses, and these traced ellipses were used to determine the relationship between surface crack length and crack depth as the crack grew through the thickness of the pole.

6.2 Approaches of Crack Growth Prediction

Two different approaches were followed to estimate the crack progression through the thickness.

6.2.1 Method 1

In this method, a simplified fracture mechanics model was employed as a less computationally-intensive approach. In the traditional fracture mechanics model of fatigue crack propagation analysis, an initial crack size and crack shape are assumed. The stress intensity factor for the assumed crack is calculated considering correction factors for crack shape and geometric boundary conditions. The instantaneous rate of crack propagation is calculated for the instantaneous crack size at incremental crack depths. The number of cycles for crack growth from the initial flaw to a critical size is determined using numerical integration.

The calculations presented in the proposed method differ from the traditional approach in the selection of the starting flaw size. Rather than using an assumed initial flaw as the starting point for life estimation, the beach marks observed on the fracture surface were used to provide data points for intermediate crack fronts. The crack depth, a, and the corresponding crack length on the pole surface, $2c$, were

measured for each beach mark traced. From these, the aspect ratio, $a / 2c$, was calculated for each idealized elliptical crack shape. For all fracture surfaces, a decrease in the aspect ratio was observed as the crack length increased, indicating evolution of a flatter crack shape with crack progression.

The methodology for step-by-step estimation of life with increasing crack length is presented in the following. The instantaneous parameters at a given step are denoted by the subscript "*i*". The estimation of fatigue life begins with Paris' equation for crack growth:

$$\left(\frac{da}{d\mathrm{N}}\right)_i = A \cdot \Delta \mathrm{K}_i{}^{\mathrm{n}} \tag{6-1}$$

Where A is the constant of crack growth, n is the exponent of stress range, and $da/d\mathrm{N}$ is the instantaneous crack growth rate. For ferrite-pearlite steel, typical values are $A = 3.6 \times 10^{10}$ and n= 3.0 (Barsom and Rolfe 1987).

The maximum stress-intensity factor range, ΔK, for a semi-elliptical surface crack at the middle of the crack front is given as (Barsom and Rolfe 1987):

$$\Delta \mathrm{K}_i = \frac{1.12 \cdot \sigma_{\mathrm{r}} \cdot \left(\mathrm{M}_{\mathrm{K}}\right)_i}{\Phi_i} \sqrt{\pi \cdot a_i} \tag{6-2}$$

Where the 1.12 multiplier is the front free-surface correction factor, σ_r is the maximum stress range as explained below, Φ is the complete elliptic integral of the second kind, and M_K is the back free-surface correction factor. σ_r is the product of the nominal stress range, S_r, and the stress concentration factor, k_t, as defined below:

$$\sigma_r = S_r \cdot k_t \tag{6-3}$$

The nominal stress range, S_r, and the stress concentration factor, k_t, were held as constant during the entire computation of fatigue life for calculations, as the crack lengths considered were small enough to allow this approximation. The stress concentration factors for each specimen type were obtained from FEA performed by Mr. Yeun Chul Park as part of this project. The geometric stress at a distance of $0.1\sqrt{(r \times t)}$ ahead of the weld toe was used to determine the stress concentration factor, following the guidelines set forth by Det Norske Veritas (2005).

Using the values for crack depth and surface crack length, the complete elliptic integral of the second kind, Φ, is numerically approximated by the series expansion:

$$\Phi_i = \frac{\pi}{2}\left\{1 - \frac{1}{4}\left(\frac{c_i^{\,2} - a_i^{\,2}}{c_i^{\,2}}\right) - \frac{3}{64}\left(\frac{c_i^{\,2} - a_i^{\,2}}{c_i^{\,2}}\right)^2 - \cdots\right\} \tag{6-4}$$

The variables in Equation (6-4) are shown in Figure 116. The back free-surface correction factor, M_K, is approximately 1.0 as long as the crack depth is less

than one-half the wall thickness, t (Barsom and Rolfe). For larger values of the crack depth, M_K is approximated by:

$$\left(\mathrm{M_K}\right)_i = 1.0 + 1.2\left(\frac{a_i}{t} - 0.5\right) \tag{6-5}$$

The instantaneous growth rate of surface crack length, $d(2c)/d\mathrm{N}$, is calculated as:

$$\frac{d(2c)}{d\mathrm{N}} = \frac{d(2c)}{da} \cdot \frac{da}{dN} \tag{6-6}$$

Where $d(2c)/da$ is the instantaneous change of the surface crack length with respect to change in the crack depth, equal to the inverse of the aspect ratio. Re-writing Equation (6-6) in incremental format:

$$\frac{\Delta(2c)_i}{(\Delta\mathrm{N})_i} = \left(\frac{\Delta a}{\Delta\mathrm{N}}\right)_i \cdot \left(\frac{\Delta(2c)}{\Delta a}\right)_i \tag{6-7}$$

$$(\Delta\mathrm{N})_i = \frac{\Delta(2c)_i \cdot \left(\dfrac{\Delta a}{\Delta(2c)}\right)_i}{\left(\dfrac{\Delta a}{\Delta\mathrm{N}}\right)_i} \tag{6-8}$$

In Equation (6-8), $\Delta(2c)_i$ is the change in the surface crack length between the current step and the next. Assuming that the crack will maintain its aspect ratio over an increment, $(\Delta a / \Delta(2c))_i$ is constant over that increment and is taken as the aspect ratio for the current step. This assumption is not entirely accurate, as the aspect ratio is continually changing. The aspect ratio was varied between subsequent increments by linearly interpolating between the aspect ratios of observed beach marks on the fracture surface with respect to the surface crack length.

Figure 117 shows the labels used during the crack propagation calculations. The shape of the idealized ellipses labeled b_1 and b_2 were known from the measurements in AutoCAD, but the corresponding number of cycles was unknown. The surface crack length at first observation, $2c_0$, was known, as was the corresponding number of cycles, N_0. The crack depth at first observation, a_0, was unknown. The value of the aspect ratio at first observation, $a_0 / 2c_0$, was interpolated based on the values of the surface crack lengths for ellipse b_1 and b_2, and the surface crack length at first observation, $2c_0$. The crack depth at first observation, a_0, was estimated using this aspect ratio.

For numerically integrating the number of cycles corresponding to a particular surface crack, the surface crack length was incremented between steps. Starting with the smallest beach mark that could be discerned on the fracture surface photograph under magnification (b_1), the value of the surface crack length was incremented by a step size of 0.1 in (2.5 mm) to form a list of values for $(2c)_i$. The surface crack length at first observation and the surface crack length for other beach marks were included

in the list of surface crack lengths. For each step, the aspect ratio of the crack was interpolated from the aspect ratios of the bounding beach marks, and the crack depth for the step was estimated from the aspect ratio and the surface crack length for the step. The surface crack length was increased by the step size and a new crack depth was calculated, until the crack depth equaled the wall thickness. This produced estimated values of the surface crack length and the corresponding crack depth as the crack depth ranged from the smallest observed beach mark to a full-thickness crack.

Figure 118 is a flowchart outlining the calculations performed. For each step, the complete elliptic integral of the second kind and the back free-surface correction were calculated using the surface crack length and the crack depth for the step, with the maximum stress range held constant. For each step, the increment in cycles, $(\Delta N)_i$, corresponding to the incremental growth to the next step was calculated. The number of cycles at first observation (corresponding to the surface crack $2c_0$), N_0, was used as the initial value for computing the number of cycles for each step. To calculate N_i corresponding to a value of $(2c)_i$ less than $2c_0$, $(\Delta N)_i$ was subtracted from the value of N_{i+1}. Similarly, for calculating N_i for values of $(2c)_i$ greater than $2c_0$, $(\Delta N)_{i-1}$ was added to the value of N_{i-1}.

The crack growths as estimated by this simplified fracture mechanics model were plotted against the observed crack progressions for three specimens. These specimens had clearly defined beach marks on the fracture surface and a surface crack length at first observation that was less than the surface crack length for a through-thickness crack. The results, discussed further in Section 6.3, were too conservative,

estimating crack propagation at a rate significantly greater than was observed during fatigue testing. In an effort to more accurately predict the crack progression, it was necessary to reconsider the assumption that the stress concentration factor was identical through the thickness as the crack progresses.

6.2.2 Method 2

In this method, the approach was similar to that of Method 1. The difference was the addition of a stress gradient correction factor, F_G, which accounted for the variation in stress on the crack face through the thickness. As the maximum principal stress decreased through the thickness, the stress-intensity factor range would decrease, causing a reduction in crack growth rate. Method 2 employed the through-thickness gradient of longitudinal stress obtained from the FEA results to correct the stress-intensity factor range as the crack depth increased, with the intent of obtaining a more accurate estimation of crack propagation.

The FEA models of the Type XI specimen created for NCHRP Project 10-70, two quadratic elements were used through the thickness, providing five nodes. This allowed for fitting up to a fourth-order curve to the longitudinal stress results through the thickness. Figure 119 shows the stress gradient through the thickness for the Type XII specimen as an example. The gradient correction factor at each incremental crack length was estimated using the following equation (Albrecht and Yamada 1977), where the stress gradient was approximated as discrete steps:

$$F_G = \frac{2}{\pi}\sum_{j=1}^{n}\frac{\sigma_{b_j}}{S_r}\left(\arcsin\frac{b_{j+1}}{a} - \arcsin\frac{b_j}{a}\right) \quad (6\text{-}9)$$

The variables of the above equation are illustrated in Figure 120, where S_r was the nominal stress range and b_j was the distance from the outer face of the pole to the j^{th} step of the stress gradient. σ_{bj} was the maximum stress range over the j^{th} step b_j determined from FEA. A step size of 0.03 in (0.76 mm), approximately 10% of the total tube thickness of $^5/_{16}$ in (8 mm), was assumed for computing the stress gradient factor. For crack depths not corresponding to nodes in the FEA model, the longitudinal stress at the nodes was fit to the following cubic equation, which was used to determine σ_{bj} for each value of b_j:

$$\sigma = -10.81a^3 + 23.30a^2 - 14.59a + 2.92 \quad (6\text{-}10)$$

While the number of nodes allowed for a fourth-order equation, a cubic equation provided the best fit to the data. F_G was calculated for each crack depth, a_i, by summing the effect of each step through the thickness, as determined from Equation (6-9). The gradient correction factor was included as a multiplier within Equation (6-2) for determining the stress-intensity factor range. The calculations were then carried out in a manner identical to Method 1.

6.3 Results of Crack Progression Analysis

The results of the crack progression analysis are presented for two specimens. Specimen X-2 represented a multi-sided high-level lighting pole with a fillet-welded pole-to-base plate connection. Specimen XII-2 was a multi-sided high-level lighting pole specimen with a stiffened fillet-welded pole-to-base plate connection. The results of Method 1 and Method 2 are discussed for each specimen.

6.3.1 Specimen X-2

A photograph of the mating fatigue fracture surfaces of specimen X-2 is presented in Figure 121, along with an overlay of the beach marks on one of the fracture surfaces. The dimensions provided are (from left to right) the pole thickness, distance along the flat, arc distance along the bend corner, and distance along the next flat for the beach mark corresponding to a through-thickness crack. Table 7 presents the crack progression calculations using Method 1. Table 8 presents the calculations using Method 2. Figure 122 shows the estimated crack growth for each method compared to the observed crack growth. Neither method effectively predicted the crack growth. This specimen shows the difficulty in predicting fatigue crack propagation. A single crack location, early detection of cracking, and multiple beach marks on the fracture surface are necessary for an effective prediction of crack length. Of the 13 specimens tested without multiple stress paths (Type X and Type XII), only a single specimen met these requirements, specimen XII-2.

6.3.2 Specimen XII-2

A photograph of the exposed fatigue fracture surface of specimen XII-2 is presented in Figure 123, along with an overlay of the beach marks. The crack shape corresponding to a through-thickness crack had to be estimated for this fracture surface because a corresponding beach mark did not exist. The crack shape was determined based on beach marks for a surface crack both larger and smaller than the through-thickness surface crack length. For the crack larger than the tube thickness, an idealized elliptical crack front was assumed using the two-fronted beach mark on the fracture surface. Table 9 and Table 10 present the crack propagation calculations using Method 1 and Method 2, respectively. Figure 124 shows the estimated crack growth for each method compared to the observed crack growth. The crack progression estimated by the Method 1 deviates significantly from the observed behavior, predicting a more rapid crack growth. However, the crack progression estimated using Method 2 followed the observed crack growth behavior. This indicated that the through-thickness stress gradient had a significant effect on the crack propagation in specimen XII-2. In Figure 119 a large through-thickness stress gradient was observed at the stiffener termination on the pole of this specimen, which explained the good correlation in the estimated and observed crack propagation through the thickness of the tube. However, it is not clear how the estimated and observed crack propagation would correlation when the through-thickness crack grew on two fronts out of the high stress gradient. At this stage, the observed crack propagation could be slower compared to the estimated crack growth. A lack of

specimens with the requisite conditions (early crack detection and visible beach marks) in the Type XII specimen population prevented verification of this method on data from multiple specimens. Therefore, it is unknown whether the through-thickness stress gradient affected crack propagation for the entire Type XII specimen population.

7. RETROFITTING OF HIGH-LEVEL LIGHTING POLES

This chapter discusses a potential retrofit scheme for high-level lighting poles that have experienced fatigue cracking in service. The reasons for retrofitting instead of replacing the cracked structures are presented, along with the details of a retrofit strategy that was previously implemented in service. A similar retrofit was devised for the cracked high-level lighting pole specimens tested within this research. This retrofit was designed using FEA to predict the fatigue resistance of a retrofitted structure. Two previously cracked specimens that were retrofitted using this design were fatigue tested to verify the effectiveness of the retrofit.

7.1 Impetus for Retrofitting

A lack of robust fatigue design guidelines in the AASHTO Specifications that represent the behavior of the structures in service has engendered populations of lighting poles in service, which are susceptible to fatigue cracking. As discussed in Section 1.1.2, fatigue cracking in these structures has been reported mostly in the base section at the pole-to-base plate connection, and at the handhole. Replacement of the base section requires completely dismantling the high-level lighting pole including luminaires, and rebuilding with a replacement base section. Retrofitting the base section can improve the fatigue performance of the structure while saving the labor and equipment costs associated with complete removal of the structure from foundation, section separation and unit replacement, and internal disassembly and assembly of mechanical and electrical equipments (see further discussion later).

7.2 Previous Retrofitting of High-Level Lighting Poles

Following the collapse of a 140 ft (43 m) tall high-level lighting pole in 2003, the Iowa DOT investigated retrofit strategies for these structures in service. Figure 4 is a photograph of the collapsed pole, showing the foundation and the base plate of the pole in place (the foreground) and the collapsed pole in the background. A state-wide inspection after the collapse revealed cracking in 20 high-level lighting poles (Dexter, 2004). Seventeen of these poles were galvanized and had geometry and connection details identical to the collapsed high-level lighting pole. Three other poles were made of weathering steel. The galvanized poles were 140 ft (43 m) tall, with a 16-sided cross-section, 1 $^1/_4$ in (32 mm) thick base plate, and eight anchor rods. The weathering steel poles were 148 ft (45 m) tall, with a 12-sided cross-section, 1 $^3/_4$ in (44 mm) thick base plate, and six anchor rods. Designs checks against the 2001 edition of the AASHTO Specification revealed that both designs had insufficient fatigue resistance when subjected to natural wind gust and vortex shedding in higher modes (Dexter 2004). Further discussion of these failures was included in Section 1.1.2.

A retrofit was designed by Wiss, Janey, Elstner Associates (WJE) for the galvanized and the weathering steel lighting poles that had developed fatigue cracking (Koob 2003). The design involved reinforcing the lower portion of the pole with a steel jacket comprising a wall and a secondary base plate, as seen in Figure 125. The wall was $^1/_2$ in (13 mm) thick and was welded with a complete-joint penetration weld to a 1 $^1/_4$ in (32 mm) thick base plate. The jacket was designed to match the existing

structure and was constructed in two halves with cover plates at the joints. A cutout was provided in the jacket wall around the reinforced handhole for fitting the existing structure and for retaining access to the interior of the pole. The jacket was fastened by $^{3}/_{4}$ in (19 mm) diameter bolts to the pole and 1 in (25 mm) diameter bolts to the base plate. Matching holes were provided in the jacket base plate at the existing anchor rod locations. The existing nuts at the anchor rods were removed for installation of the jacket and then tightened on to the jacket base plate. A total of six retrofits were completed, at a cost of about $15,000 each as installed. By comparison, the replacement cost of a re-designed lower section was estimated at $45,000 per pole, which provided the impetus for testing the jacket retrofit.

The fatigue resistance of the retrofit jacket was assessed using the fatigue design provisions of the AASHTO Specification. The design nominal stress range at the jacket wall-to-base plate weld due to vortex shedding was 4.8 ksi (33 MPa), which was determined using the section modulus of only the jacket, without the cracked pole underneath. The complete joint penetration weld between the jacket wall and the base plate was characterized as a Category E detail, and the design stress range slightly exceeded the CAFL of 4.5 ksi (31 MPa) for this detail category. However, it was assumed that the existing pole and the retrofit jacket would act compositely, reducing the stress range in the jacket below the CAFL.

To verify the response of retrofitted structures under site specific wind loads, two retrofitted structures were instrumented with anemometers and strain gages under the direction of Dr. Robert Connor of Lehigh University with assistance from Iowa

State University to measure temporal and spatial variation of wind speed and direction, and resulting strains in the jacket and the existing pole (Koob 2003). Strain gages were provided along two longitudinal paths on the jacket wall and the pole wall, both offset 120° from the handhole centerline, at 3 in (76 mm) above the top of the retrofit jacket base plate (Gages 1 and 2), at 4 $^{3}/_{4}$ in (121 mm) below the top of the retrofit jacket (Gages 3 and 4), and at 6 in (152 mm) above the top of the retrofit jacket (Gages 5 and 6). Measurements were taken over 77 days, and the equivalent measured stress range was computed as 1.58 ksi (10.9 MPa) at 3 in (76 mm) above the jacket base plate. The jacket wall-to-base plate full-penetration connection was characterized as an AASHTO Category E detail, with a CAFL of 4.5 ksi (31 MPa). The equivalent measured stress range at the handhole was 1.53 ksi (10.5 MPa). The handhole was considered to be an AASHTO Category E detail. The equivalent measured stress range at a typical bolt hole, considered to be an AASHTO Category C detail with a CAFL of 10 ksi (69 MPa), was 4.21 ksi (29.0 MPa). The measurements indicated that the retrofit design was a cost-effective solution for providing infinite life for the high-level lighting poles.

7.3 Retrofit Jacket for NCHRP Project 10-70

A steel jacket, similar in concept to the jacket design by WJE for retrofitting the Iowa poles, was evaluated as part of the NCHRP Project 10-70. This jacket was designed for retrofitting unstiffened high-level lighting pole specimens that had developed fatigue cracks during testing. FEA was employed to produce an efficient design, as the nominal-stress approach employed for the Iowa retrofit was deemed

overly conservative. Figure 126 shows the design drawings for the jacket. The jacket retrofit consisted of two halves of a multi-sided pole section and a base plate, with a $^{3}/_{8}$ in (10 mm) thick wall extending 60 in (1524 mm) above a 2 $^{1}/_{2}$ in (64 mm) thick base plate. The jacket was intended to fit flush against the existing 16-sided pole. Accordingly, the jacket wall-to-base plate connection was made with a double bevel complete joint penetration groove weld (without a backing ring) with the reinforcement on the inner face ground flush. The groove weld was deposited from both sides with the weld root back-gouged and the weld quality was ascertained by Ultrasonic Testing (UT). A 1 in (25 mm) high by $^{3}/_{4}$ in (19 mm) wide chamfer was provided on the inner underside corner of the jacket base plate to clear the existing weld reinforcement at the pole-to-base plate connection on the cracked pole. A cut-out matching the handhole was provided in the jacket wall. Holes were provided in the base plate of the jacket matching the existing anchor rods. Four cover plates were used to splice the two halves of the jacket; two on the base plate and two on the wall.

The jacket was fastened to the wall and the base plate of the retrofitted pole using $^{7}/_{8}$ in (22 mm) diameter A325 bolts, with $^{1}/_{8}$ in (3 mm) washers between the fasteners and the structure. In addition, anchor rods for securing the existing structure to the foundation plate in the laboratory test setup (refer to Section 2.2.2) were tightened across the jacket base plate. The bolted connections were designed as slip critical to develop composite action between the jacket and the pole. The bolts on the pole wall were located centrally on the flat sides between the bend corners.

7.4 Finite Element Analysis of the Jacket Retrofit

To be cost-effective and efficient, the design philosophy of the retrofitted jacket specimens was to ensure infinite life without further growth of existing fatigue cracks. 3D FEA of the retrofitted structure was performed to determine the critical stresses in the retrofitted structure, to develop a cost-effective retrofit design and to assess the fatigue resistance of the jacket retrofit. As discussed in the subsequent section, the jacket wall-to-base plate connection was the most fatigue critical detail. The fatigue resistance of the jacket wall-to-base plate welded connection was analytically assessed following the protocols developed for the NCHRP Project 10-70 (Roy et al. 2011b).

Two separate 3D FEA were performed to determine both the geometric stress and the notch stress, as defined in Section 1.1.3. This was necessary as the geometric stress is taken at a defined distance from a weld toe modeled as a sharp notch, whereas the notch stress is taken on the surface of a rounded weld toe. Separating these analyses prevented computationally-intensive models. A model of the cracked specimen with the jacket retrofit, hereafter referred to as Model 1, was developed to determine the behavior of the retrofitted structure and to identify the critically stressed regions. A submodel of the most critically stressed region at the jacket wall-to-base plate connection in the Model 1, hereafter referred to as Model 2, was then developed to determine the local geometric stress and the geometric stress concentration factor. Two other 3D FEA models were created to determine the notch stress at the weld toe notch. The larger model, hereafter referred to as the Model 3, was analyzed to predict

the effect of a uniform tensile stress in the jacket wall perpendicular to the groove weld toe. A submodel of the weld toe with a rounded notch, hereafter referred to as Model 4, was developed with a refined mesh to determine the notch stress. All FEA were performed using ABAQUS version 6.8.

7.4.1 3D Model 1

Model 1 was developed by modifying the FEA model for the Type XI specimen created by Mr. Yeun Chul Park as part of this project to include the retrofit jacket around the existing model. The dimensions of Type XI specimens are shown in Figure 13 and Figure 14. The jacket was modeled as per details shown in Figure 126. The retrofitted Model 1 as meshed is shown in Figure 127 and Figure 128. The figures show the parts disassembled, with only one-half of the jacket and the structure shown in each figure for clarity. To reduce the size of the model, the top part of the Type XI pole model was trimmed at 24 in (610 mm) from the top of the jacket. Existing fatigue cracks were simulated in the pole on both the front (handhole) and back sides of the pole wall, reproducing the worst-case fatigue cracking observed in the Type XI specimens. Further discussion of modeling these cracks will follow. Holes of 1 in (25 mm) diameter were provided in the model at the ends of the seams to simulate arrest holes at the crack tips that would be drilled before retrofitting the cracked structures. The objective was to determine if the arrest holes along with retrofitting would prevent further crack growth.

The 3D FEA models were created using 20-node solid hexahedron elements C3D20R (Simulia 2008). The elements were second-order serendipity-type,

incorporating isoparametric formulation with reduced integration. This element was chosen because of its capability of producing accurate stress analyses (Simulia 2008). Two elements were provided across the thickness of the pole and the jacket to capture the change in stress through the thickness. The maximum edge dimension was set to $^{3}/_{4}$ in (19 mm), corresponding to a maximum aspect ratio for elements of 4:1, as recommended in the FEA protocol set forth for the project.

Fatigue cracks in the original structure were approximated in Model 1 by adding seam features along the toe of the backing ring to pole weld. On each side (handhole and opposite), the cracks symmetrically covered a 90^{o} segment. Tie constraints were used to approximate the bolted connections between the jacket and the pole. The bolt head for a $^{7}/_{8}$ in (22 mm) diameter bolt was approximated by a 1 $^{3}/_{8}$ in (35 mm) diameter annular region with a $^{15}/_{16}$ in (24 mm) hole at each bolt location. The nodes on the inside surface of the jacket in this annular region were fixed to their counterpart on the exterior of the pole wall. Figure 129 is a cutaway view showing the inside surface of the jacket, with the pole removed for clarity. The shaded regions represent surfaces whose included nodes were fixed to the pole. The same procedure was followed to fix the bottom of the retrofit base plate to the existing structure base plate and to fix the inside surface of splice plates to the retrofit jacket at bolt locations. Contact definitions were created between the interior surface of the jacket and the exterior of the pole as well as between the interior of splice plates and the exterior of the jacket to prevent one analytical surface from “passing through” another.

A stress-based submodeling technique was used to analyze Model 1 because of the change in stiffness of the structure caused by the retrofit jacket. As such, the displacement solutions of the Type XI specimen model at the interface boundary of the retrofitted structures could not be used for analyzing Model 1. However, the stress field in the pole wall above the jacket was unaffected by the jacket retrofit of this cantilevered structure. An offset of 24 in (610 mm) was provided between the top of the retrofit and the submodel boundary. The applied load was 4.6 kips (20.5 kN) at a height of 144 $^{1}/_{2}$ in (3670 mm) above the original base plate, corresponding to a 5 ksi (34 MPa) nominal ($^{Mc}/_{I}$) stress at the pole-to-base plate connection in the original structure and a 3.73 ksi (26 MPa) nominal stress at the pole-to-base plate connection of the retrofit jacket, where the original structure is not included as part of the section modulus of the retrofit jacket.

Support boundary conditions were created in the Model 1 to approximate the testing conditions, discussed in Section 2.2.2. For areas on the actual retrofitted structure in contact with the leveling nuts and lock nuts, the corresponding nodes in the FEA model were restrained against displacement in all three directions. This prevented rotation of the surfaces and movement of the nodes within these areas. This approximation generally agreed with more detailed model of the Type XI specimen that incorporated the anchor rods, leveling nuts, lock nuts, and interface contact between the nuts and the base plate. This simplified boundary condition decreased the computational resources required without compromising the accuracy at the jacket wall-to-base plate connection.

The FEA results for the cracked Type XI specimen and Model 1 are shown in Figure 130. The plots are scaled to a maximum principal stress equal to the maximum geometric stress in the retrofit jacket, 9.36 ksi (65 MPa). Figure 130(a) shows the cracked specimen subjected to a 4.6 kip (20.5 kN) load at the load point, corresponding to a 5 ksi (34 MPa) nominal tensile stress at the original pole base on the handhole side. The model is identical to Model 1 without the retrofit jacket or bolt holes, and is shown for comparative purposes. Figure 130(b) and Figure 130(c) are the retrofitted pole and the retrofit jacket, shown in an exploded view with the back half of the model not shown for clarity. A region of elevated stress was observed at the rounded crack tip in the cracked Type XI specimen model results. The FEA results for Model 1 in Figure 130(b) show a reduction in the maximum principal stress at the pole-to-base plate connection. Another load case was also run for Model 1, with the same 4.6 kip (20.5 kN) load applied in the opposite direction to produce a tensile geometric stress on the side opposite the handhole. The results for this finite element analysis are shown in Figure 131. The geometric stress at the jacket wall-to-base plate connection was highest opposite the handhole, therefore this side was chosen for submodel analysis.

7.4.2 3D Model 2

Submodel analysis of the jacket wall-to-base plate connection was performed to refine the mesh size for determination of the converged geometric stress at the groove weld toe. The region chosen for Model 2 is shown in Figure 132. A portion of the wall thickness was trimmed away from the interior and a portion of the base plate

thickness was trimmed away from the bottom to avoid using displacements at nodes with a contact definition in Model 1 to induce displacements in Model 2. The size of Model 2 was chosen such that the cut boundaries were sufficiently away from the locations of interest and did not influence the stress solutions.

The mesh was refined for Model 2, and a separate partition was provided at a distance of $0.1\sqrt{(r \times t)}$, equal to 0.212 in (5.4 mm), above the groove weld toe on the jacket wall for determining the geometric stress. Where r was taken as half the nominal outer flat-to-flat distance of the jacket, 12 $^3/_8$ in (314 mm), and t was the jacket wall thickness, $^3/_8$ in (10 mm). The maximum element size for Model 2 was 0.212 in (5.4 mm), equal to $0.1\sqrt{(r \times t)}$. This was chosen to maintain a uniform element size along the height of the model. Two elements were used across the pole thickness to capture the variation in stress through the thickness.

Displacement-based submodeling was used and the displacement solution from Model 1 was used to drive the analysis. As stated before, the applied load was 4.6 kips (20.5 kN), corresponding to a 3.73 ksi (26 MPa) nominal stress at the jacket wall-to-base plate connection.

The FEA results for Model 2 are shown in Figure 133. The model is shown in Figure 133(a) split at the center, along the plane on which the geometric stress was evaluated on the jacket surface. The stress in the x-x direction along the outer surface is plotted in Figure 133(b). The results predict a geometric stress of 9.36 ksi (65 MPa) and a geometric stress concentration factor, k_g, of 2.51 when divided by the nominal stress of 3.73 ksi (26 MPa). This geometric stress concentration factor was used for

assessing the fatigue resistance of the jacket wall-to-base plate connection, as detailed in Section 7.5.

7.4.3 Notch Stress Models

Model 3 was created with the same nominal weld geometry as the retrofit models, to determine the theoretical stress concentration of the in-service weld. The dimensions of Model 3 are shown in Figure 134. The shaded area is the extent of Model 4. At an idealized weld toe notch with zero radius, the theoretical stress concentration is infinite. To obtain a converged stress at the weld toe notch, the weld toe was approximated as circular with a radius, r_w, of 0.04 in (1.0 mm) as per the analytical protocols adopted for the project. The element size was set to 0.04 in (1.0 mm), placing one element over the weld toe radius. Boundary conditions were created by restraining displacement in all nodes on the underside of the base plate portion. Model 3 was loaded with a 10 ksi (69 MPa) tensile pressure applied to the top surface of the pole wall as shown in Figure 134. The boundary conditions and load were chosen to determine the stress concentration due only to the abrupt change of direction along the surface in the longitudinal direction at the weld toe, and were purposefully not identical to the in-service condition.

Model 4 was created to provide a more refined mesh over the weld toe radius, to obtain a converged notch stress. The dimensions of Model 4 are shown in Figure 135. Model 4 consisted of a symmetrical 5^o sector of Model 3 at the centerline. The weld radius consisted of six elements, with a size of 0.008 in (0.20 mm) in the longitudinal direction. Biased meshing was used along the pole wall and weld surface,

with the elements transitioning from a nominal length of 0.008 in (0.20 mm) at the weld toe to 0.027 in (0.69 mm) at the ends. This maintained the recommended 4:1 aspect ratio while saving computational resources by placing the finest mesh only at the area of interest.

The FEA results for Model 4 are shown in Figure 136. The section was cut along the centerline of the submodel, and shows the maximum principal stress on the surface of the cut. The results predict a notch stress of 14.17 ksi (98 MPa) and a theoretical stress concentration factor, k_t, of 1.42 when divided by the 10 ksi (69 MPa) applied stress. The theoretical stress concentration factor was used for assessing the fatigue resistance of the jacket wall-to-base plate connection, as detailed in Section 7.5.

7.5 Assessment of Fatigue Resistance of Jacket Wall-to-Base Plate Connection

The fatigue resistance of the retrofit jacket was estimated using a stress-life approach based on the fatigue effective notch stress at the weld toe. The nominal stress at the base weld toe of the retrofit jacket was calculated by the equation:

$$\sigma_{nom} = \frac{M}{S_x} \qquad (7\text{-}1)$$

Where M was the nominal moment at the weld toe, and S_x was the section modulus of 173.65 in^3 (2846 cm^3). As stated in Section 7.4.1, the applied load in the finite element analysis model was 4.6 kip (20.5 kN). The distance from the load application

point to the weld toe was 140.63 in (3572 mm), yielding a moment of 646.9 kip-in (73.2 kN-m). Assuming that the cracked pole does not contribute to the section modulus, the nominal stress was computed as 3.73 ksi (26 MPa). The nominal stress and the geometric stress, σ_g, were used to calculate the geometric stress concentration factor, k_g, using the equation:

$$k_g = \frac{\sigma_g}{\sigma_{nom}} \tag{7-2}$$

As previously stated, the calculated value of the geometric stress concentration was 2.51.

The fatigue notch factor, k_f, accounting for the effect of the notch geometry at the weld toe, as well as the material properties was estimated by the equation (Peterson 1945):

$$k_f = 1 + \frac{k_t - 1}{\left(1 + \frac{a_n}{r_w}\right)} \tag{7-3}$$

The theoretical stress concentration factor, k_t, was estimated earlier as 1.42. The notch radius, r_w, was 0.04 in (1.0 mm). The material constant a_n was given by the following empirical equation (SAE 1968):

$$a_n = \left[\frac{300}{F_u(\text{ksi})}\right]^{1.8} \times 10^{-3}(\text{in}) \qquad (7\text{-}4)$$

Where F_u is the ultimate strength of the material, which was assumed as 70 ksi (483 MPa) for the jacket and the weld metal, which conformed to ASTM A572 and AWS 7013 electrodes. The calculated value for a_n was 0.014 in (0.36 mm). The fatigue notch factor was calculated as 1.31.

The service endurance limit, $S_{e(s)}$, was calculated using the geometric stress concentration factor, the fatigue notch factor, and the endurance limit for the material, S_e, according to the equation:

$$S_{e(s)} = \frac{S_e}{k_f \cdot k_g} \qquad (7\text{-}5)$$

An approximation of the endurance limit for steel is that the endurance limit is equal to one half of the ultimate strength. Substituting into Equation (7-5) yields:

$$S_{e(s)} = \frac{F_u}{2 \cdot k_f \cdot k_g} \qquad (7\text{-}6)$$

Using this analysis method, the service endurance limit takes the place of the CAFL determined by the AASHTO Specification detail category. The nominal stress range

was calculated as before, and compared to the limiting value of the service endurance limit. Completing Equation (7-6), the endurance limit for the retrofit jacket was 10.64 ksi (73 MPa); above the CAFL for a Category C detail.

7.6 Laboratory Testing

To confirm the effectiveness of the retrofit jacket design, full-scale fatigue testing was conducted with the retrofit jacket fitted to previously cracked specimens. A single replicate of the retrofit jacket design was fabricated by a local fabricator at a cost of $6,200. The jacket was fitted to specimens by the laboratory technicians. Figure 137 shows the jacket ready to be installed on specimen XI-9, after which the assembly was known as specimen JRXI. Both jacket halves and the splice plates were installed prior to fitting the specimen into the testing setup. Installation outside of the testing setup provided greater mobility around the specimen, as the proximity of the setup to the strong wall limited access to the handhole side. All $^{7}/_{8}$ in (22 mm) diameter bolts were pretensioned to yield using an impact wrench. The washers and lock nuts at the base plate were installed following the configuration and procedure discussed in Section 2.2.

Specimen JRXI was elaborately gaged for static testing. The stresses in the longitudinal direction along the exterior jacket surfaces are plotted in Figure 138 on a path in the loading plane extending from the weld toe at the jacket base opposite the handhole. A 1mm strip gage was provided abutting the jacket weld toe, with a $^{1}/_{4}$ in gage located 6 in (152 mm) away. The measured stresses at strain gages, the FEA results, and the nominal stress are provided for comparison. The results are for an

applied load of 4.6 kip (20.5 kN), corresponding to a nominal stress of 3.73 ksi (26 MPa) at the jacket wall-to-base plate weld toe on the jacket wall. As stated, the nominal stress was calculated with the assumption that the cracked structure did not contribute to the section modulus. While the same general decay away from the weld toe was observed in both the FEA prediction and the measured stresses, the stress measured at the gage abutting the weld toe was 40.0% less than the FEA prediction. At 6 in (152 mm) away from the weld toe, the stress measured at the $^1/_4$ in gage was 25.0% less than the FEA prediction. The FEA result oscillated over the area shown due to the effect of the bolt holes provided in the jacket wall for connection to the original pole. The FEA result was not greater than the nominal stress except within the influence of the weld toe, indicating that the nominal stress result was more conservative than the FEA estimate, and load sharing was predicted by FEA. That the measured stresses were lower than the FEA result indicated that the actual structure experienced additional load sharing when compared to the FEA result.

Two separate fatigue tests were conducted on the retrofit jacket. The first test was conducted with specimen XI-9 and the second test with specimen X-3. The testing nominal stress range was 10 ksi (69 MPa) at the jacket wall-to-base plate connection weld toe on the jacket wall. The applied load range was 19% more than the load range required to produce 10 ksi (69 MPa) nominal stress range in the Type XI specimen. Testing continued until the retrofit jacket was run-out for Category C at 8.2 million cycles. Upon removal, cracking was observed in specimen XI-9 at the handhole. Cracking had initiated at a lack-of-fusion defects at the handhole frame-to-

pole weld from both lower corners of the handhole reinforcing frame. The cracks did not propagate beyond the compressive stress field created by the bolted connection between the jacket and pole. This cracking was unexpected, but the lack of fatigue cracking in the retrofit jacket confirmed that propagation of cracks in the underlying specimen was not problematic. The retrofit jacket was then installed on specimen X-3. Testing continued until the retrofit jacket was run-out for Category C at 8.2 million cycles. The testing was uneventful, with the retrofit jacket remaining uncracked and the existing cracks in specimen X-3 remaining unchanged.

7.7 Retrofitting Conclusions

The retrofit jacket developed as part of NCHRP Project 10-70 detailed in this chapter was determined to be a cost-effective solution to replacement of a fatigue-cracked high-level lighting pole. The retrofit jacket was designed using a stress-life approach, which provided a more accurate estimation of the CAFL of the retrofit jacket pole-to-base plate connection than the nominal stress approach employed by the AASHTO Specification. According to the AASHTO Specification, the CAFL for the retrofit jacket pole-to-base plate connection was 4.5 ksi (31 MPa). The stress-life approach predicted a CAFL of 10.64 ksi (73 MPa). Full-scale fatigue testing of the retrofit jacket revealed a minimum CAFL of 10 ksi (69 MPa). By taking advantage of a design approach that was not overly conservative, less material was required for fabrication of the retrofit. This added to the cost-effectiveness of the retrofit jacket, which cost less than 15% of the replacement cost for a new high-level lighting pole. For situations in which a large population of high-level lighting poles is under-

designed for the in-service loading, a retrofit program will limit the budgetary impact of providing the required level of safety for motorists.

8. CONCLUSIONS

The research reported in this thesis was performed as part of NCHRP Project 10:70: Cost-effective connection details for highway signs, luminaires, and traffic signal structures to establish the fatigue resistance of pole-to-base plate connections for high-level lighting support structures. Finite and infinite life fatigue performance of cost-effective connection details for new construction and retrofitting existing structures were evaluated by experimental and analytical studies. The research findings formed the basis for the proposed revision to the fatigue design provisions of the existing AASHTO Specifications for Supports Structures for Highway Signs, Luminaires, and Traffic Signals.

Fatigue tests were conducted on twenty-three full-scale high-level lighting pole specimens. Three of these (Type X) employed a fillet-welded pole-to-base plate connection. Ten other specimens (Type XI) employed a full-penetration groove welded connection with a backing ring that was welded to both the pole and the plate. The other ten specimens (Type XII) employed a fillet-welded stiffened pole-to-base plate connection that was designed (by others) as part of the project by parametric FEA for optimized fatigue performance. Fatigue tests were conducted at multiple stress range levels to generate data for both finite and infinite life. Location and propagation of fatigue cracks were recorded during the tests, and origin and growth of fatigue cracks were evaluated by post-mortem fractographic studies. Using simplistic fracture mechanics analyses, attempts were made to predict crack propagation based on an observed surface crack length.

Response characteristics of each specimen type were evaluated by static tests. Behavior of the specimens under load, and the stresses at the critical details were assessed by measuring strains using conventional bondable electrical resistance strain gages, as well as with modern non-contact 3D-ICP. Procedures were developed for consistent measurements of stresses using 3D-ICP in regions of high stress concentrations and stress gradients, which provided a spatial distribution of surface stresses rather than discrete strain measures at the gages.

A possible correlation between the weld geometry and the scatter observed in the fatigue test data was investigated. The weld profiles of Type XI specimens at discrete sections were measured by a novel approach using the digital images from 3D-ICP, which was less effort-intensive compared to the traditional metallographic technique. Effects of weld size and weld toe angle were considered through the worst and the best possible combinations of the weld geometric parameters and FEA, and the scatter on the predicted fatigue life was assessed.

Finally a cost-effective retrofit design for cracked high-level lighting poles was developed by FEA based on a concept that was previously used in service. Fatigue tests were conducted on two retrofitted specimens that were cracked during earlier fatigue tests, and the infinite life fatigue resistance of the retrofit design was established.

8.1 Behavior of Pole-to-Base Plate Connections

1. Significant secondary out-of-plane bending of the pole was observed at the pole-to-base plate connection. This occurred due to the tendency of

ovalization of a pole section under load, which was restrained to a circular section at the base plate junction. This incompatibility of deformation between the pole and the plate had to be accommodated by the out-of-plane bending of the pole wall.

2. The in-plane membrane stresses in the pole wall were augmented by high out-of-plane bending stresses near the pole-to-base plate connection. This was manifested by a peak at the weld toe followed by a valley in the normal stress profile in the vertical direction. Away from the pole base the bending stresses dissipated, which generally occurred at about 5 in (127 mm) away from the base plate.

3. The measured stress along the pole surface in the vertical direction at the pole-to-base plate weld toe was less than the FEA prediction for all specimens. The measured stress 6 in (152 mm) away from the pole-to-base plate connection, however, showed a good correlation. Apparently, the difference at the weld toe was due to the idealized weld in the FE model, where the weld toe was modeled as a sharp notch of zero root radius.

4. The addition of the optimized stiffener design to the fillet-welded pole-to-base plate connection of test geometry increased the section modulus and decreased the nominal stress at the fillet weld toe on the pole. Strain gage measurements indicated that the stiffeners reduced out-of-plane bending of the pole wall at the pole-to-base plate connection.

5. The use of 3D-ICP technique required a thorough understanding of both the hardware and software. The efficacy of the technique improved with operator experience.

8.2 Fatigue Testing

1. Fatigue cracking in the fillet-welded pole-to-base plate connection of the test geometry (Type X specimens) occurred at the fillet weld toe on the pole.
2. Fatigue cracking in the groove-welded pole-to-base plate connection of the test geometry (Type XI specimens) occurred at weld toe of the fillet reinforcement on the pole, with secondary cracking at the interior backing ring seal weld toe on the pole.
3. Fatigue cracking in the stiffened fillet-welded pole-to-base plate connection of the optimized test geometry (Type XII specimens) occurred primarily at the weld toe of the stiffener termination on the pole. Additional cracking at the fillet weld toe on the pole of the fillet-welded pole-to-base plate connection was observed in three specimens. However, the connection geometry arrested crack growth.
4. Crack growth at the pole-to-base plate connections was generally exponential. The majority of the fatigue life was spent in growing fatigue cracks to a detectable size. In a stiffened pole-to-base plate connection, crack growth at the stiffener termination on the pole increased after the crack at the weld toe branched into the pole wall. The majority of the fatigue life was expended by that point.

5. The backing ring at the full-penetration groove-welded pole-to-base plate connection provided an alternate load path, when the backing ring was welded to the base plate and the pole and the fatigue crack appeared at the groove weld toe first. Crack growth at this connection was retarded by the presence of an alternate load path through the backing ring and more remaining fatigue life was observed after first crack detection compared to other pole-to-base plate connections.

6. Due to predominant out-of-plane bending of the pole wall at the pole-to-base plate connections, fatigue resistances of these connections in the finite and infinite life regions corresponded to different detail categories as defined in the AASHTO LRFD Bridge Design Specifications. The detail categories in the AASHTO Bridge Specification were developed primarily based on fatigue testing of beam specimens, where in-plane stresses were predominant. For the pole-to-base plate connections, the infinite life fatigue resistance always corresponded to a higher fatigue category than that for the finite life resistance.

7. The fillet-welded pole-to-base plate connection of the test geometry (Type X specimens) demonstrated a finite-life fatigue resistance of AASHTO Category E′ details. Limited test results indicated that the CAFL for this detail is likely greater than 4.5 ksi (31 MPa) corresponding to that of AASHTO Category E. More replicates are required to adequately establish the CAFL. While the finite-life fatigue resistance agreed with the classification of this detail in the

AASHTO Specification, the infinite life fatigue resistance was higher than that of the specification recommendation.

8. The groove-welded pole-to-base plate connection of the test geometry (Type XI specimens) demonstrated a finite-life fatigue resistance of AASHTO Category E details. The CAFL for this detail is 7 ksi (48 MPa) corresponding to that of AASHTO Category D. While the finite life fatigue resistance agreed with the classification of this detail in the AASHTO Specification, the infinite life fatigue resistance was higher than that of the specification recommendation.

9. The stiffened fillet-welded pole-to-base plate connection of the optimized test geometry (Type XII specimens) demonstrated a finite-life fatigue resistance of AASHTO Category E details. The CAFL for this detail is 7 ksi (48 MPa) corresponding to that of AASHTO Category D. The fatigue resistance of this detail is greater than the current classification of this detail in the AASHTO Specification as Category E′.

8.3 Effect of Weld Geometry on Fatigue Performance

1. The scatter observed in the fatigue test results was primarily due to the inherent variability in macro- and micro-discontinuities at the weld toe.

2. Scatter exceeding the usual variability was observed in some test results, which were due to the variation in the fabricated weld geometry and particularly the weld toe angle from the specified nominal value.

8.4 Origin and Propagation of Fatigue Cracks

1. Fatigue cracks in the pole-to-base plate connections initiated from slag-inclusion micro-discontinuities at the weld toes and propagated in two stages. In the first stage, classical semi-elliptical crack propagation was evident through the thickness of the pole wall. After the crack broke through the pole wall, the crack progressed on two fronts around the perimeter of the pole in the second stage. In the stiffened pole-to-base plate connection, crack growth from the weld root at the stiffener termination is possible in the presence of an unusually large lack of fusion.
2. Simple fracture mechanics analysis provided a realistic prediction of the observed crack propagation on the pole surface in the presence of a high stress gradient, and when a stress gradient correction factor was considered. In other situations, the simple models failed to adequately capture the boundary conditions and the stress states on the crack face. A more elaborate crack propagation analyses using 3D FEA may be required for a more accurate assessment.

8.5 Jacket Retrofitting

1. The steel jacket provided a cost-effective retrofit solution for unstiffened fillet and groove-welded pole-to-base plate connections that developed fatigue cracking in service. The cost of the retrofit jacket, including fabrication and labor, was less than 15% of the replacement cost for a high-level lighting pole.

2. The retrofit jacket exhibited a CAFL of 10 ksi (69 MPa) at the jacket shell to base plate full-penetration groove weld for the test geometry.

8.6 Recommendations for Further Research

This research evaluated the fatigue performance of the fillet-welded tube-to-transverse plate connections for high-level lighting structures on a limited number of specimens that were mostly tested in the finite life region. Compared to the fatigue test results of TPF-5(116), these connections employing thicker base plate and increased number of fasteners exhibited improved fatigue resistance. While groove-welded and stiffened fillet-welded pole-to-base plate connections exhibit superior performance compared to the fillet-welded connection, this connection is more fabrication-friendly and cost-effective. Infinite life fatigue resistance of the unstiffened fillet-welded connection should be verified by testing more replicates.

Fatigue resistance of the pole-to-base plate connections was determined for particular connection geometries. The fatigue performance of these connections depends on their geometric parameters. Other geometric configurations should be tested to verify their fatigue resistance.

The effect of weld geometry on scatter observed in the fatigue test results was investigated only for one type of specimen (Type XI) due to time constraints. Further effort could be put towards investigating the effect of variation in weld geometry on the other test specimens.

An investigation into estimating the remaining fatigue life from the observed surface crack size was not completed due to limited scope and lack of sufficient

information regarding beach marks. A dye system to mark the crack front at intervals during fatigue testing would provide crack shape data from fatigue tests. Further fatigue testing with a method for marking the crack front would produce a larger sample size for evaluation. A more robust 3D fracture mechanics model is also needed to capture the stress effects as the cracks grow.

Based on the effectiveness of the retrofit strategy developed for the high-level lighting poles, the retrofit may be extended to other structures, such as cantilevered mast arm sign/signal structures.

TABLES

Table 1. AASHTO detail categories and corresponding constant amplitude fatigue limits

Detail Category	CAFL (ksi)
A	24
B	16
B'	12
C	10
C'	12
D	7
E	4.5
E'	2.6

Table 2. Test Results Type X Specimen

Specimen Type	Specimen ID	Detail	Nominal Stress Parameters S_{min} (ksi)	Nominal Stress Parameters S_r (ksi)	Description of Crack Location and Origin	First Observation Length (in)	First Observation # of Cycles	12 in Crack # of Cycles	Final Length (in)	Final # of Cycles	Comments
X	1	Pole Base	-2.7	5.4							Run-out at 17.00E+06 cycles
		Handhole									
	1 Re-run 1	Pole Base	-4.0	8.0							Run-out at 13.00E+06 cycles
		Handhole									
	1 Re-run 2	Pole Base	-5.0	10.0	At tube-to-end plate fillet weld toe on the tube wall	1.50	1.38E+06	1.59E+06	17.00	1.78E+06	Crack terminated fatigue test
		Handhole									Did not crack
	2	Pole Base	-4.0	8.0	At tube-to-end plate fillet weld toe on the tube wall	1.00+1.50	1.75E+06	2.06E+06	12.00	2.39E+06	Crack terminated fatigue test
		Handhole									Did not crack
	3	Pole Base	-4.0	8.0	At tube-to-end plate fillet weld toe on the tube wall on handhole side and opposite.	3.88	.68E+06	.77E+06	17.00	1.02E+06	Crack terminated fatigue test
		Handhole									Did not crack

Table 3. Test Results Type XI Specimen

Specimen Type	Specimen ID	Detail	Nominal Stress Parameters S_{min} (ksi)	Nominal Stress Parameters S_r (ksi)	Description of Crack Location and Origin	First Observation Length (in)	First Observation # of Cycles	12 in Crack # of Cycles	Final Length (in)	Final # of Cycles	Comments
XI	1	Pole Base	-6.0	12.0	At tube-to-end plate weld toe on the tube wall on opposite side of hand hole	5.00	.75E+06	.98E+06	16.06	1.13E+06	
			-5.8	11.6	From the toe of weld termination on the tube wall at the top of backing ring on opposite side of hand hole	12.25	1.13E+06	1.06E+06	12.25	1.13E+06	Backing ring crack terminated fatigue test
		Handhole	-4.5	9.0							Did not crack
	2	Pole Base	-6.0	12.0	At tube-to-end plate weld toe on the tube wall on hand hole side	2.38	1.56E+06	3.09E+06	14.75	3.49E+06	
			-5.8	11.6	From the toe of weld termination on the tube wall at the top of backing ring on hand hole side	4.38	3.13E+06	3.43E+06	12.50	3.49E+06	Backing ring crack terminated fatigue test
		Handhole	-4.5	9.0							Did not crack
	3	Pole Base	-6.0	12.0	At tube-to-end plate weld toe on the tube wall on handhole side	3.13	.33E+06		11.44	.77E+06	
			-6.0	12.0	At tube-to-end plate weld toe on the tube wall on opposite side of hand hole	3.25	.33E+06	.62E+06	8.38+6.63	.77E+06	
			-5.8	11.6	From the toe of weld termination on the tube wall at the top of backing ring on opposite side of hand hole	2.19	.59E+06		10.63	.77E+06	Backing ring crack terminated fatigue test
		Handhole	-4.5	9.0							Did not crack
	4	Pole Base	-3.5	7.0							Run-out at 14.70E+06 cycles
		Handhole	-2.6	5.3							
	4 Re-run 1	Pole Base	-5.0	10.0	At tube-to-end plate weld toe on the tube wall on handhole side	1.75	.65E+06		11.56	2.15E+06	
			-5.0	10.0	At tube-to-end plate weld toe on the tube wall on opposite side of hand hole	2.06	.71E+06	1.30E+06	19.88	2.15E+06	
			-4.8	9.6	From the toe of weld termination on the tube wall at the top of backing ring on opposite side of hand hole	1.13	1.59E+06	2.15E+06	12.75	2.15E+06	Backing ring crack terminated fatigue test
		Handhole	-3.8	7.5							Did not crack
	5	Pole Base	-3.5	7.0							Run-out at 14.70E+06 cycles
		Handhole	-2.6	5.3							

Table 3. Continued

Specimen Type	Specimen ID	Detail	Nominal Stress Parameters S_{min} (ksi)	Nominal Stress Parameters S_r (ksi)	Description of Crack Location and Origin	First Observation Length (in)	First Observation # of Cycles	12 in Crack # of Cycles	Final Length (in)	Final # of Cycles	Comments
XI	5 Re-run 1	Pole Base	-5.0	10.0	At tube-to-end plate weld toe on the tube wall on hand hole side	0.63	.68E+06		15.63	2.86E+06	
			-5.0	10.0	At tube-to-end plate weld toe on the tube wall on opposite side of hand hole	1.69+0.81	.68E+06	2.24E+06	15.38	2.86E+06	
			-4.8	9.6	From the toe of weld termination on the tube wall at the top of backing ring on opposite side of hand hole	2.75	1.79E+06	2.86E+06	12.75	2.86E+06	Backing ring crack terminated fatigue test
		Handhole	-3.8	7.5							Did not crack
	6	Pole Base	-3.5	7.0							Run-out at 14.70E+06 cycles
		Handhole	-2.6	5.3							
	6 Re-run 1	Pole Base	-5.0	10.0	At tube-to-end plate weld toe on the tube wall on hand hole side	0.19+0.75	.84E+06	2.24E+06	24.50	2.51E+06	
			-5.0	10.0	At tube-to-end plate weld toe on the tube wall on opposite side of hand hole	0.88	.54E+06	1.73E+06	20.00	2.51E+06	
			-4.8	9.6	From the toe of weld termination on the tube wall at the top of backing ring on opposite side of hand hole	1.13	2.12E+06	2.45E+06	15.50	2.51E+06	Backing ring crack terminated fatigue test
			-4.8	9.6	From the toe of weld termination on the tube wall at the top of backing ring on hand hole side	1.50	2.29E+06		4.88	2.51E+06	
		Handhole	-3.8	7.5							Did not crack
	7	Pole Base	-3.5	7.0							Run-out at 14.70E+06 cycles
		Handhole	-2.6	5.3							
	7 Re-run 1	Pole Base	-5.0	10.0	At tube-to-end plate weld toe on the tube wall on hand hole side	2.06	.77E+06		9.38	1.80E+06	
			-5.0	10.0	At tube-to-end plate weld toe on the tube wall on opposite side of hand hole	1.13+1.5+1.5	.50E+06	1.16E+06	21.19	1.80E+06	
			-4.8	9.6	From the toe of weld termination on the tube wall at the top of backing ring on opposite side of hand hole	1+0.69+0.75	1.45E+06	1.75E+06	13.25	1.80E+06	Backing ring crack terminated fatigue test
		Handhole	-3.8	7.5							Did not crack

Table 3. Continued

Specimen Type	Specimen ID	Detail	Nominal Stress Parameters S_{min} (ksi)	Nominal Stress Parameters S_r (ksi)	Description of Crack Location and Origin	First Observation Length (in)	First Observation # of Cycles	12 in Crack # of Cycles	Final Length (in)	Final # of Cycles	Comments
XI	8	Pole Base	-7.0	14.0	At tube-to-end plate weld toe on the tube wall on hand hole side	0.63	0.10E+06		9.88	0.53E+06	
			-7.0	14.0	At tube-to-end plate weld toe on the tube wall on opposite side of hand hole	0.50	0.10E+06	0.29E+06	22.38	0.53E+06	
			-6.8	13.5	From the toe of weld termination on the tube wall at the top of backing ring on opposite side of hand hole	2.75+.75	0.39E+06		9.88	0.53E+06	Backing ring crack terminated fatigue test
			-6.8	13.5	From the throat of weld termination on tube wall at top of backing ring opposite hand hole	5.63	0.47E+06		9.50	0.53E+06	
			-6.8	13.5	From the center of the backing ring seam weld opposite hand hole.	4.75	0.47E+06		7.88	0.53E+06	
		Handhole	-5.3	10.6							Did not crack
	9	Pole Base	-8.0	16.0	At tube-to-end plate weld toe on the tube wall on hand hole side	2.5+2.75	.14E+06	0.37E+06	19.00	.60E+06	
			-8.0	16.0	At tube-to-end plate weld toe on the tube wall on opposite side of hand hole	7.88+0.63	.14E+06	.47E+06	17.06	.60E+06	
			-7.7	15.4	From the toe of weld termination on the tube wall at the top of backing ring on hand hole side	25.75	.60E+06		25.75	.60E+06	Backing ring crack terminated fatigue test
		Handhole	-6.0	12.0							Did not crack
	10	Pole Base	-8.0	16.0	At tube-to-end plate weld toe on the tube wall on hand hole side	2.25	0.06E+06	.19E+06	16.31	.34E+06	
			-8.0	16.0	At tube-to-end plate weld toe on the tube wall on opposite side of hand hole	2.75	.15E+06	.34E+06	6+6.13	.34E+06	
			-7.7	15.4	From the toe of weld termination on the tube wall at the top of backing ring on hand hole side	12.88+3.94	.34E+06	.34E+06	12.88+3.94	.34E+06	Backing ring crack terminated fatigue test
		Handhole	-6.0	12.0							Did not crack

Table 4. Test Results Type XII Specimen

Specimen Type	Specimen ID	Detail	Nominal Stress Parameters S_{min} (ksi)	Nominal Stress Parameters S_r (ksi)	Description of Crack Location and Origin	First Observation Length (in)	First Observation # of Cycles	12 in Crack # of Cycles	Final Length (in)	Final # of Cycles	Comments
XII	1	Stiffener	-6.0	12.0	At tube-to-stiffener weld toe on the tube wall on loading side	0.50	.23E+06	.72E+06	14.25	.79E+06	Crack terminated fatigue test
			-6.0	12.0	At tube-to stiffener weld toe on the tube wall on opposite of loading side	1.50	.53E+06		8.13	.79E+06	
		Pole Base	-4.3	8.5	At tube-to-end plate fillet weld toe on the tube wall on loading side	0.75	.38E+06		4.63	.79E+06	
			-4.3	8.5							
	2	Stiffener	-6.0	12.0	At tube-to-stiffener weld toe on the tube wall on loading side	1.00	.40E+06		9.00	.91E+06	Crack terminated fatigue test
			-6.0	12.0	At tube-to stiffener weld toe on the tube wall on opposite of loading side	0.50	.40E+06	.88E+06	13.38	.91E+06	
		Pole Base	-4.3	8.5							
			-4.3	8.5							
	3	Stiffener	-6.0	12.0							Crack terminated fatigue test
			-6.0	12.0	At tube-to stiffener weld toe on the tube wall on opposite of loading side	1.00	.58E+06	1.04E+06	12.88	1.06E+06	
		Pole Base	-4.3	8.5							
			-4.3	8.5							
	4	Stiffener	-3.5	7.0							Run-out at 14.70E+06 cycles
			-3.5	7.0							
		Pole Base	-2.5	5.0							
			-2.5	5.0							
	4 Re-run 1	Stiffener	-5.0	10.0	At tube-to-stiffener weld toe on the tube wall on loading side	0.25	.61E+06	1.59E+06	40.75	2.31E+06	Crack terminated fatigue test
			-5.0	10.0							
		Pole Base	-3.6	7.1							
			-3.6	7.1							

Table 4. Continued

Specimen Type	Specimen ID	Detail	Nominal Stress Parameters S_{min} (ksi)	Nominal Stress Parameters S_r (ksi)	Description of Crack Location and Origin	First Observation Length (in)	First Observation # of Cycles	12 in Crack # of Cycles	Final Length (in)	Final # of Cycles	Comments
XII	5	Stiffener	-3.5	7.0							Run-out at 14.70E+06 cycles
			-3.5	7.0							
		Pole Base	-2.5	5.0							
			-2.5	5.0							
	5 Re-run 1	Stiffener	-5.0	10.0	At tube-to-stiffener weld toe on the tube wall on loading side	1.13	4.69E+06	6.04E+06	13.38	6.12E+06	Crack terminated fatigue test
			-5.0	10.0							
		Pole Base	-3.6	7.1							
			-3.6	7.1							
	6	Stiffener	-3.5	7.0	From the root of stiffener to pole fillet top weld	0.63	4.06E+06	5.85E+06	15.13	5.94E+06	Crack terminated fatigue test
			-3.5	7.0							
		Pole Base	-2.5	5.0							
			-2.5	5.0							
	7	Stiffener	-3.5	7.0							Run-out at 14.70E+06 cycles
			-3.5	7.0							
		Pole Base	-3.6	5.0							
			-2.5	5.0							
	7 Re-run 1	Stiffener	-5.0	10.0							
			-5.0	10.0	At tube-to-stiffener weld toe on the stiffener top on opposite of loading side	0.75	6.24E+06	7.98E+06	12.00	7.98E+06	Crack terminated fatigue test
		Pole Base	-5.1	7.1							
			-3.6	7.1							

Table 4. Continued

Specimen Type	Specimen ID	Detail	Nominal Stress Parameters S_{min} (ksi)	Nominal Stress Parameters S_r (ksi)	Description of Crack Location and Origin	First Observation Length (in)	First Observation # of Cycles	12 in Crack # of Cycles	Final Length (in)	Final # of Cycles	Comments
XII	8	Stiffener	-8.0	16.0	At tube-to-stiffener weld toe on the tube wall on loading side	0.94	.15E+06	.43E+06	15.75	.49E+06	Crack terminated fatigue test
			-8.0	16.0	At tube-to-stiffener weld toe on the stiffener top on opposite of loading side	0.75	.05E+06		14.19	.49E+06	
		Pole Base	-5.7	11.3	At tube-to-end plate fillet weld toe on the tube wall on loading side left bend	1.38	.05E+06		7.19	.49E+06	
			-5.7	11.3	At tube-to-end plate fillet weld toe on the tube wall on loading side right bend	2.00	.30E+06		3.56	.49E+06	
			-5.7	11.3	At tube-to-end plate fillet weld toe on the tube wall on opposite of loading side left bend	2.56	.09E+06		8.06	.49E+06	
			-5.7	11.3	At tube-to-end plate fillet weld toe on the tube wall on opposite of loading side right bend	2.63	.30E+06		2.63	.49E+06	
	9	Stiffener	-8.0	16.0	At tube-to-stiffener weld toe on the tube wall on loading side	0.88	.20E+06	.42E+06	12.63	.43E+06	Crack terminated fatigue test
			-8.0	16.0	At tube-to-stiffener weld toe on the stiffener top on opposite of loading side	1.00	.38E+06				
		Pole Base	-5.7	11.3							
			-5.7	11.3							
	10	Stiffener	-8.0	16.0	At tube-to-stiffener weld toe on the tube wall on loading side	1.13	.05E+06		16.75	.47E+06	
			-8.0	16.0	At tube-to-stiffener weld toe on the stiffener top on opposite of loading side	1.13	.11E+06	.37E+06	18.50	.47E+06	Crack terminated fatigue test
		Pole Base	-5.7	11.3	At tube-to-end plate fillet weld toe on the tube wall on loading side left bend	1.38	.27E+06		1.75	.47E+06	
			-5.7	11.3							

Table 5. Type XI specimen weld profile measurements

Specimen	Section	H_1	V_1	θ	L	H_2	V_2	H_3	V_3
X1-1	1	0.331	0.858	161.3	0.092	0.047	0.717	0.110	0.484
	2	0.522	0.975	142.9	0.096	0.097	0.689	0.161	0.554
	3	0.421	1.124	162.7	0.072	0.069	0.672	0.138	0.441
	4	0.445	0.892	147.6	0.074	0.101	0.628	0.149	0.545
XI-2	1	0.379	0.962	156.1	0.107	0.071	0.767	0.143	0.603
	2	0.359	0.985	156.7	0.108	0.071	0.730	0.119	0.611
	3	0.352	0.980	156.3	0.100	0.073	0.767	0.137	0.590
	4	0.310	0.969	168.3	0.107	0.025	0.797	0.070	0.638
XI-3	1	0.418	0.901	154.0	0.068	0.082	0.642	0.144	0.507
	2	0.386	0.941	155.5	0.091	0.078	0.654	0.125	0.540
	3	0.398	0.932	158.9	0.073	0.061	0.713	0.118	0.543
	4	0.426	0.963	155.5	0.075	0.087	0.694	0.141	0.549
	5	0.417	0.955	157.6	0.071	0.075	0.691	0.153	0.536
	6	0.433	0.978	145.1	0.076	0.093	0.710	0.193	0.447
	7	0.325	1.129	162.0	0.071	0.026	0.703	0.085	0.475
	8	0.370	1.002	156.3	0.077	0.059	0.814	0.137	0.467
XI-4	1	0.430	0.972	154.9	0.101	0.092	0.692	0.167	0.480
	2	0.502	0.971	134.0	0.077	0.139	0.671	0.216	0.532
	3	0.463	0.899	146.7	0.082	0.094	0.641	0.173	0.432
	4	0.510	0.890	149.7	0.071	0.098	0.647	0.179	0.473
	5	0.425	0.873	169.6	0.089	0.059	0.668	0.132	0.491
	6	0.455	0.833	147.5	0.089	0.081	0.670	0.145	0.524
XI-5	1	0.419	0.929	152.1	0.080	0.061	0.763	0.143	0.449
	2	0.373	0.920	162.0	0.087	0.050	0.707	0.111	0.419
	3	0.446	0.915	150.8	0.055	0.087	0.685	0.157	0.437
	4	0.437	0.940	153.5	0.111	0.070	0.744	0.162	0.470
	5	0.412	0.937	146.9	0.085	0.099	0.679	0.153	0.460
	6	0.448	0.926	151.0	0.096	0.079	0.679	0.159	0.470

Table 5. Continued

Specimen	Section	H_1	V_1	θ	L	H_2	V_2	H_3	V_3
XI-6	1	0.504	0.933	137.6	0.097	0.117	0.743	0.217	0.577
	2	0.479	0.896	128.2	0.046	0.105	0.723	0.245	0.401
	3	0.446	0.979	150.7	0.091	0.093	0.711	0.155	0.565
	4	0.421	0.954	144.5	0.075	0.105	0.677	0.177	0.500
	5	0.471	0.861	146.8	0.095	0.088	0.655	0.127	0.568
	6	0.444	0.879	147.0	0.115	0.088	0.683	0.137	0.565
	7	0.435	0.815	160.3	0.063	0.036	0.692	0.107	0.550
XI-7	1	0.371	0.971	147.6	0.071	0.079	0.716	0.132	0.564
	2	0.345	0.995	144.6	0.081	0.064	0.722	0.109	0.602
	3	0.382	1.005	146.1	0.106	0.084	0.714	0.128	0.593
XI-8	1	0.390	0.868	144.4	0.074	0.105	0.628	0.149	0.521
	2	0.385	0.867	138.7	0.080	0.103	0.667	0.148	0.552
	3	0.346	0.896	154.8	0.089	0.054	0.687	0.088	0.605
	4	0.414	0.922	133.6	0.087	0.126	0.617	0.173	0.541
	5	0.343	0.915	145.0	0.077	0.069	0.630	0.112	0.549
XI-9	1	0.363	0.878	141.9	0.074	0.090	0.663	0.128	0.576
	2	0.363	0.865	148.8	0.077	0.086	0.609	0.121	0.555
XI-10	1	0.514	0.902	134.0	0.074	0.131	0.781	0.185	0.597
	2	0.276	1.092	160.0	0.079	0.041	0.780	0.067	0.651
	3	0.401	0.961	150.7	0.114	0.085	0.803	0.157	0.591
	4	0.374	0.881	150.1	0.110	0.082	0.727	0.141	0.614
	5	0.382	0.857	139.5	0.075	0.073	0.738	0.134	0.626
	6	0.365	0.883	144.5	0.077	0.066	0.759	0.133	0.614

Table 6. Weld profile geometry measurement results

	H_1	V_1	θ	L	H_2	V_2	H_3	V_3
Standard Deviation, σ	0.055	0.065	8.9	0.015	0.034	0.050	0.024	0.063
Mean, μ	0.408	0.934	150.1	0.084	0.143	0.701	0.080	0.534
μ+2σ	0.518	1.064	167.9	0.115	0.211	0.801	0.129	0.660
μ−2σ	0.299	0.803	132.3	0.054	0.075	0.602	0.032	0.408

Table 7. Specimen X-2 crack propagation estimate, Method 1

Label	$2c$	$a/2c$	a	Φ	M_K	ΔK	da/dN ($\times 10^6$)	$d(2c)/dN$ ($\times 10^6$)	ΔN ($\times 10^6$)	N ($\times 10^6$)	Comments
b_1	0.74	0.154	0.114	1.215	1.000	10.328	0.397	2.572		1.582	
									0.0233		
	0.80	0.154	0.123	1.215	1.000	10.719	0.443	2.887		1.605	
									0.0346		
	0.90	0.153	0.137	1.215	1.000	11.336	0.524	3.438		1.640	
									0.0291		
	1.00	0.152	0.152	1.214	1.000	11.913	0.609	4.018		1.669	
									0.0249		
	1.10	0.150	0.166	1.214	1.036	12.900	0.773	5.136		1.694	
									0.0195		
	1.20	0.149	0.179	1.213	1.089	14.121	1.014	6.783		1.713	
									0.0147		
	1.30	0.148	0.193	1.213	1.141	15.355	1.303	8.783		1.728	
									0.0114		
	1.40	0.147	0.206	1.212	1.192	16.602	1.647	11.178		1.739	
									0.0089		
$2c_0$	1.50	0.146	0.219	1.212	1.243	17.858	2.050	14.011		1.748	First Observation
									0.0071		
	1.60	0.145	0.232	1.211	1.293	19.123	2.517	17.326		1.755	
									0.0058		
	1.70	0.144	0.245	1.211	1.342	20.394	3.054	21.168		1.761	
									0.0047		
	1.80	0.143	0.258	1.210	1.390	21.671	3.664	25.579		1.766	
									0.0039		
	1.90	0.142	0.270	1.210	1.437	22.950	4.352	30.603		1.770	
									0.0033		
	2.00	0.141	0.282	1.209	1.484	24.231	5.122	36.284		1.773	
									0.0022		
b_2	2.08	0.140	0.292	1.209	1.521	25.257	5.800	41.330		1.775	
									0.0005		
	2.10	0.140	0.294	1.209	1.530	25.513	5.978	42.664		1.776	
									0.0023		
	2.20	0.139	0.306	1.208	1.575	26.793	6.924	49.782		1.778	
									0.0010		
	2.25	0.139	0.312	1.208	1.597	27.433	7.432	53.631		1.779	

Constants

t= 0.3125 in

σ_r= 18.72 ksi

Values for $2c$ and a from fracture surface photograph.

Table 8. Specimen X-2 crack propagation estimate, Method 2

Label	$2c$	$a/2c$	a	Φ	M_K	F_G	ΔK	da/dN ($\times 10^6$)	$d(2c)/dN$ ($\times 10^6$)	ΔN ($\times 10^6$)	N ($\times 10^6$)	Comments
b_1	0.74	0.154	0.114	1.215	1.000	2.559	11.295	0.519	3.364		1.518	
										0.0178		
	0.80	0.154	0.123	1.215	1.000	2.426	11.113	0.494	3.217		1.536	
										0.0311		
	0.90	0.153	0.137	1.215	1.000	2.281	11.051	0.486	3.185		1.567	
										0.0314		
	1.00	0.152	0.152	1.214	1.000	2.135	10.869	0.462	3.051		1.598	
										0.0328		
	1.10	0.150	0.166	1.214	1.036	1.994	10.994	0.478	3.179		1.631	
										0.0315		
	1.20	0.149	0.179	1.213	1.089	1.859	11.215	0.508	3.399		1.663	
										0.0294		
	1.30	0.148	0.193	1.213	1.141	1.728	11.336	0.524	3.534		1.692	
										0.0283		
	1.40	0.147	0.206	1.212	1.192	1.601	11.359	0.528	3.581		1.720	
										0.0279		
$2c_0$	1.50	0.146	0.219	1.212	1.243	1.479	11.288	0.518	3.538		1.748	First Observation
										0.0283		
	1.60	0.145	0.232	1.211	1.293	1.362	11.127	0.496	3.413		1.776	
										0.0293		
	1.70	0.144	0.245	1.211	1.342	1.248	10.880	0.464	3.214		1.806	
										0.0311		
	1.80	0.143	0.258	1.210	1.390	1.186	10.981	0.477	3.328		1.837	
										0.0301		
	1.90	0.142	0.270	1.210	1.437	1.155	11.328	0.523	3.680		1.867	
										0.0272		
	2.00	0.141	0.282	1.209	1.484	1.140	11.808	0.593	4.199		1.894	
										0.0191		
b_2	2.08	0.140	0.292	1.209	1.521	1.140	12.299	0.670	4.773		1.913	
										0.0042		
	2.10	0.140	0.294	1.209	1.530	1.144	12.476	0.699	4.989		1.917	
										0.0200		
	2.20	0.139	0.306	1.208	1.575	1.142	13.074	0.805	5.784		1.937	
										0.0086		
	2.25	0.139	0.312	1.208	1.597	1.151	13.489	0.884	6.377		1.946	

Constants

t =	0.3125 in
σ_r =	8 ksi

Values for $2c$ and a from fracture surface photograph.

Table 9. Specimen XII-2 crack propagation estimate, Method 1

Label	$2c$	$a/2c$	a	Φ	Mk	ΔK	da/dN ($\times 10^6$)	$d(2c)/dN$ ($\times 10^6$)	ΔN ($\times 10^6$)	N ($\times 10^6$)	Comments
b_1	0.49	0.314	0.154	1.333	1.000	16.340	1.571	4.994		0.402	
									0.0020		
$2c_0$	0.5	0.314	0.157	1.333	1.004	16.562	1.636	5.203		0.404	First Observation
									0.0192		
	0.6	0.313	0.188	1.332	1.121	20.239	2.984	9.539		0.423	
									0.0021		
b_1	0.62	0.313	0.194	1.332	1.144	20.996	3.332	10.660		0.426	
									0.0075		
	0.7	0.309	0.216	1.328	1.230	23.914	4.924	15.937		0.433	
									0.0063		
	0.8	0.304	0.243	1.324	1.335	27.625	7.590	24.935		0.439	
									0.0040		
	0.9	0.300	0.270	1.319	1.436	31.386	11.130	37.124		0.443	
									0.0027		
	1	0.295	0.295	1.315	1.534	35.176	15.669	53.070		0.446	
									0.0013		
b_1	1.07	0.292	0.313	1.312	1.600	37.837	19.501	66.770		0.447	

Constants

t=	0.3125 in
Δσ=	27.96 ksi

Values for 2c and a from fracture surface photograph.

Table 10. Specimen XII-2 crack propagation estimate, Method 2

Label	$2c$	$a/2c$	a	Φ	M_K	F_G	ΔK	da/dN ($\times 10^6$)	$d(2c)/dN$ ($\times 10^6$)	ΔN ($\times 10^6$)	N ($\times 10^6$)	Comments
b_1	0.49	0.314	0.154	1.333	1.000	1.940	13.603	0.906	2.881		0.401	
										0.0035		
$2c_0$	0.5	0.314	0.157	1.333	1.004	1.891	13.443	0.875	2.782		0.404	First Observation
										0.0359		
	0.6	0.313	0.188	1.332	1.121	1.722	14.958	1.205	3.851		0.440	
										0.0052		
b_1	0.62	0.313	0.194	1.332	1.144	1.664	14.992	1.213	3.881		0.445	
										0.0206		
	0.7	0.309	0.216	1.328	1.230	1.547	15.876	1.441	4.663		0.466	
										0.0214		
	0.8	0.304	0.243	1.324	1.335	1.414	16.763	1.696	5.571		0.487	
										0.0179		
	0.9	0.300	0.270	1.319	1.436	1.292	17.408	1.899	6.335		0.505	
										0.0158		
	1	0.295	0.295	1.315	1.534	1.186	17.903	2.066	6.997		0.521	
										0.0100		
b_1	1.07	0.292	0.313	1.312	1.600	1.115	18.110	2.138	7.321		0.531	

Constants

t=	0.3125 in
S_t=	12 ksi

Values for $2c$ and a from fracture surface photograph.

FIGURES

Figure 1. Example of a high-level lighting pole in service

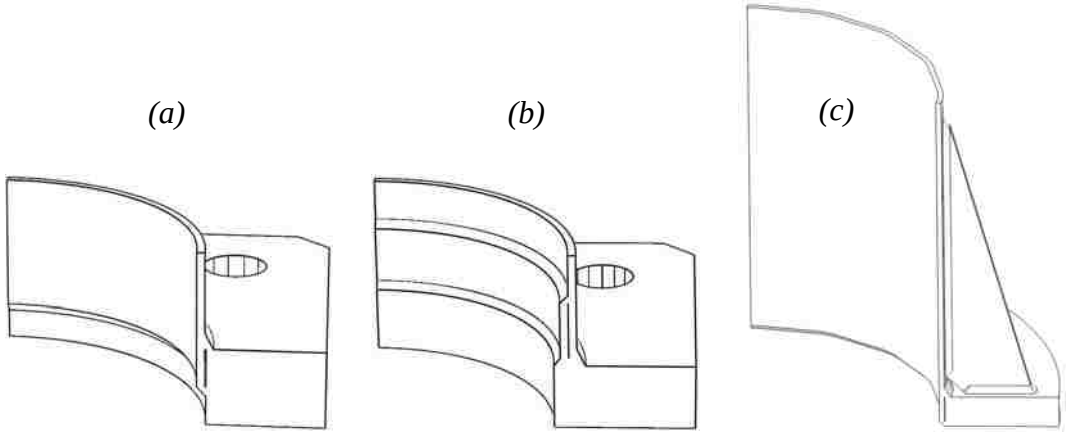

Figure 2. Tube-to-base plate connections: *a*, fillet-welded connection; *b*, full-penetration welded connection; *c*, stiffened fillet-welded connection.

Figure 3. Example of a handhole on an in-service structure

Figure 4. Close-up of collapsed tower *(reprinted from Dexter, 2004)*

Figure 5. Handhole crack at corner *(reprinted from Koob, 2006)*

Figure 6. Stool base connection detail *(reprinted from Dexter, 2004)*

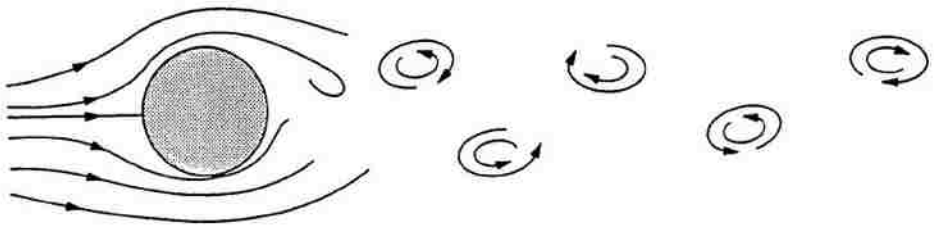

Figure 7. Schematic of a von Karman vortex street in the wake of a cylinder *(reprinted from Kaczinski et al., 1998)*

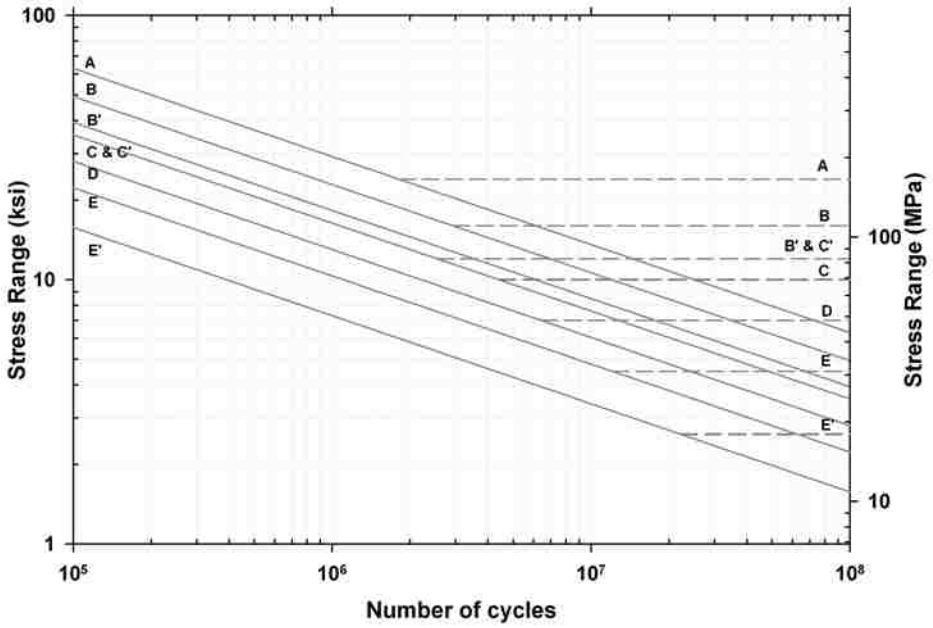

Figure 8. AASHTO Bridge Specification stress-life design curves

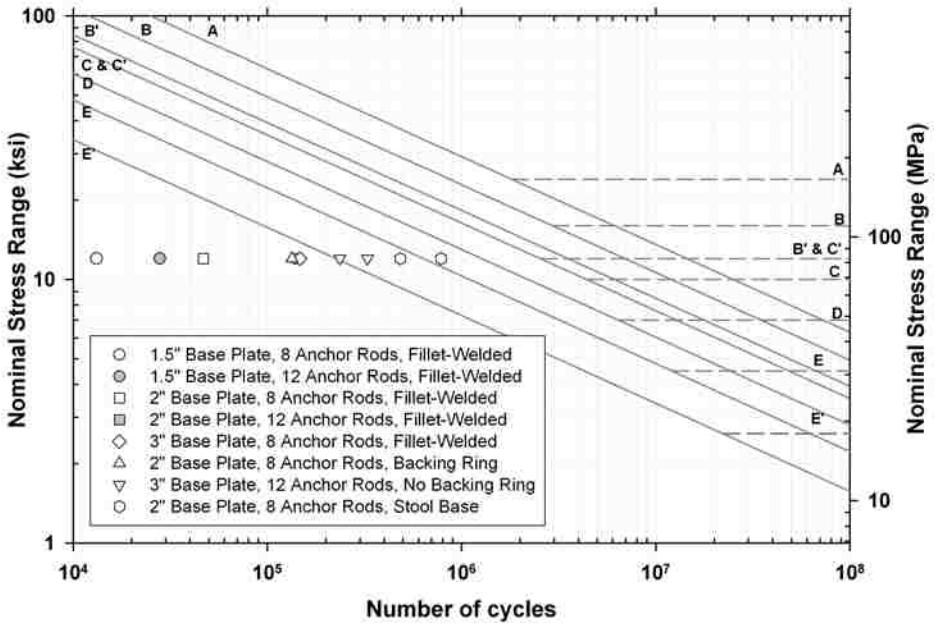

Figure 9. University of Texas at Austin test results, first phase

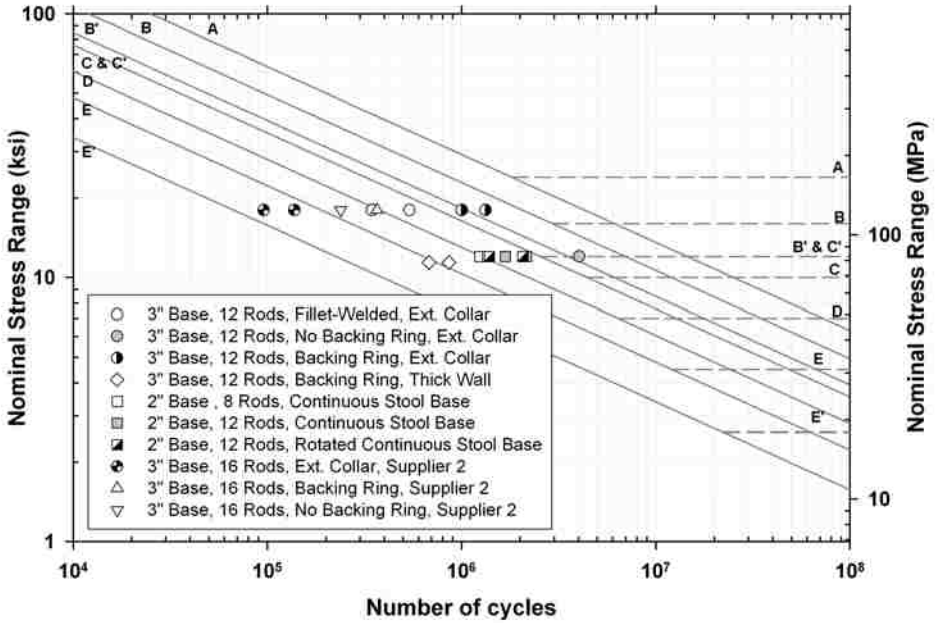

Figure 10. University of Texas at Austin test results, second phase

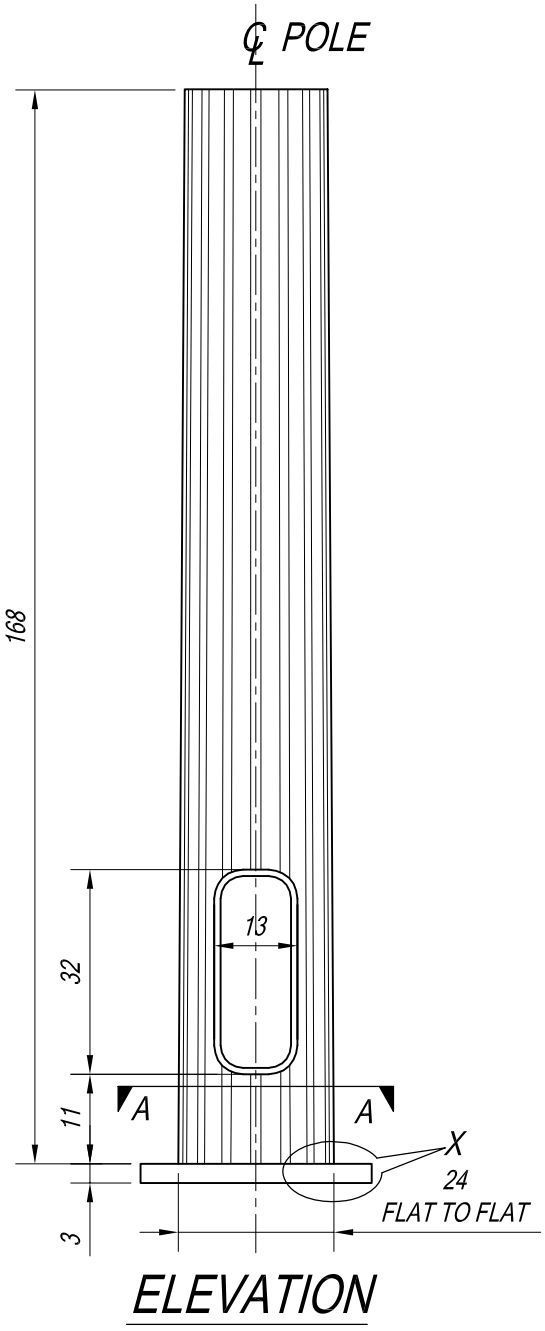

Figure 11. Type X specimen dimensions, part 1 of 2

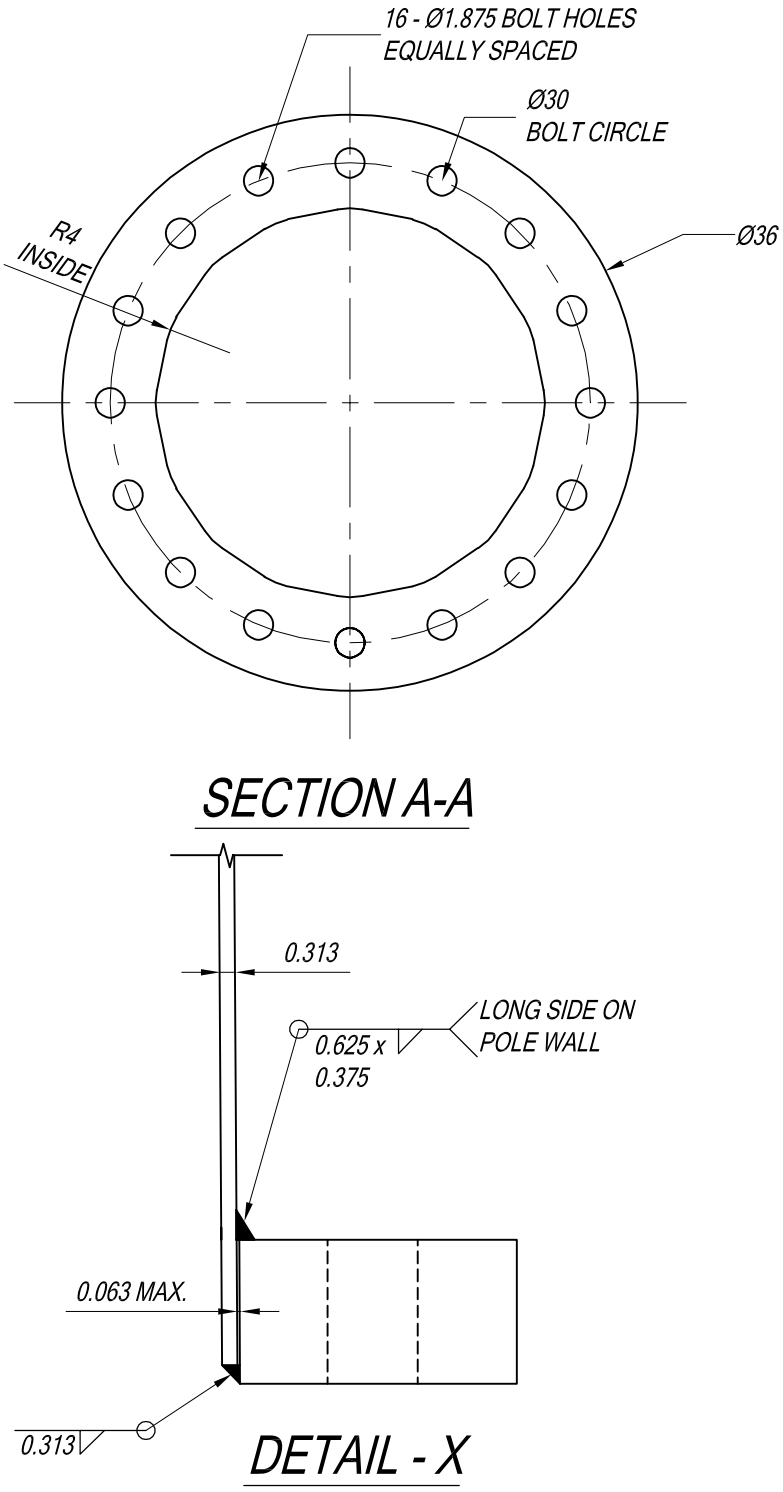

Figure 12. Type X specimen dimensions, part 2 of 2

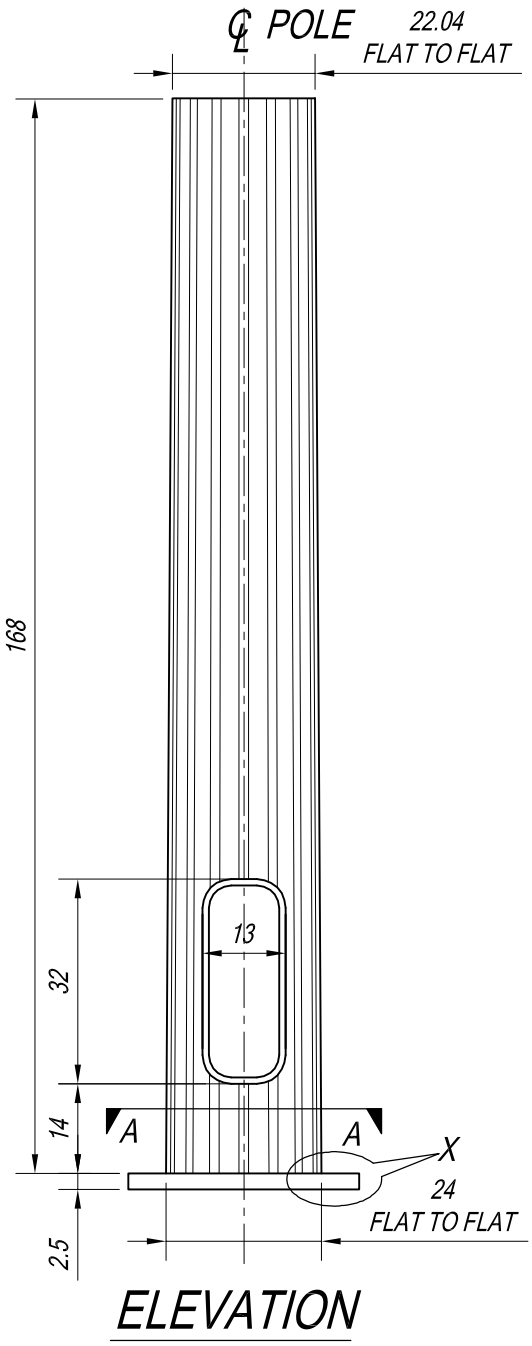

Figure 13. Type XI specimen dimensions, part 1 of 2

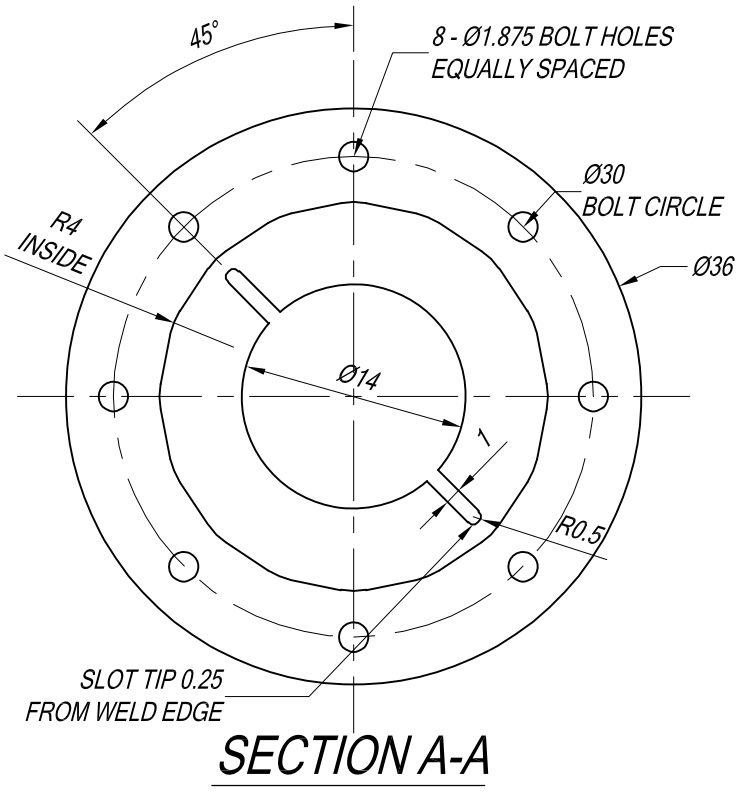

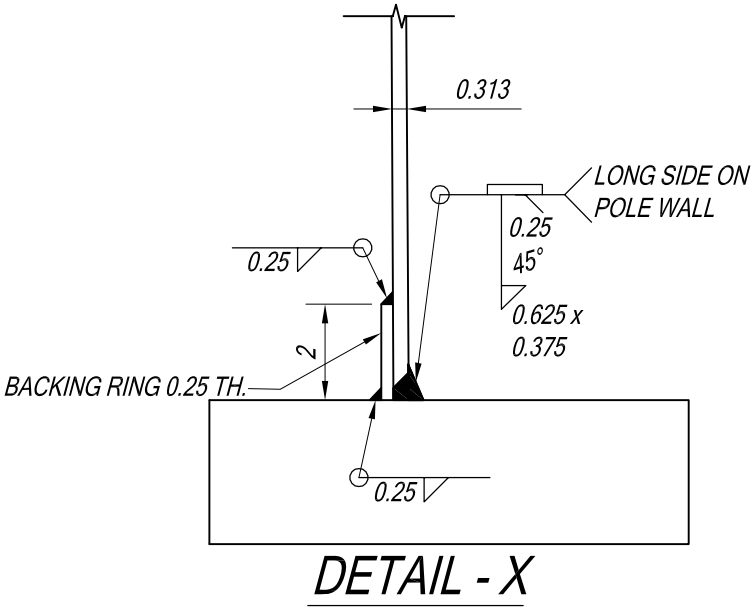

Figure 14. Type XI specimen dimensions, part 2 of 2

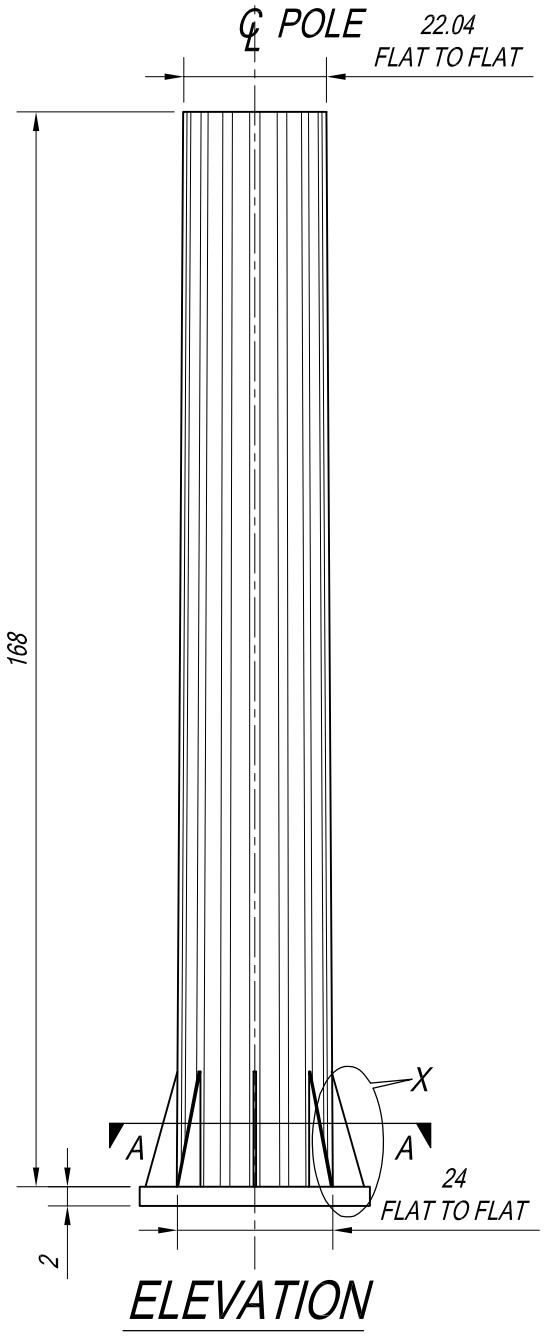

Figure 15. Type XII specimen dimensions, part 1 of 3

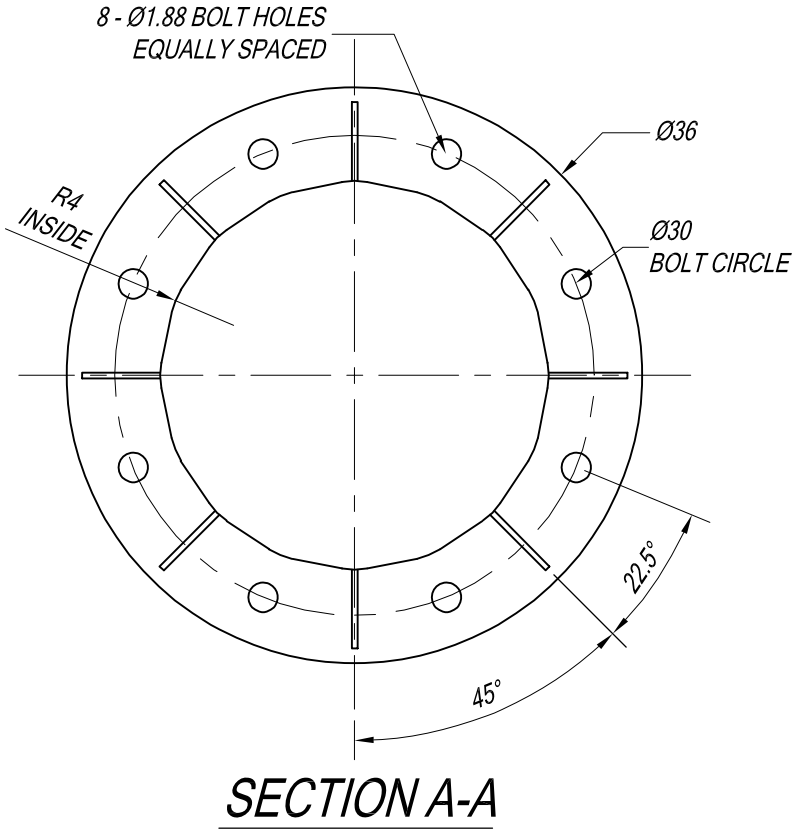

Figure 16. Type XII specimen dimensions, part 2 of 3

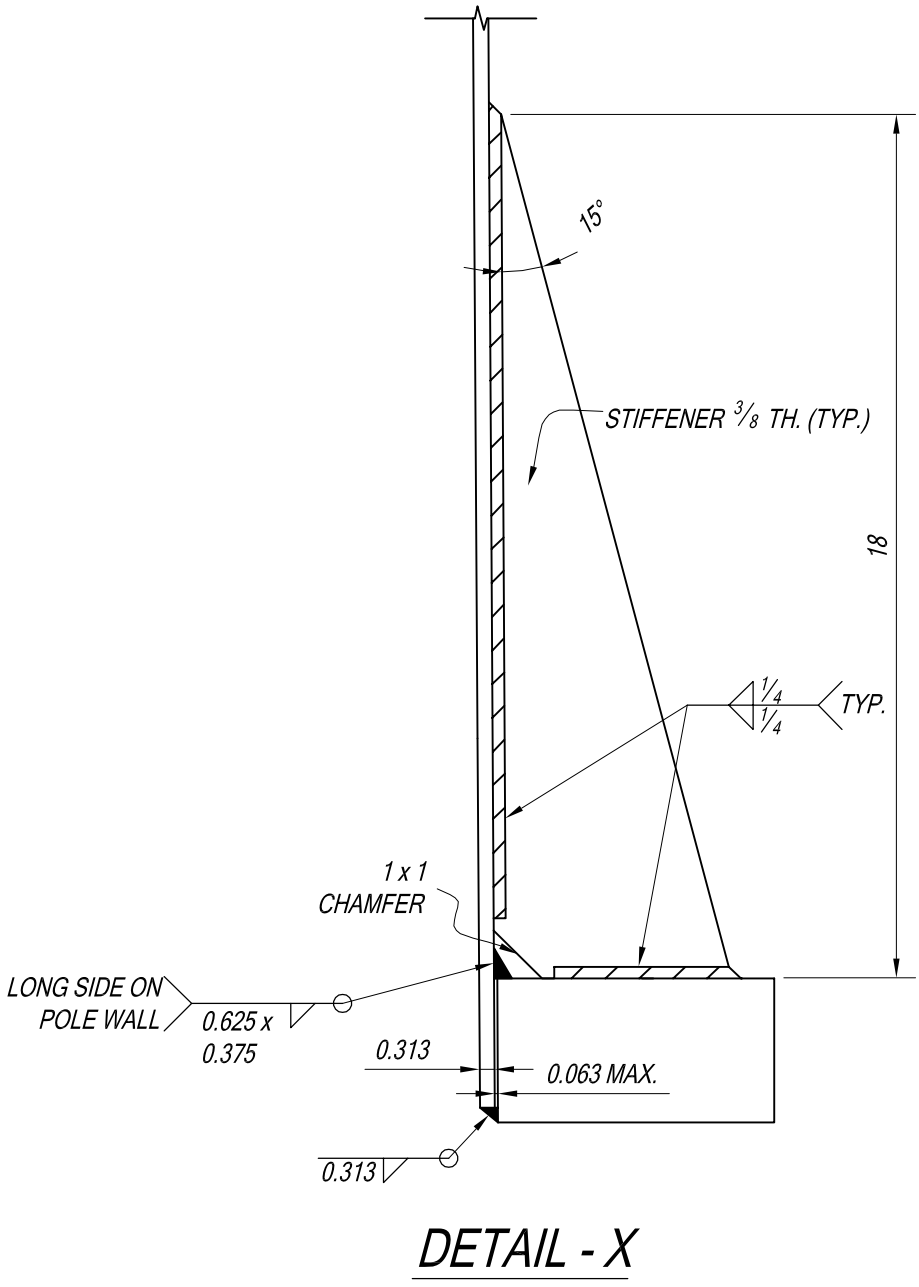

Figure 17. Type XII specimen dimensions, part 3 of 3

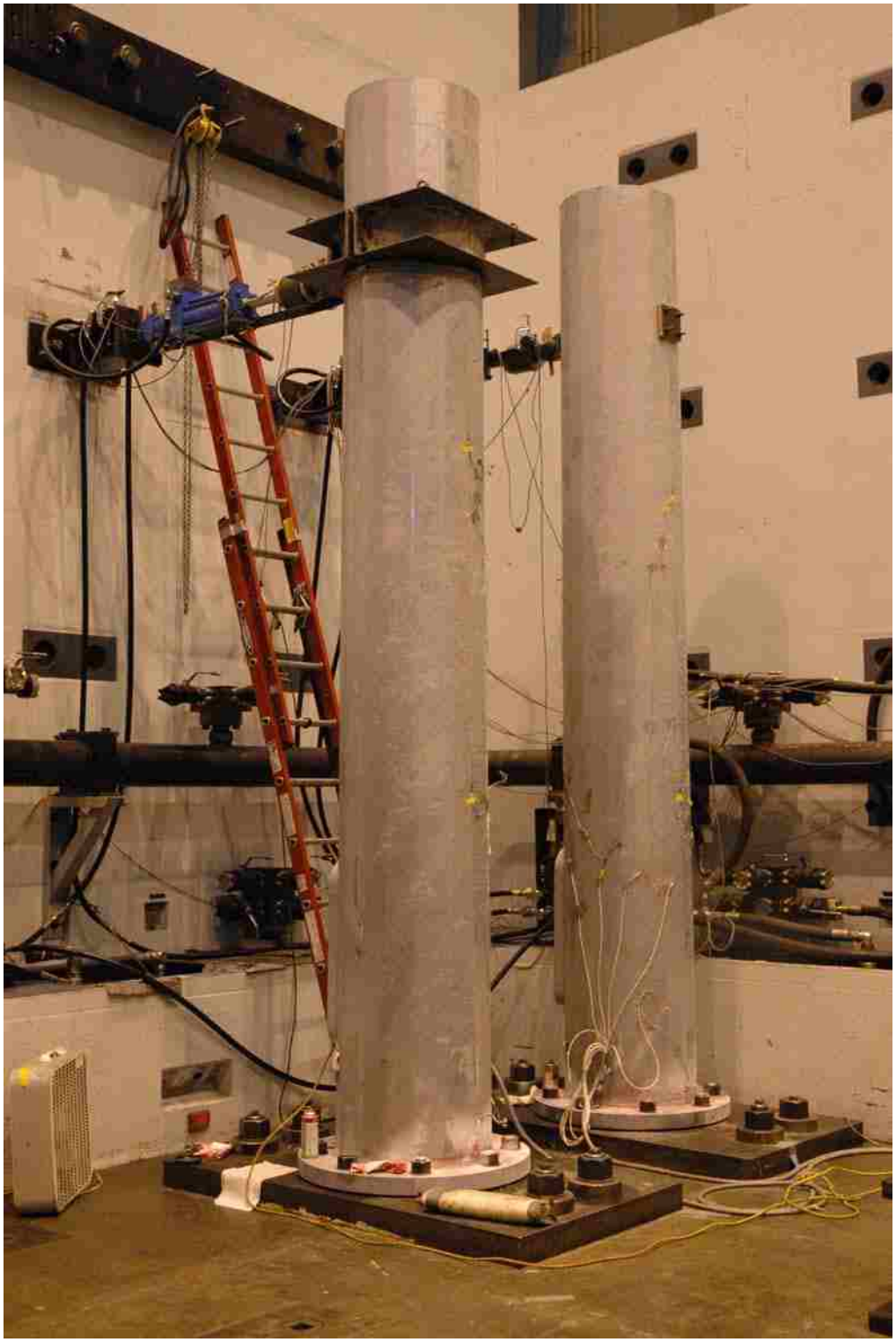

Figure 18. Fatigue testing setup at ATLSS

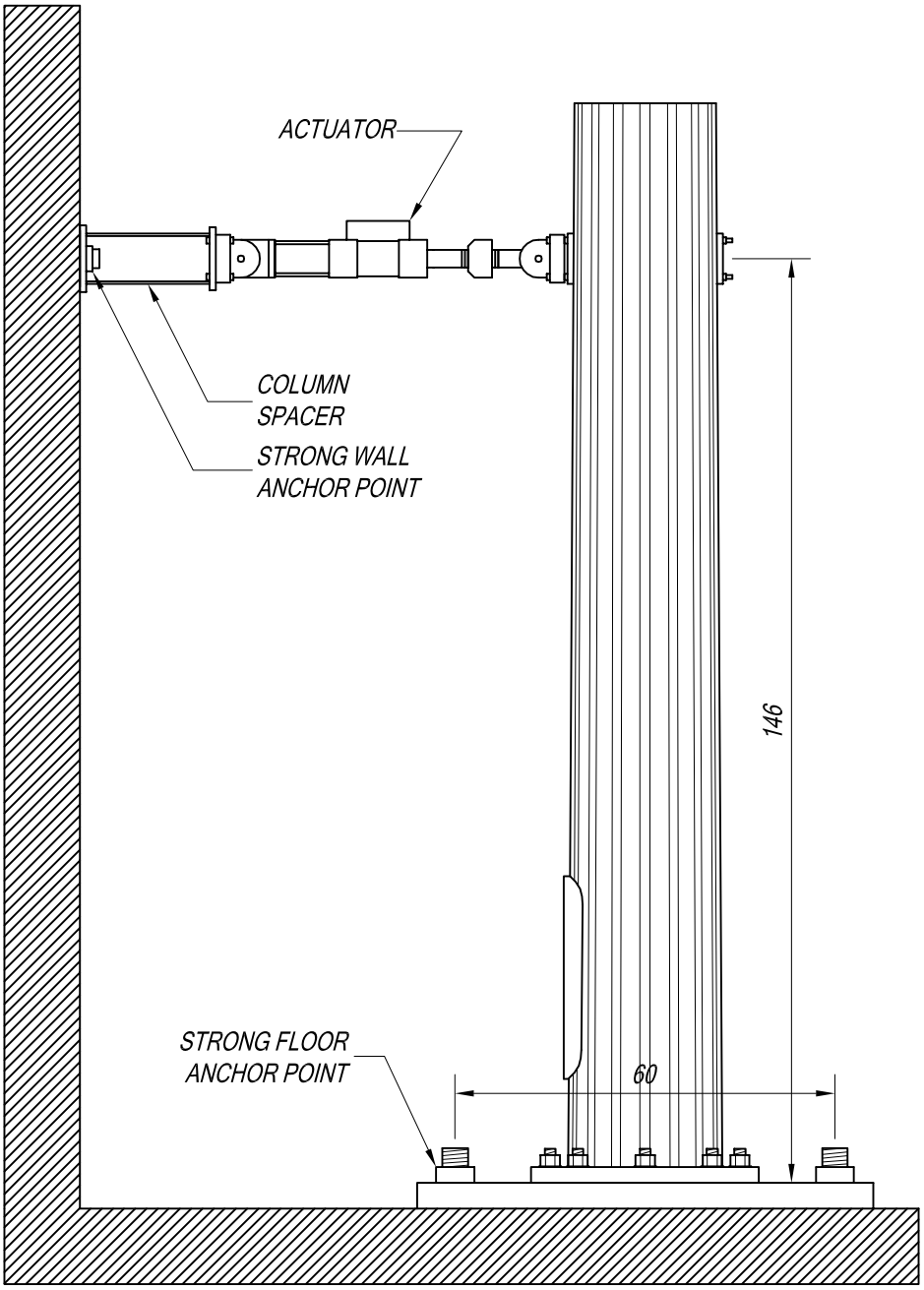

Figure 19. Elevation schematic of testing setup

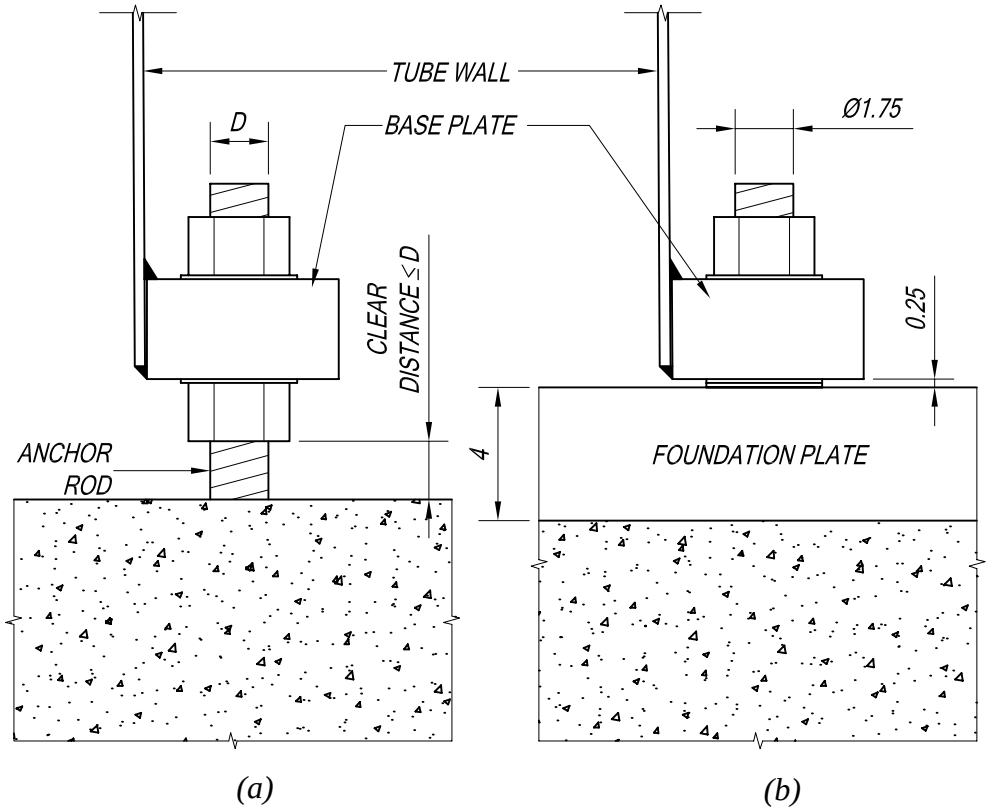

Figure 20. Comparison between boundary conditions: *a*, in-service; *b*, laboratory.

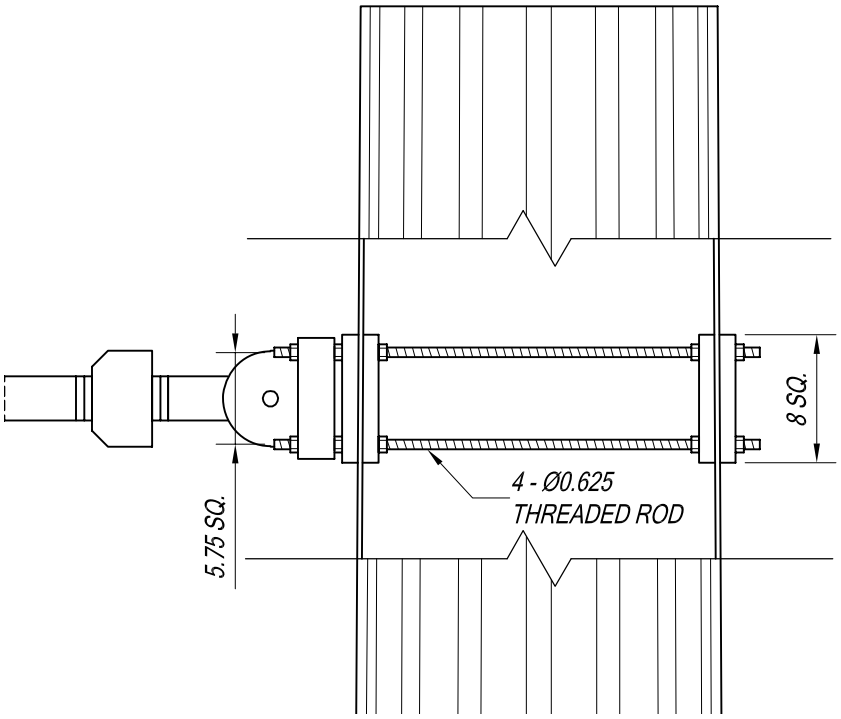

Figure 21. Loading rod connection schematic

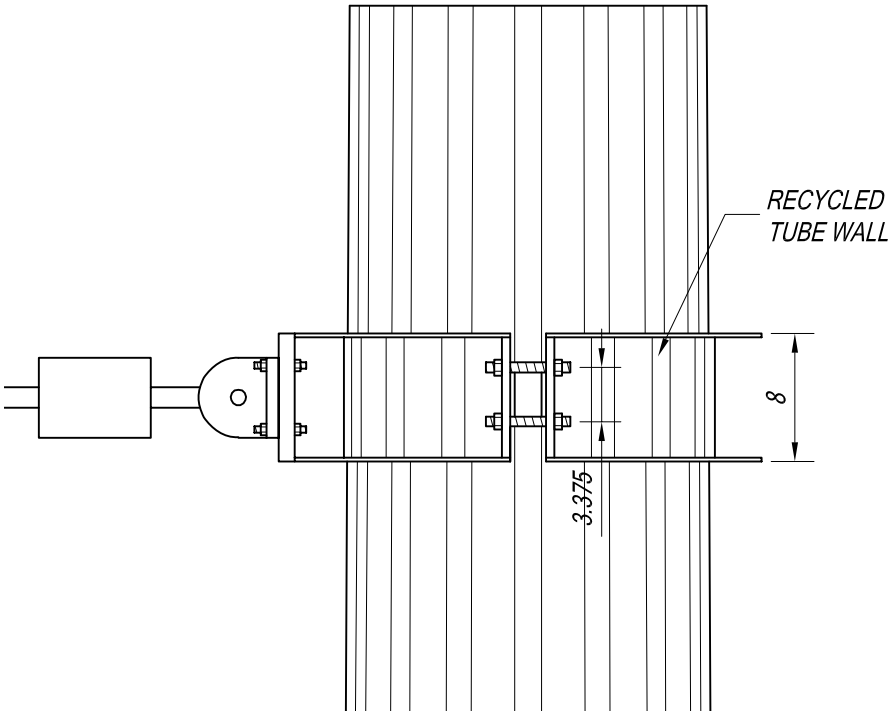

Figure 22. Loading collar connection schematic

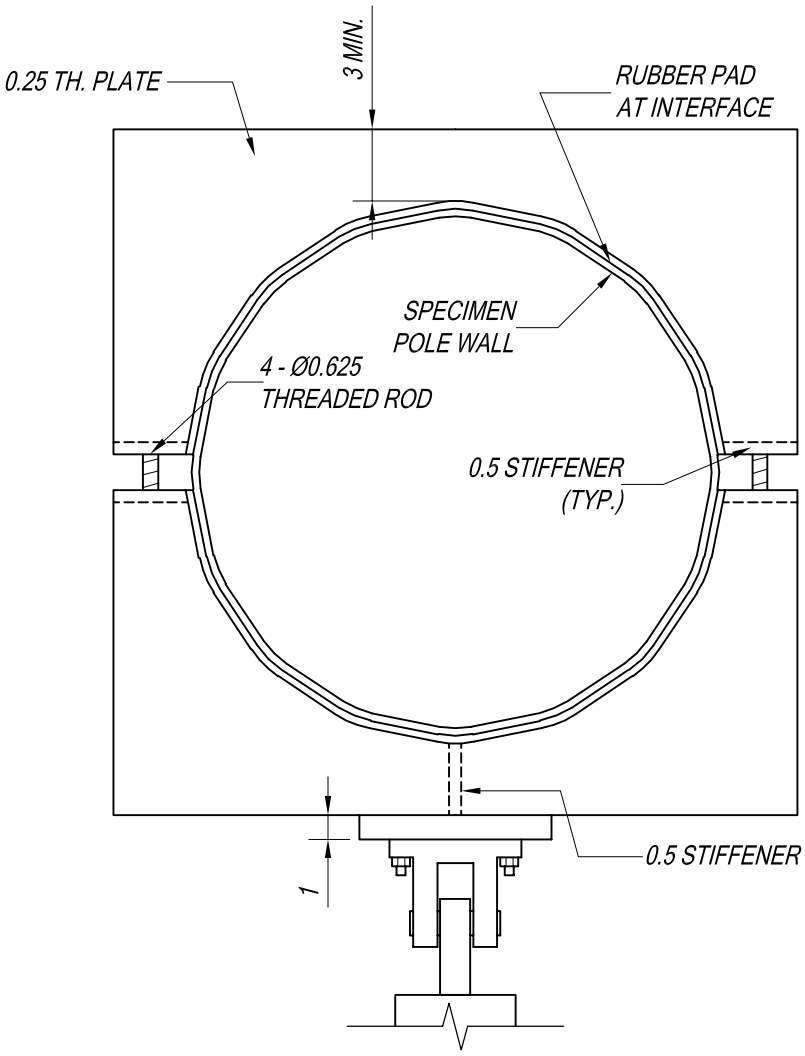

Figure 23. Loading collar plan view

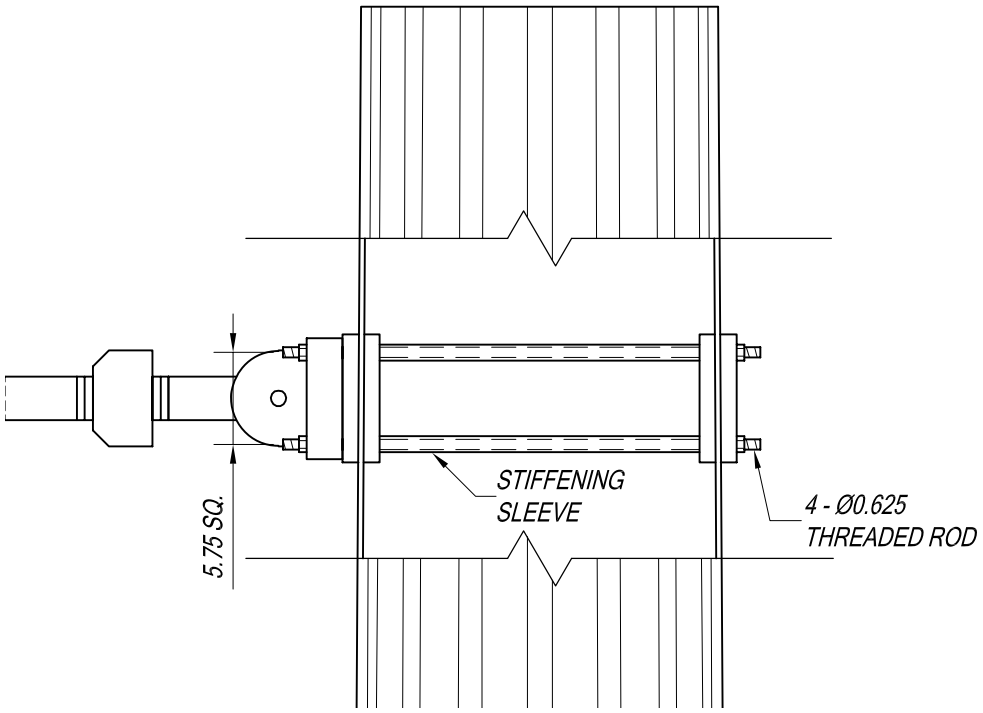

Figure 24. Fully pretensioned connection schematic

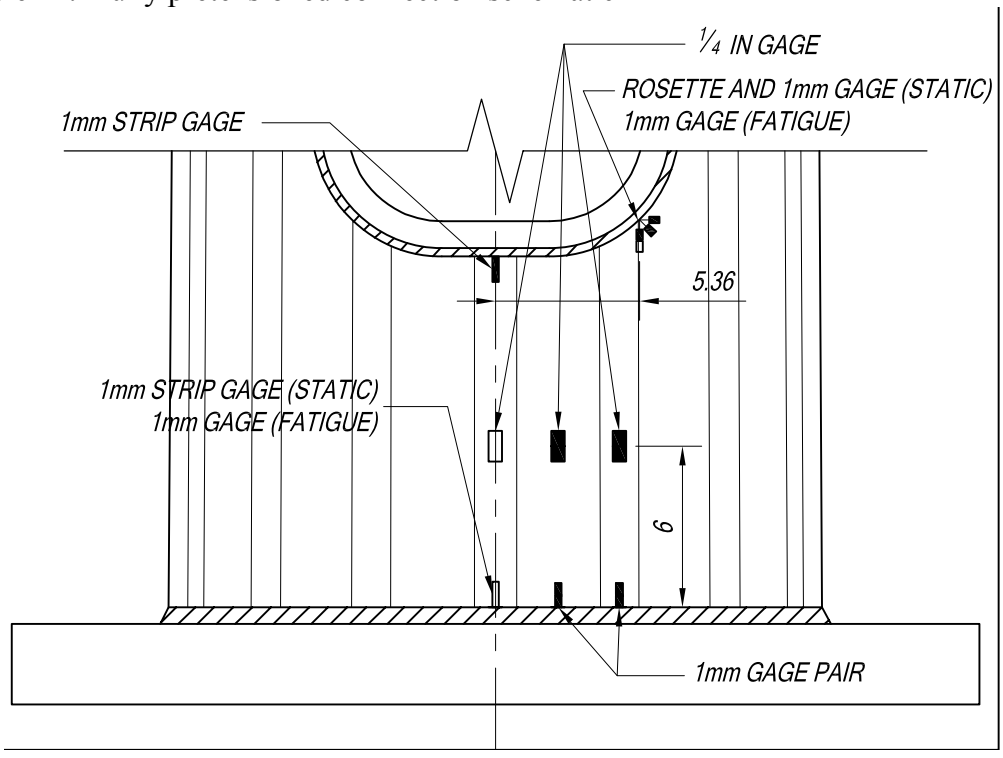

Figure 25. Type X specimen elaborately instrumented specimen strain gaging plan

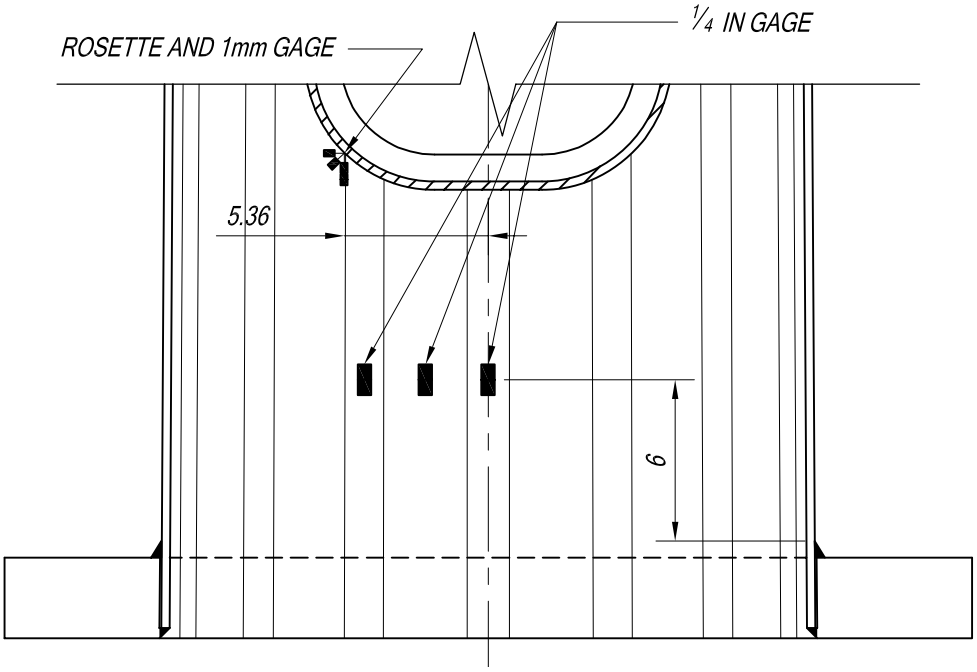

Figure 26. Type X specimen extensively instrumented specimen strain gage plan, interior

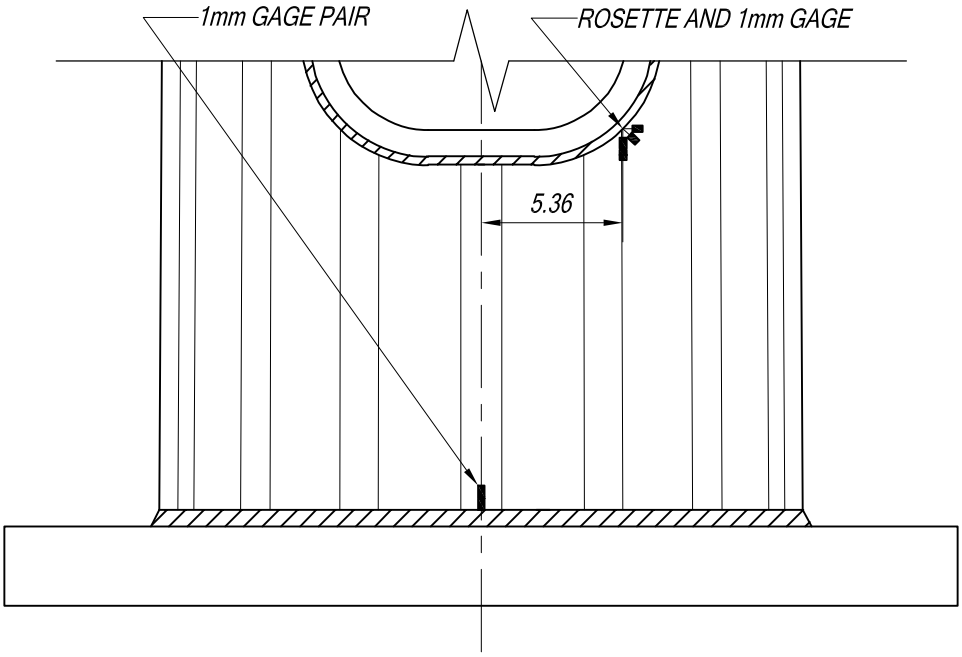

Figure 27. Type XI specimen elaborately instrumented specimen strain gaging plan, handhole side

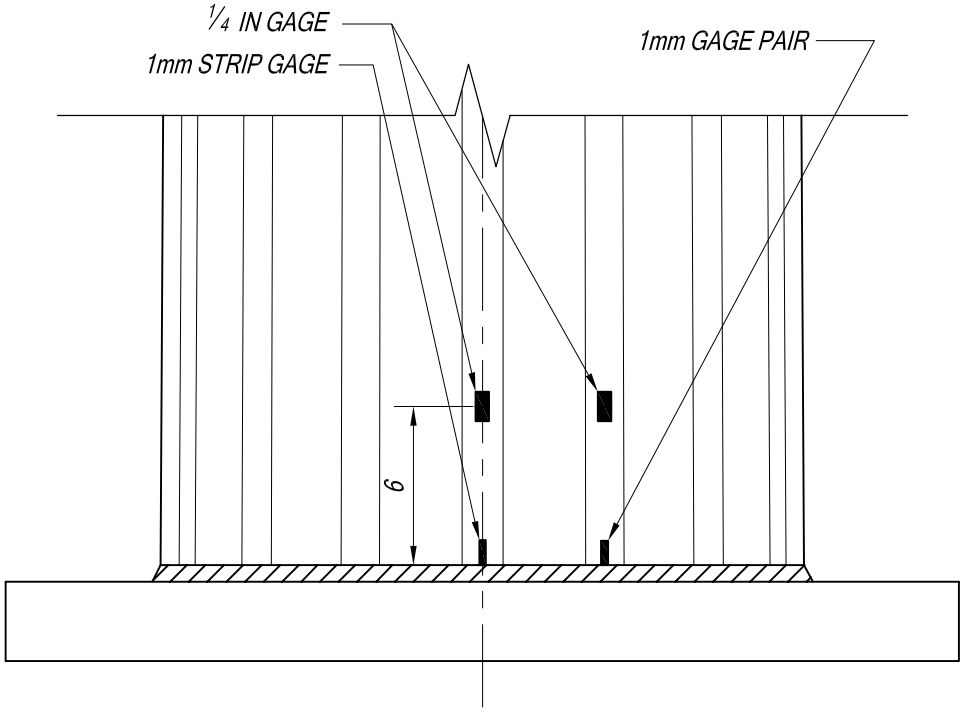

Figure 28. Type XI specimen elaborately instrumented specimen strain gaging plan, opposite side

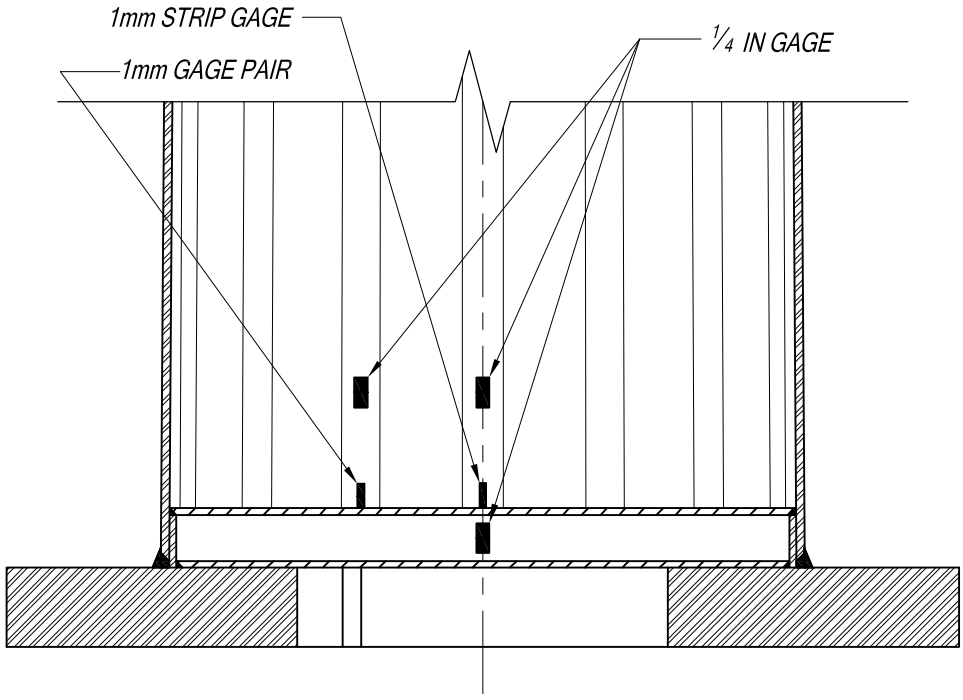

Figure 29. Type XI specimen elaborately instrumented specimen strain gaging plan, tube inside surface

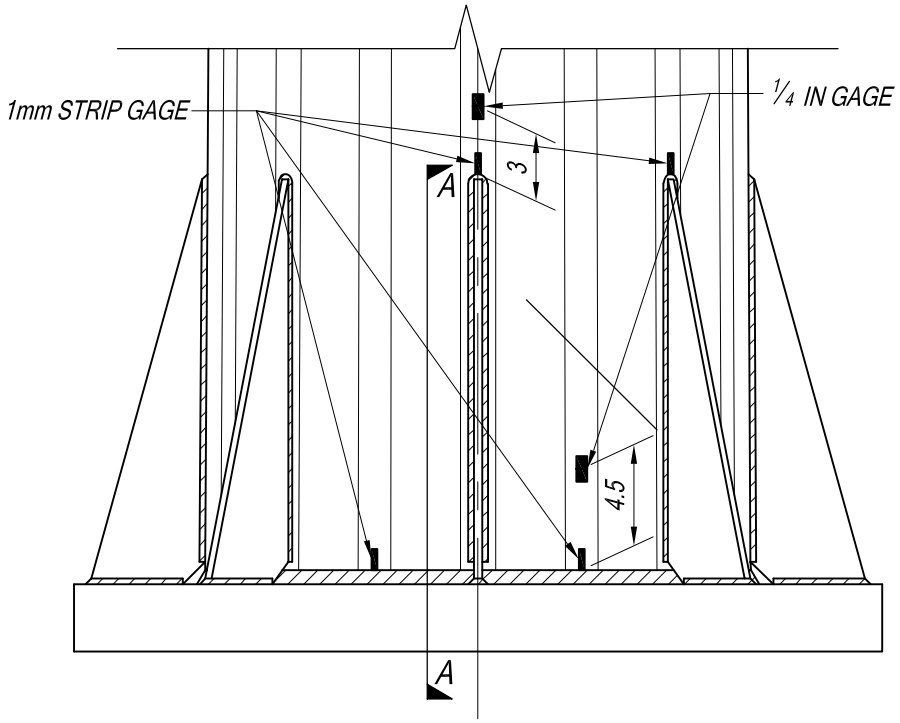

Figure 30. Type XII specimen elaborately instrumented specimen strain gaging plan

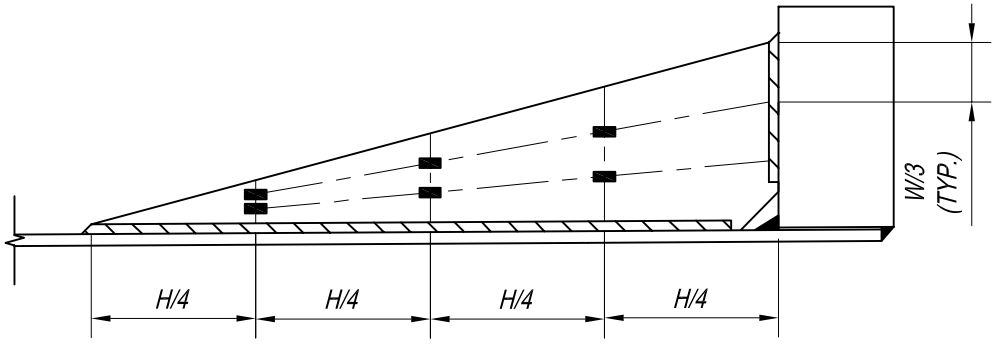

Figure 31. Type XII specimen elaborately instrumented stiffener, view A-A

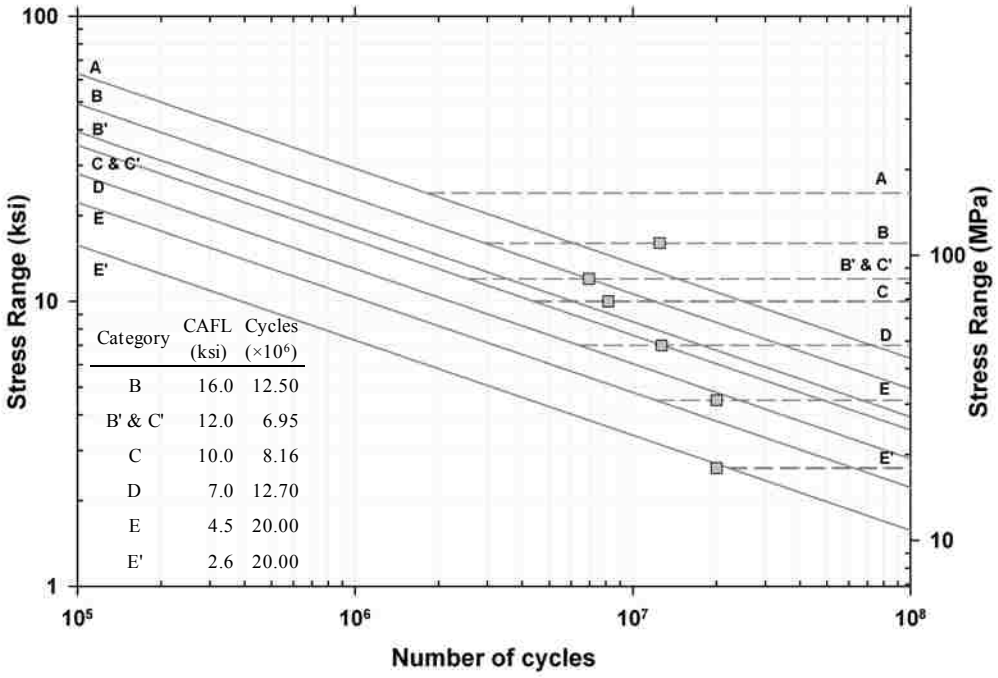

Figure 32. Dynamic testing run-out values

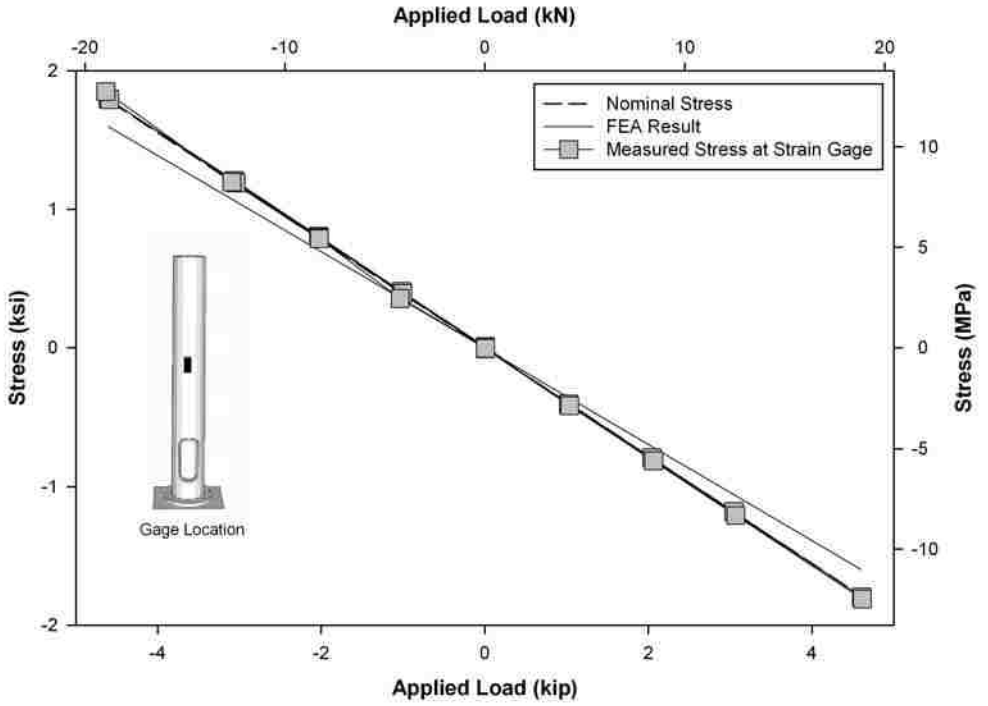

Figure 33. Type X control gage comparison of nominal stress, FEA result, and measured values from static test

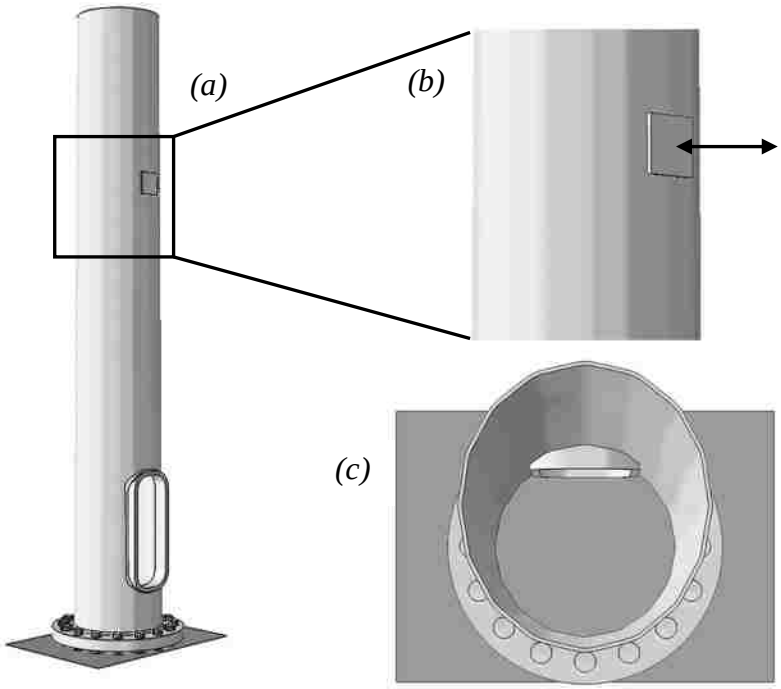

Figure 34. Type X FEA model: *a*, global view; *b*, close-up of loading area; *c*, top view of deformed shape.

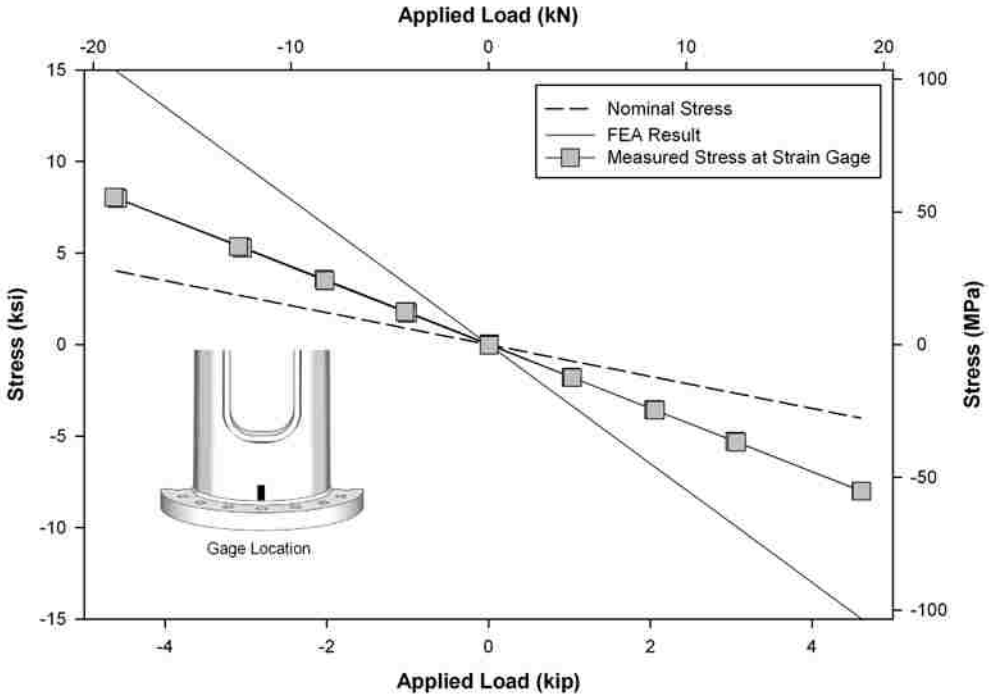

Figure 35. Type X strain gage comparison of nominal stress, FEA result, and measured values from static test. Gage abutting weld toe at pole base.

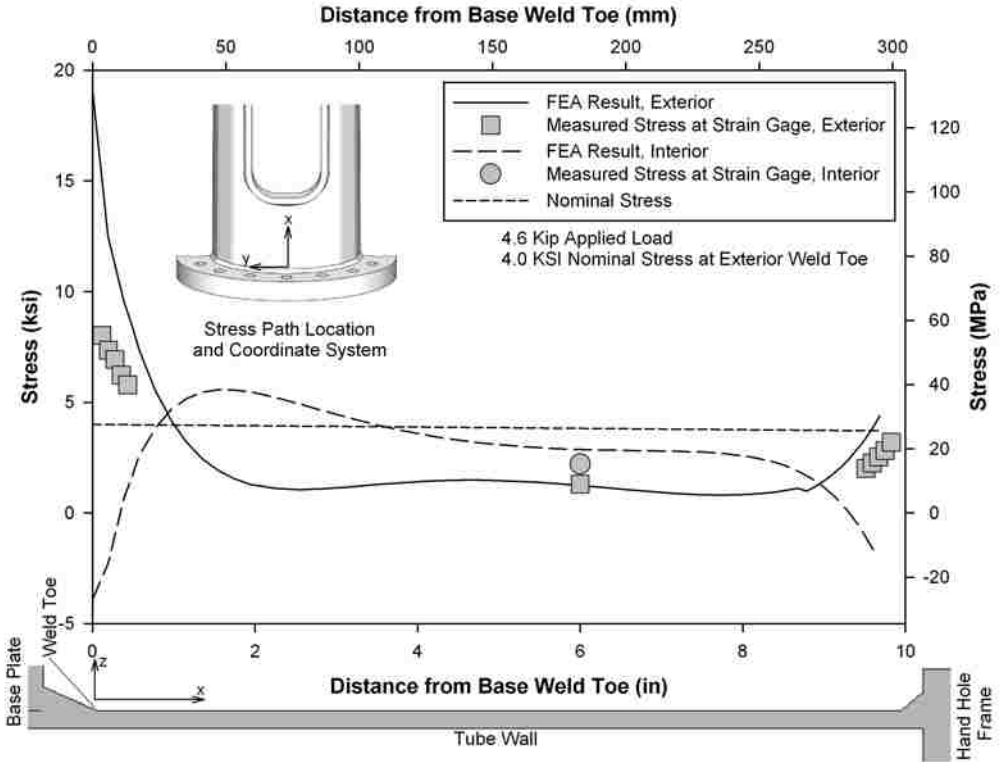

Figure 36. Type X comparison of FEA result, strain gage values, and nominal stress

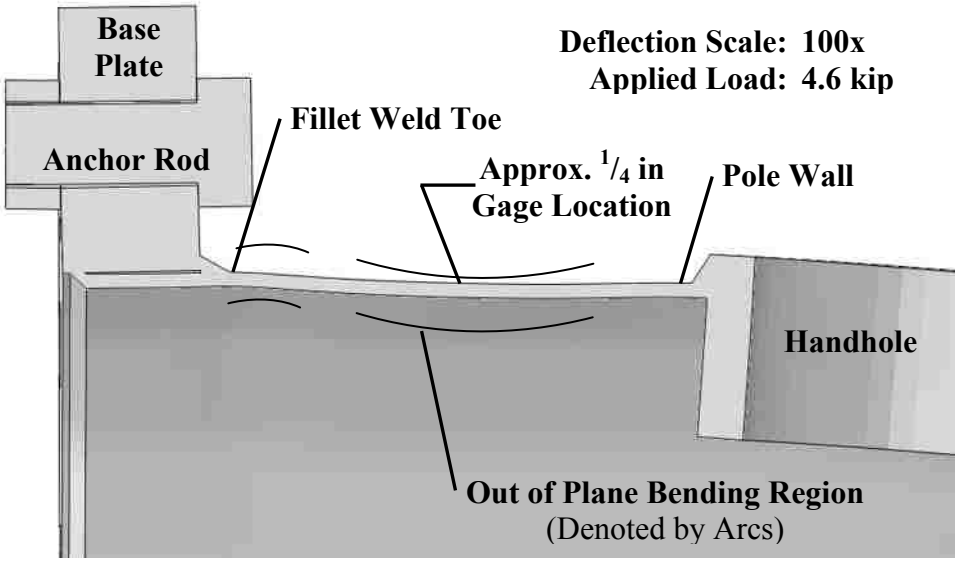

Figure 37. Cross-section of Type X FEA, showing displaced shape

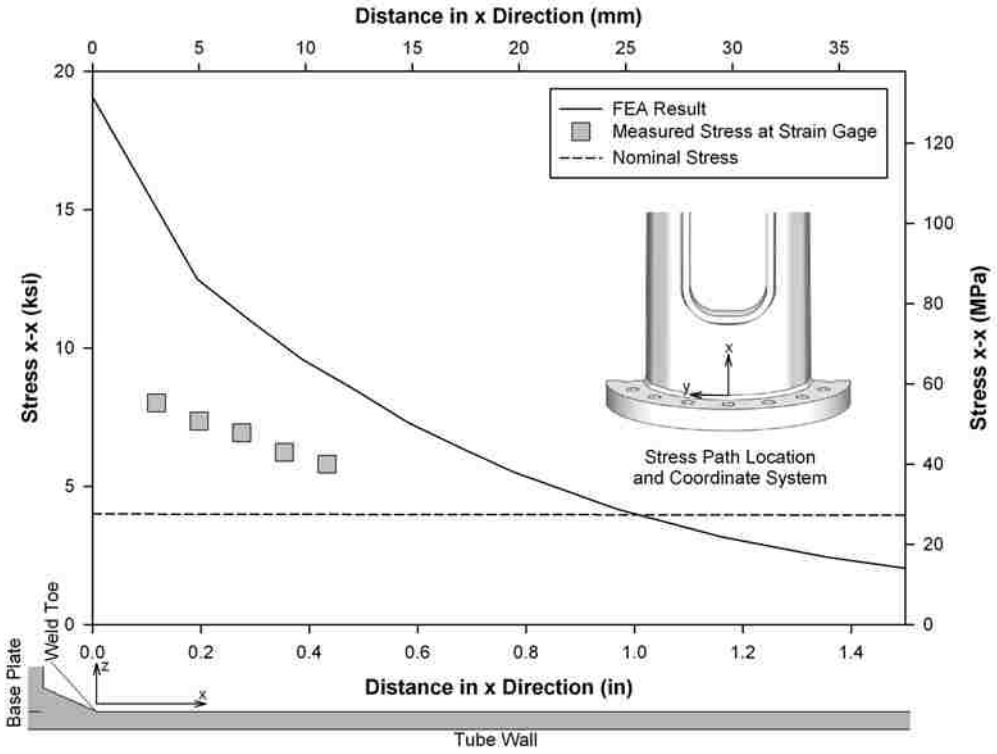

Figure 38. Stress profile in specimen X-2 above pole base on handhole side, in the loading plane

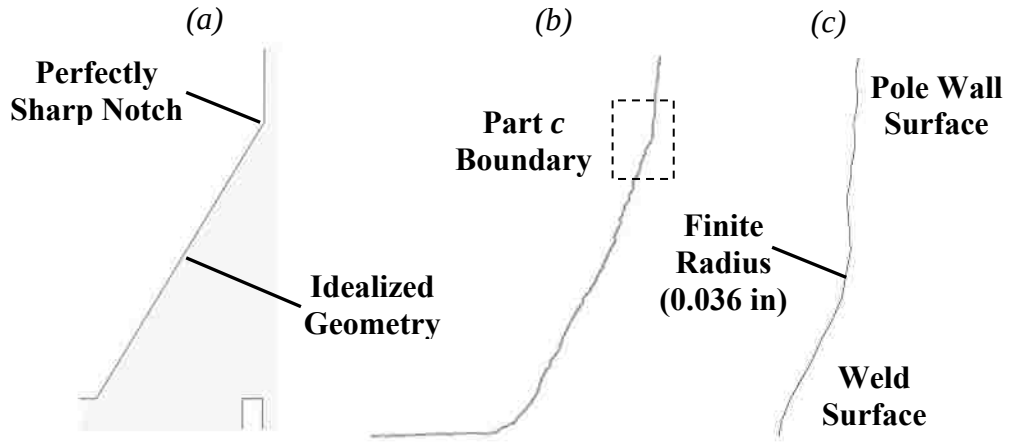

Figure 39. Differences in weld shape: *a*, FEA model; *b*, 3D-ICP section of weld profile; *c*, enlarged view of 3D-ICP.

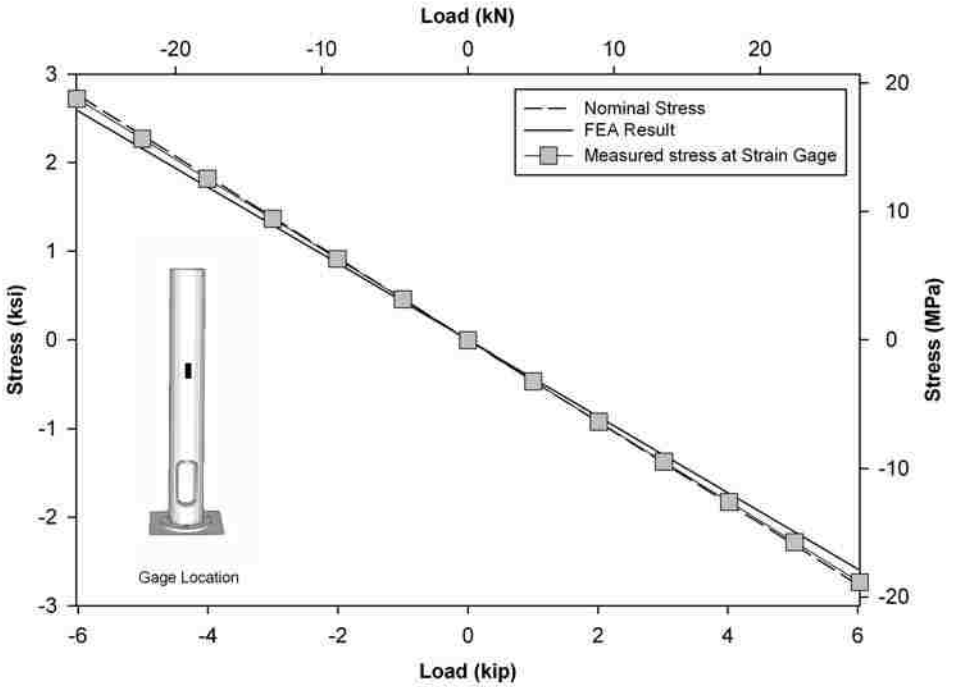

Figure 40. Type XI control gage comparison of nominal stress, FEA result, and measured values from static test

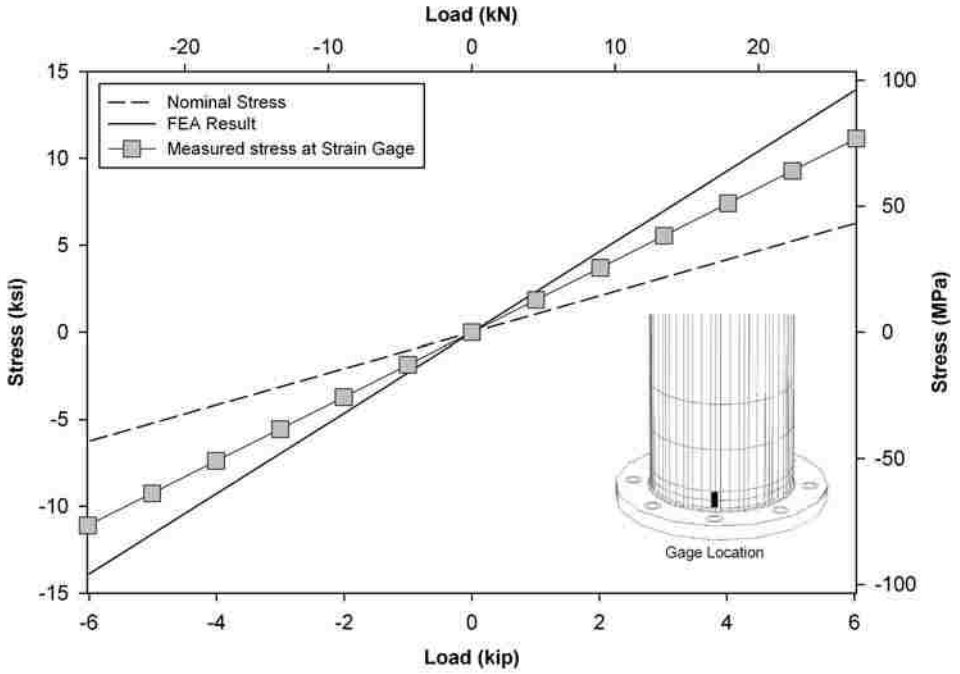

Figure 41. Type XI strain gage comparison of nominal stress, FEA result, and measured values from static test. Gage abutting weld toe at pole base.

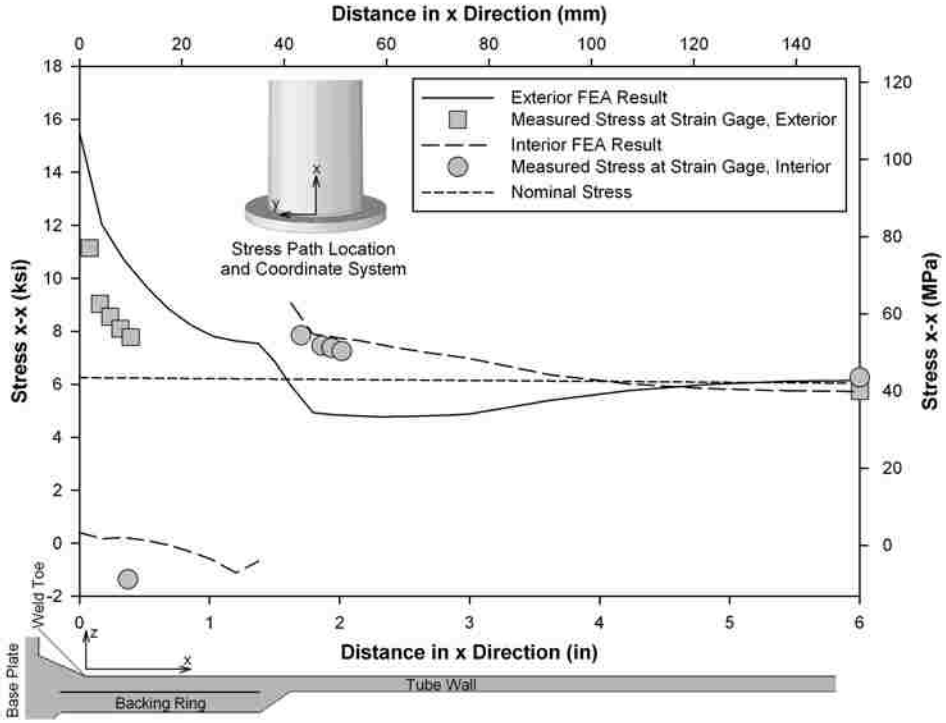

Figure 42. Type XI comparison of FEA result, strain gage values, and nominal stress

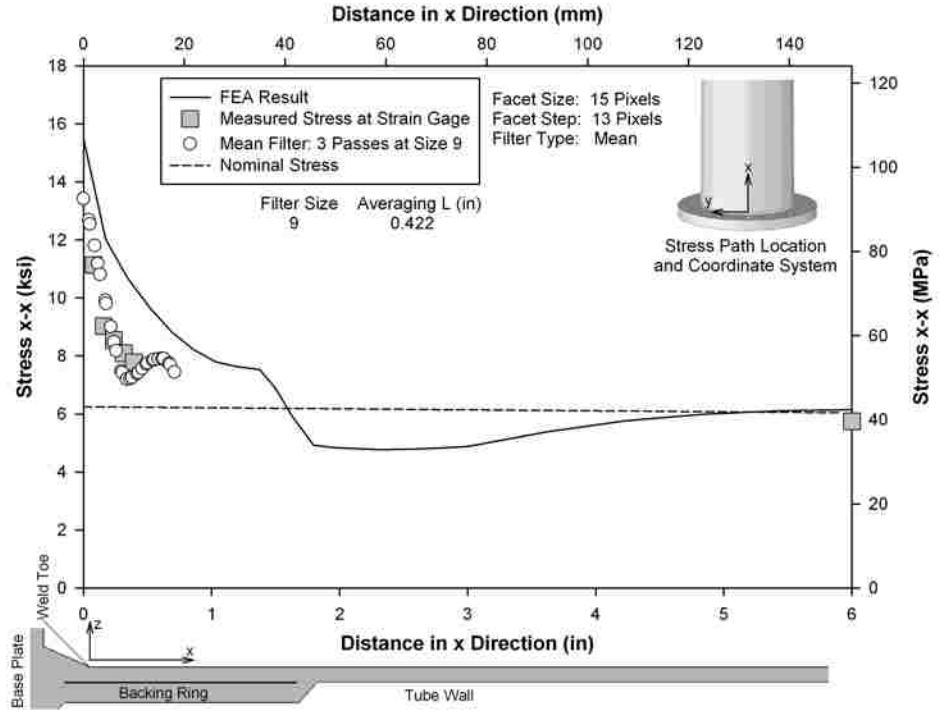

Figure 43. Stress profile in specimen XI-6 above pole base opposite to the handhole, in the loading plane

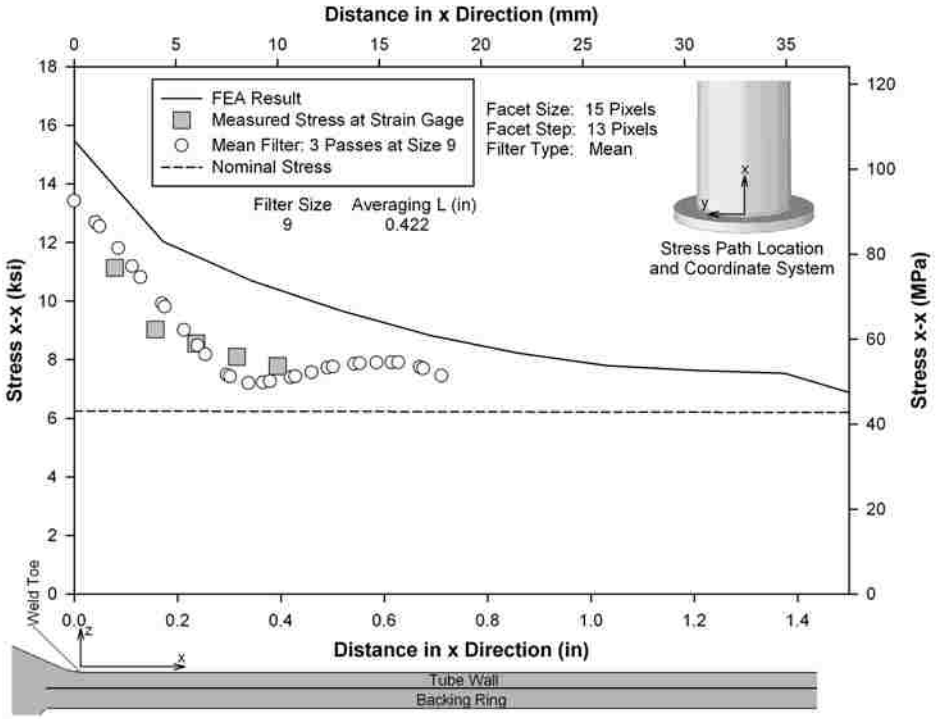

Figure 44. Enlarged view of stress profile in specimen XI-6 abutting pole-to-base plate weld toe

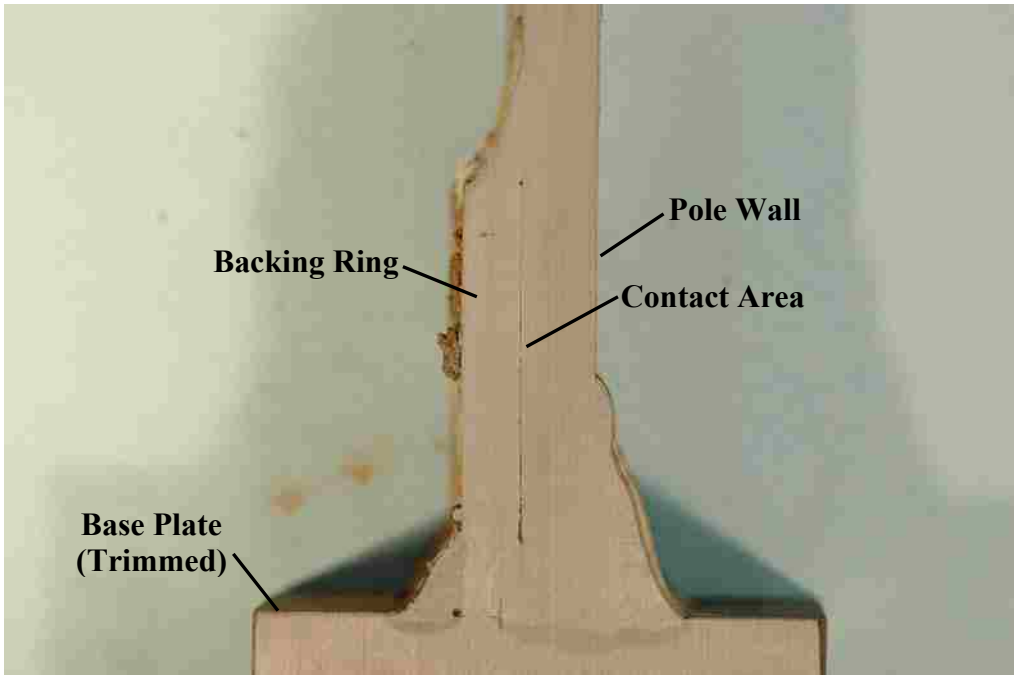

Figure 45. Non-uniform contact between backing ring and pole wall in Specimen XI-7

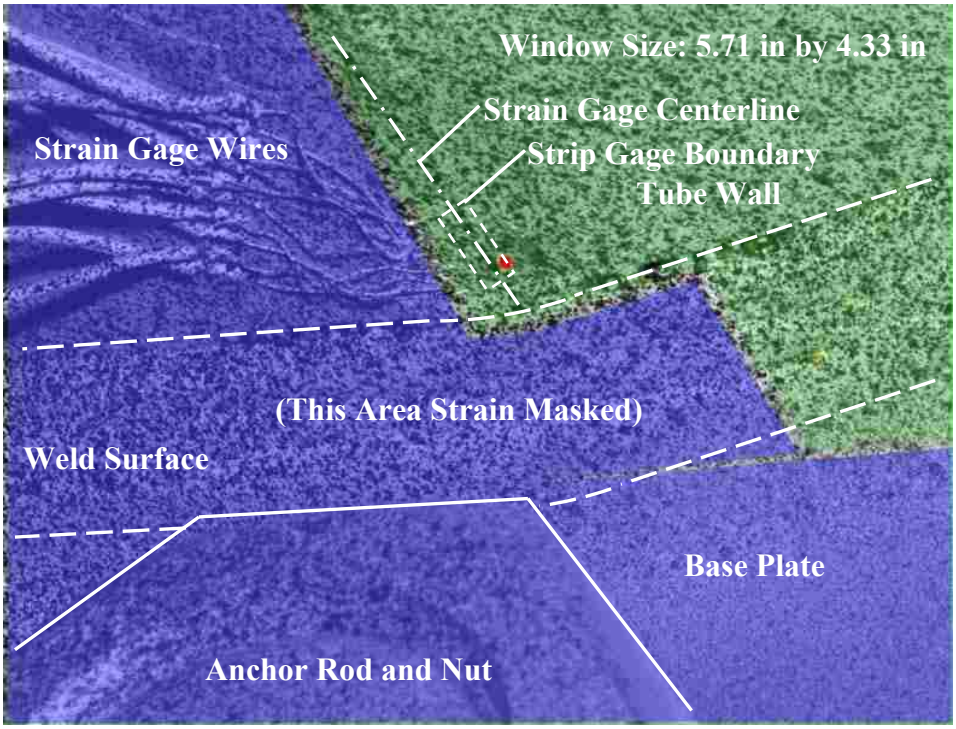

Figure 46. 3D-ICP camera image of Type XI pole base opposite actuator

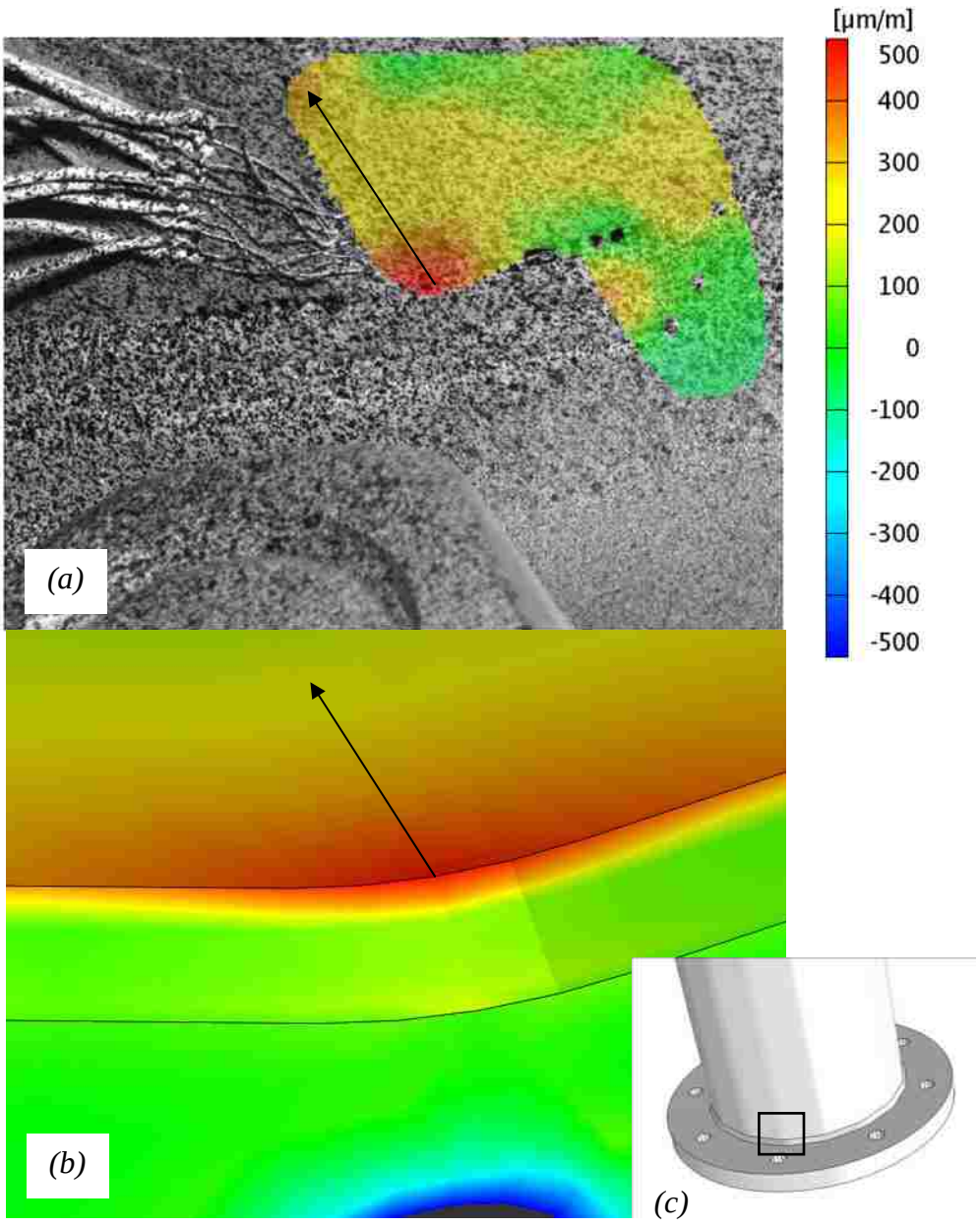

Figure 47. Type XI strain comparison at pole base centerline opposite actuator (arrows indicate strain direction): *a*, 3D-ICP contour plot; *b*, FEA contour plot; *c*, global view with comparison area highlighted.

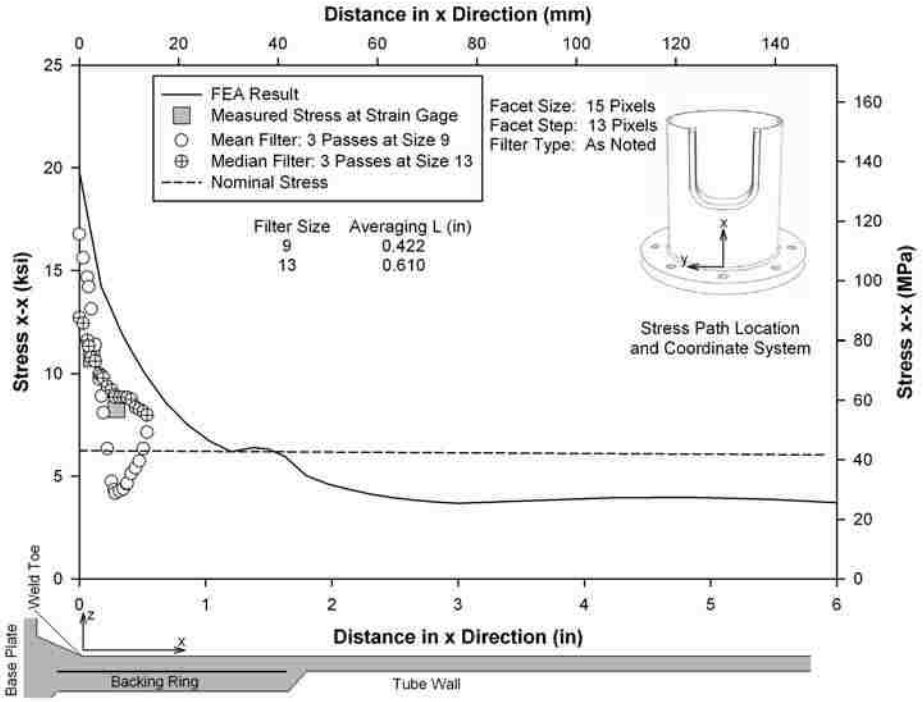

Figure 48. Specimen XI-6 comparison of FEA result, 3D-ICP result, and strain gage values above pole base on actuator side

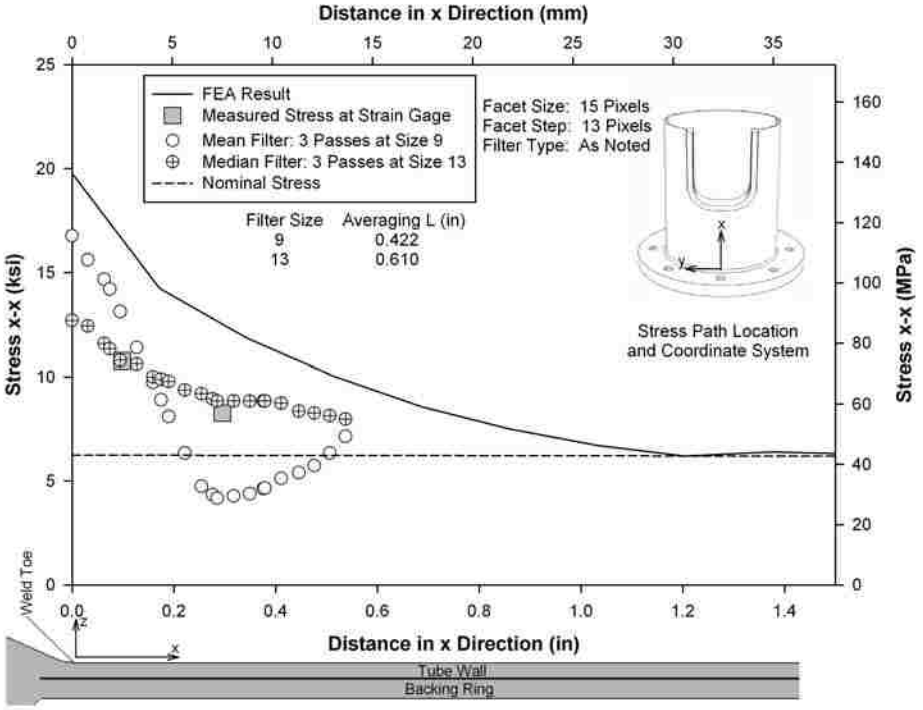

Figure 49. Enlarged view of Specimen XI-6 comparison of finite element analysis result, 3D-ICP result, and strain gage values at pole base weld toe on actuator side

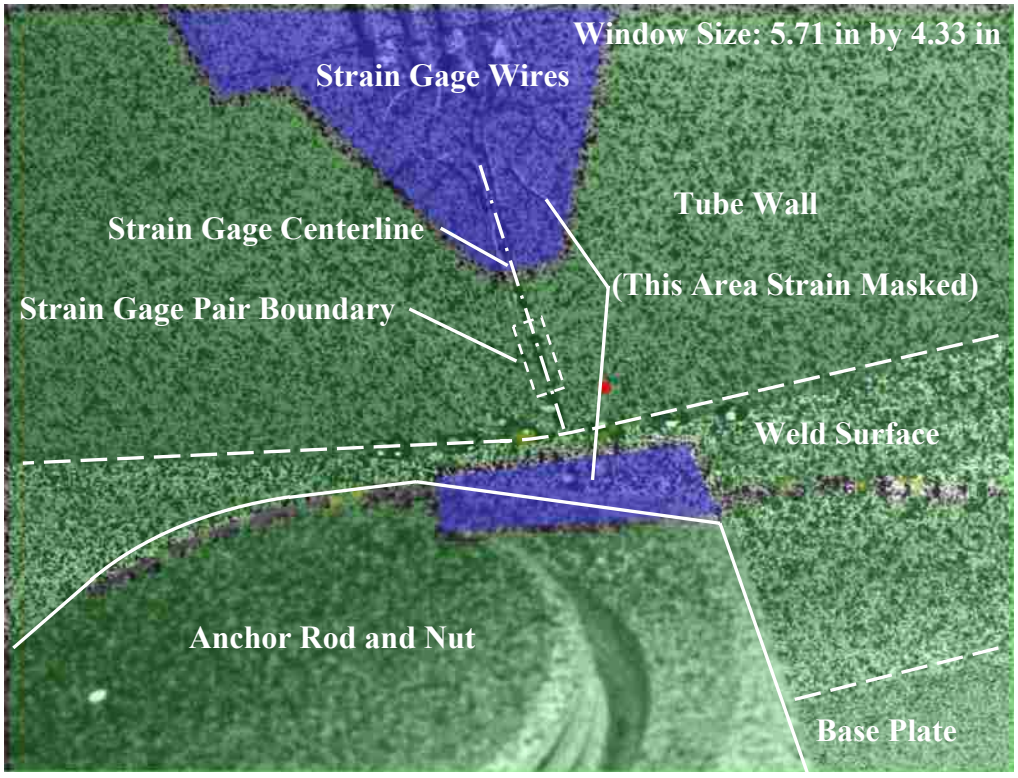

Figure 50. 3D-ICP camera image of Type XI pole base centerline on actuator side

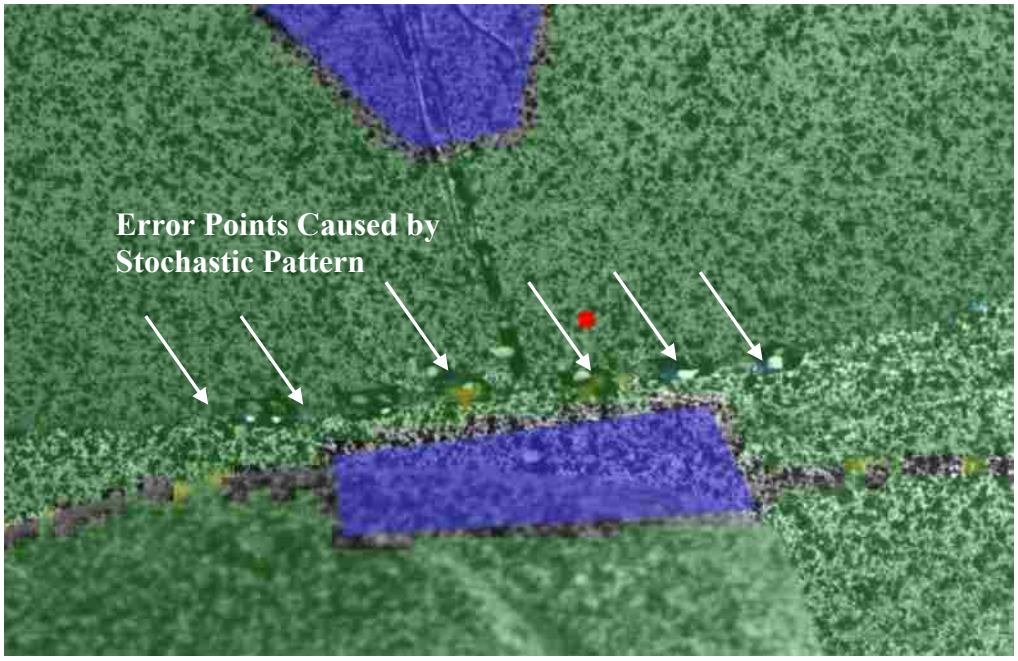

Figure 51. Enlarged view of 3D-ICP camera image of Type XI pole base centerline on actuator side

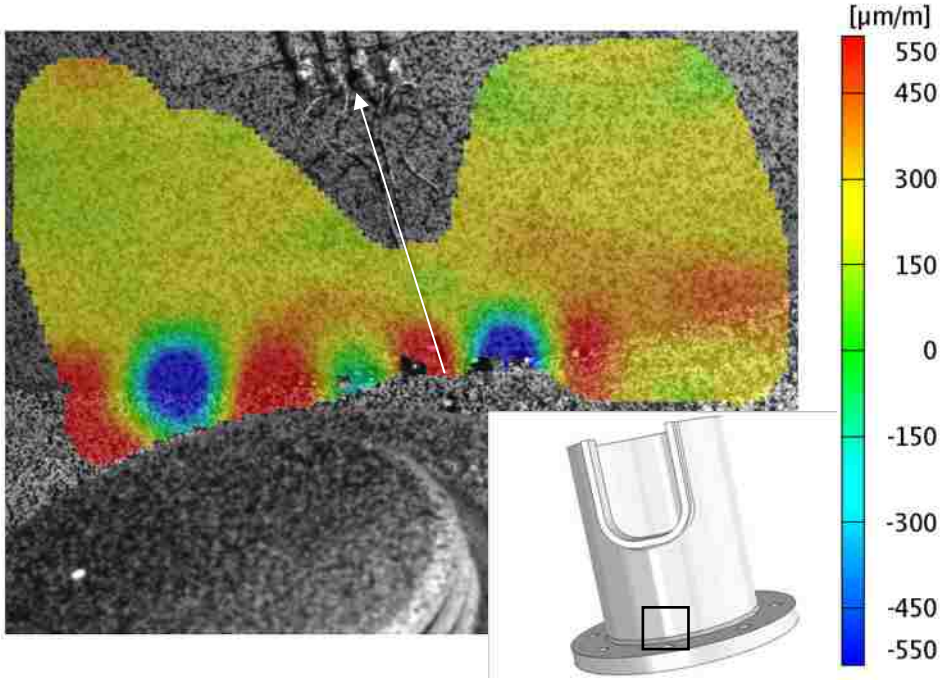

Figure 52. Type XI 3D-ICP strain contour plot at pole base centerline on actuator side using mean filter (arrow indicates strain direction). Inset shows location on structure.

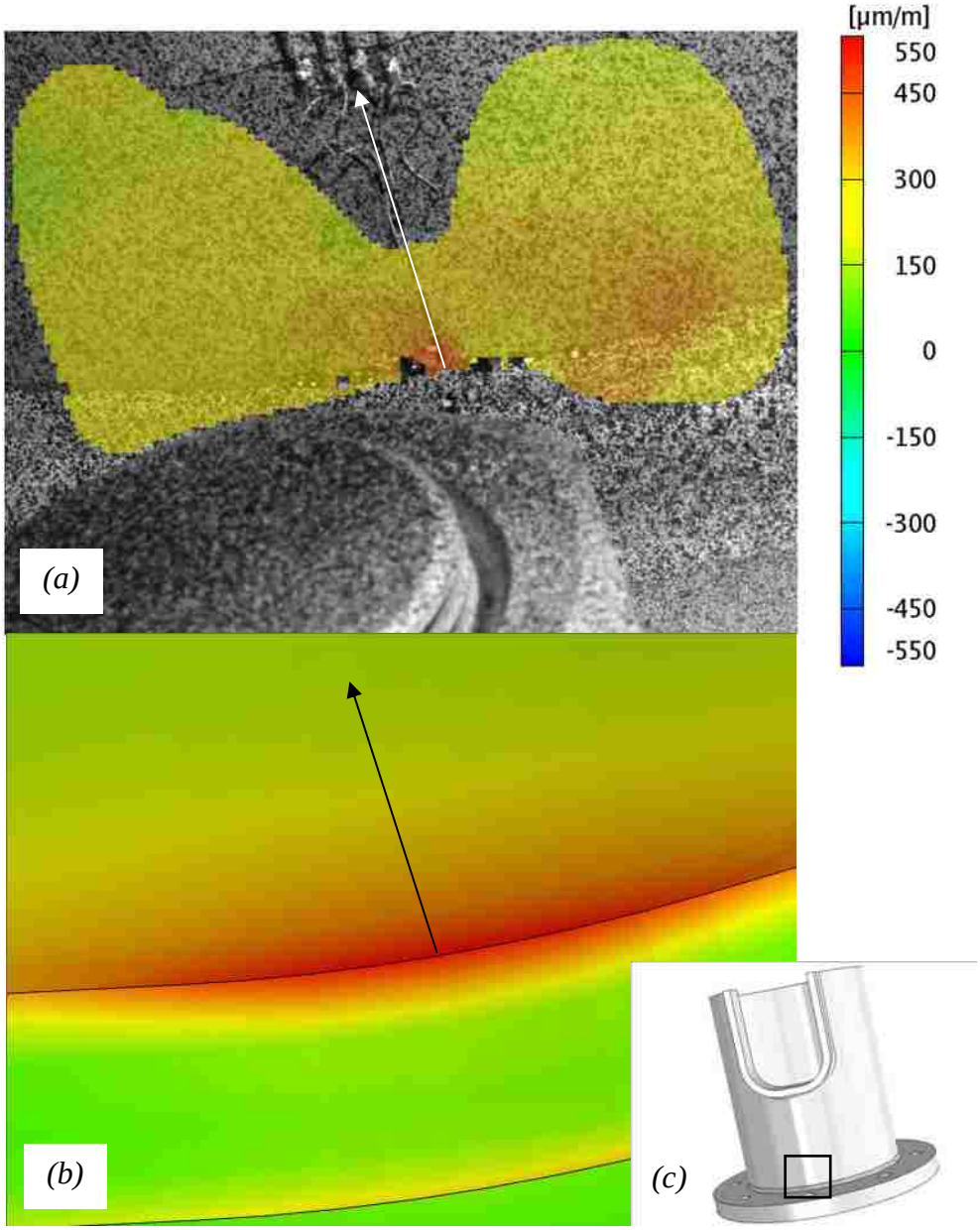

Figure 53. Type XI strain comparison at pole base centerline on actuator side (arrows indicate strain direction): *a*, 3D-ICP contour plot using median filter; *b*, FEA contour plot; *c*, global view with comparison area highlighted.

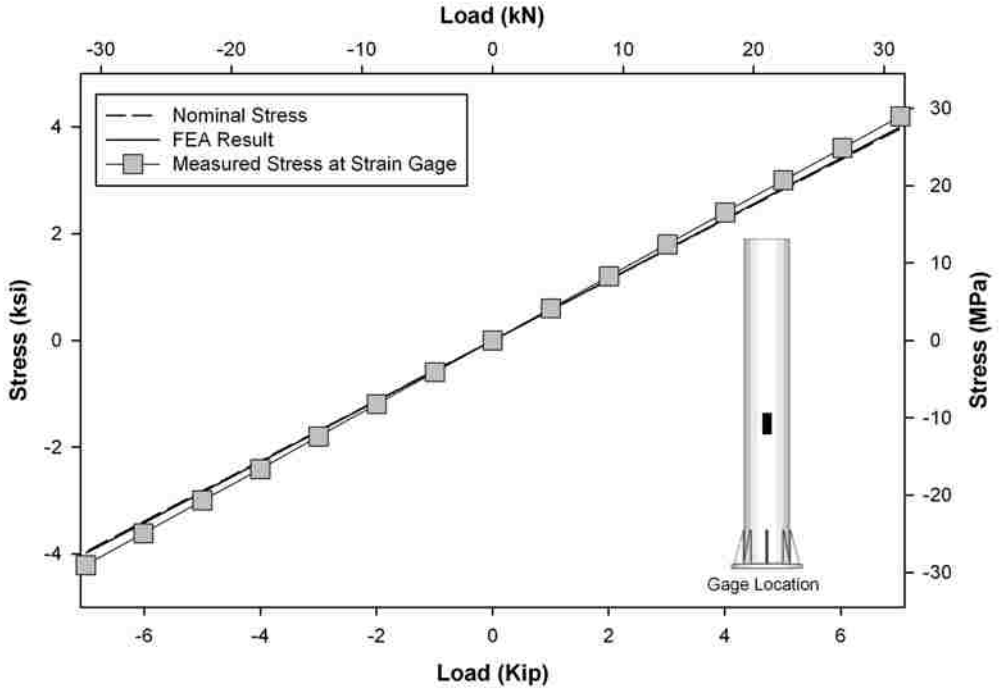

Figure 54. Type XII control gage comparison of nominal stress, FEA result, and measured values from static test

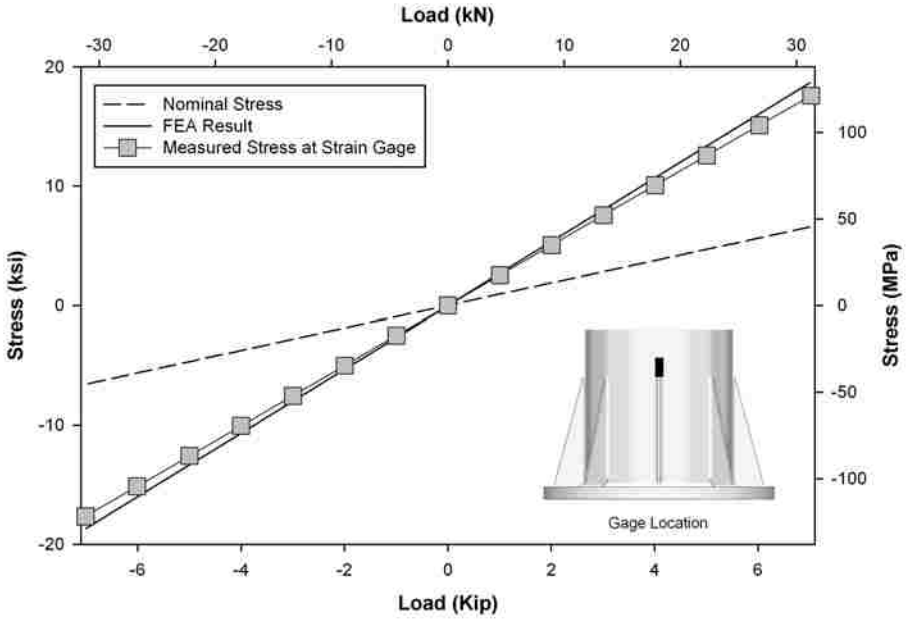

Figure 55. Type XII strain gage comparison of nominal stress, FEA result, and measured values from static test. Gage abutting weld toe at stiffener termination.

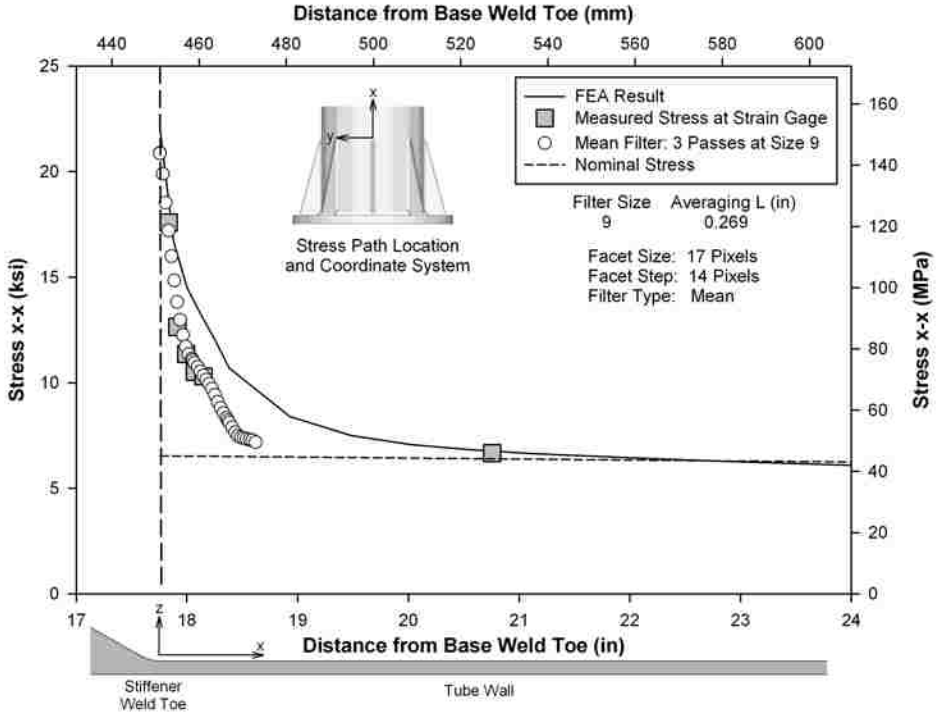

Figure 56. Stress profile in specimen XII-3 above stiffener termination, in the loading plane

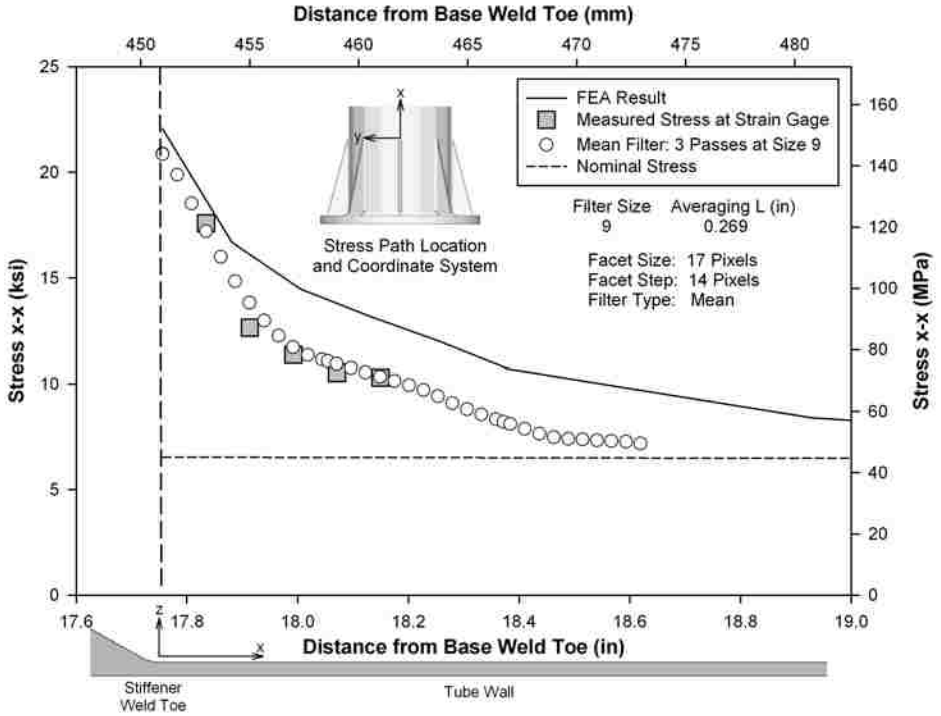

Figure 57. Enlarged view of stress profile in specimen XII-3 abutting stiffener weld toe

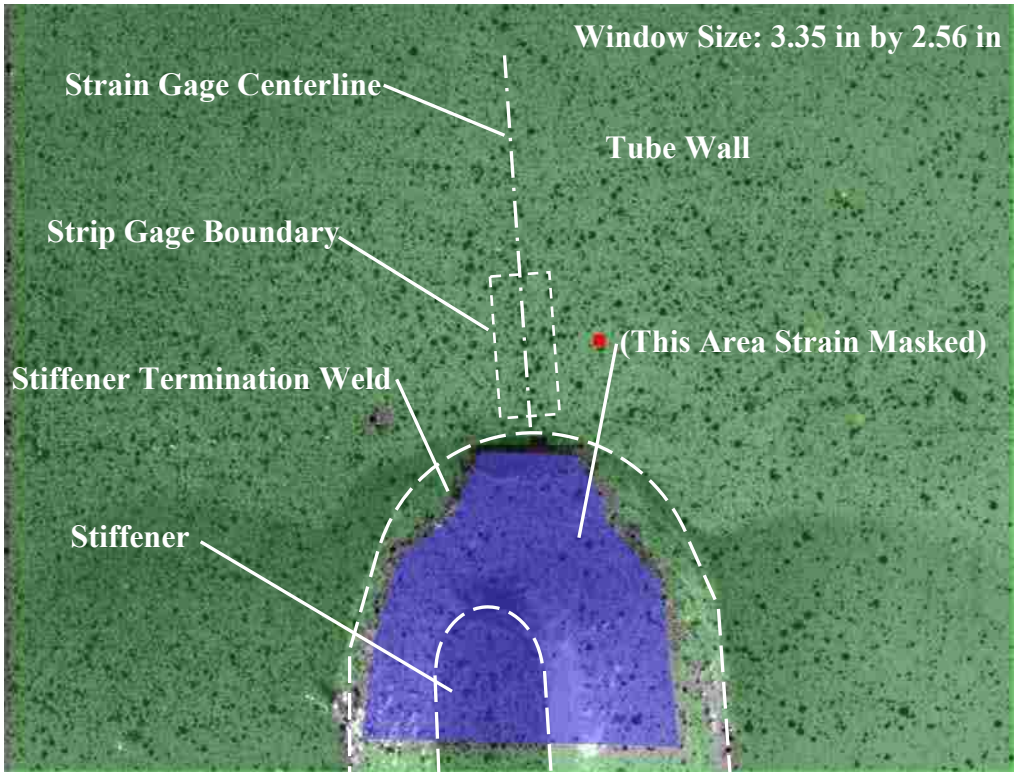

Figure 58. 3D-ICP camera image of Type XII at stiffener termination

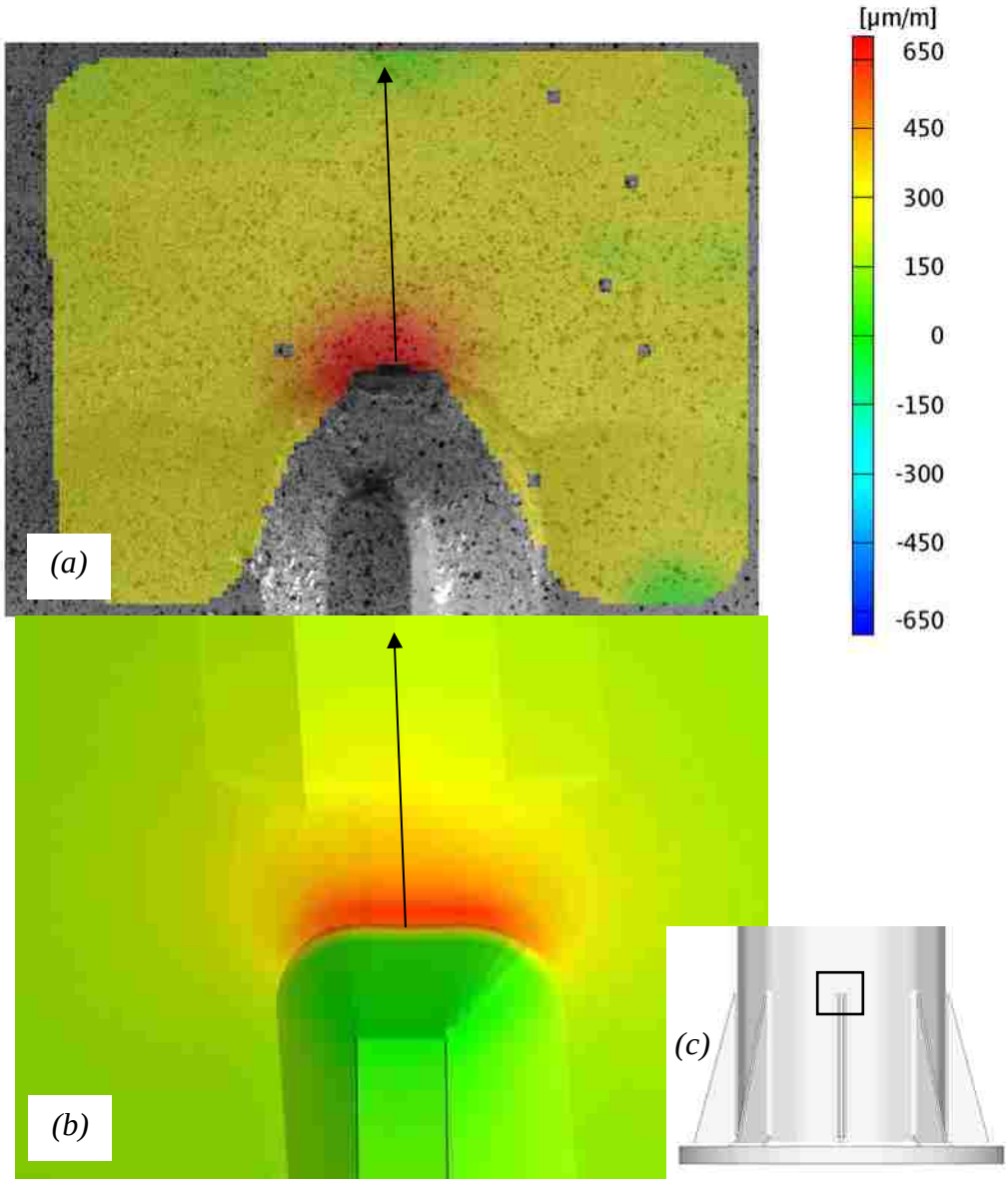

Figure 59. Type XII strain comparison at stiffener termination opposite actuator (arrows indicate strain direction): *a*, 3D-ICP contour plot; *b*, FEA contour plot; *c*, global view with comparison area highlighted.

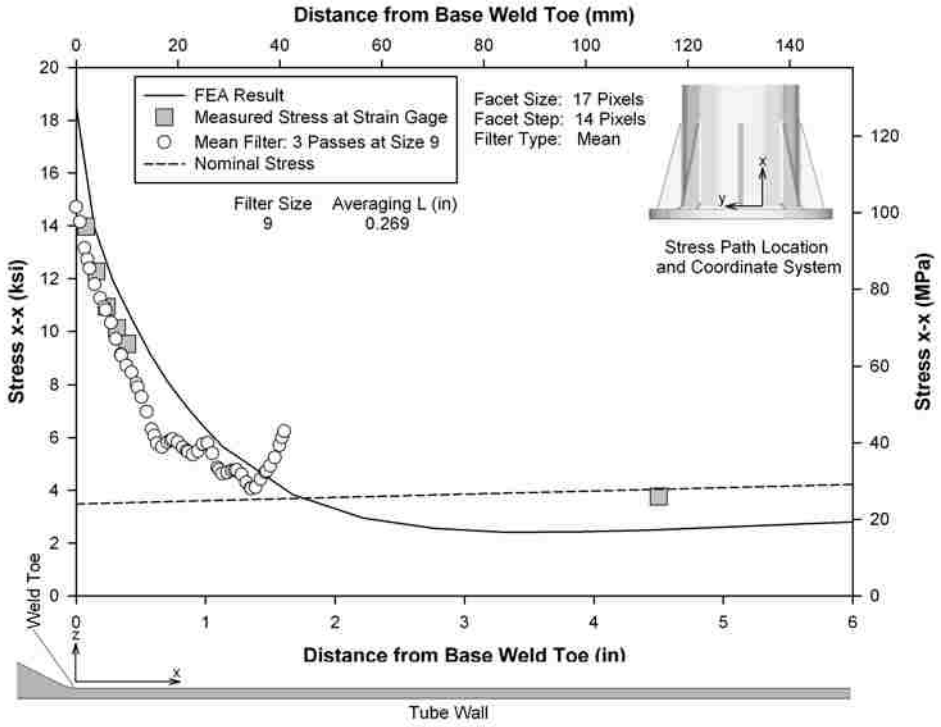

Figure 60. Stress profile in specimen XII-3 at pole-to-base plate weld, in the loading plane

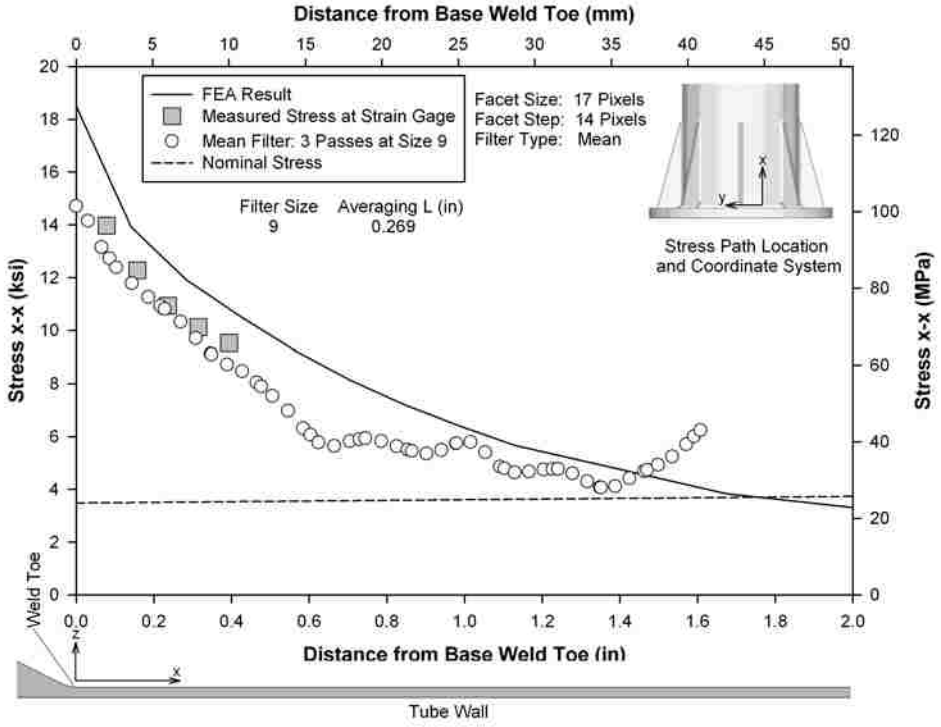

Figure 61. Enlarged view of stress profile in specimen XII-3 abutting pole-to-base plate weld

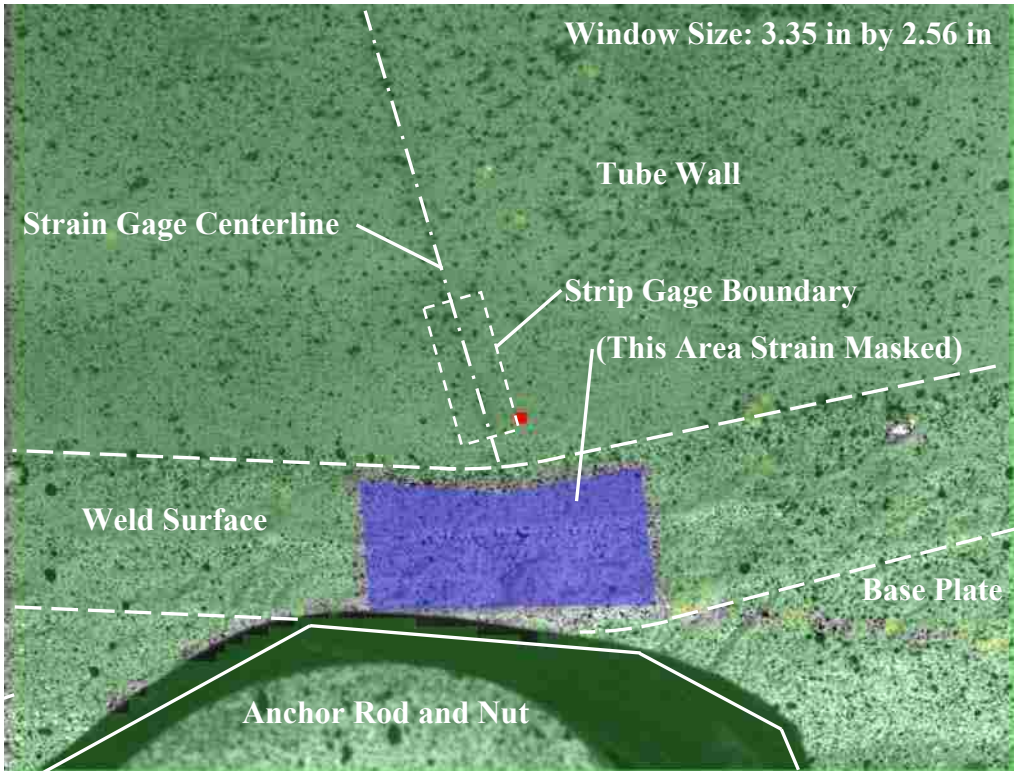

Figure 62. 3D-ICP camera image of Type XII at pole base bend opposite actuator

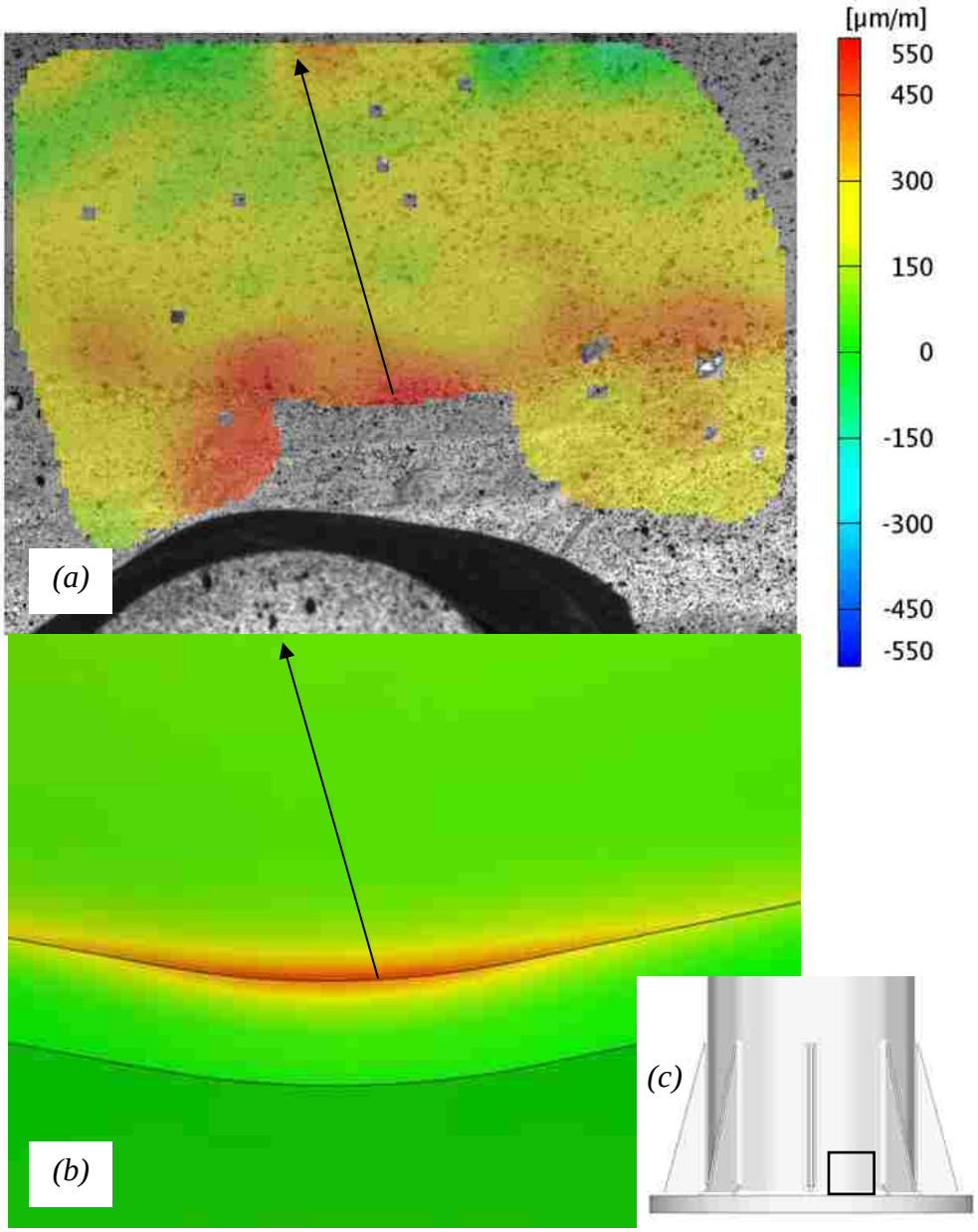

Figure 63. Type XII strain comparison at pole base bend opposite actuator (arrows indicate strain direction): *a*, 3D-ICP contour plot; *b*, FEA contour plot; *c*, global view with comparison area highlighted.

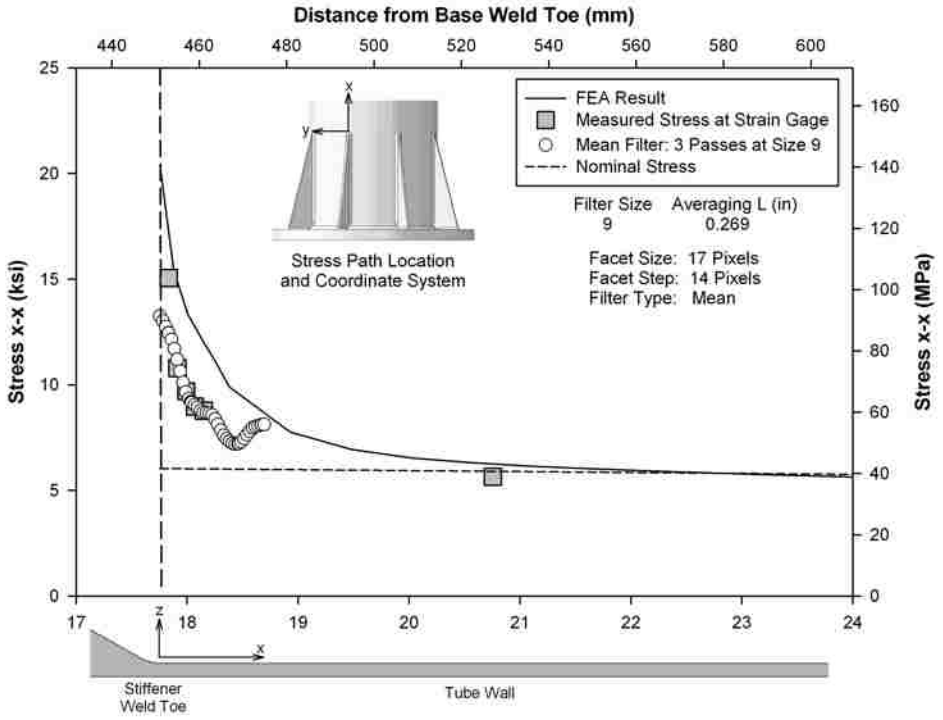

Figure 64. Stress profile in specimen XII-3 above stiffener termination, in the loading plane, bolt-on-center

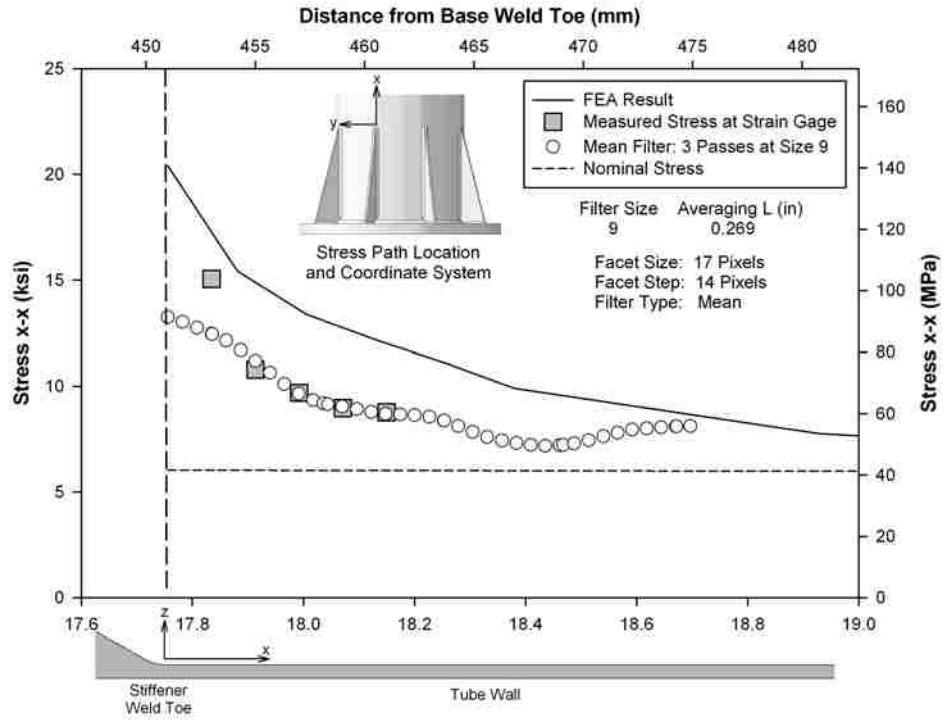

Figure 65. Enlarged view of stress profile in specimen XII-3 abutting stiffener weld toe, bolt-on-center

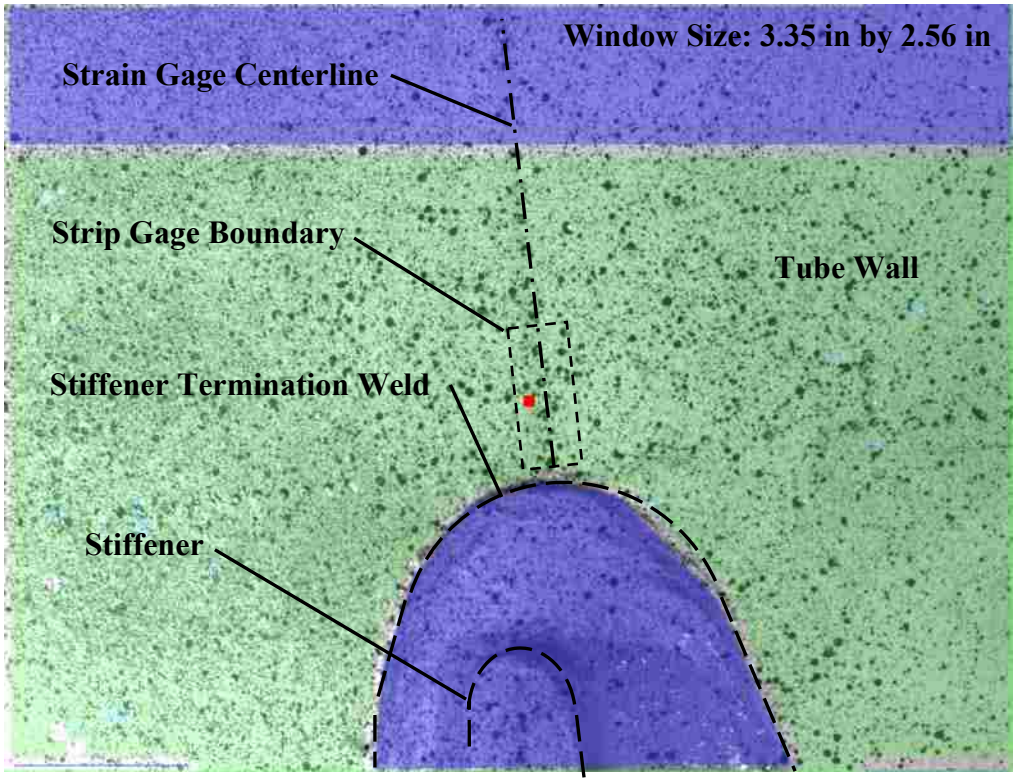

Figure 66. 3D-ICP camera image of Type XII at stiffener termination

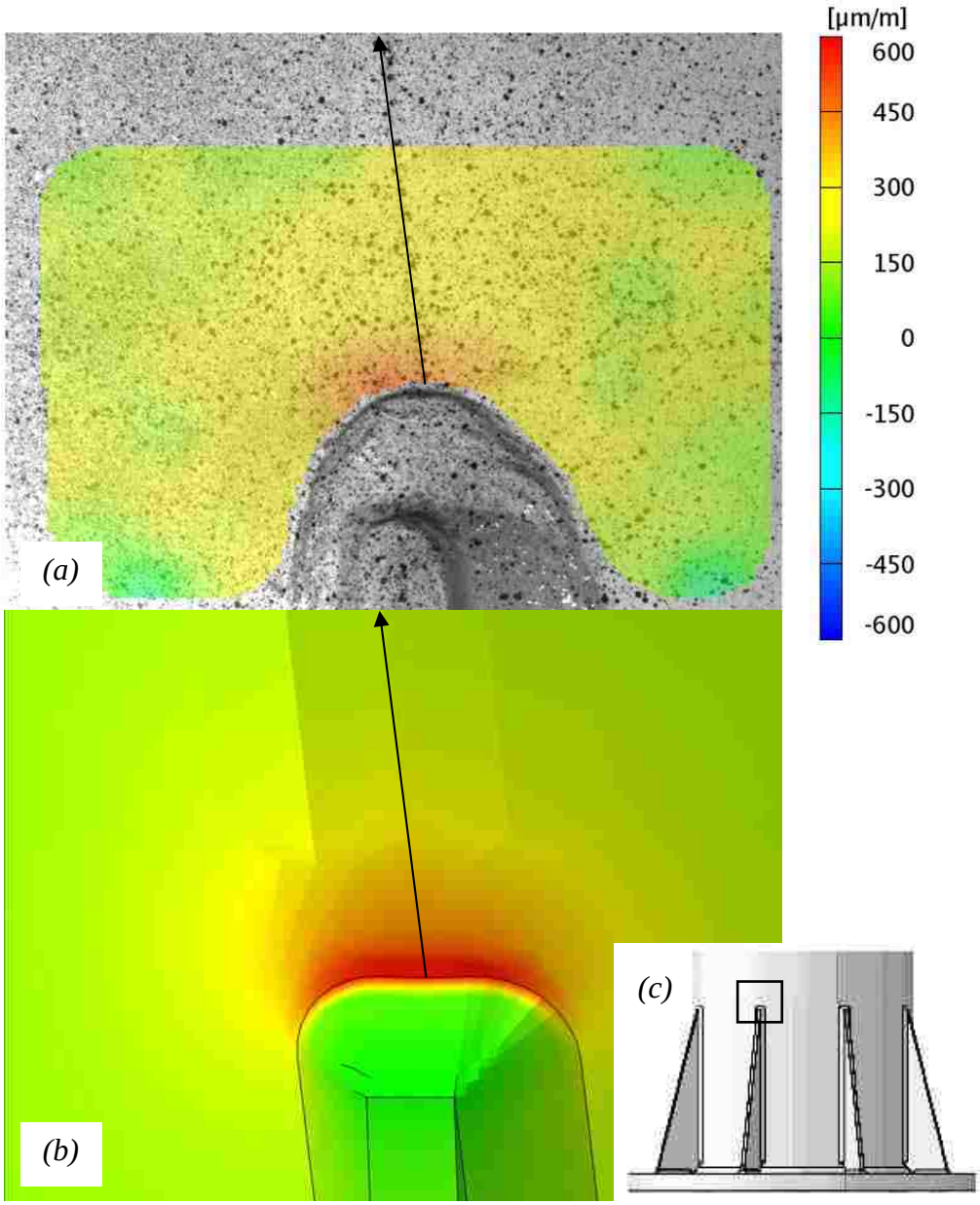

Figure 67. Type XII strain comparison at stiffener termination opposite actuator (arrows indicate strain direction): *a*, 3D-ICP contour plot; *b*, FEA contour plot; *c*, global view with comparison area highlighted.

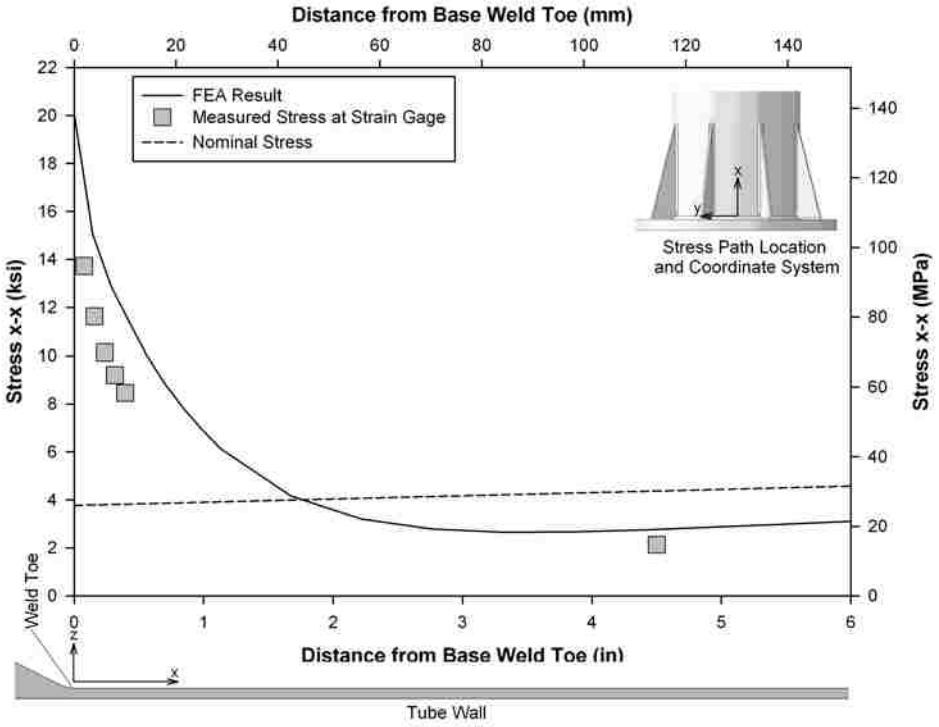

Figure 68. Stress profile in specimen XII-3 at pole-to-base plate weld, in the loading plane, bolt-on-center

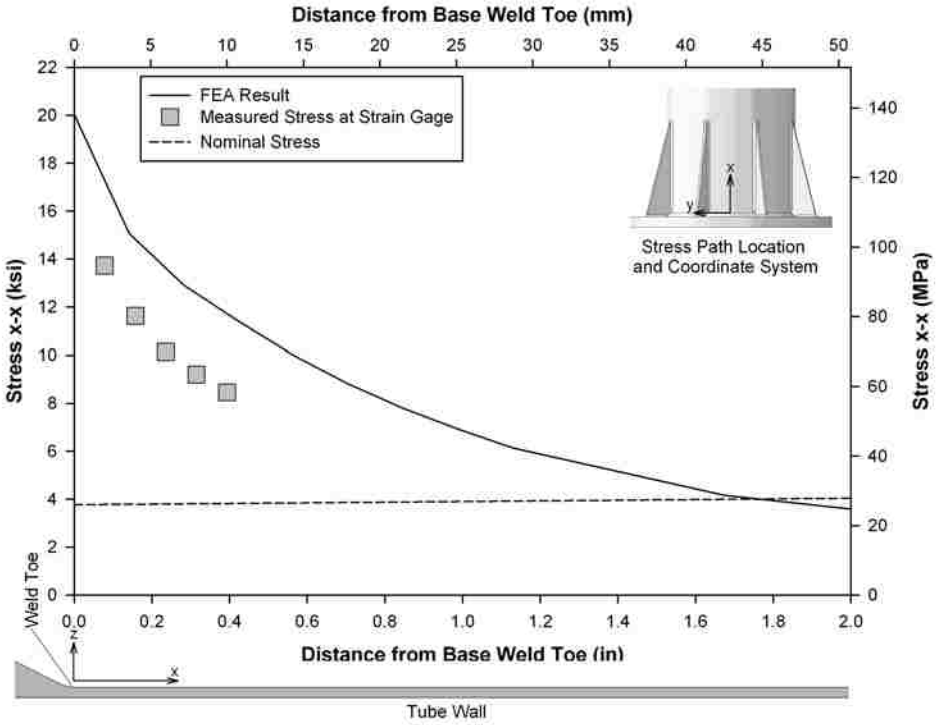

Figure 69. Enlarged view of stress profile in specimen XII-3 at pole-to-base plate weld, in the loading plane, bolt-on-center

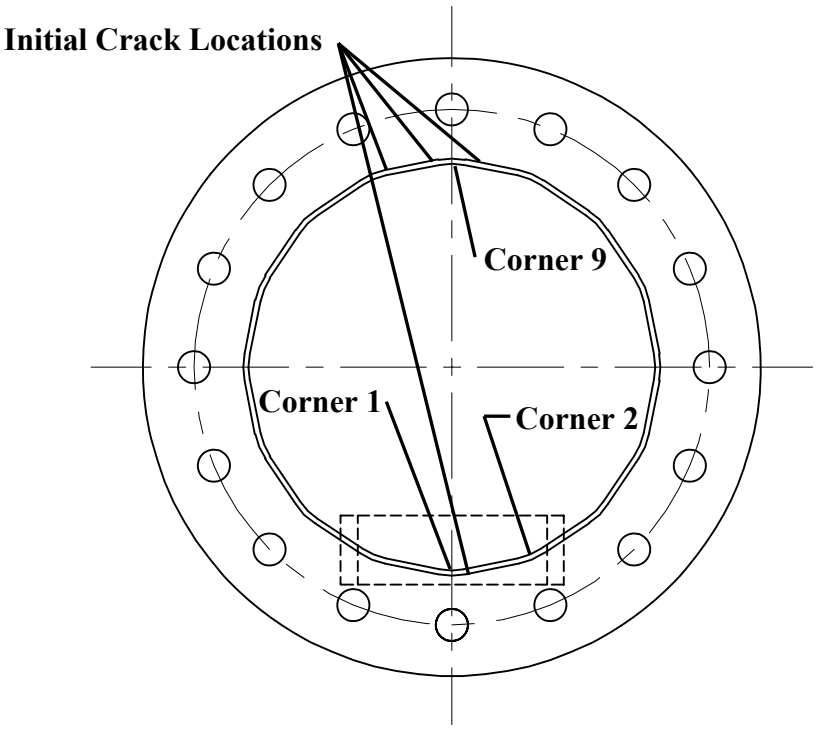

Figure 70. Crack initiation points in Type X specimens

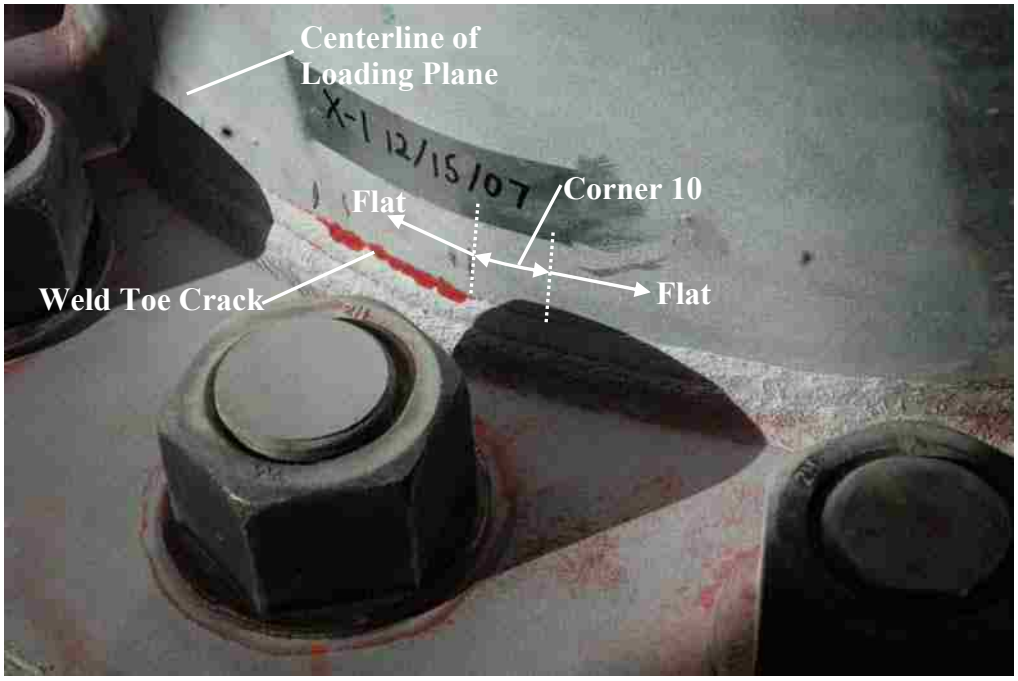

Figure 71. Crack of specimen X-1 at first observation

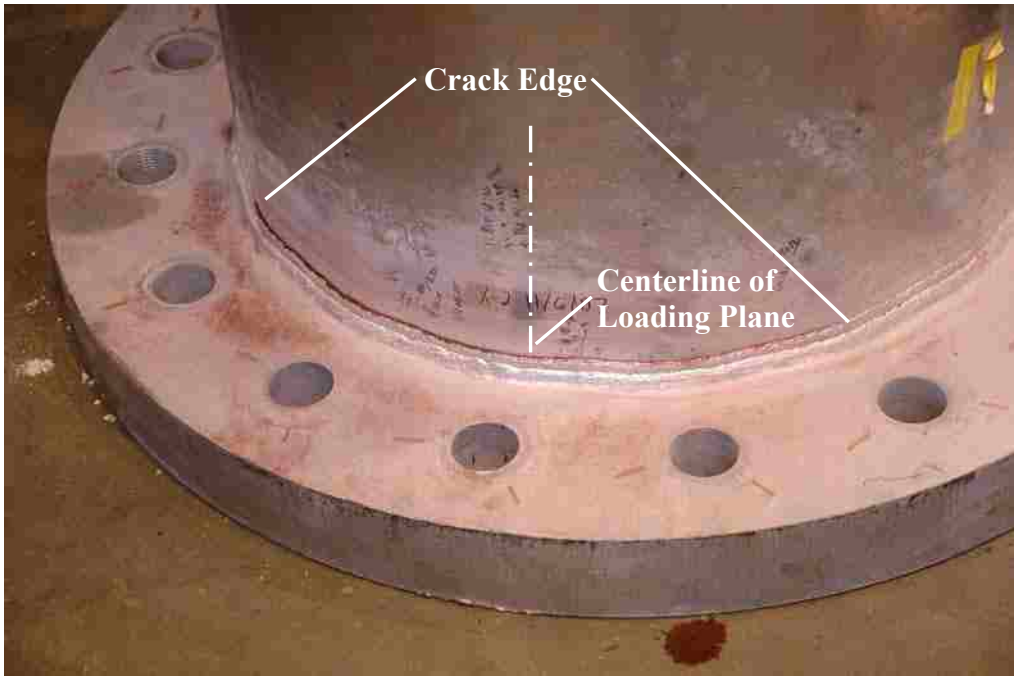

Figure 72. Final crack at termination of fatigue testing of specimen X-2

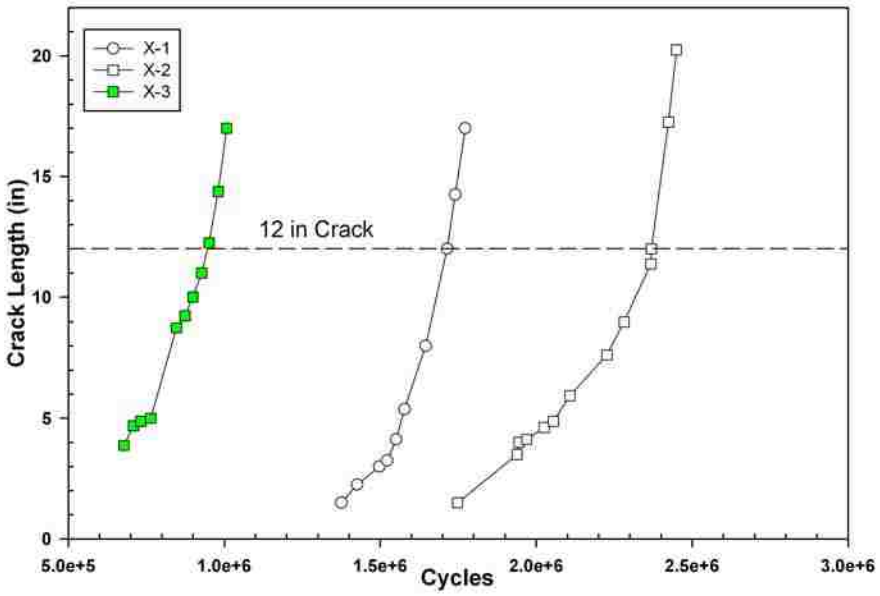

Figure 73. Crack growth versus number of cycles for Type X specimen

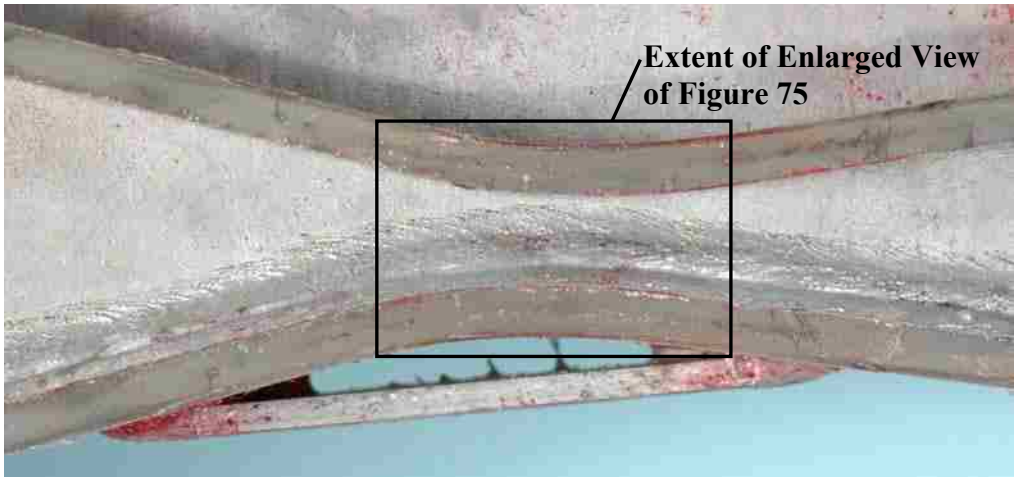

Figure 74. Specimen X-2 fracture surfaces

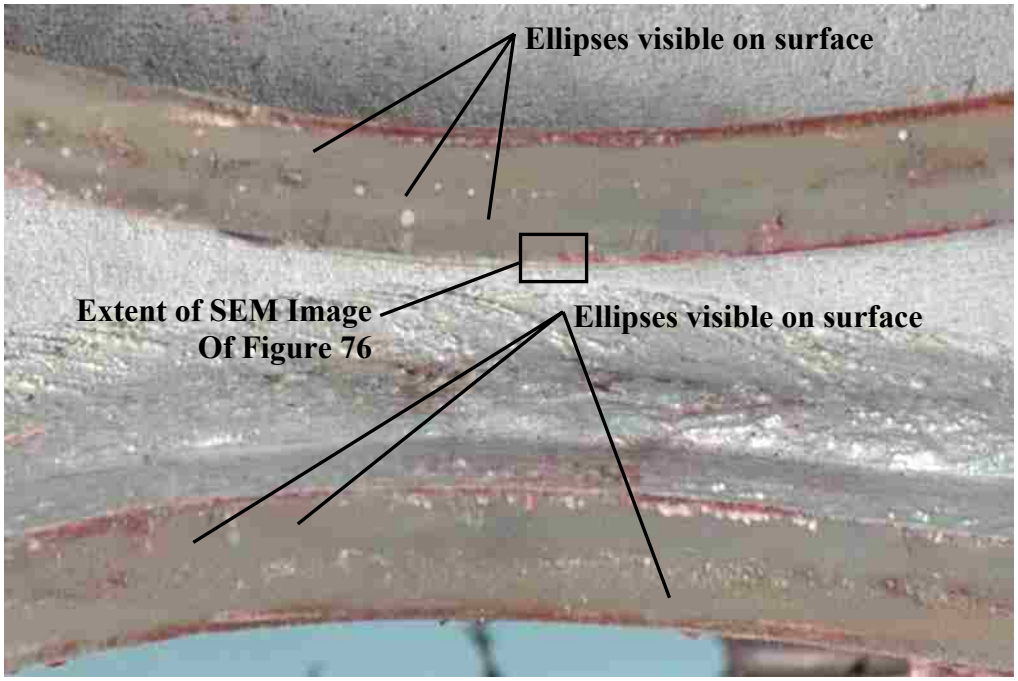

Figure 75. Enlarged view of specimen X-2 fracture surfaces (refer Figure 74)

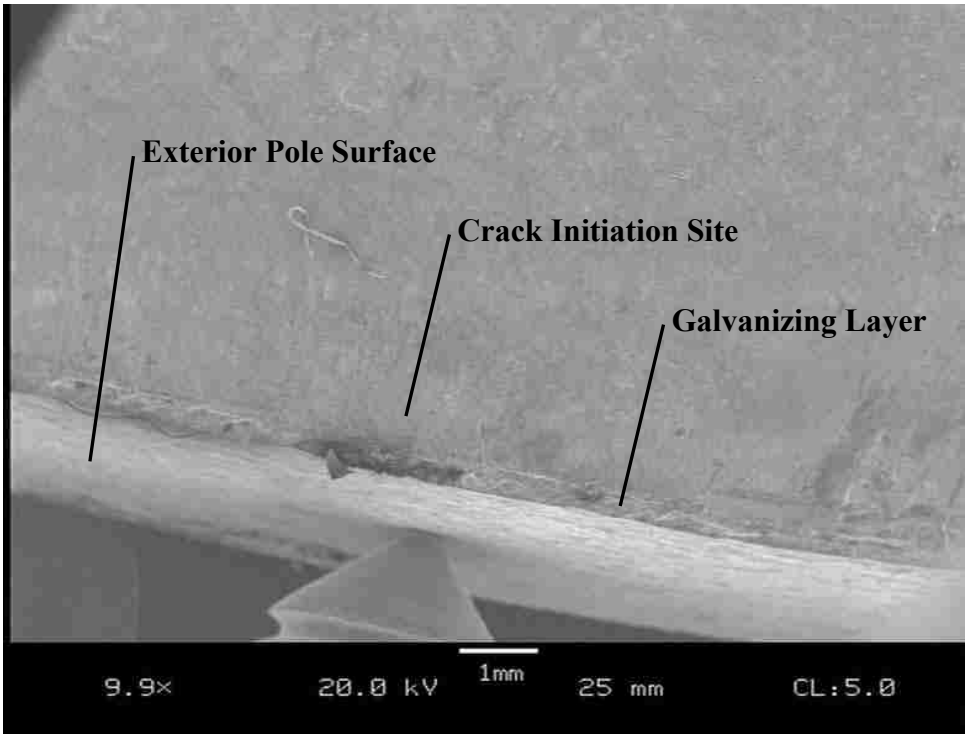

Figure 76. Scanning electron micrograph of typical crack initiation site for specimen X-2 (refer Figure 75)

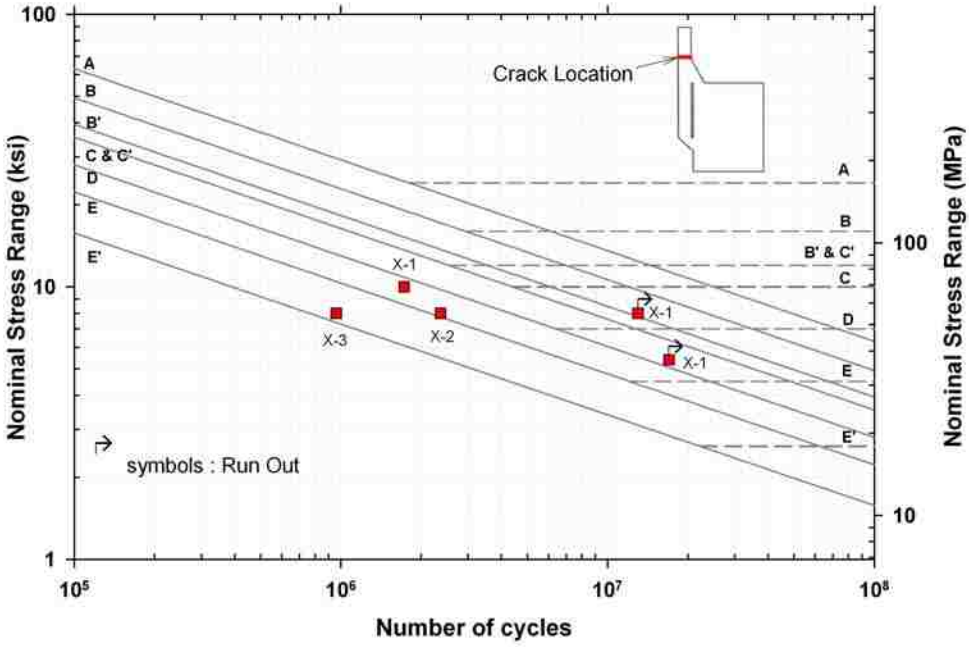

Figure 77. Test results of Type X specimen

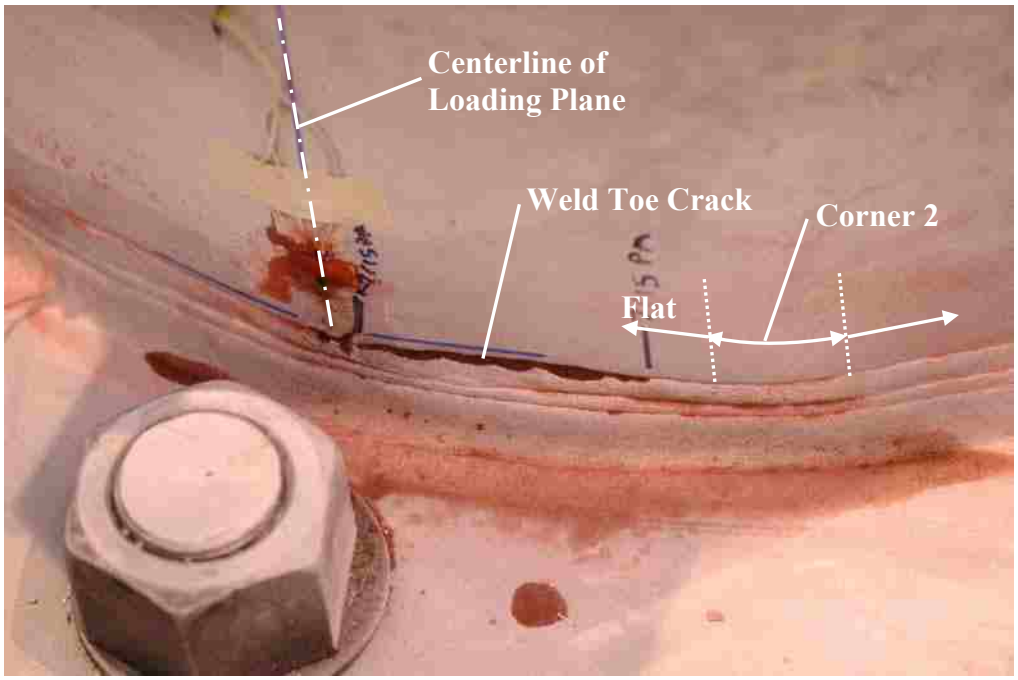

Figure 78. Crack of specimen XI-3 at first observation

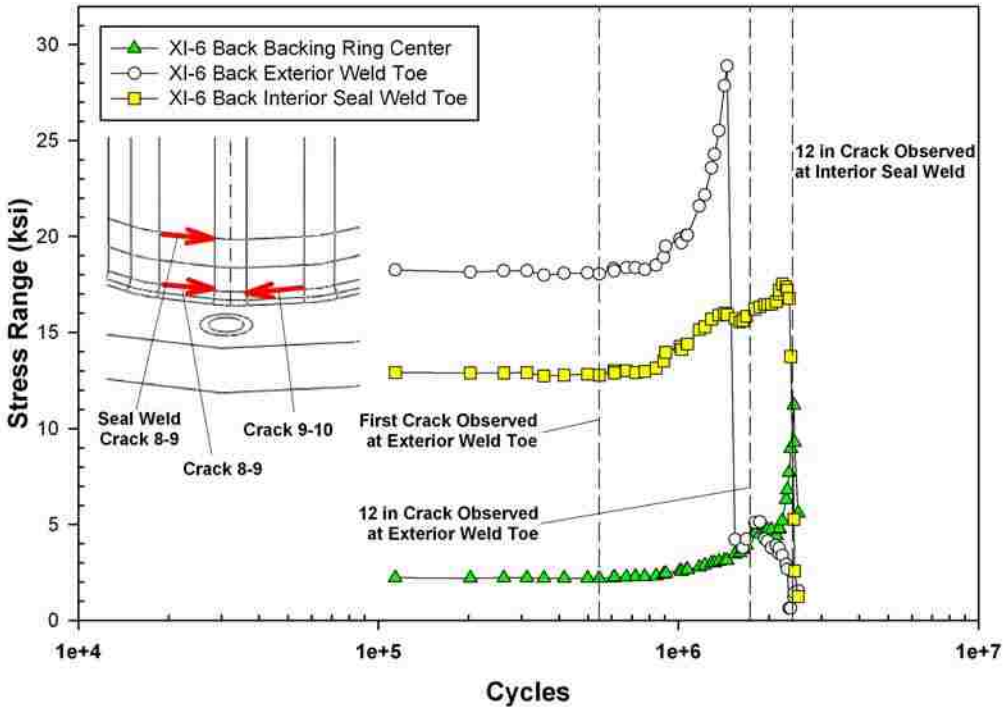

Figure 79. Measured strain range at center of backing ring for Specimen XI-6

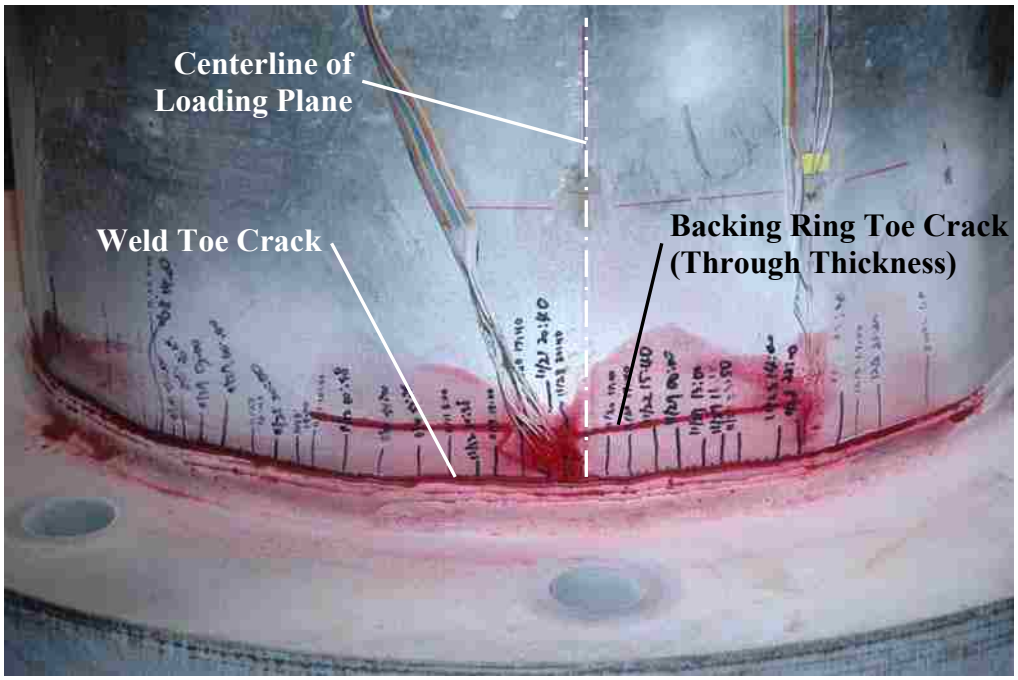

Figure 80. Final crack at termination of fatigue testing of specimen XI-6

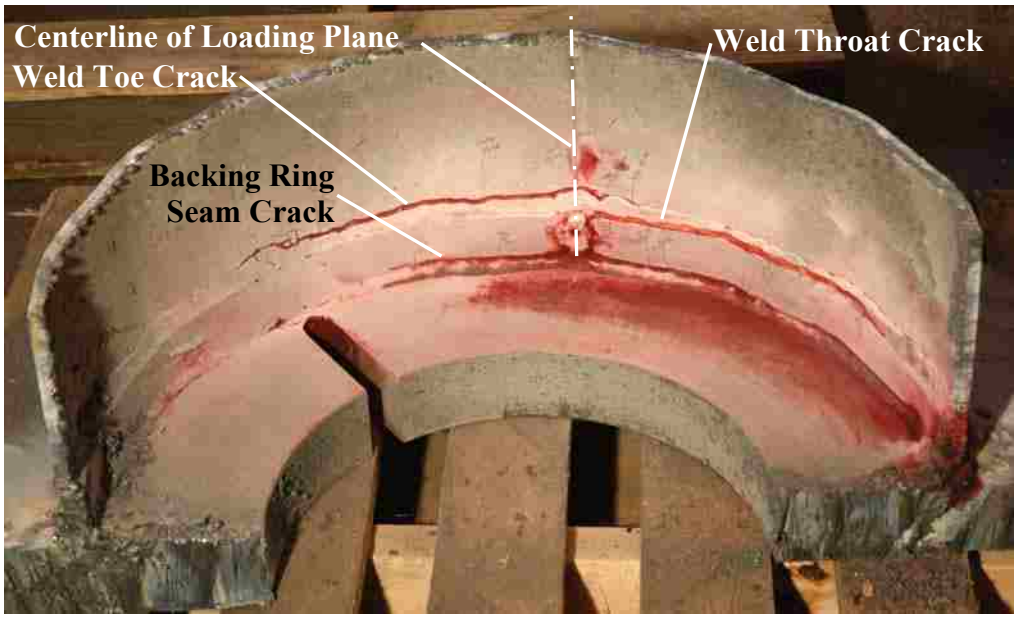

Figure 81. Fatigue cracks in specimen XI-8

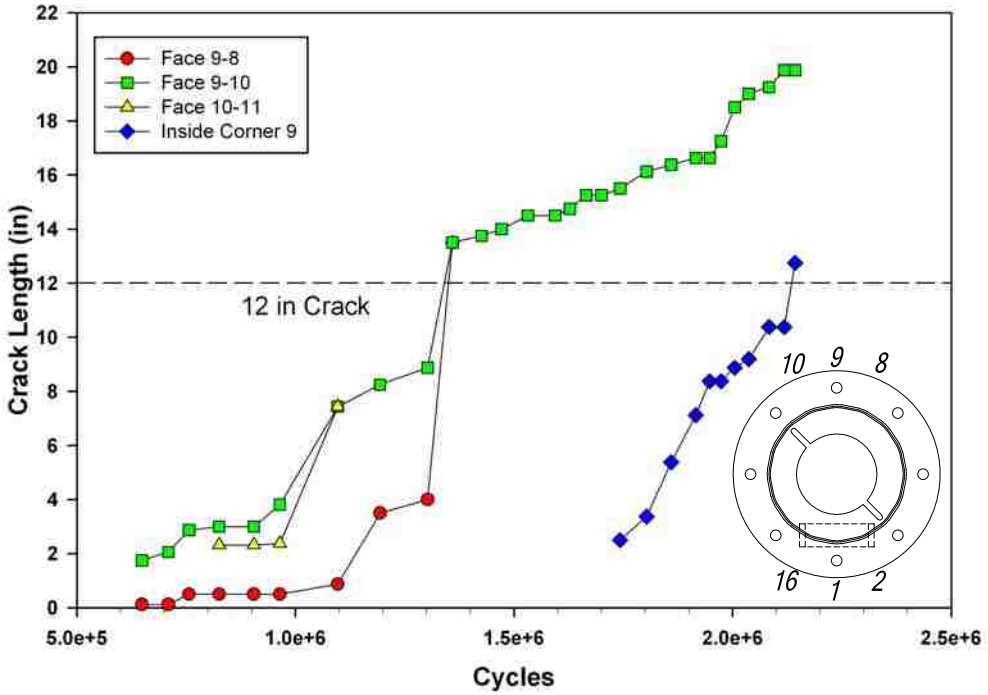

Figure 82. Crack growth in specimen XI-4

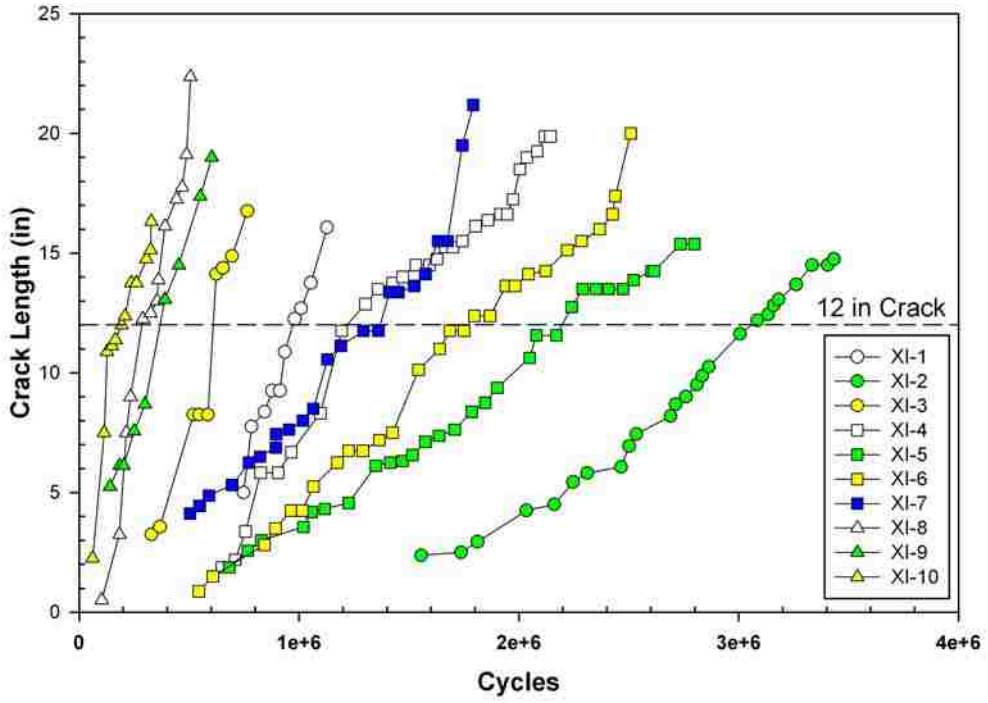

Figure 83. Crack growth versus number of cycles for Type XI specimen

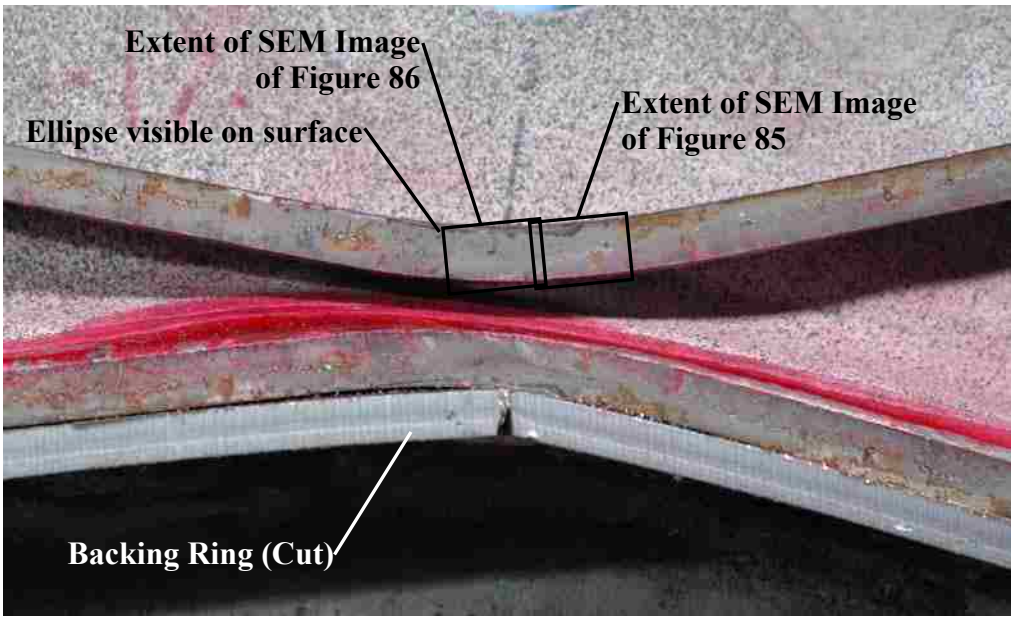

Figure 84. Specimen XI-3 fracture surfaces

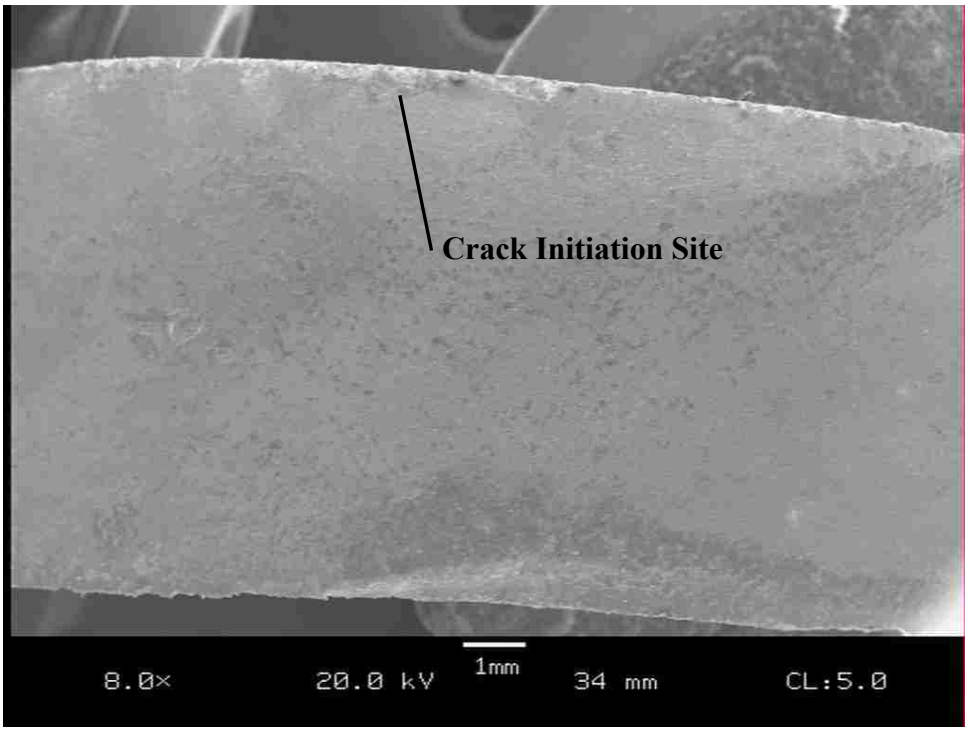

Figure 85. Scanning electron micrograph of typical crack initiation site for specimen XI-3, image 1 (refer Figure 84)

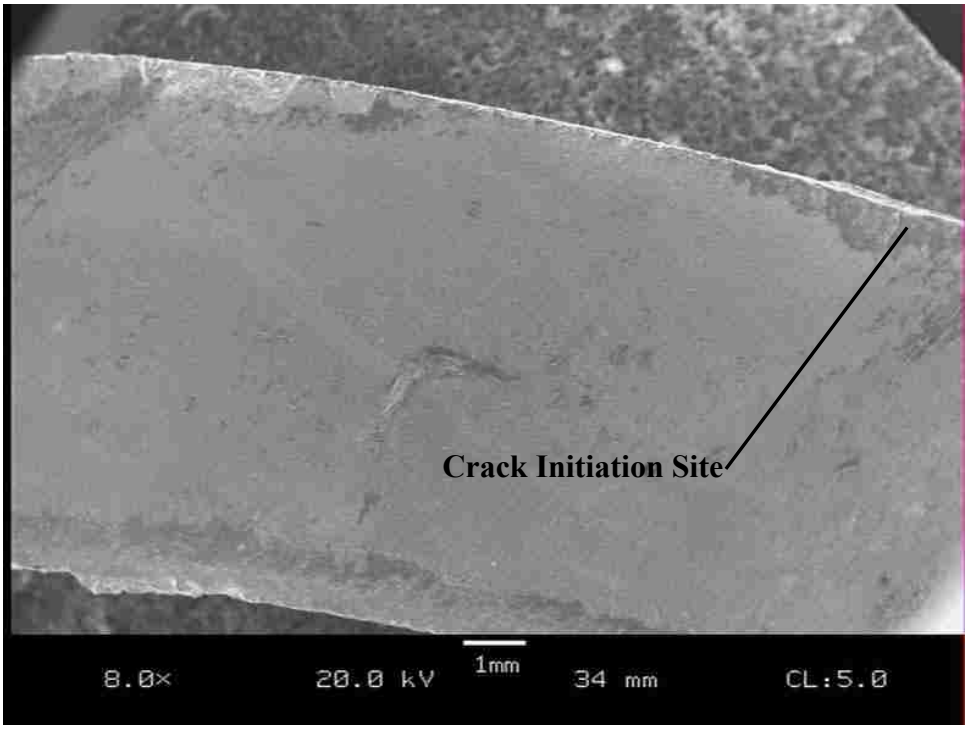

Figure 86. Scanning electron micrograph of typical crack initiation site for specimen XI-3, image 2 (refer Figure 84)

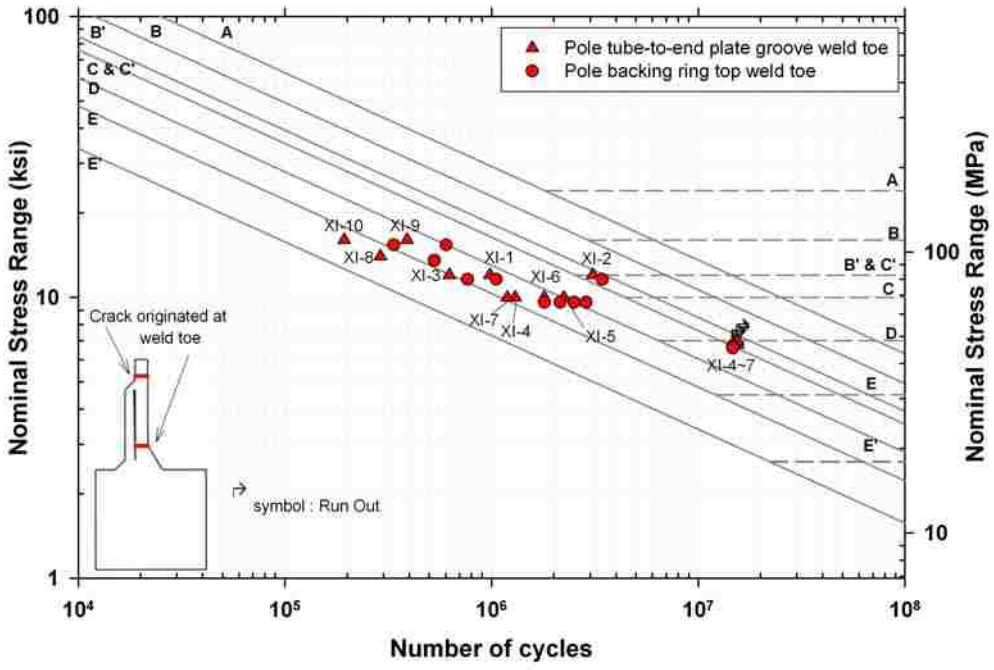

Figure 87. Test results of Type XI specimens

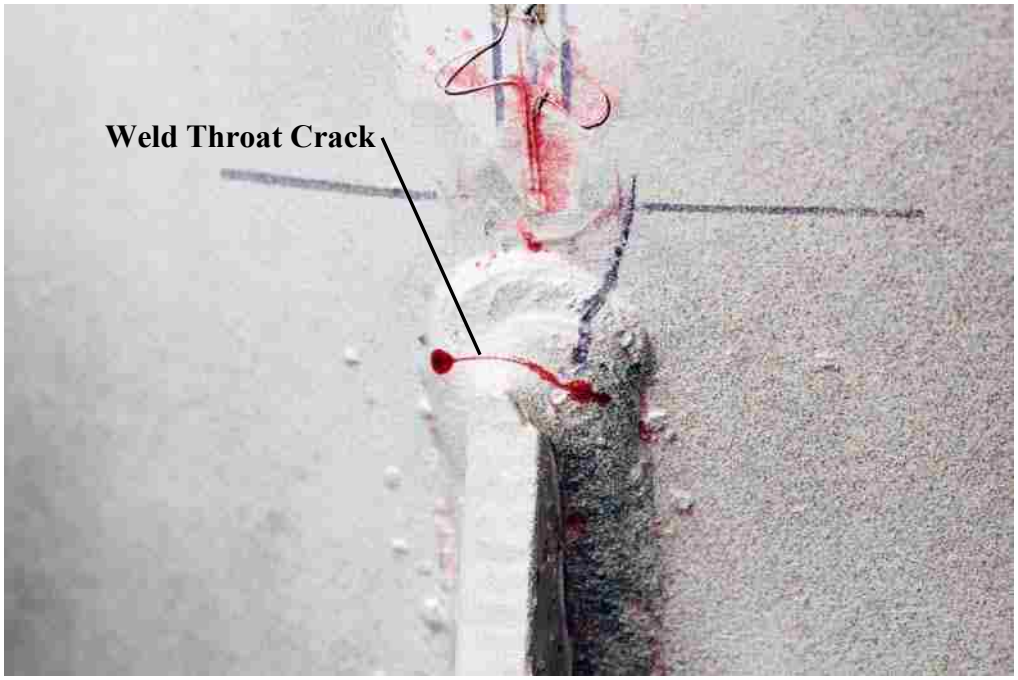

Figure 88. Crack of specimen XII-6 at first observation

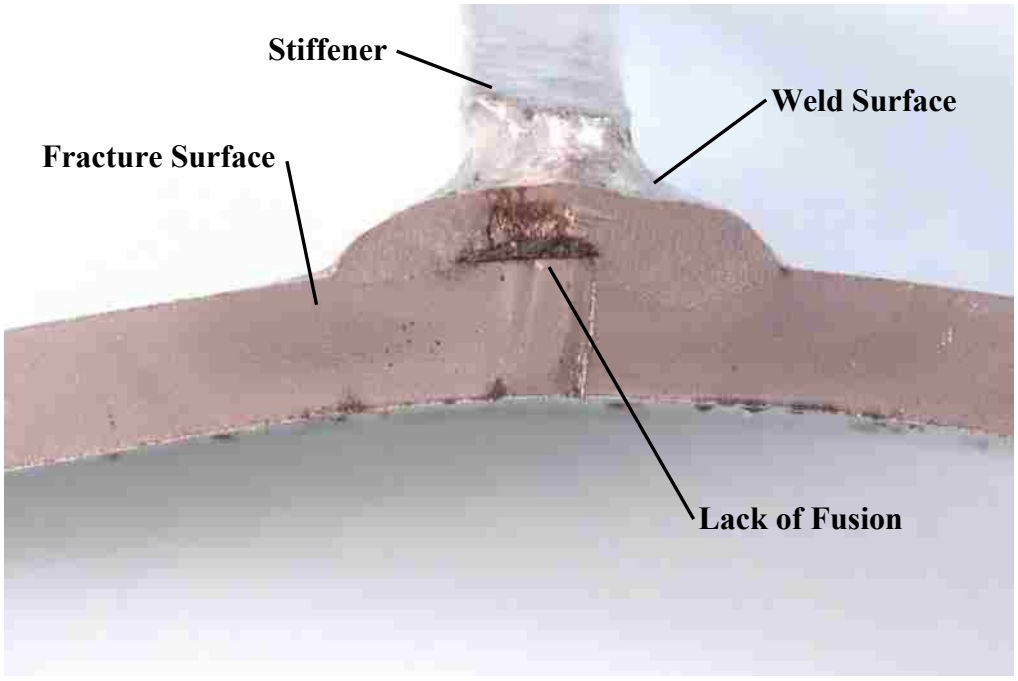

Figure 89. Fatigue cracking from lack of fusion defect in specimen XII-6

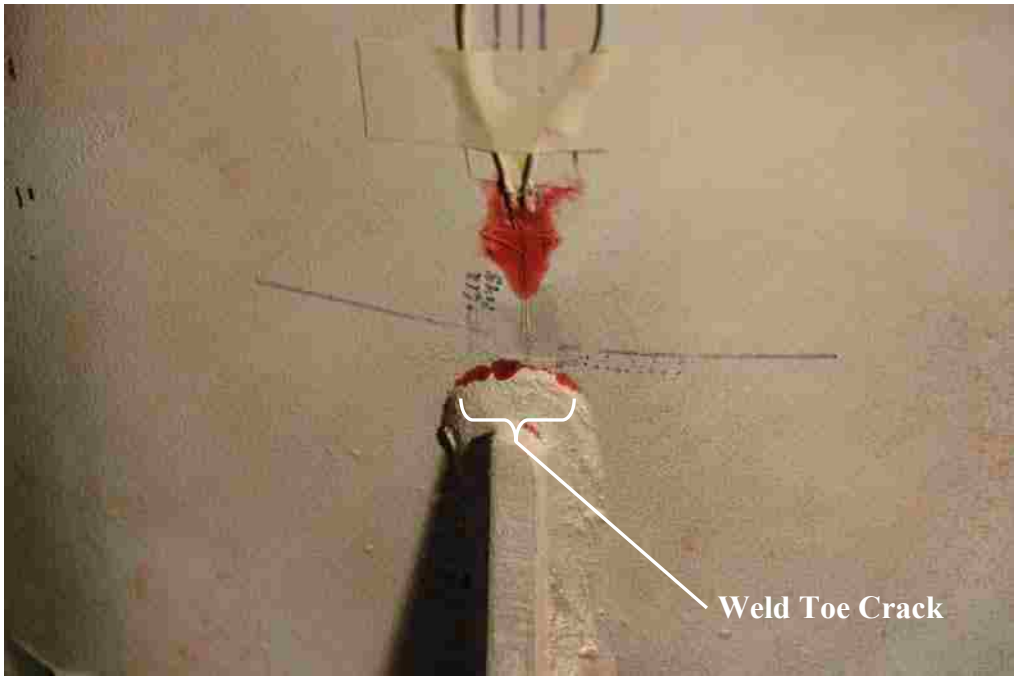

Figure 90. Crack of specimen XII-4 at first observation

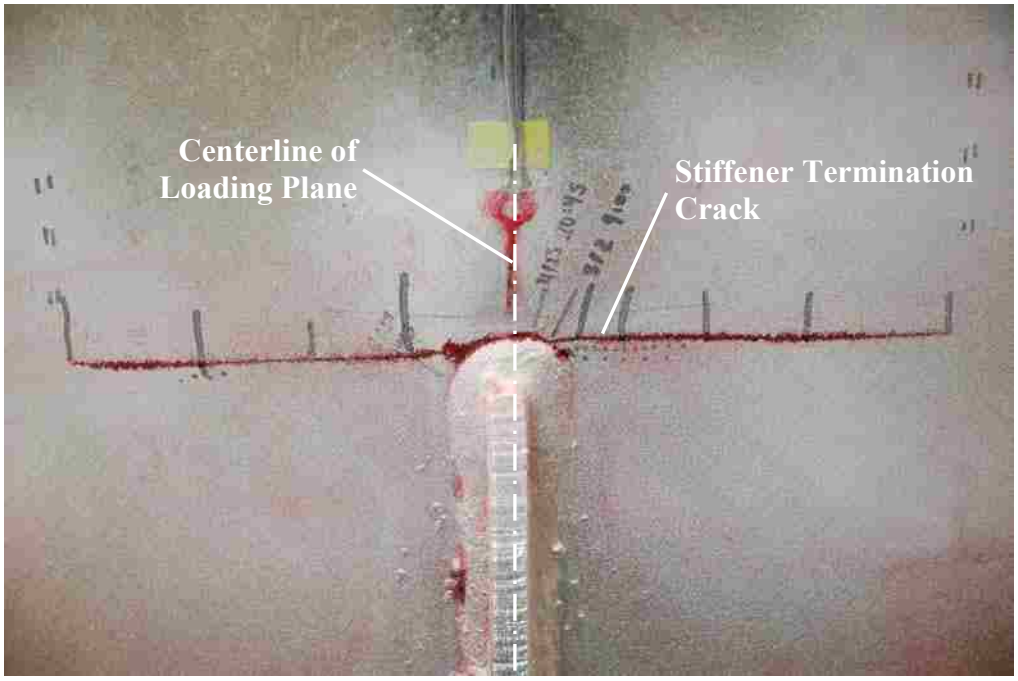

Figure 91. Final crack at termination of fatigue testing of specimen XII-2

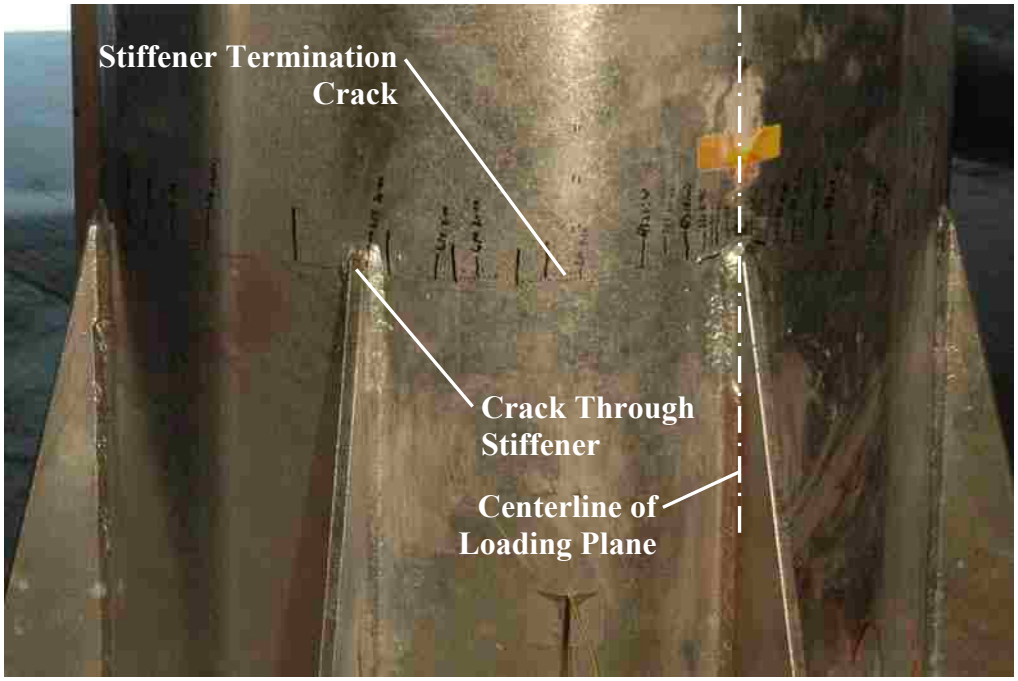

Figure 92. Final crack at termination of fatigue testing of specimen XII-4

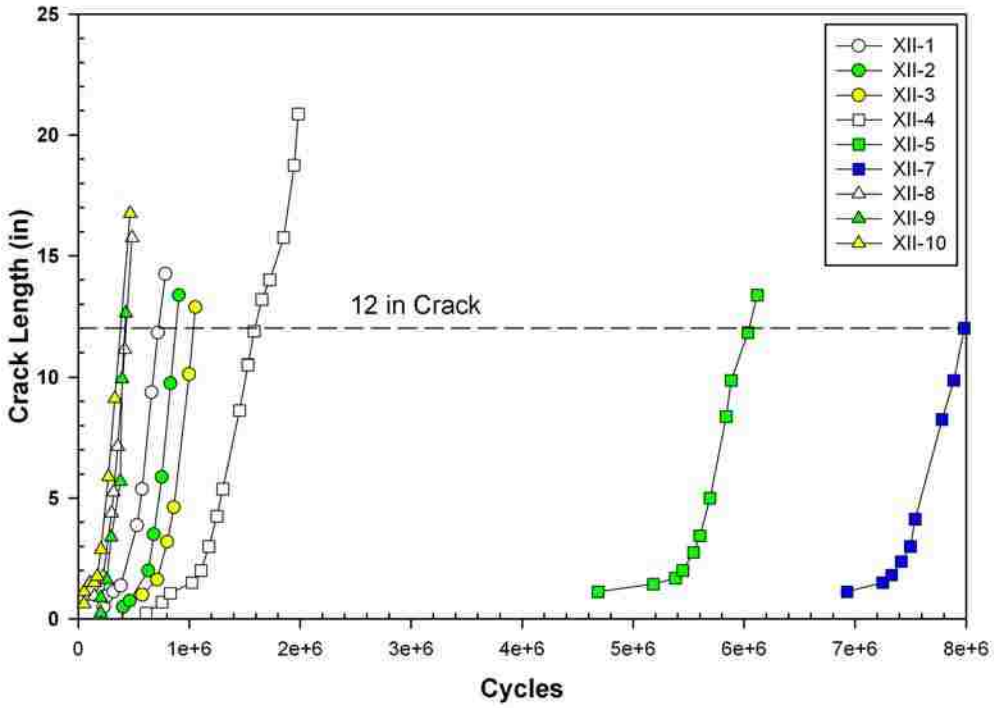

Figure 93. Crack growth versus number of cycles for Type XII specimen

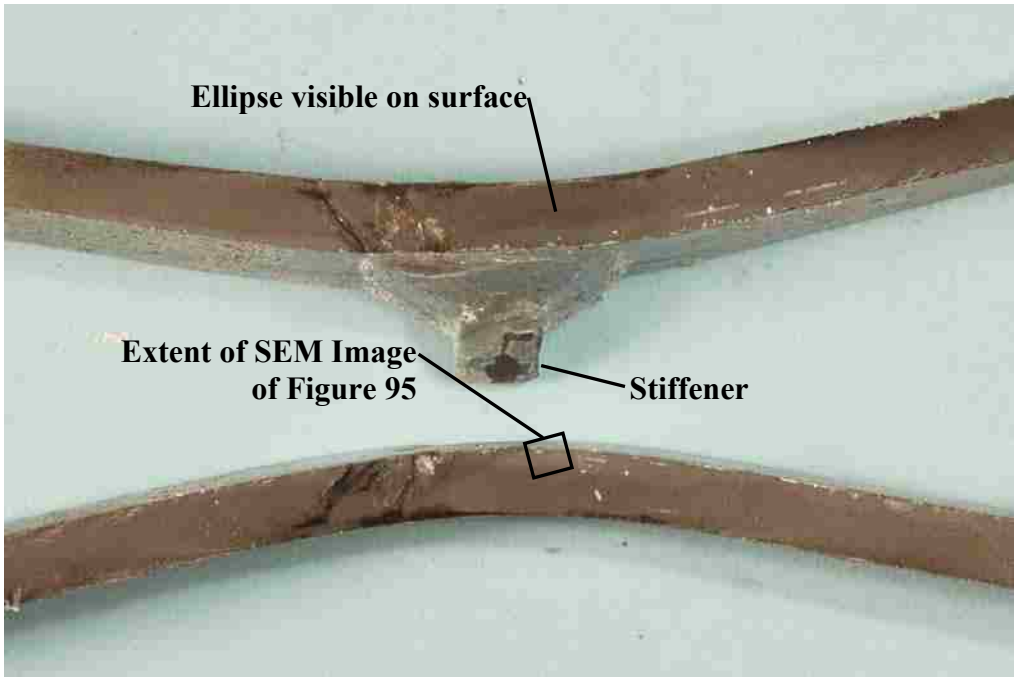

Figure 94. Specimen XII-1 fracture surfaces

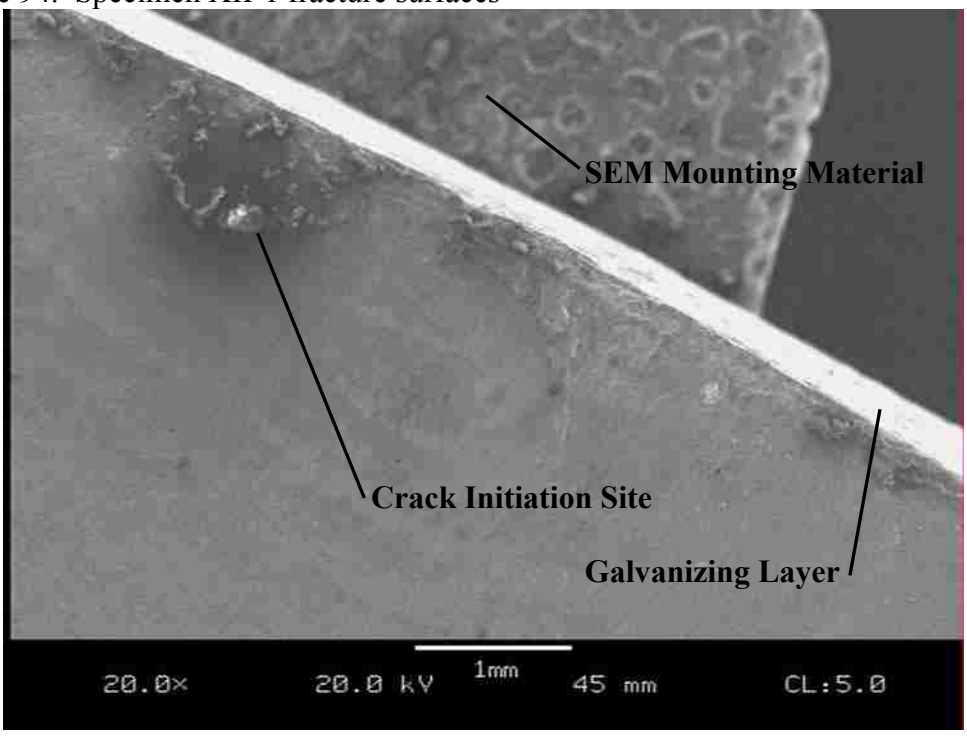

Figure 95. Scanning electron micrograph of typical crack initiation site for specimen XII-1 (refer Figure 94)

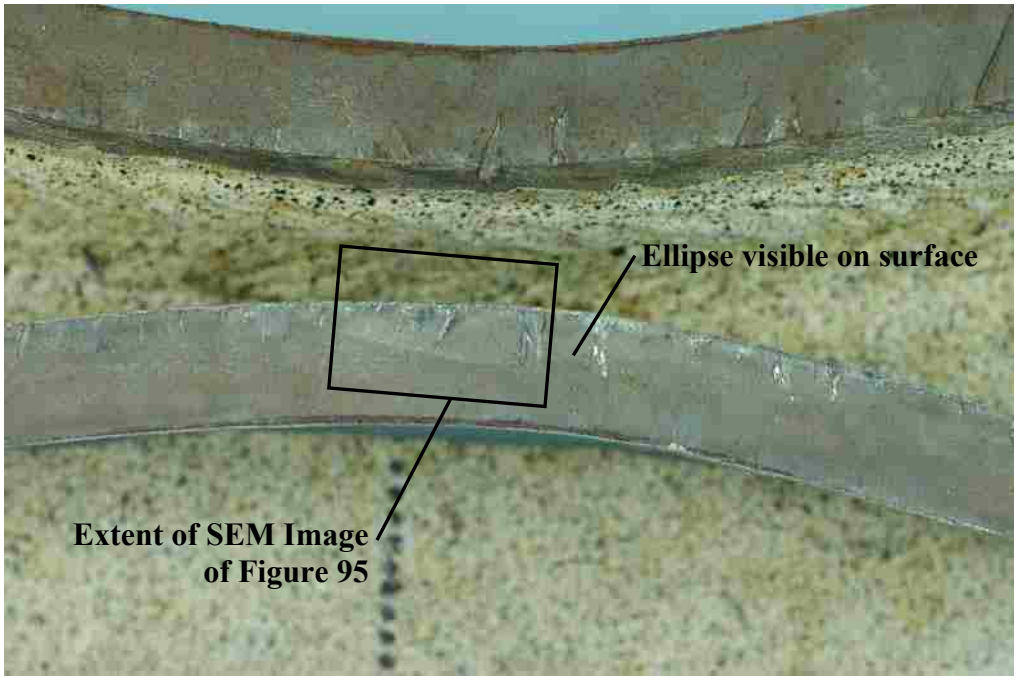

Figure 96. Specimen XII-1 fracture surfaces at pole base

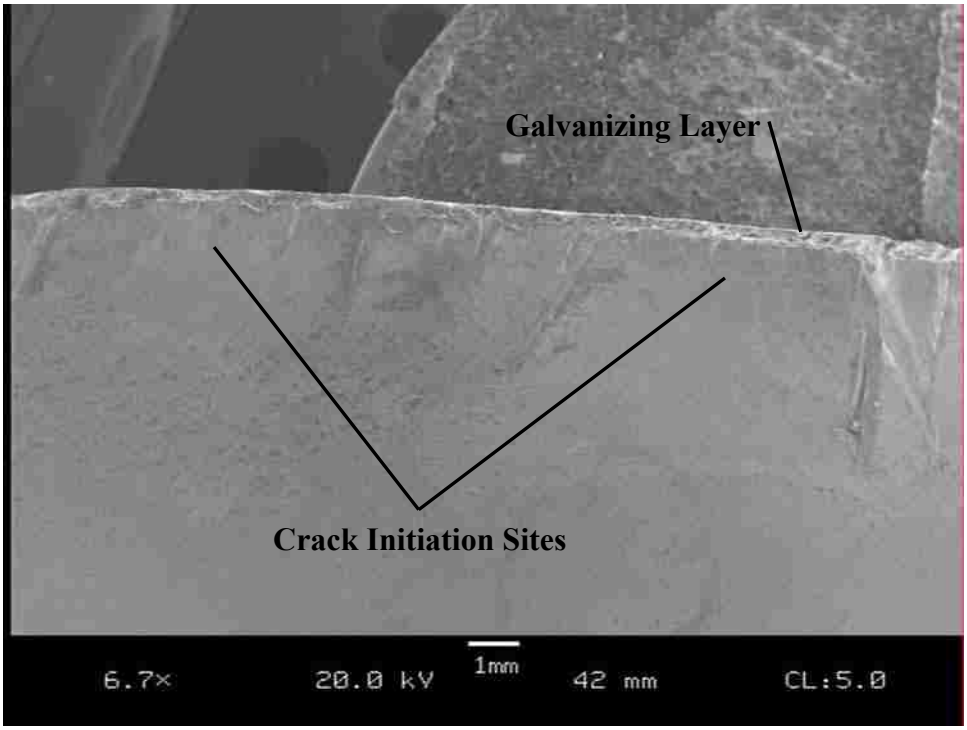

Figure 97. Scanning electron micrograph of typical crack initiation sites for specimen XII-1 at pole base (refer Figure 96)

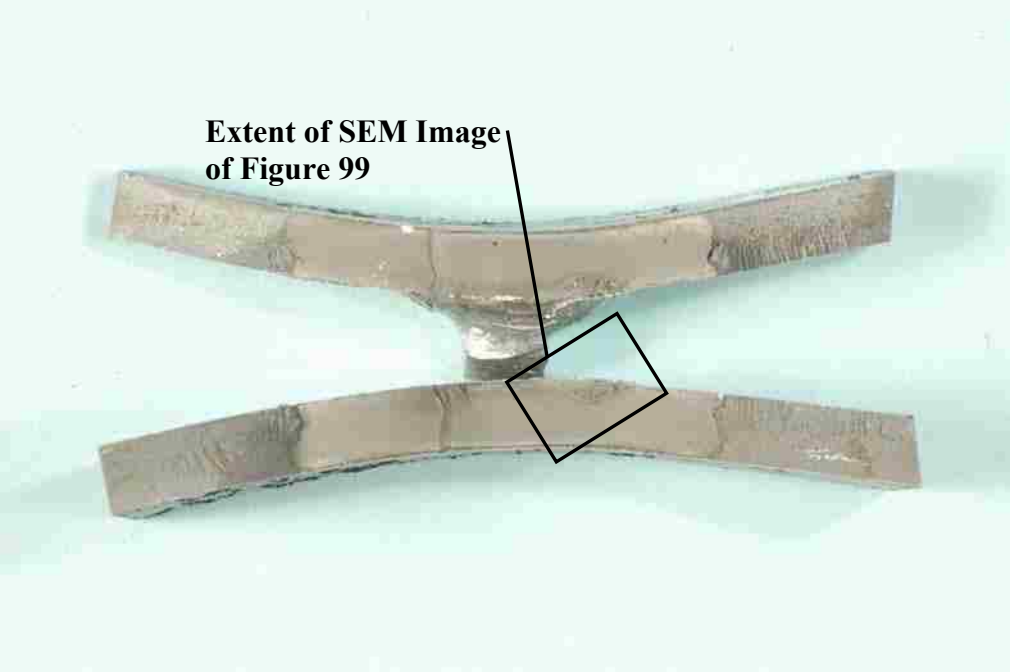

Figure 98. Specimen XII-9 fracture surface

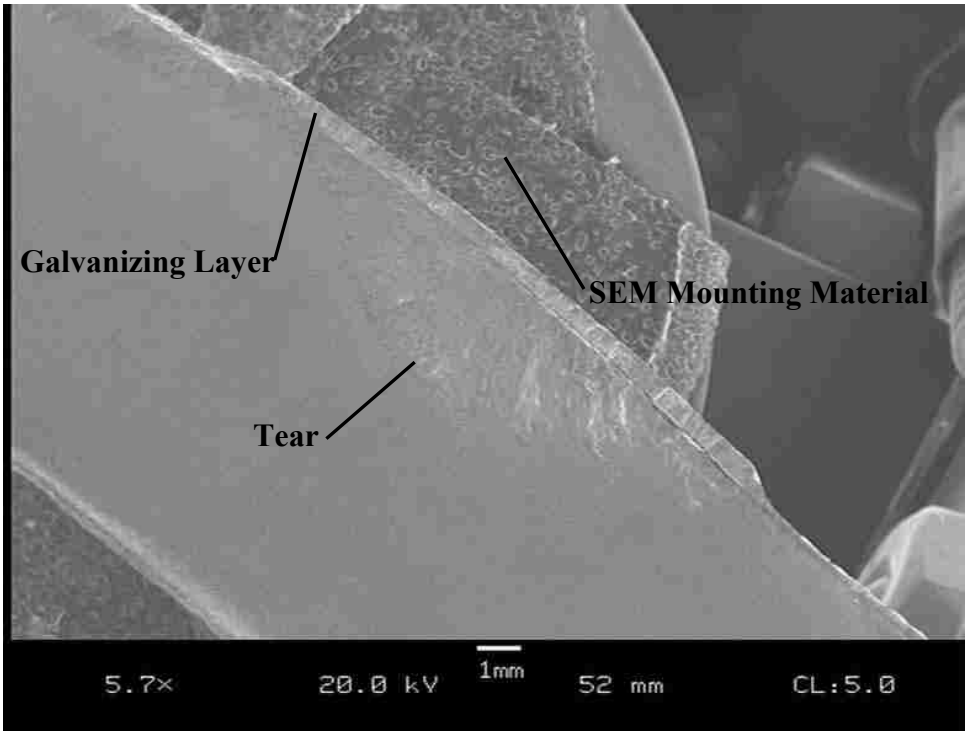

Figure 99. Scanning electron micrograph of crack initiation site for specimen XII-9 (refer Figure 98)

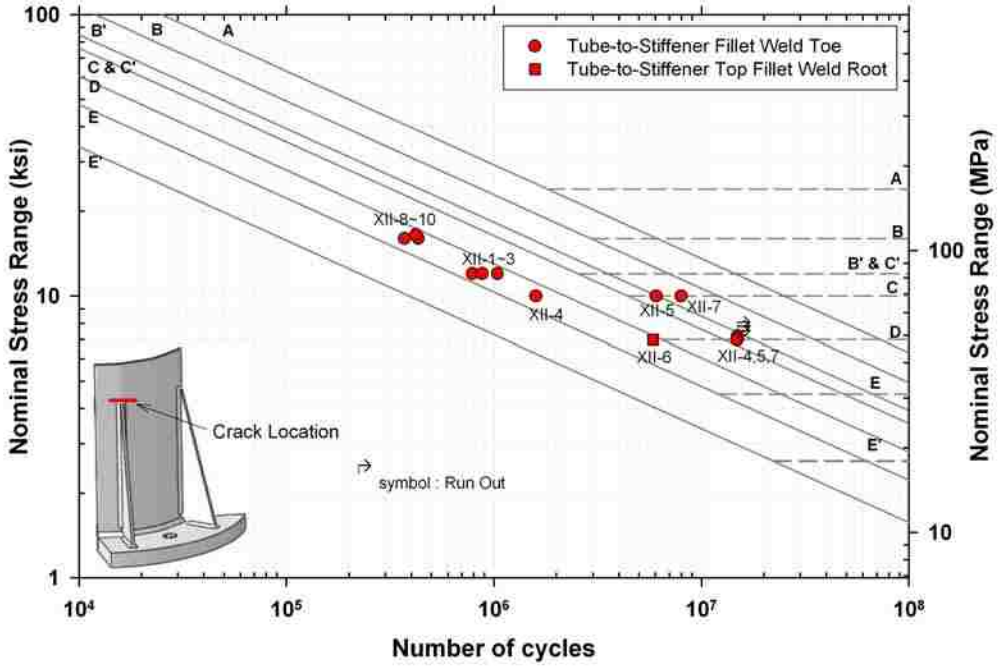

Figure 100. Test results of Type XII specimens

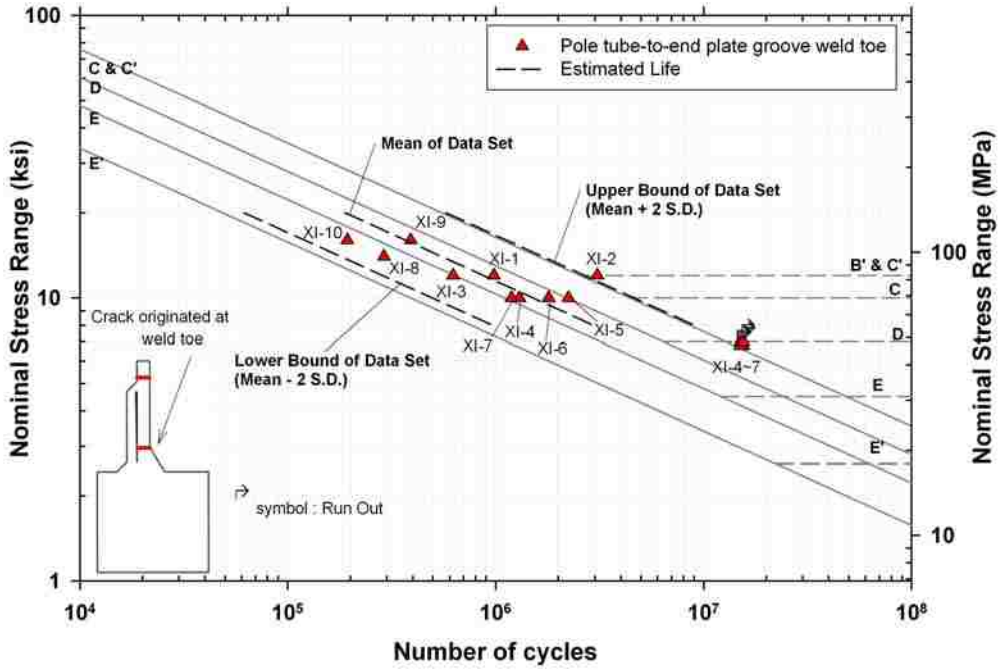

Figure 101. Analysis of fatigue test results of Type XI specimens

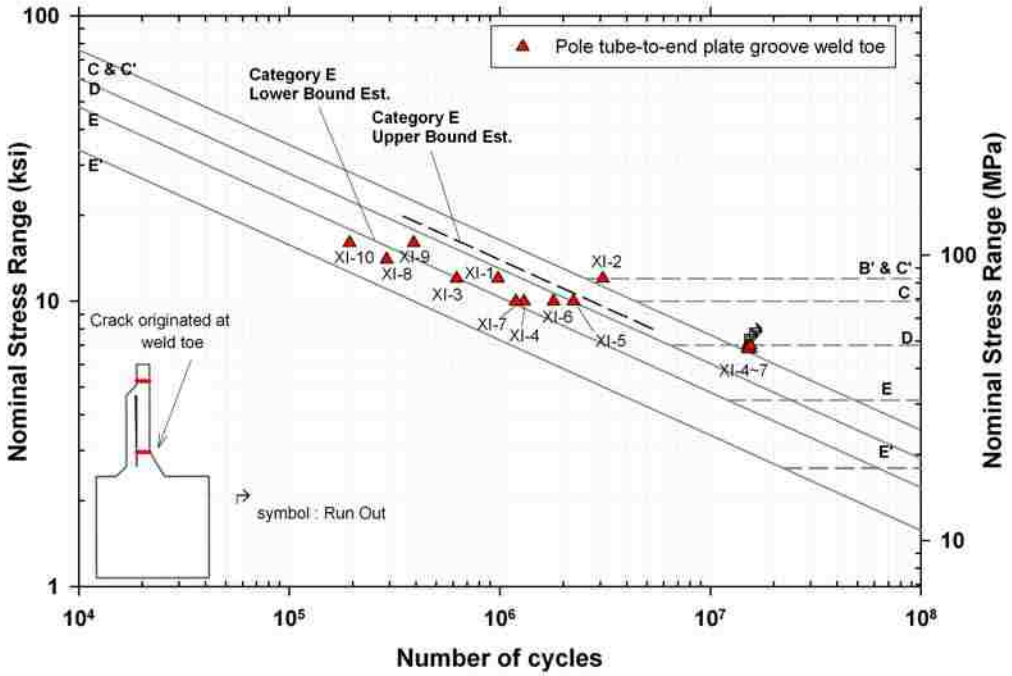

Figure 102. Category E upper and lower bounds plotted with Type XI test results

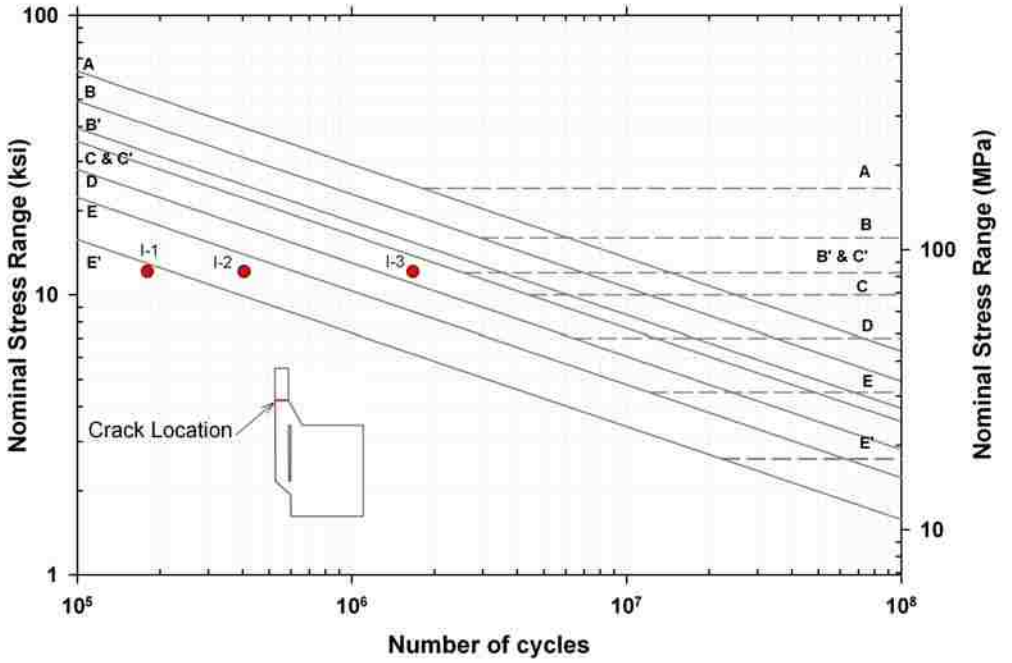

Figure 103. Test results, select Type I specimens

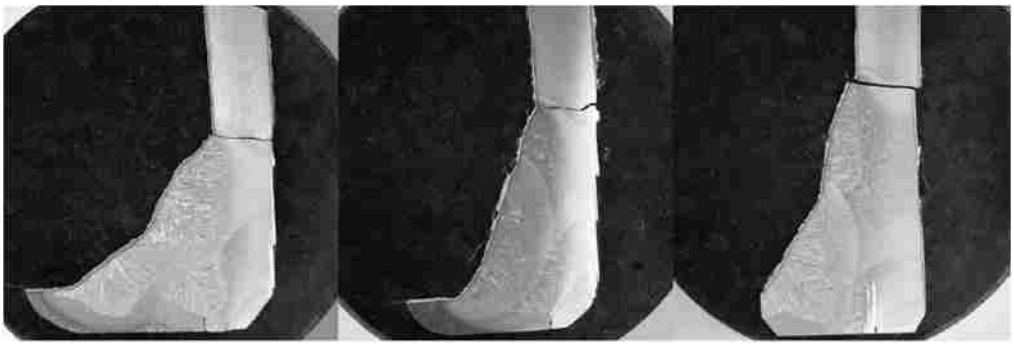

(a) *(b)* *(c)*

Figure 104. Type I specimen mast arm weld profiles: *a*, Specimen I-1; *b*, Specimen I-2; *c*, Specimen I-3.

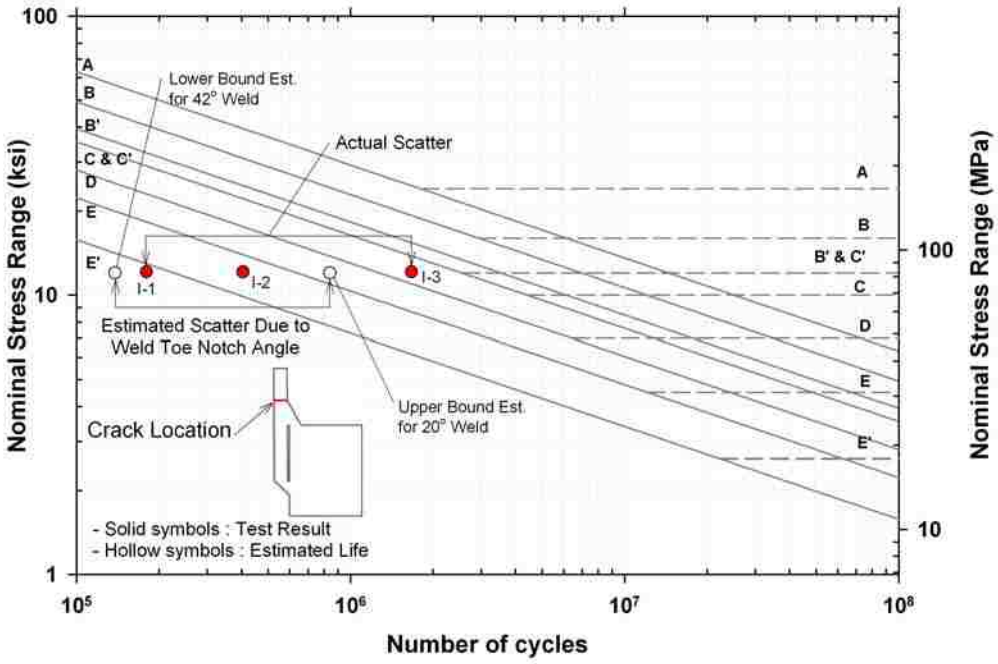

Figure 105. Effect of weld angle, Type I specimens

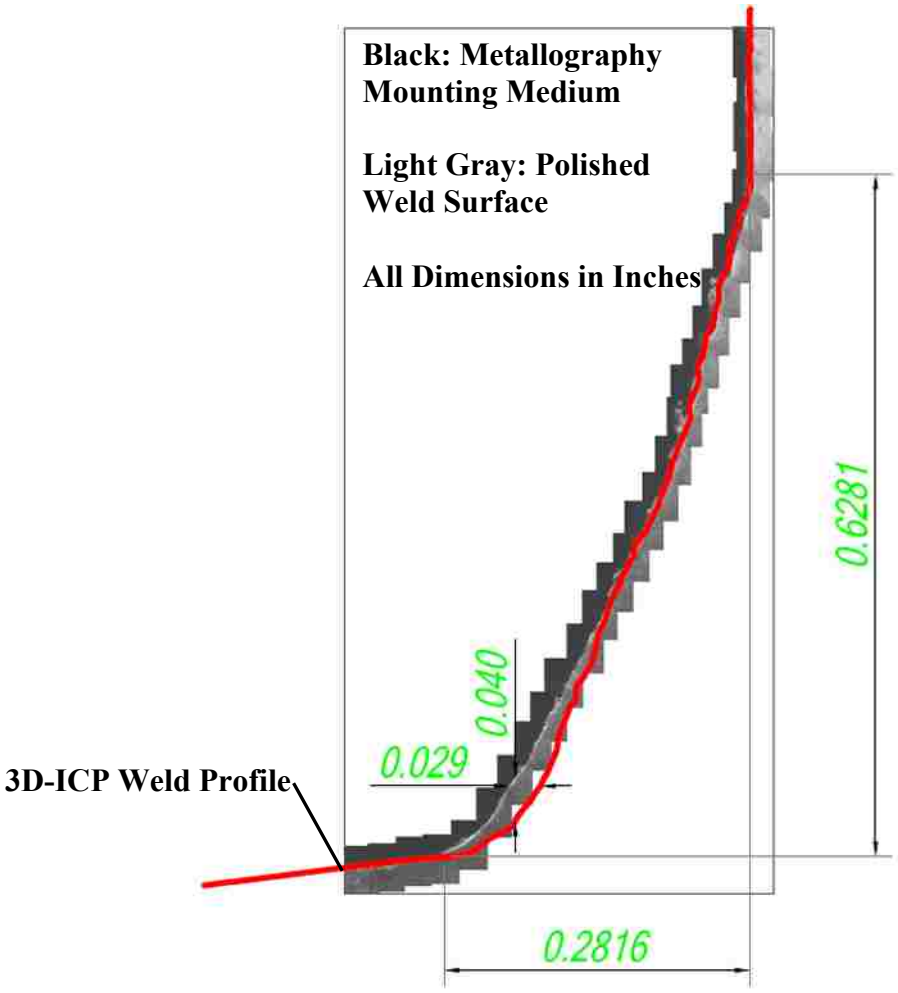

Figure 106. 3D-ICP weld profile over a cross section of same location captured through visual microscopy

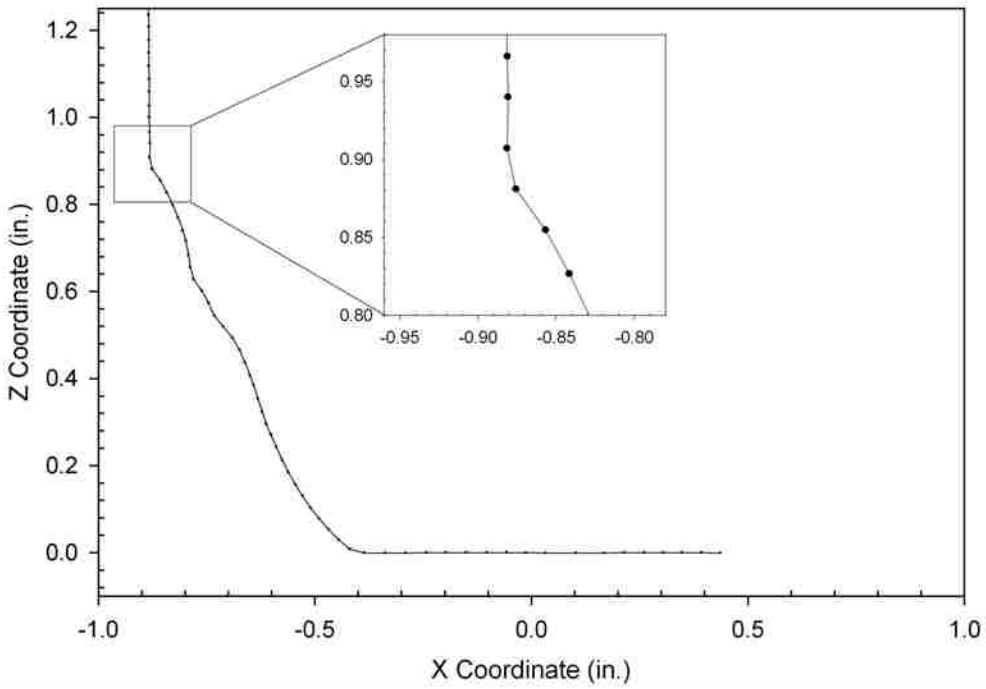

Figure 107. Specimen XI-1 weld profile obtained through 3D-ICP

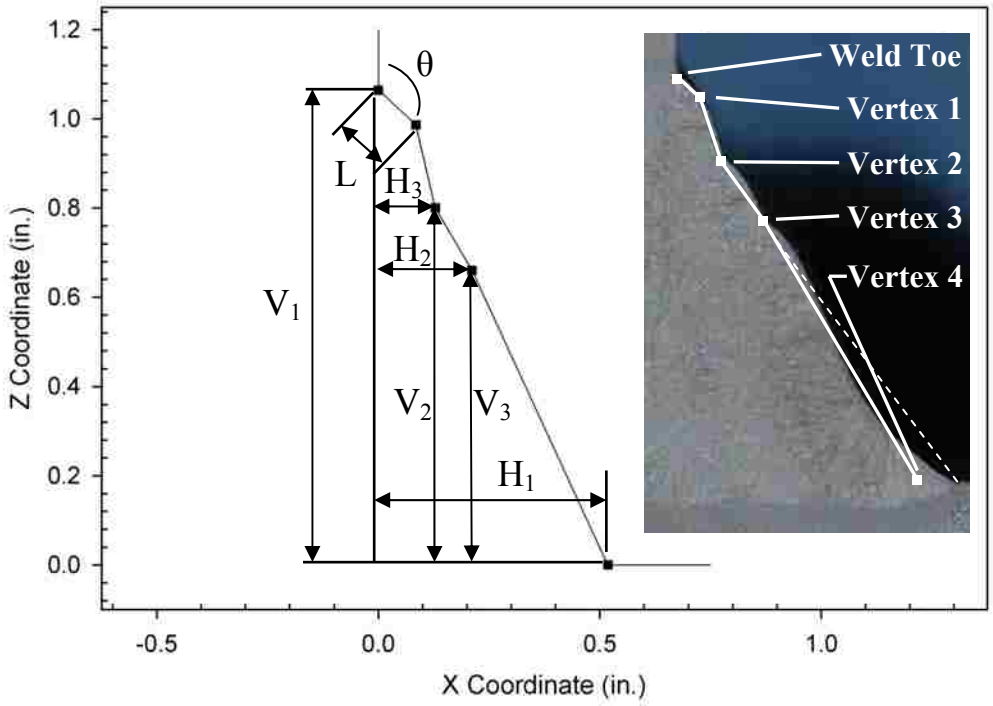

Figure 108. Weld dimension parameters. Inset shows weld idealization over typical weld profile.

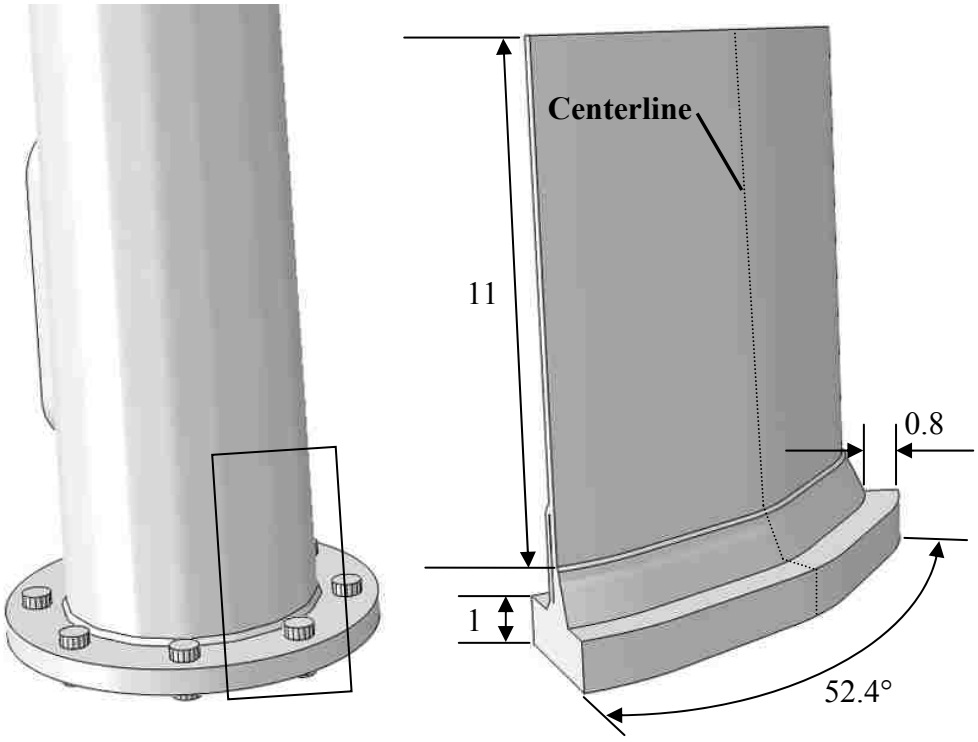

Figure 109. Submodeling: *a*, Region shown on global FEA model; *b*, Submodel dimensions (inches).

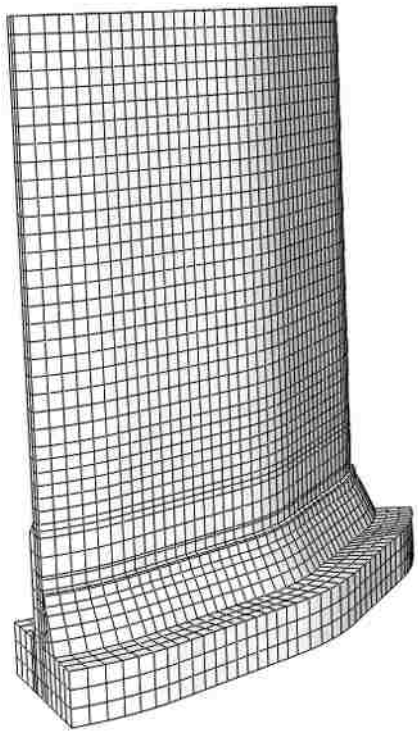

Figure 110. Submodel finite element mesh for geometric stress method

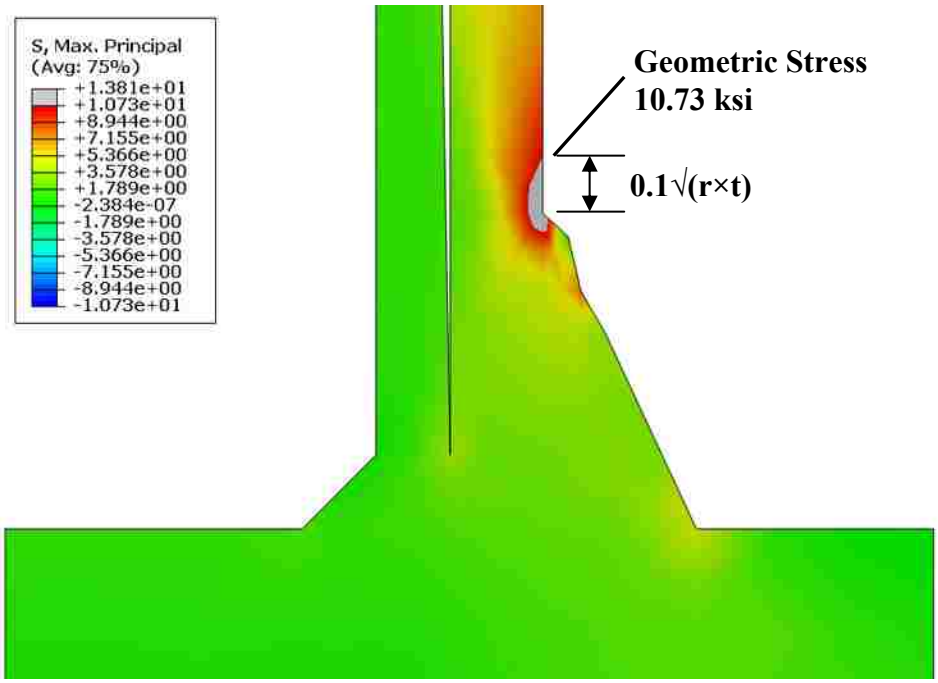

Figure 111. Geometric stress result for worst-considered weld geometry

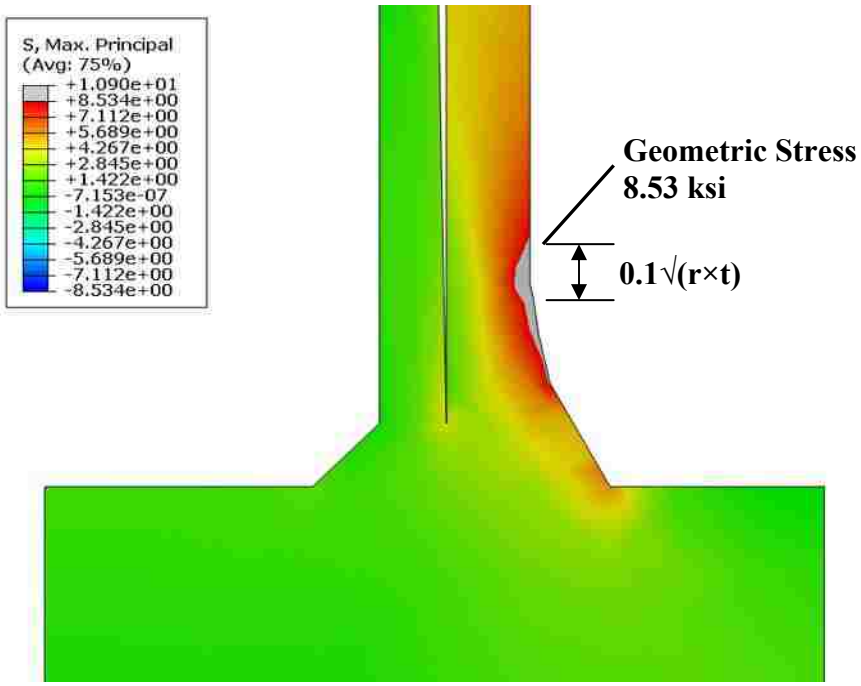

Figure 112. Geometric stress result for best-considered weld geometry

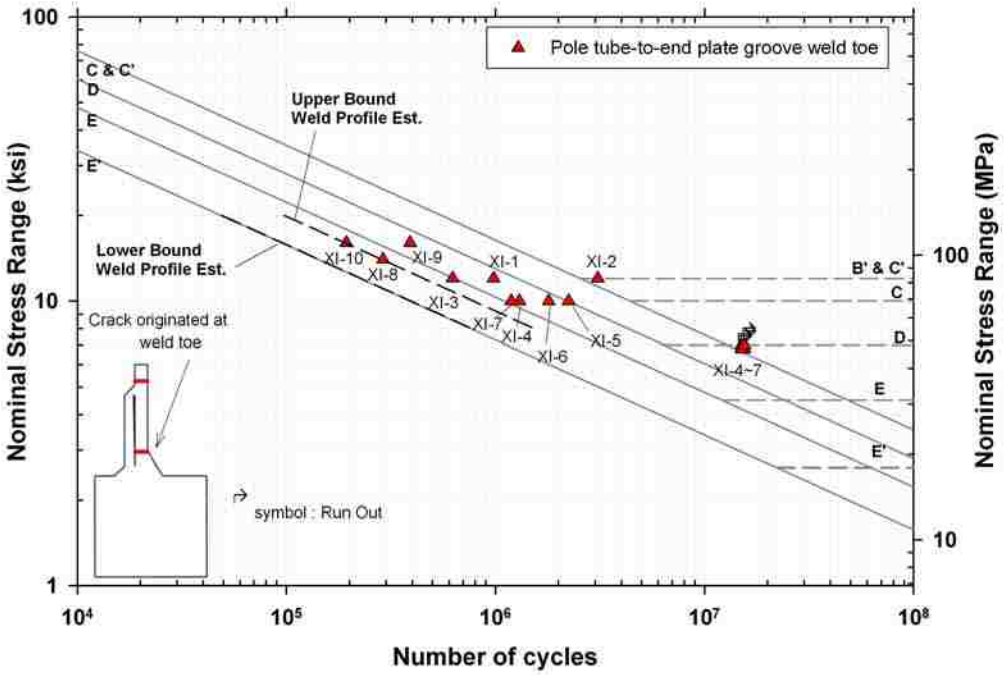

Figure 113. Upper and lower bound estimates of fatigue life based on weld geometry plotted with Type XI test results

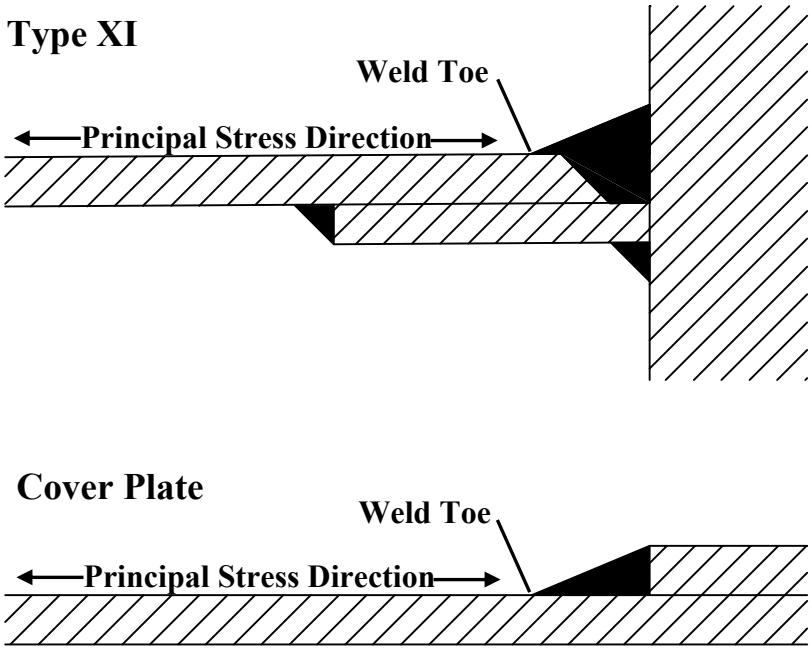

Figure 114. Comparison of Type XI welded connection and Category E cover plate connection.

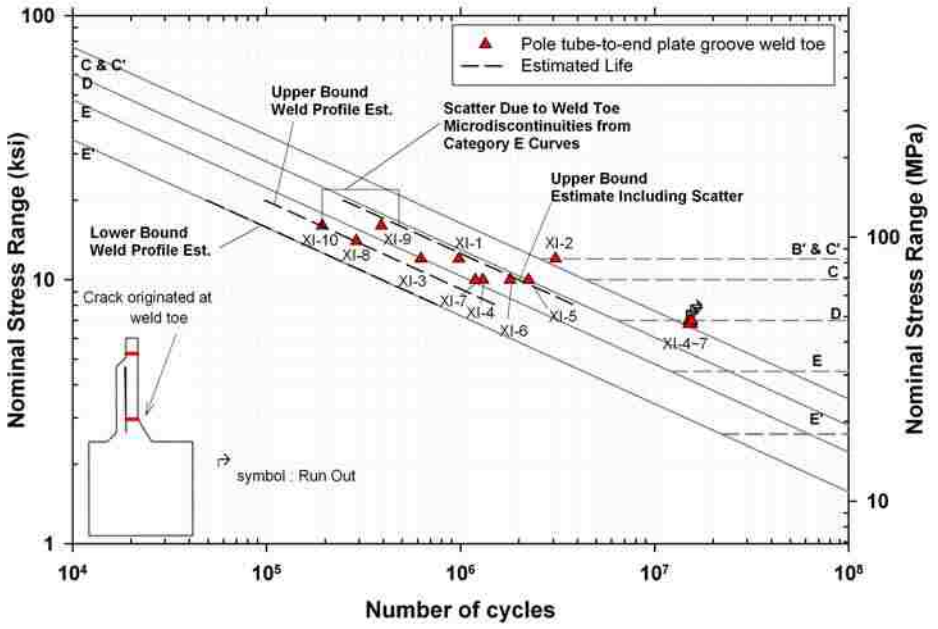

Figure 115. Category E scatter attributed to weld toe notch effects added to scatter attributed to variation in weld geometry, plotted with Type XI test results

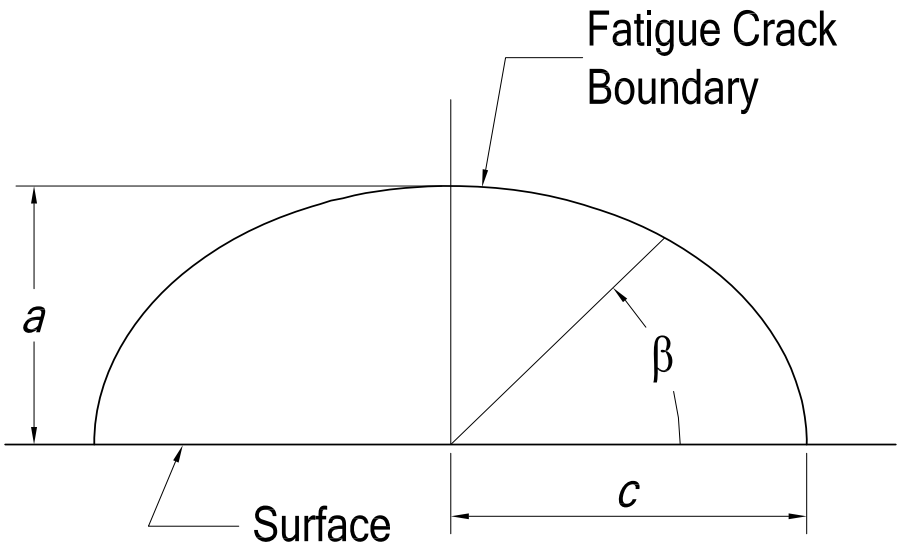

Figure 116. Variables used to calculate the complete elliptic integral of the second kind

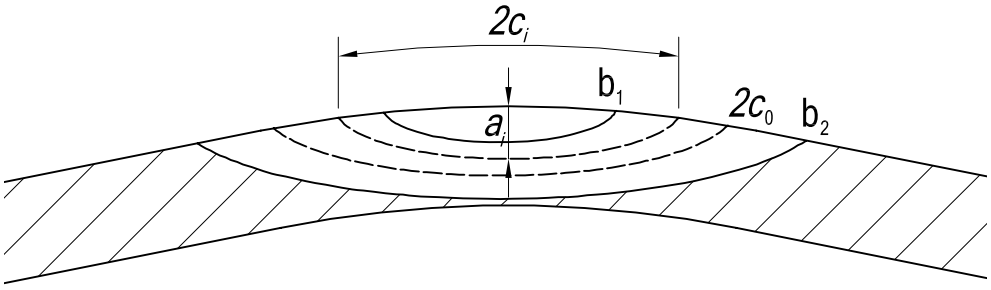

Figure 117. Labels used within crack propagation calculations

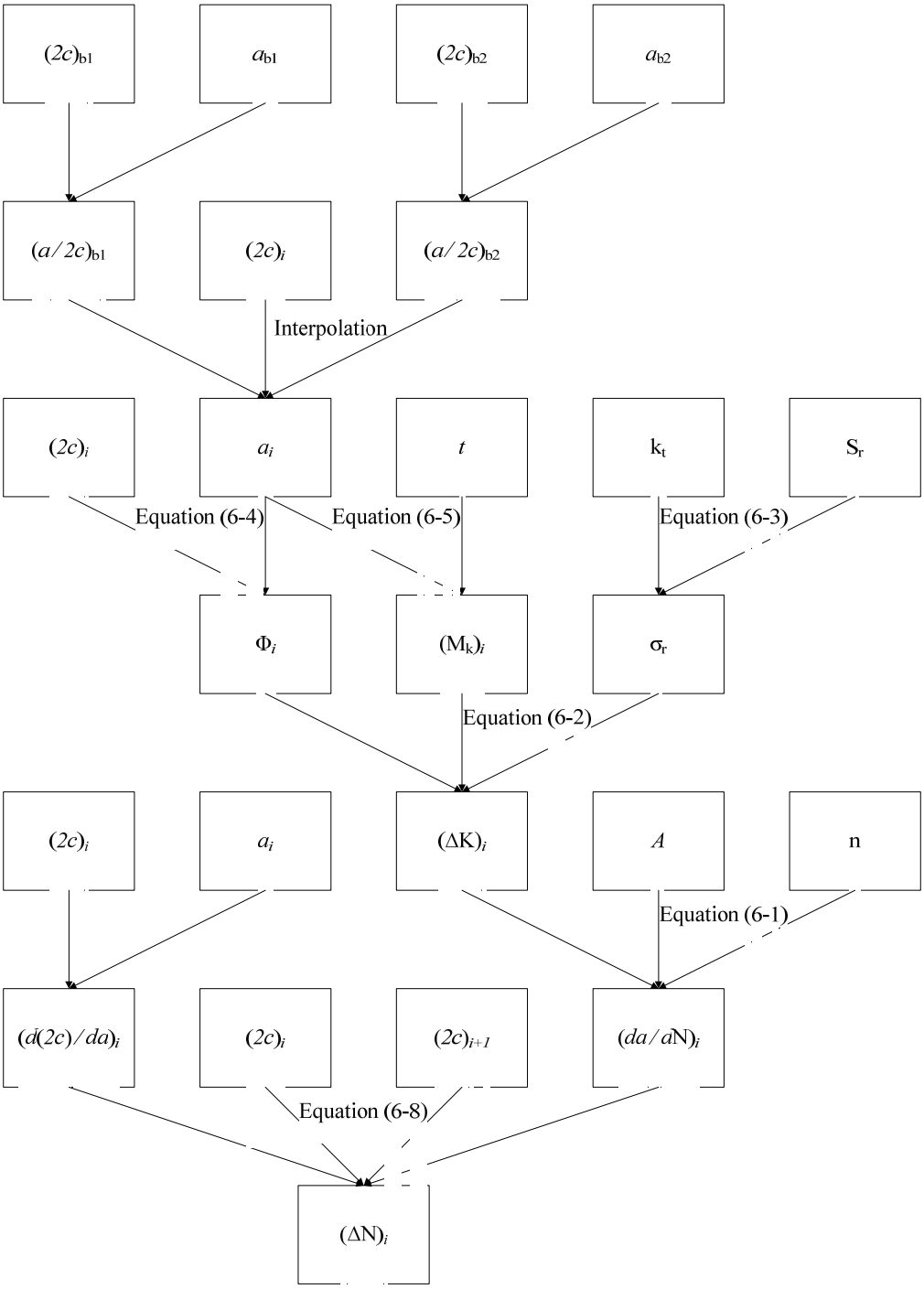

Figure 118. Flowchart of crack progression analysis

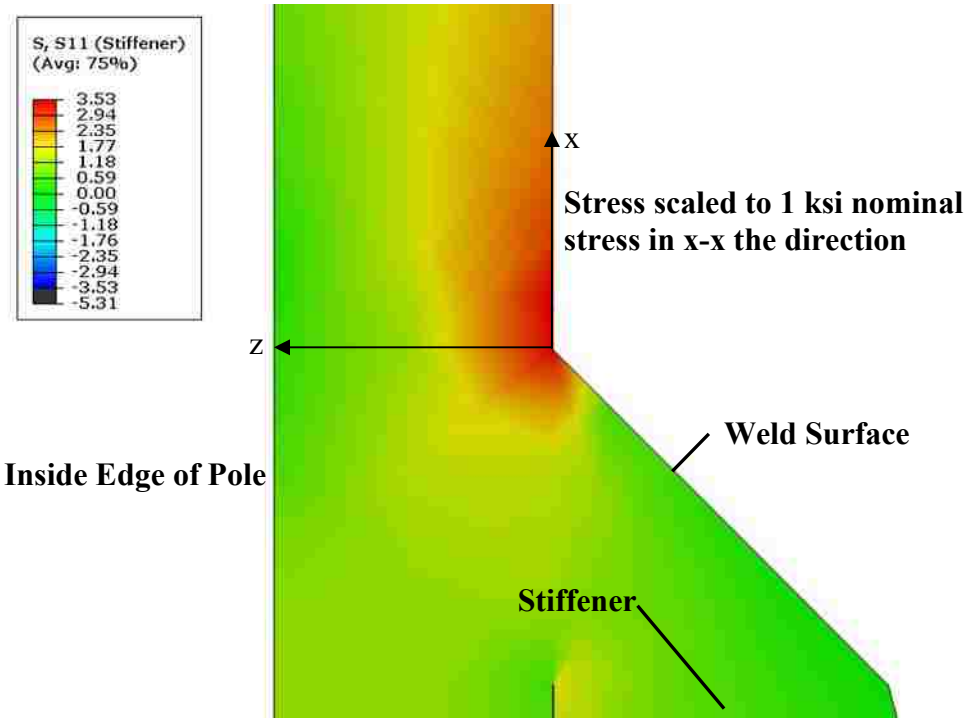

Figure 119. Type XII specimen stress concentration factor through thickness. *From analysis by Mr. Yeun Chul Park.*

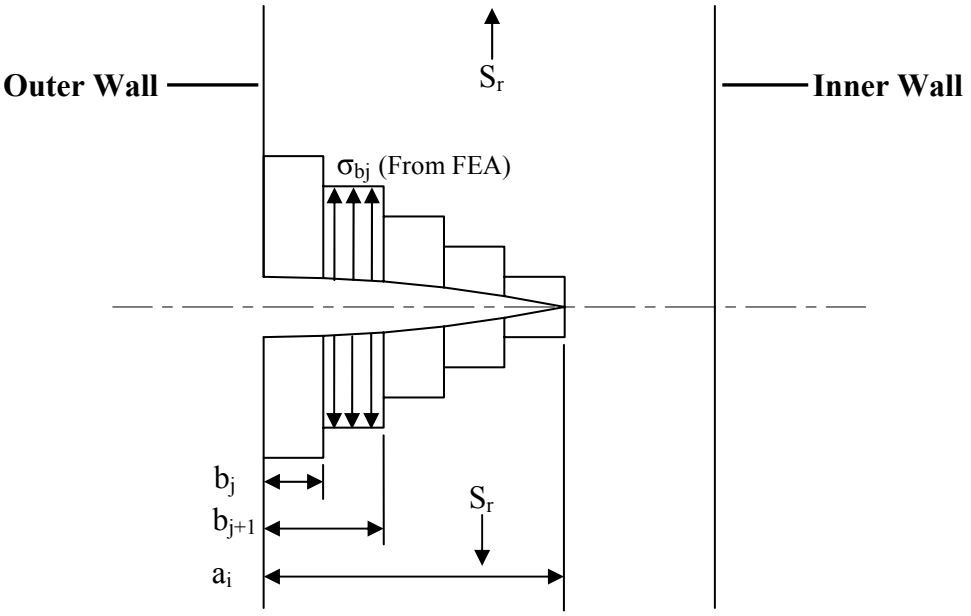

Figure 120. Variables used for calculating the geometry correction factor using Method 2

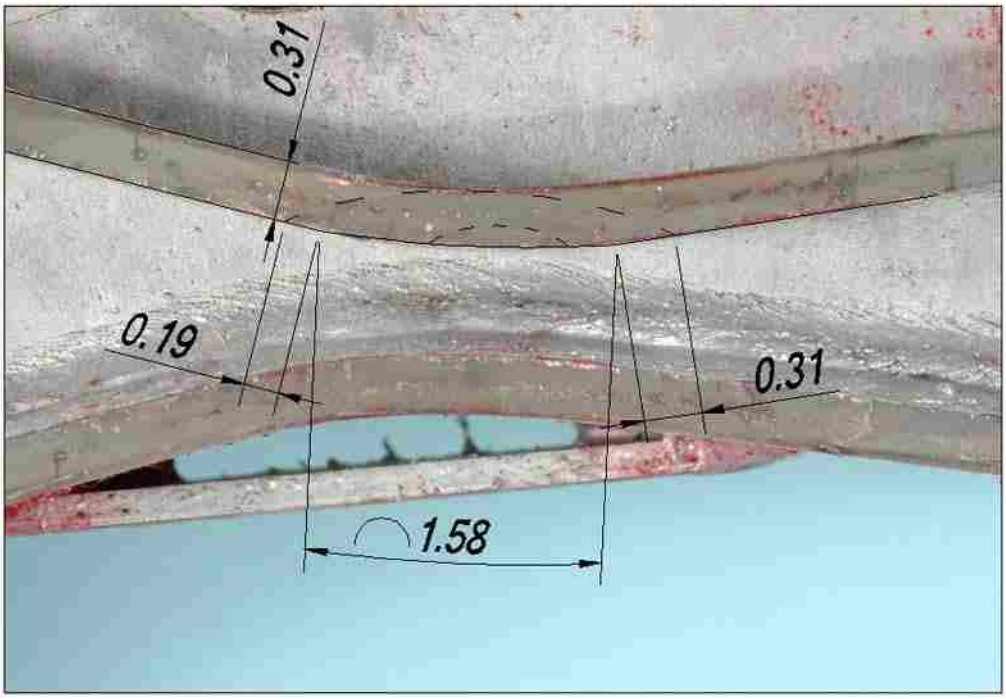

Figure 121. Specimen X-2 fracture surface with observed beach marks

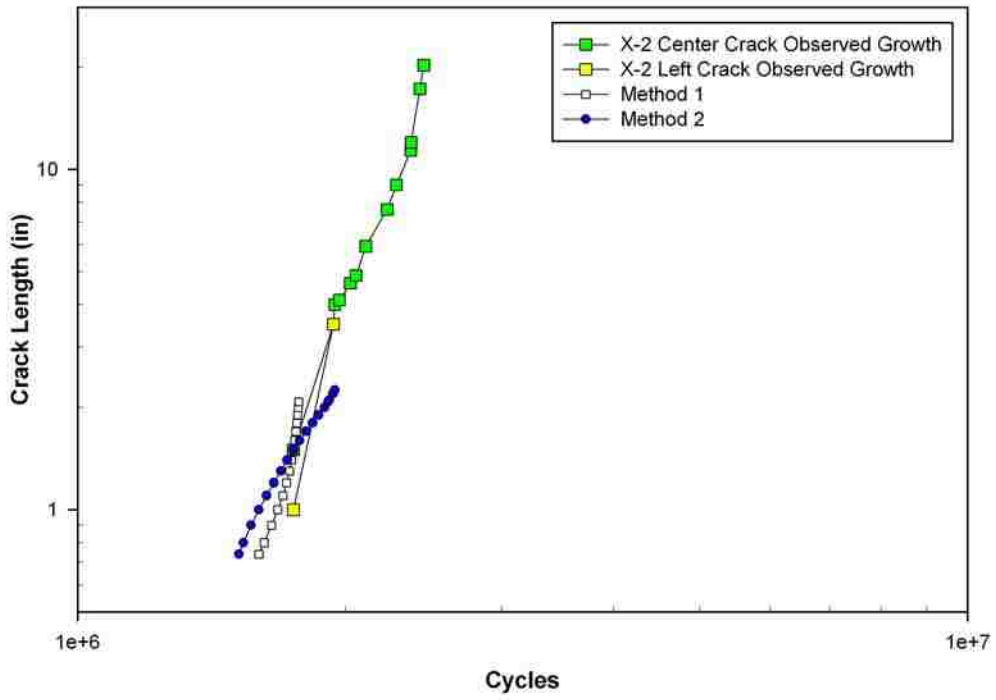

Figure 122. Specimen X-2 observed crack growth and estimated crack growth

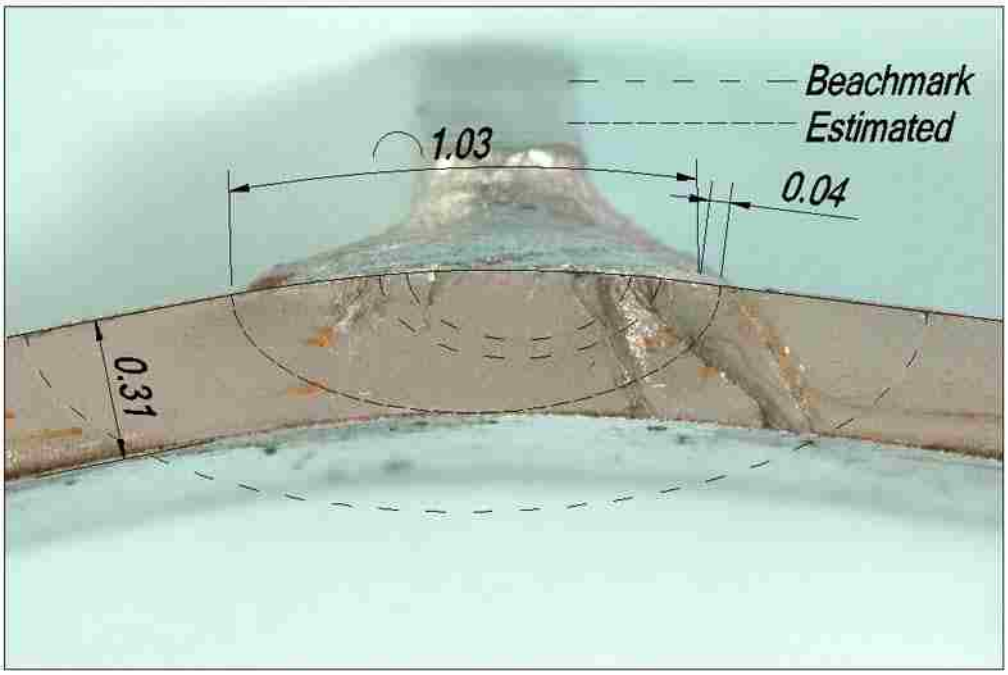

Figure 123. Specimen XII-2 fracture surface with observed beach marks

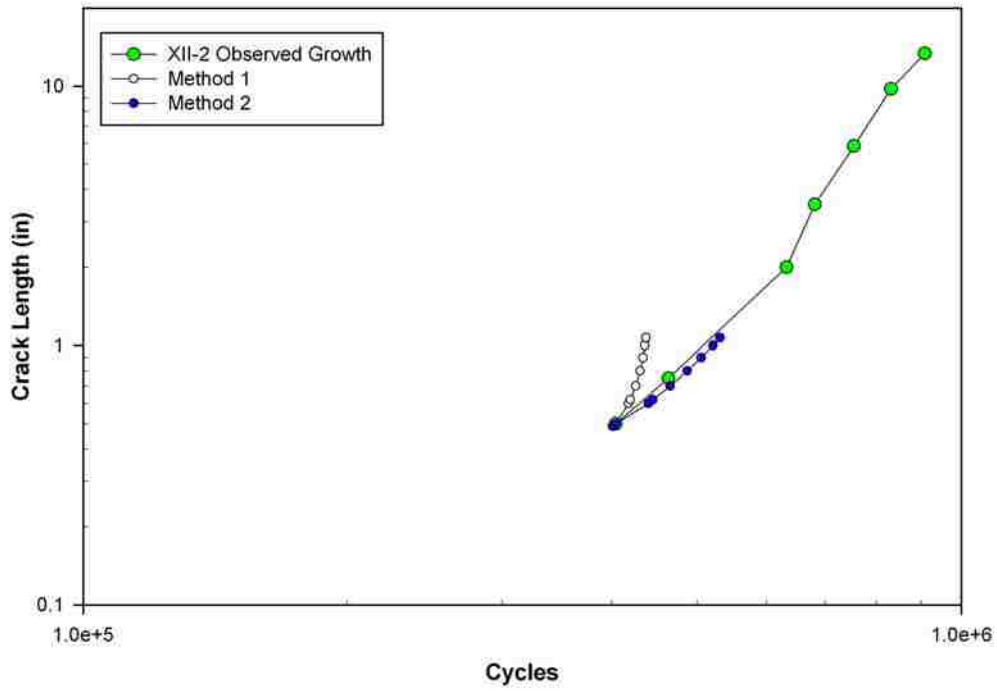

Figure 124. Specimen XII-2 observed crack growth and estimated crack growth

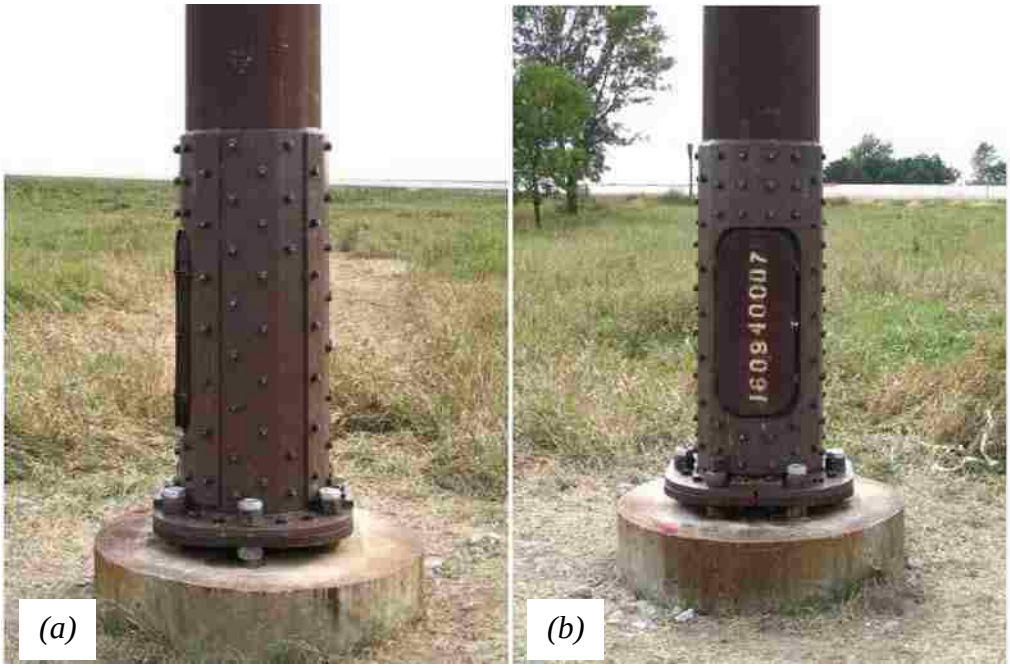

Figure 125. Iowa DOT retrofit jacket: *a*, side view; *b*, front view. *(reprinted from Koob, 2006)*

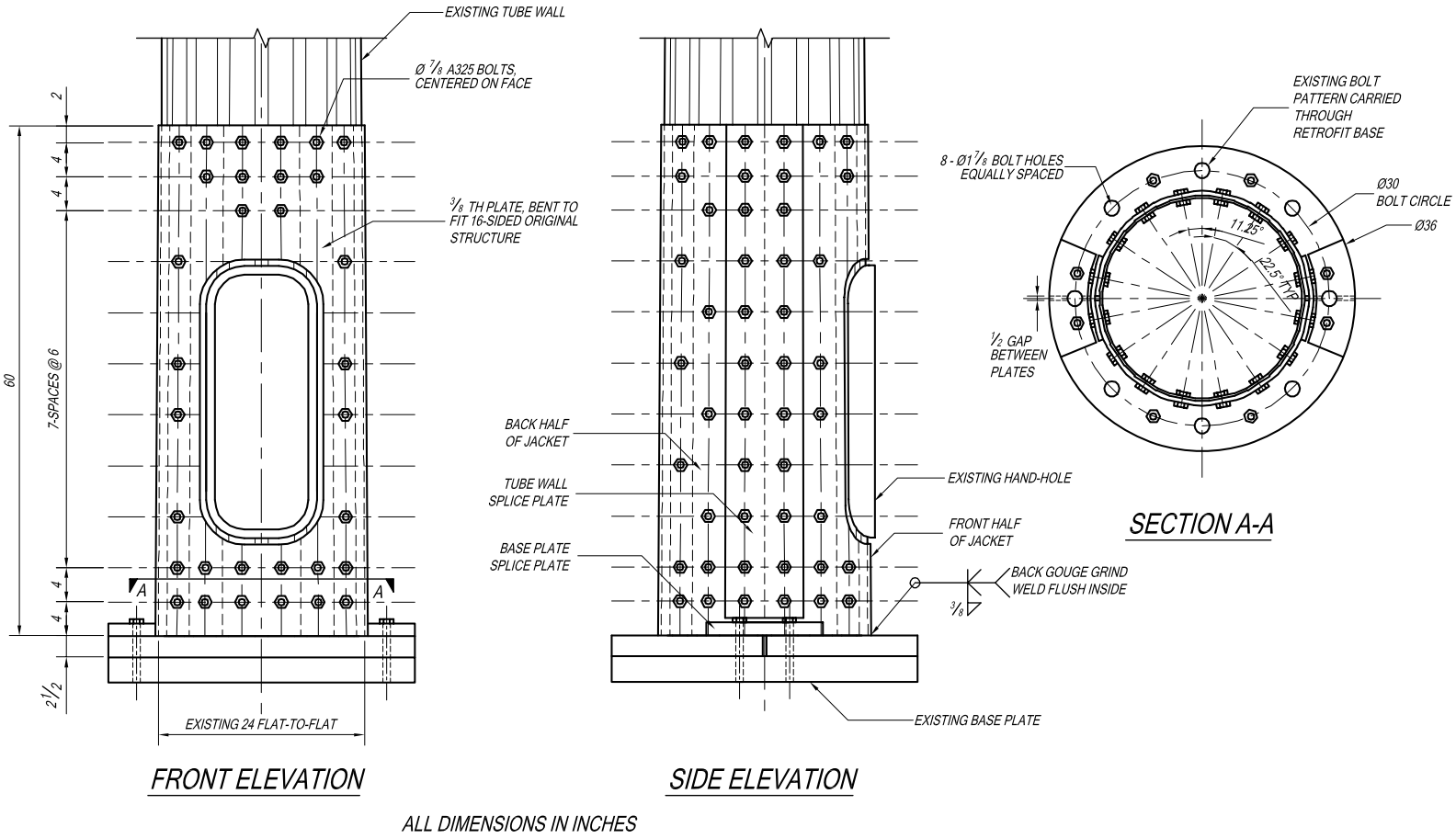

Figure 126. Retrofit jacket for use with cracked test specimens

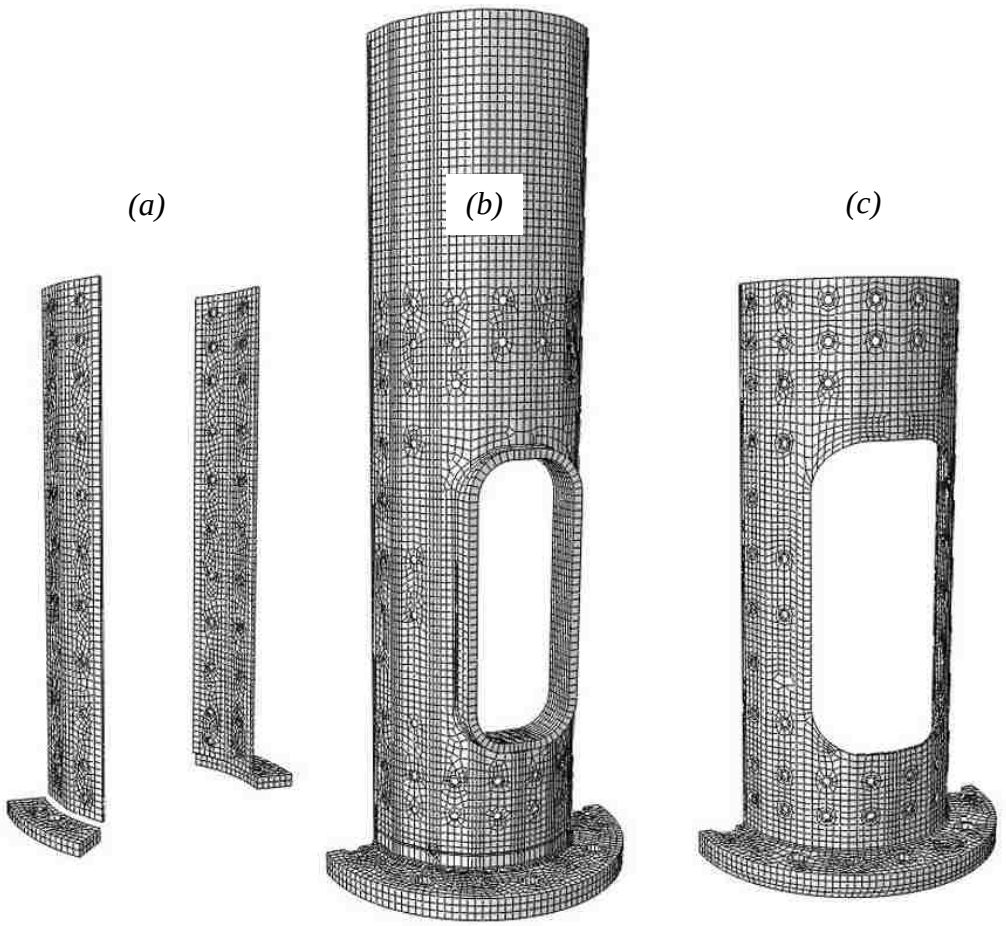

Figure 127. Front side exploded view of Model 1: *a*, splice plates; *b*, retrofitted pole; *c*, retrofit jacket.

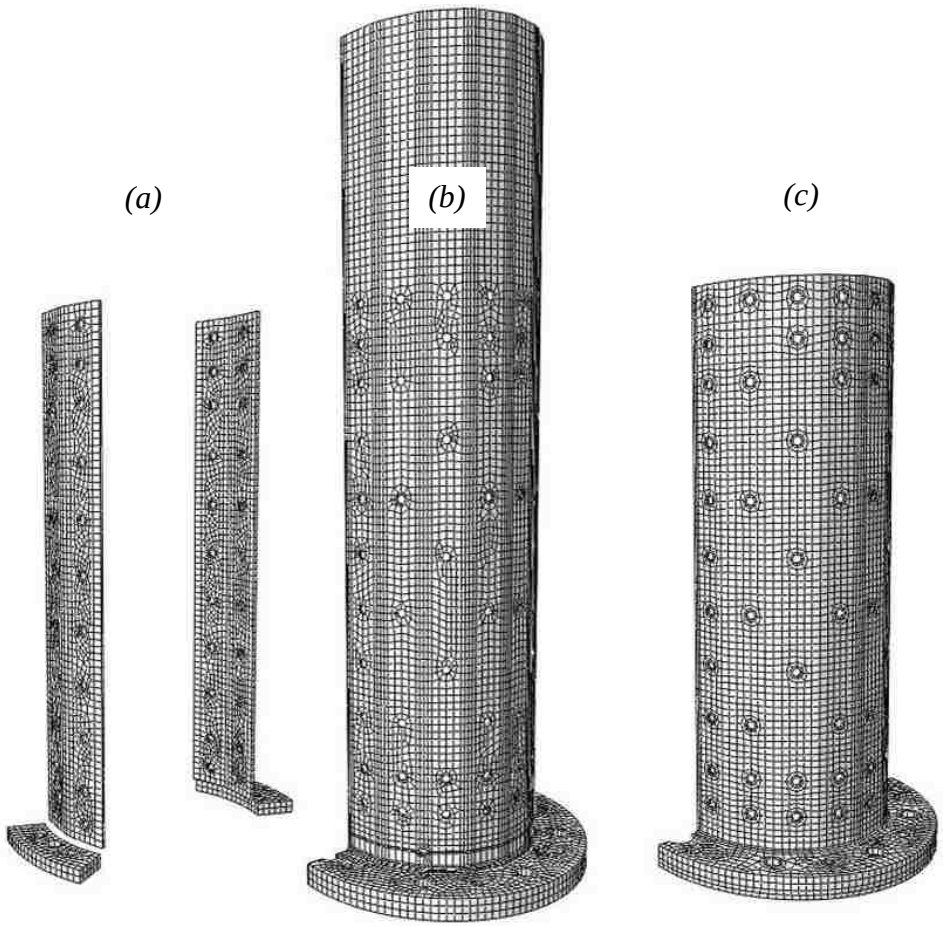

Figure 128. Back side exploded view of Model 2: *a*, splice plates; *b*, retrofitted pole; *c*, retrofit jacket.

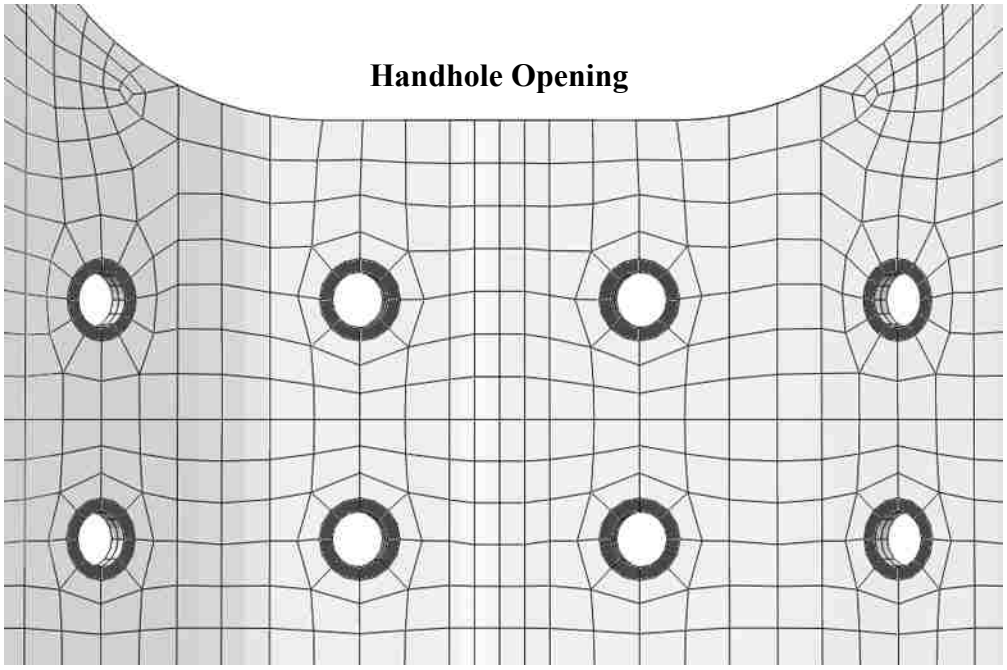

Figure 129. Model 1 interior surface of jacket

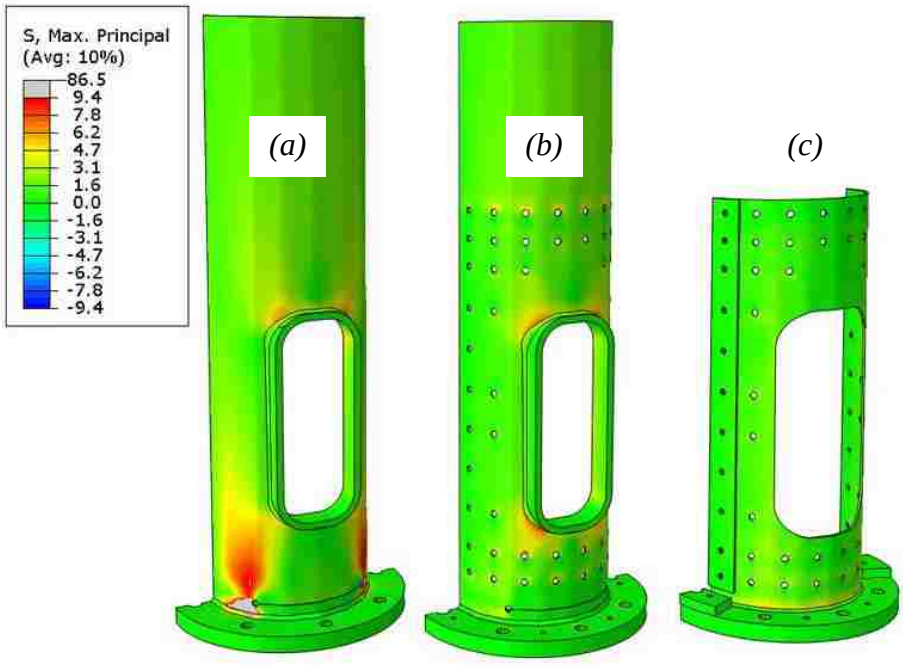

Figure 130. Retrofit jacket FEA comparison, handhole side: *a*, cracked pole without jacket; *b*, retrofitted pole; *c*, retrofit jacket.

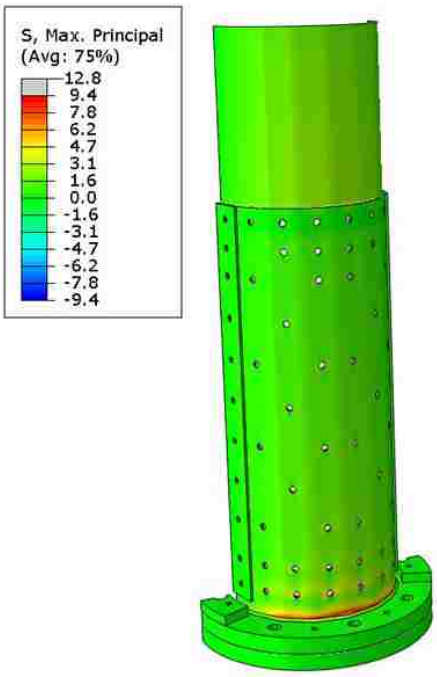

Figure 131. Model 1 FEA results

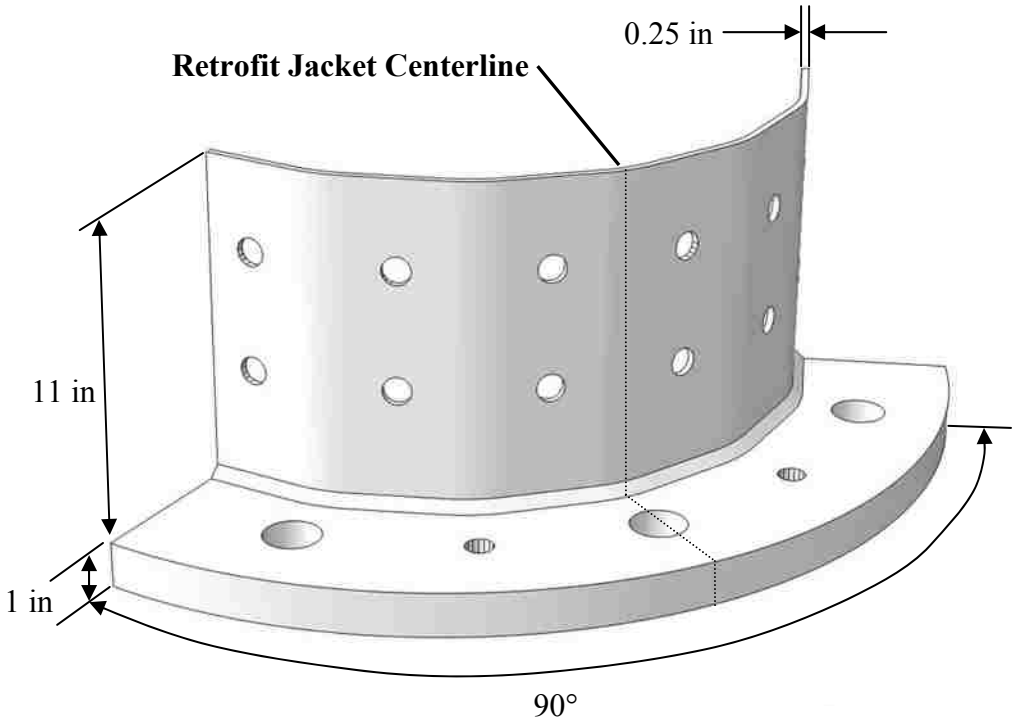

Figure 132. Model 2 dimensions

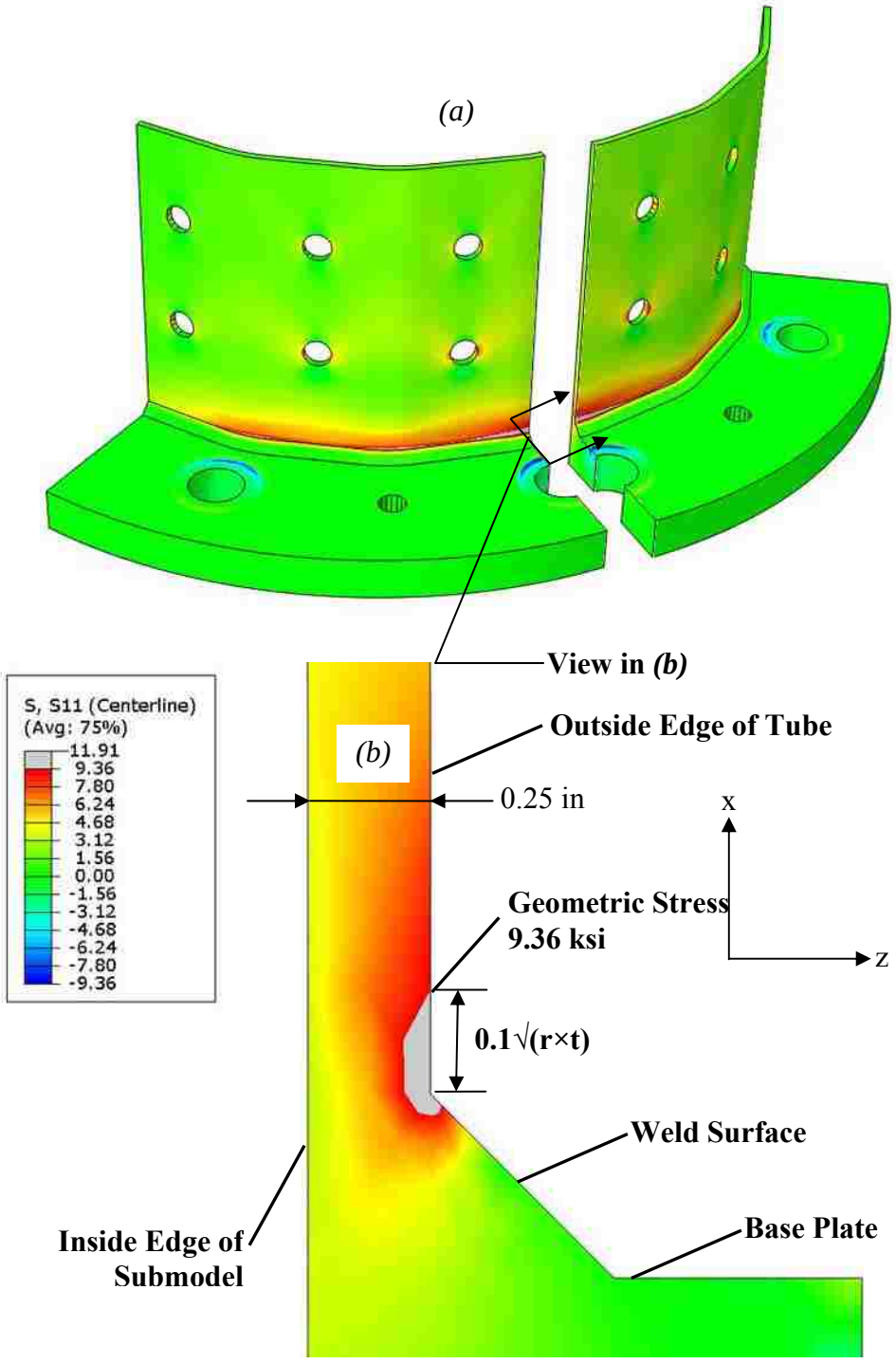

Figure 133. Model 2 results: *a*, exploded at centerline; *b*, stress profile through thickness.

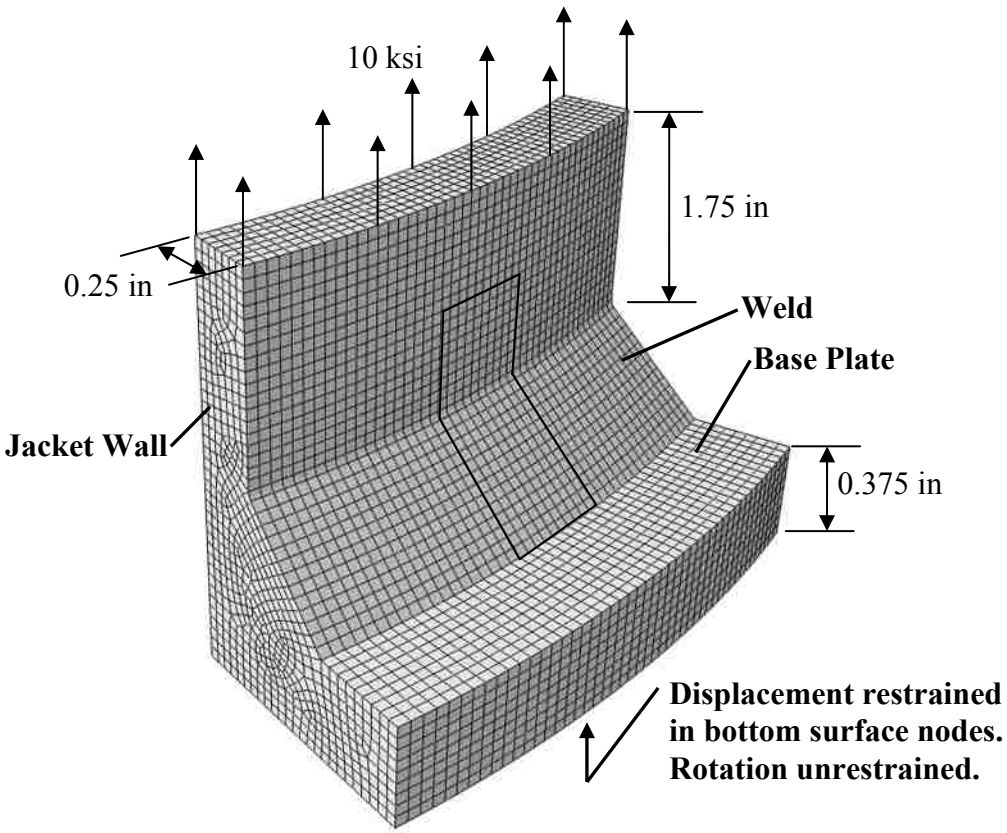

Figure 134. Model 3 dimensions. Extents of Model 4 highlighted on surface.

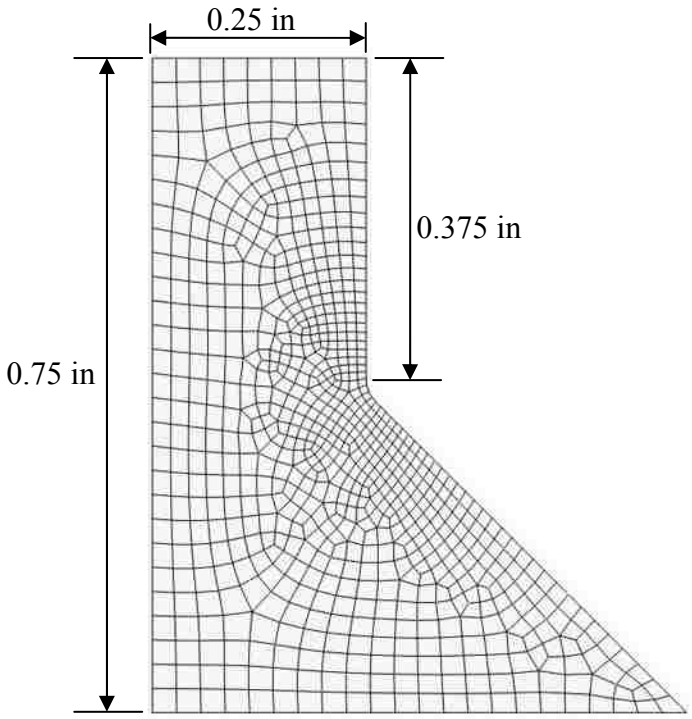

Figure 135. Cross-section of Model 4 showing salient dimensions and mesh

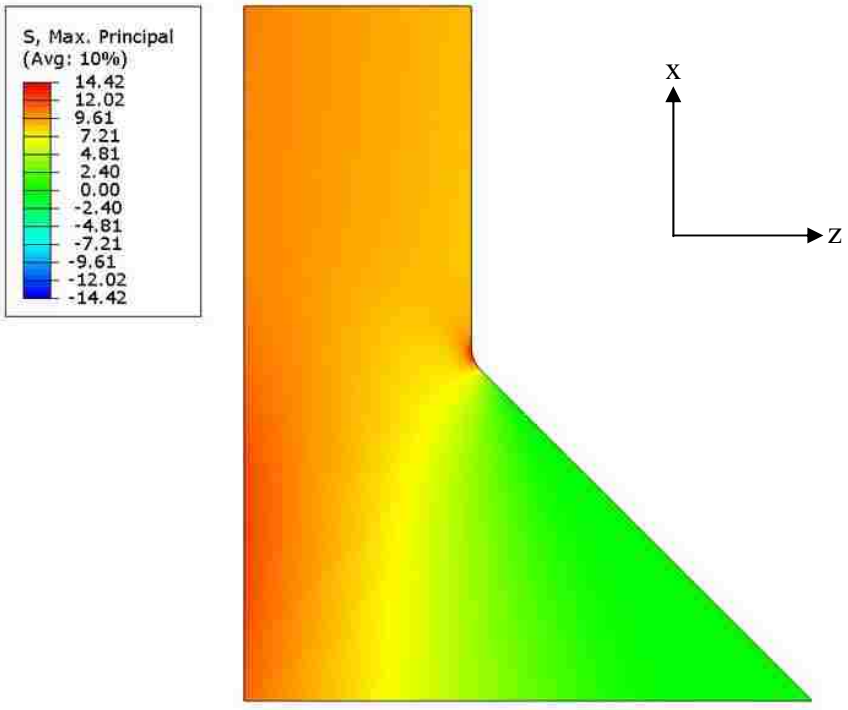

Figure 136. Cross-section of Model 4 results showing contour of maximum principal stress

Figure 137. Retrofit jacket ready for connection to Specimen XI-9

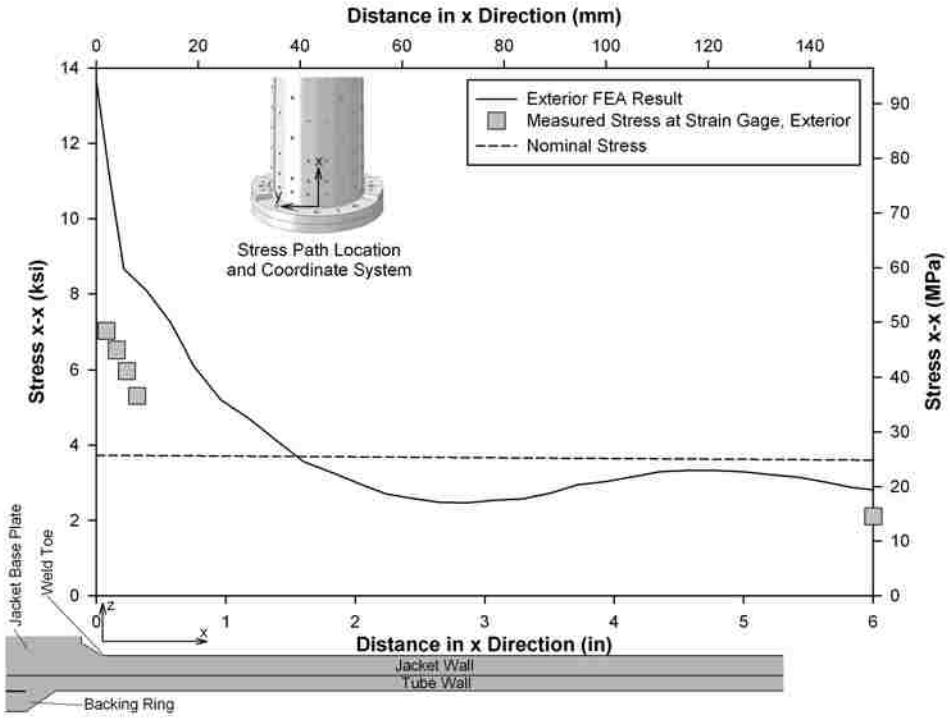

Figure 138. Stress profile in specimen JRXI above jacket base opposite to the handhole, in the loading plane

REFERENCES

AASHTO. (2009). *AASHTO Standard Specifications for Structural Supports for Highway Signs, Luminaires, and Traffic Signals*. 5th ed. Washington, D.C.: American Association of State Highway and Transportation Officials.

Albrecht, P.A., and Yamada, K. (1977). "Rapid Calculation of Stress Intensity Factors." *Journal of the Structural Division* 103, no. 2: 377-389. ASCE.

Anderson, T.H. (2007). "Fatigue Life Investigation of Traffic Signal Mast-Arm Connection Details." Master's thesis, The University of Texas at Austin, Austin TX.

Bannantine, J.A., Comer, J.J., Handrock, J.L. (1990). *Fundamentals of Metal Fatigue Analysis*. Englewood Cliffs, NJ: Prentice-Hall.

Barsom, J.M., and Rolfe, S.T. (1987). *Fracture and Fatigue Control in Structures*. 2nd ed. Englewood Cliffs, NJ: Prentice-Hall.

Dexter, R.J., (2004). "Investigation of Cracking of High-mast Lighting Towers." Ames, IA: report prepared for Iowa DOT Office of Bridges and Structures.

DNV. (2005). *Recommended Practice DNV-RP-C203: Fatigue Design of Offshore Steel Structures*. Høvik, Norway: Det Norske Veritas.

Fisher, J.W., Frank, K.H., Hirt, M.A., and McNamee, B.M. (1970). *Effect of Weldments on the Fatigue Strength of Steel Beams*. NCHRP Report 102. Washington, D.C.: Highway Research Board.

Fisher, J.W., Slutter, R.G., Miki, C., (1981). *Fatigue Behavior of Steel Light Poles*. Report No. FHWA/CA/SD-81/82. Sacramento, CA: prepared for California Department of Transportation.

Kaczinski, M.R. et al. (1998). *Fatigue-Resistant Design of Cantilevered Signal, Sign, and Light Supports*. NCHRP Report 412. Washington, D.C.: Transportation Research Board.

Keating, P., and Fisher, J.W. (1986). *Evaluation of Fatigue Tests and Design Criteria on Welded Details.* NCHRP Report 286. Washington, D.C.: Transportation Research Board.

Koenigs, M.T. (2003). "Fatigue Resistance of Traffic Signal Mast-Arm Connection Details." Master's thesis, The University of Texas at Austin, Austin, TX.

Koob, M.J. (2006). "Base Connection Retrofits for High Mast Towers and Pole Luminaries." In *Proc. 1st Int. Conf. on Fatigue and Fracture in the Infrastructure*, August 6-9, Philadelphia, PA.

McGinnis, M.J. (2006). "Experimental and Numerical Development of the Core-Drilling Method for the Nondestructive Evaluation of In-situ Stresses in Concrete Structures." Doctoral dissertation, Lehigh University, Bethlehem, PA.

Ocel, J.M. (2006). "The Behavior of Thin Hollow Structural Section (HSS) to Plate Connections" Doctoral dissertation, The University of Minnesota, Minneapolis, MN.

Park, Y.C., S. Roy, R. Sause, and J. W. Fisher. (2009). "Fatigue Performance Evaluation of Full Penetration Tube-to-Base Plate Groove Welded Connections." In *Proc. 2nd Int. Conf. on Fatigue and Fracture in the Infrastructure*, July 26-29, Philadelphia, PA.

Peterson, R.E. (1945). "Relation Between Life Testing and Conventional Tests of Materials." *Bulletin ASTM*, no. 145.

Rios, C.A. (2007). "Fatigue Performance of Multi-Sided High-Mast Lighting Towers." Master's thesis, The University of Texas at Austin, Austin, TX.

Roy, S., J. W. Fisher, C. LaBarbera, R. Sause, E. J. Kaufmann, B. T. Yen, and S. P. Pessiki. (2006). "Interim Report: NCHRP Project 10-70." ATLSS Center, Lehigh University, Bethlehem, PA.

Roy, S. and Y. C. Park. (2007). "Quarterly Progress Report, April 2007 to July 2007: NCHRP Project 10-70." ATLSS Center, Lehigh University, Bethlehem, PA.

Roy, S., Y. C. Park, R. Sause, and J. W. Fisher. (2008). "Evaluating Fatigue Performance of Sign, Signal and Luminaire Structures." In *Proc. IABSE Annual Meetings and Congress*, Sept. 17-19, Chicago, IL.

Roy, S., Y. C. Park, R. Sause, and J. W. Fisher. (2009). "Fatigue Performance of Stiffened Tube-to-End Plate Socket Connections in High-mast Structures." In *Proc. 2nd Int. Conf. on Fatigue and Fracture in the Infrastructure*, July 26-29, Philadelphia, PA.

Roy, S., Y. C. Park, R. Sause, and J. W. Fisher. (2010). "Fatigue Performance of Groove Welded Tube-to-End Plate Connections in Highway Sign, Luminaire

and Traffic Signal Structures." In *Proc. TRB 89th Annual Meeting*, Jan. 10-14, Washington, D.C.

Roy, S., Y. C. Park, R. Sause, and J. W. Fisher. (2010). "Fatigue Resistance of Pole-to-Base Plate Connections in High Level Lighting Structures." In *Proc. ASCE Structures Congress*, May 12-14, Orlando, FL.

Roy, S., Y. C. Park, R. Sause, and J. W. Fisher. (2011). "Fatigue Performance of Stiffened Pole-to-Base Plate Socket Connections in High-mast Structures." *Journal of Structural Engineering*, Pending Publication. ASCE.

Roy, S., Y. C. Park, R. Sause, J. W. Fisher, and E. J. Kaufmann. (2011b). *Cost-Effective Connection Details for Highway Sign, Luminaire, and Traffic Signal Structures*. NCHRP Web-Only Document 176. ATLSS Center, Lehigh University, Bethlehem, PA.

SAE. (1968). *Fatigue Design Handbook*. vol. 4. Warrendale, PA: Society of Automotive Engineers.

Schmidt, T. (2009). "3D ARAMIS Sensitivity, Accuracy and Data Validity Considerations." Internal Corporate Reference Document. West Conshohocken, PA: Trilion Quality Systems LLC.

Simulia. (2008). *ABAQUS/Analysis User's Manual, Version 6.8*. Providence, RI, USA: Simulia Corp.

Stam, A. P. (2009). "Fatigue Performance of Base Plate Connections Used in High Mast Lighting Towers." Master's thesis, The University of Texas at Austin, Austin, TX.

Warpinski, M. K. (2006). "The Effect of Base Connection Geometry on the Fatigue Performance of Welded Socket Connections in Multi-sided High-mast Lighting Towers." Master's thesis. Lehigh University, Bethlehem, PA.

APPENDIX A OBSERVED CRACK LENGTHS DURING FATIGUE TESTING

The following tables are the crack length observations recorded during fatigue testing. The corner of the cross-section directly underneath and centered with the actuator is corner 1. The corner directly to the right of corner 1 when facing the pole is corner 2. The numbers progress counter-clockwise up to corner 16. Corners 1 and 9 are in the loading plane. Faces on the surface are designated by the two corners at their ends. When a crack initiated on a face, the corner closest to the initiation point is the first corner identified in the name of the face. For example, a crack at Face 9-8 indicates the crack was first observed on the side opposite the actuator, between the corner at the loading plane and the next adjacent corner to its left, closest to the corner at the loading plane. All cracks are at the exterior base weld toe on the tube wall unless otherwise noted. All crack lengths presented are in inches.

Table A-1 Crack length observations specimen X-1

Specimen X-1	
Cycles	Crack at Face 10-9
1,376,091	1.500
1,426,236	2.250
1,497,196	3.000
1,522,206	3.250
1,551,434	4.125
1,577,980	5.375
1,645,974	8.000
1,714,952	12.000
1,740,399	14.250
1,772,589	17.000

Table A-2. Crack length observations specimen X-2

Specimen X-2		
Cycles	Crack at Face 9-10	Crack at Face 9-8
1,748,172	1.500	1.000
1,938,821	3.500	3.500
1,944,783	4.000	Joined 9-10
1,969,470	4.125	
2,025,342	4.625	
2,055,540	4.875	
2,108,193	5.938	
2,227,110	7.625	
2,281,807	9.000	
2,367,905	11.375	
2,369,883	12.000	
2,424,337	17.250	
2,449,490	20.250	

Table A-3. Crack length observations specimen X-3

Specimen X-3		
Cycles	Crack at Face 1-2	Crack at Face 9-8
678,075	3.875	
708,831	4.688	0.500
732,392	4.875	1.000
764,596	5.000	1.000
846,177	8.750	1.000
874,208	9.250	1.000
899,198	10.000	1.000
927,573	11.000	2.125
951,203	12.250	3.000
980,318	14.375	3.000
1,007,389	17.000	3.000

Table A-4. Crack length observations specimen XI-1

	Specimen XI-1			
Cycles	Crack at Face 9-8	Crack at Face 9-10	Crack at Corner 9	Backing Ring Corner 9
748,572	5.000			
784,605	6.000	1.750		
844,036	6.250	2.125		
879,027	6.688	2.563		
913,090	6.875	2.375		
935,337	7.625	2.375	0.875	
981,114	8.000	3.375	0.875	
1,009,230	8.438	3.375	0.875	
1,053,690	13.750	13.750	13.750	
1,128,252	Joined 9-10	16.0625	Joined 9-10	12.25

Table A-5. Crack length observations specimen XI-2

	Specimen XI-2	
Cycles	Crack at Corner 2	Backing Ring Face 1-2
1,556,363	2.375	
1,737,180	2.500	
1,812,070	2.938	
2,034,883	4.250	
2,161,810	4.500	
2,247,105	5.438	
2,311,048	5.813	
2,465,865	6.063	
2,502,179	6.938	
2,534,195	7.438	
2,690,058	8.188	
2,713,160	8.688	
2,760,105	9.000	
2,810,457	9.500	
2,835,655	9.875	
2,865,203	10.250	
3,006,320	11.625	
3,085,130	12.188	
3,134,212	12.438	4.375
3,159,690	12.813	4.375
3,182,067	13.063	5.750
3,261,590	13.688	6.313
3,333,714	14.500	6.750
3,405,600	14.500	7.750
3,433,740	14.750	12.500

Table A-6. Crack length observations specimen XI-3

	Specimen XI-3				
Cycles	Crack at Face 1-2	Crack at Face 8-9	Crack at Face 9-10	Crack at Corner 9	Backing Ring Corner 9
328,545	3.125	1.000	2.250		
367,888		1.000	2.563		
520,056	3.750	4.250	4.000		
546,190	8.375	4.250	4.000		
585,499					2.188
623,794	8.625	5.625	6.750	1.750	2.188
653,992	9.000	5.875	6.750	1.750	2.375
695,880	9.188	5.875	7.250	1.750	5.875
765,348	11.438	8.375	6.625	1.750	10.625

Table A-7. Crack length observations specimen XI-4

	Specimen XI-4					
Cycles	Crack at Face 9-8	Crack at Face 9-10	Crack at Face 10-11	Crack at Face 1-2	Crack at Face 16-1	Backing Ring Corner 9
649,048	0.125	1.75				
709,267	0.125	2.0625		1.375		
756,490	0.5	2.875				
825,548	0.5	3	2.325	1.75		
905,000				1.875		
964,350	0.5	3.8125	2.375	2.0625		
1,096,600	0.875	7.4375	7.4375	2.375		
1,193,555	3.5	8.25	Joined 9-10	2.625		
1,302,560	4	8.875		3		
1,359,090	13.5	13.5		3.375		
1,425,880	Joined 9-10	13.75		3.375		
1,471,453		14		3.375	0.5625	
1,531,640		14.5				
1,594,046		14.5		3.8125		1.125
1,627,750		14.75		3.8125	0.5625	3.875
1,665,360		15.25		4.25	0.5625	4.125
1,700,030		15.25		4.25	0.5625	4.5
1,742,631		15.5				2.5
1,803,521		16.125		5.3125	1.1875	3.375
1,859,450		16.375			1.4375	5.375
1,915,900		16.625			1.6875	7.125
1,947,574						8.375
1,973,845		17.25		6.75		
2,004,764		18.5		10.75	10.75	8.875
2,036,979		19		11.5625	Joined 1-2	9.1875
2,083,398		19.25				10.375
2,118,174		19.875				
2,143,170						12.75

Table A-8. Crack length observations specimen XI-5

	Specimen XI-5				
Cycles	Crack at Face 16-1	Crack at Face 1-2	Crack at Face 8-9	Crack at Face 9-10	Backing Ring Corner 9
682,584		0.625	1.063	0.813	
767,305		1.063	1.438	1.125	
829,000		1.250	1.563	1.438	
1,019,970		1.750	1.813	1.750	
1,056,970	1.000	1.750	2.188	2.000	
1,117,382	1.500	2.125	2.188	2.125	
1,225,525	1.500	2.125	2.438	2.125	
1,349,680	1.500	2.750	3.125	3.000	
1,414,820	1.625	2.750	3.125	3.125	
1,471,210	2.188	3.250	3.188	3.125	
1,515,899	2.188	3.438	3.438	3.125	
1,574,610	2.188	3.750	3.625	3.500	
1,637,823	2.313	4.500	3.875	3.500	
1,708,460	8.313	8.313	4.000	3.625	
1,785,960	Joined 1-2	8.313	4.625	3.750	3.563
1,846,755		9.188	4.625	4.125	3.563
1,902,465		9.188	5.000	4.375	3.563
2,049,015		10.813	6.000	4.625	3.563
2,080,426		11.188	6.625	4.938	3.563
2,170,920		11.563	6.625	4.938	3.563
2,240,583		12.563	12.750	12.750	3.563
2,290,800		12.563	13.500	Joined 8-9	3.563
2,351,800		13.000	13.500		3.563
2,408,481		13.000	13.500		4.375
2,473,597		13.375	13.500		4.375
2,522,190		13.688	13.875		4.375
2,603,530		14.375	14.250		4.375
2,615,186		14.375	14.250		6.250
2,734,625		15.125	15.375		6.250
2,798,570		15.625	15.375		6.250
2,864,958					12.750

Table A-9. Crack length observations specimen XI-6

	Specimen XI-6						
Cycles	Crack at Face 8-9	Crack at Face 9-10	Crack at Face 16-1	Crack at Face 1-16	Crack at Face 1-2	Backing Ring Face 8-9	Backing Ring Corner 1
544,675	0.875						
608,790	1.500						
842,709	2.813			0.188	0.750		
892,915	3.500		0.563	0.188	0.750		
962,809	4.250						
1,014,153	4.250		0.563	0.500	1.000		
1,065,809	4.750	0.500	0.563	0.500	1.000		
1,174,495	5.750	0.500	0.563	3.625	3.625		
1,225,531	5.750	1.000	1.250	4.000	Joined 1-16		
1,290,759	5.750	1.000	6.500	6.500			
1,365,449	6.188	1.000	Joined 1-16	6.500			
1,425,103	6.500	1.000		7.000			
1,543,973	10.125	10.125		7.500			
1,639,733	11.000	Joined 8-9		8.000			
1,686,564	11.750			8.375			
1,750,623	11.750			9.250			
1,797,346	12.375			9.250			
1,869,019	12.375			9.875			
1,941,873	13.625			9.875			
1,982,377	13.625			10.188			
2,043,473	14.125			10.188			
2,121,004	14.250			10.188		1.125	
2,220,254	15.125			11.688		1.125	
2,285,152	15.500			12.563		3.750	1.500
2,368,179	16.000			12.938		7.500	3.188
2,426,263	16.625			13.438			
2,438,777	17.375			14.125			
2,508,909	20.000			24.500		15.500	4.875

Table A-10. Crack length observations specimen XI-7

	Specimen XI-7								
				Weld Throat		Backing	Backing	Backing	Backing
	Crack at	Crack at	Crack at	Crack at	Crack at	Ring	Ring	Ring	Ring Throat
Cycles	Face 8-7	Face 9-8	Face 9-10	Corner 9	Face 1-16	Face 9-10	Face 9-8	Face 8-9	Corner 9
504,176	1.125	1.500	1.500						
547,920	1.125	1.813	1.500						
590,935	1.125	2.250	1.500						
695,890	1.125	2.250	1.938						
772,280	1.125	3.188	1.938		2.063				
822,643	1.125	3.188	2.188		2.063				
894,288	1.125	3.188	2.563		2.063				
896,452	1.125	3.750	2.563		2.438				
954,851	1.125	3.938	2.563	1.188	2.625				
1,017,604	1.125	4.188	2.688	1.188	2.625				
1,065,082	1.125	4.688	2.688	1.188	3.063				
1,128,960	7.625	7.625	2.938	1.188	3.375				
1,190,170	Joined 9-8	7.625	3.500	1.188	3.625				
1,292,790		8.063	3.688	1.188	5.688				
1,361,659		8.063	3.688	1.188	6.188				
1,412,339		13.375	13.375		6.375				
1,452,993		13.375	Joined 9-8		6.938	1.000	0.688	0.750	
1,524,583		13.625			7.125	1.000	0.688	2.000	
1,575,181		14.125			7.625	1.000	0.688	2.000	
1,632,623		15.500			7.813	1.000	0.688	2.000	5.875
1,674,999		15.500			8.188	1.000	0.688	2.000	5.875
1,742,736		19.500			8.875	1.000	0.688	2.000	5.875
1,793,142		21.188			9.375				13.250

Table A-11. Crack length observations specimen XI-8

	Specimen XI-8							
					Backing	Backing	Backing	Backing
	Crack at	Crack at	Crack at	Crack at	Ring	Ring	Ring Throat	Ring Base
Cycles	Face 9-8	Face 9-10	Face 1-16	Face 1-2	Face 9-10	Face 9-8	Corner 8	Corner 9
103,404		0.500		0.625				
183,775	1.500	1.750	1.500	2.000				
214,090	4.375	3.125	5.000	5.000				
233,926	9.000	9.000	Joined 1-2	5.000				
289,913	12.250	Joined 9-8		7.750				
325,630	12.500			8.000				
354,656	13.000			8.000				
360,873	13.875			8.500				
390,950	16.125			8.500	2.750	0.750		
443,697	17.250			9.250	2.750	0.750		
468,512	17.750			9.250	7.563	7.563	5.625	4.750
488,196	19.125			9.875		Joined 9-10		
506,822					9.875		9.500	7.875
528,909	22.375			9.875	21.500		21.500	

Table A-12. Crack length observations specimen XI-9

	Specimen XI-9					
			Weld Throat			Backing
Cycles	Crack at Face 8-9	Crack at Face 9-10	Crack at Corner 9	Crack at Face 16-1	Crack at Face 1-2	Ring Corner 1
140,481	1.875	0.625		2.500	2.750	
183,988	2.625	2.000		3.125	3.000	
202,435	3.000	2.000		3.125	3.000	
250,052	3.000	2.000		7.563	7.563	
299,344	3.313	2.313		8.688	Joined 16-1	
390,335	5.000	3.625	1.250	13.063		
453,433	5.875	4.375	1.250	14.500		
550,855	7.125	5.750	1.250	17.375		
603,162	17.063	17.063		19.000		25.750
	Joined 9-10					

Table A-13. Crack length observations specimen XI-10

		Specimen XI-10			
Cycles	Crack at Corner 1	Crack at Face 8-9	Crack at Face 9-10	Backing Ring Corner 1	Backing Ring Seam Corner 1
60,947	2.250				
113,513	7.500				
126,976	10.875				
148,889	11.125	2.750			
164,839	11.375	3.625			
193,475	12.000	3.625	0.500		
208,735	12.375	4.625	0.500		
237,633	13.750	4.625	0.500		
260,783	13.750	4.625	1.250		
305,755	14.750	4.625	2.250		
325,143	15.125	4.625	2.250		
328,127	16.313	6.000	6.125	12.875	3.938

Table A-14. Crack length observations specimen XII-1

	Specimen XII-1		
Cycles	Stiffener Crack at Corner 1	Base Crack at Corner 16	Stiffener Crack at Corner 9
229,080	0.500		
256,598	0.938		
315,710	1.125		
383,299	1.375	0.750	
529,197	3.875	2.938	1.500
575,711	5.375	2.938	2.000
662,577	9.375	4.000	4.250
719,600	11.813	4.313	5.875
787,241	14.250	4.625	8.125

Table A-15. Crack length observations specimen XII-2

	Specimen XII-2	
Cycles	Stiffener Crack at Corner 1	Stiffener Crack at Corner 9
404,206	1.000	0.500
463,905	1.188	0.750
632,040	1.375	2.000
680,907	2.125	3.500
754,341	3.875	5.875
831,611	6.125	9.750
908,560	9.000	13.375

Table A-16. Crack length observations specimen XII-3

Specimen XII-3	
Cycles	Stiffener Crack at Corner 9
577,080	1.000
713,228	1.625
802,870	3.188
862,096	4.625
1,000,000	10.125
1,056,157	12.875

Table A-17. Crack length observations specimen XII-4

Specimen XII-4	
Cycles	Stiffener Crack at Corner 1
611,019	0.250
756,550	0.688
829,320	1.063
1,025,840	1.500
1,107,544	2.000
1,177,742	3.000
1,250,580	4.250
1,303,070	5.375
1,454,950	8.625
1,528,596	10.500
1,586,342	11.875
1,654,860	13.188
1,727,783	14.000
1,850,890	15.750
1,946,251	18.750
1,983,406	20.875
2,013,186	24.000
2,065,460	28.375
2,104,600	30.750
2,146,270	32.750
2,205,670	34.500
2,276,900	37.813
2,311,226	40.750

Table A-18. Crack length observations specimen XII-5

Specimen XII-5	
Cycles	Stiffener Crack at Corner 1
4,685,342	1.125
5,183,800	1.438
5,380,750	1.688
5,447,028	2.000
5,544,185	2.750
5,602,470	3.438
5,692,382	5.000
5,838,480	8.375
5,884,354	9.875
6,034,300	11.822
6,119,292	13.375

Table A-19. Crack length observations specimen XII-6

Specimen XII-6	
Cycles	Weld Root Crack at Corner 9
4,059,074	0.625
4,128,520	0.875
4,733,100	1.313
4,853,015	1.563
5,023,710	1.750
5,170,897	2.375
5,385,500	3.313
5,507,750	4.438
5,586,270	5.375
5,678,660	7.250
5,816,203	11.000
5,943,147	15.125

Table A-20. Crack length observations specimen XII-7

Specimen XII-7	
Cycles	Stiffener Crack at Corner 9
6,927,169	1.125
7,248,856	1.500
7,328,694	1.813
7,416,234	2.375
7,498,674	3.000
7,540,845	4.125
7,783,125	8.250
7,889,589	9.875
7,983,334	12.000

Table A-21. Crack length observations specimen XII-8

	Specimen XII-8					
Cycles	Stiffener Crack at Corner 1	Base Crack at Corner 16	Base Crack at Corner 2	Stiffener Crack at Corner 9	Base Crack at Corner 8	Base Crack at Corner 10
47,904		2.188		0.750		
88,780		2.750		0.750	2.563	
145,290	0.938	4.000		1.063	3.563	
225,148	1.750	5.375		2.000	5.375	
300,433	4.375	6.500	2.000	4.000	6.375	2.625
319,346	5.250	6.500	2.000	4.625	7.000	2.625
355,800	7.125	6.500	2.000	7.375	7.000	2.625
419,431	11.125	6.500	2.000	10.125	7.000	2.625
485,124	15.750	7.188	3.563	14.188	8.063	2.625

Table A-22. Crack length observations specimen XII-9

	Specimen XII-9	
Cycles	Stiffener Crack at Corner 1	Stiffener Crack at Corner 9
202,605	0.250	
204,863	0.875	
257,408	1.625	
298,290	3.375	
379,452	5.688	1.000
394,929	9.938	1.375
429,607	12.625	2.188

Table A-23. Crack length observations specimen XII-10

	Specimen XII-10		
Cycles	Stiffener Crack at Corner 1	Base Crack at Corner 16	Stiffener Crack at Corner 9
51,690	0.625		
53,181	1.125		
105,543	1.500		1.125
146,570	1.500		1.375
171,856	1.750		2.375
206,941	2.875		3.750
272,038	5.875	1.375	6.375
328,790	9.125	1.750	9.250
469,177	16.750	1.750	18.500

APPENDIX B 3D-ICP BACKGROUND

Three-dimensional image correlation photogrammetry (3D-ICP) is a non-contact optical measurement technique that combines the principles of photogrammetry with an image correlation algorithm to generate the displacement field at discrete points. 3D-ICP was investigated as a possible alternative to strain gages for measuring the stresses along the surface of a structure.

Stereo photogrammetry is the technique by which measurements in a third dimension are made by superimposing a pair of two-dimensional photographs. The known relative orientation of two digital cameras is used to produce a three-dimensional space in which the coordinates of points can be determined. To begin the process, the two cameras capture digital images of the target surface. A given point on the surface will be shown in each digital image, and the two-dimensional coordinates in each digital image are determined for the point. These coordinates are used to create an imaginary line extending from each camera lens to the target surface, intersecting at the given point. By triangulating these two lines, the three-dimensional coordinates of the given point are determined. This is repeated over the entire surface to form a point cloud. The superimposed digital photographs generate a discretized pixilated view of the target surface. Multiple pictures are taken of the same surface at different load steps in order to create displacement information by comparing the position of points at each load step. Strain data is derived from this displacement data.

B.1 Equipment

The hardware utilized for these measurements consisted of two digital cameras rigidly mounted to a common bar, connected to a computer. The system used was an ARAMIS 2M system, manufactured by Gesellschaft für Optische Messtechnik (GOM) of Braunschweig, Germany and marketed in the United States by Trilion Quality Systems. The ARAMIS system is comprised of the hardware and software. The 2M designation refers to the resolution of each camera, 1600 by 1200 pixels, which is approximately 2 megapixels. Figure B-1 is a photograph of the assembled equipment. A collection of calibration tiles are available to calibrate the system for differently sized measurement areas and desired resolutions. The calibration tiles consist of a matte black ceramic tile, on which is printed an array of white circular shapes. The ARAMIS software was utilized for calibration, capturing images, and post-processing.

B.2 Calibration

A calibration process, involving the calibration tiles, was required before each measurement session. The calibration process was used to define the three-dimensional space in which displacement of points on the target surface could be tracked. The calibration tile selected for the measurements on the poles was 55 mm (2.2 in) by 44 mm (1.7 in), as this provided the required measurement area with sufficient offset for preventing aberrations at the boundary from affecting the data in the area of interest. These boundary effects are detailed in Section B.8. Calibration involved taking multiple pictures of the calibration tile at various distances from the cameras and at

various tilts. By tracking the location of specific points on the calibration tile, a measurement volume was created.

B.3 Stochastic Pattern

To provide discrete points on the target surface for pattern recognition, a stochastic pattern was applied on the target surfaces using commercially available spray paints. Matte finish paints were used to avoid pattern recognition errors in the image correlation algorithms caused by glare on the target surface. To provide the highest possible contrast for pattern recognition, a pattern of black speckles was applied over a white base coat. The recommended speckle size should register between five and seven pixels when captured by the cameras. The suitable speckle sizing was achieved by trial and error using a freehand approach (pressing the nozzle of the paint can at different intensity), as stencils were not available in the required size.

B.4 Facets

The ARAMIS software divided the captured images into facets. The relevant terminology is illustrated in Figure B-2. A facet was a square group of pixels, the center of which in the three-dimensional space was considered as a computation point representing all of the pixels within the facet. The facets were defined by two measures, the facet size and the facet step. The facet size was defined as the number of pixels along a side of the facet. The facet step was the distance from one edge of one facet to the same edge of the adjacent facet. The accuracy of the measurement depends on the facet size. Too small of a facet size will generate errors at coarse spots in the

stochastic pattern where a facet is completely covered by a speckle. Too large of a facet size will fail to capture the detail of the surface. A smaller facet step will require more time to compute displacement and strain data, as more facets are created over the surface. The computer on which the calculations are made determines the practical limit for the facet step. A facet step which is too large will not capture local variations in strain. Depending upon the pattern size on the target surface the facet size and step were chosen for each measured area to limit the observed noise in the data.

B.5 Measurement

Once images of the target area were captured at the desired load steps, the displacements and strains were computed. Facets were defined on the image captured for the unloaded configuration, and image correlation algorithms were used to track the movement of those facets under load. The displacement at a computation point was calculated by differencing its coordinates from the initial load step to the load step of interest. The calculated strain is the engineering strain, the change in the gage length divided by the original gage length. The strains at a computation point are calculated by considering the displacements typically within a three facet by three facet square region. The calculated strains are for the center computation point. The distance between the outer computation points of this square is considered as the gage length. Adopting a gage length equal to the gage length of a conventional strain gage placed at the location of interest allowed direct comparison of strain measurements from 3D-ICP to conventional strain gage measurements. The gage length is calculated by the following equations:

$$\text{Gage Length (pixels)} = \text{Facet Step} \cdot (\text{Strain Length} - 1) \tag{B-1}$$

$$\text{Gage Length (in)} = \text{Gage Length (pixels)} \cdot \frac{\text{Field of View (in)}}{\text{Camera Linear Resolution (pixels)}} \tag{B-2}$$

The facet step and the strain length are both input by the user. The field of view is displayed in the calibration report, and is determined by the camera focal length and calibrated focal distance. The linear resolution of the camera is dependent on the hardware, which was 1600 pixels for the measurements discussed.

B.6 Filtering

Random variation of the speckle size in the pattern coupled with errors in image correlation can obscure the distribution of strains along the surface. To remedy this, data was filtered during post-processing. Figure B-3(a) is a contour plot of strains obtained from 3D-ICP measurements. Figure B-3(b) is the result of the same measurement after filtering the strain data during post-processing. The area shown is around a stiffener termination on the pole of specimen XII-3. The measurements were made when the pole was subjected to a 7 kip (31.1 kN) load that resulted in a nominal stress of 6.6 ksi (45.5 MPa) at the stiffener termination. The nominal stress was computed by dividing the applied moment at the section by the section modulus. The noise in the unfiltered plot obscured the distribution of strain on the target surface.

Three filtering methods are available: mean, median, and gradient. All methods

will be explained in terms of strain but are equally applicable to displacement. A square grid of computation points, with an odd number of computation points along the sides, was selected. The strain data compiled from these computation points provided the strain at the center computation point in the grid. The number of points that form the side of the grid is defined as the filter size.

In mean filtering, the center computation point is set equal to the mean value of strain at the computation points within the filter boundary. In median filtering, the center computation point is set equal to the median value of the strain at computation points within the filter boundary. Gradient filtering is a conditional mean filtering where computation points are excluded from filtering when the slope between adjacent points exceeds a maximum slope defined by the user.

In addition to the filter size, filtering was defined by the number of filtering passes. When the filtering algorithm was applied to each individual computation point and its surrounding grid, this constituted a filter pass. The second filter pass started with the resulting values from the first pass. The ARAMIS System documentation: Sensitivity, Accuracy and Data Validity Considerations (Schmidt 2009), recommended a minimum of three passes using a filter size of seven when determining strains. Two passes with a filter size of five were recommended for displacement.

A series of parametric studies were conducted to determine the effects of filter type, number of filter passes, and filter size on 3D-ICP measurements. The 3D-ICP results for specimen XII-2 were selected due to the relatively minimal amount of noise in the original data. Figure B-4, Figure B-5, and Figure B-6 progress from one filter

pass to three filter passes and compare the mean and median filters against the unfiltered results and measured values at strain gages. One filter pass was insufficient to reveal a conclusive pattern in the data. After two filter passes the median filter results showed plateaus in the plot, at 18.1 in (460 mm) and 18.4 in (467 mm) from the base weld toe. The lack of a smooth stress curve along the surface of a section in bending indicated that the noise in the original data was not fully filtered out. Of note, however, was the excellent correlation to the measured values at the strain gages for the mean filter results. The results after three filter passes showed a generally smooth variation in stress from the weld toe along the pole surface. Agreement with the measured values was still good, with the exception of the second strain gage. This indicated that three filter passes was sufficient to remove the prominence of noise in the results, at a slight expense of accuracy over an abrupt change in slope of stress versus distance within the stress field. Three filter passes were used in the subsequent parametric study of filter size.

Figure B-7, Figure B-8, and Figure B-9 show the effect of filter size on 3D-ICP results when using a median filter. The size 7 filter results showed noticeable plateaus that indicated this combination was not effectively capturing the behavior. The size 9 filter results generally followed the measurements at the four strain gages furthest from the weld toe. However, the filter algorithm was less effective at the weld toe, as over a high gradient at the edge of the measured area the median filter was unable to capture enough computation points with high stress results to affect the median value. The effect was even more pronounced for the size 11 filter results. The median filter did not

capture the change in slope between the strain gage adjacent to the weld toe and the third gage from the weld toe. The plotted results did not correlate with the measured strain values accordingly.

Figure B-10, Figure B-11, and Figure B-12 show the effect of filter size on 3D-ICP results when using a mean filter. The size 7 filter results displayed the highest stress result at the weld toe of any method with three filter passes. This showed the capability for capturing a localized stress concentration with 3D-ICP, however the quality of the results suffered over the remainder of the plot. The size 9 filter results displayed the best combination of correlation to the measured stress at the strain gages and a generally smooth plot. The size 9 filter did slightly flatten out the change in slope near the weld toe, and the 3D-ICP result is correspondingly higher compared to the measured stress at the second gage from the weld toe. The size 11 filter results indicated that the size 9 filter was a practical limit for 3D-ICP measurement at a weld toe. The larger filter size did not capture the change in slope near the weld toe and the results did not correlate to the measured stress at the strain gage adjacent to the weld toe. Based on these results, a size 9 filter with three filter passes was used for 3D-ICP results at other locations.

B.7 Masking

Strain masking is the technique by which computation points are intentionally excluded from displacement and strain calculations. Masked computation points do not affect the filtered results for surrounding computation points. Strain masking on the weld surface was needed due to the change in surface orientation between the pole wall

and the weld surface. Without masking, the filtering algorithm included points along the weld surface, which have a significantly lower stress in the direction of interest, along the pole exterior surface in the longitudinal direction. To illustrate the requirement for strain masking, Figure B-13 shows the stress along the pole exterior surface in the longitudinal direction, here labeled the x-x axis, of FEA at the weld toe. Also plotted on the figure are the measured stresses normal to the weld toe at a conventional 1 mm strip gage for reference. The stress in the x-x direction rapidly decreases on the surface of the weld, away from the weld toe.

Strain masking was used to exclude computation points on the weld surface during post-processing. Figure B-14 shows the same stress obtained from 3D-ICP in the same location and along the same path using mean filtering with and without strain masking. The strains measured at the conventional 1 mm strip gage are also plotted for reference. Including the computation points on the weld surface reduced the mean value of all the computation points on the pole wall within the filter boundary. The two plots converge at the tenth point from the weld toe, the first computation point in which a point on the weld surface is not included in the filter boundary.

B.8 Boundary Effects

During data processing, noise in the data manifested on the strain contour plots as "blotches" of spurious data not fitting with the surrounding strain contours at the edges of the measured area. Investigation into this noise revealed that the boundary noise was limited to a distance equal to the filter averaging length when using a mean filter. Boundary noise was less pronounced when using a median filter, which was

better suited to removing a single point of noise. A possible reason for this is that all computation points less than the number of computation points equal to the filter size away from the measurement boundary had fewer computation points within the filter boundary. With fewer measurements to average, the effect of a spurious data point was amplified. The strain gage location was centered in the frame for all measurements, preventing boundary noise from affecting the data at the strain gage location. Based on these observations, the 3D-ICP data from the number of computation points equal to the filter size from the measurement boundary were omitted from the plots comparing 3D-ICP measurements to conventional strain gage measurements and FEA results.

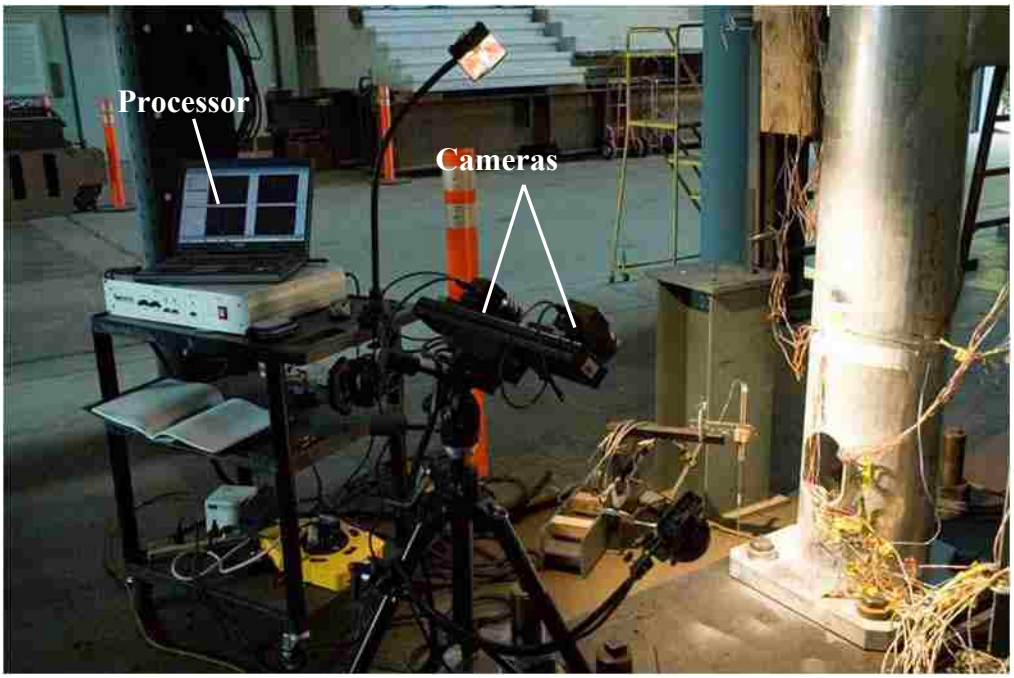

Figure B-1. Three-dimensional image correlation equipment used

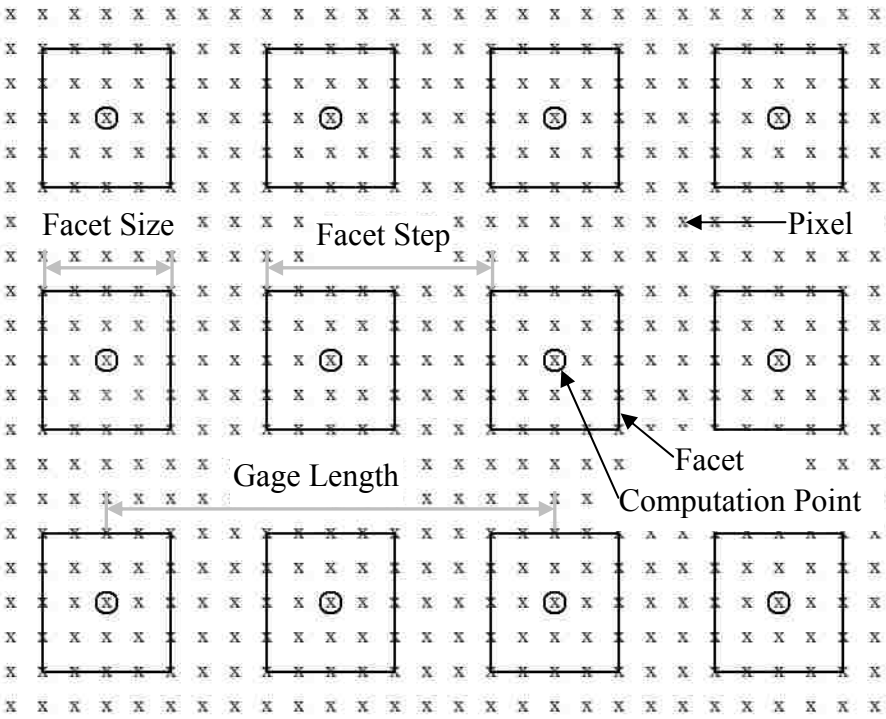

Figure B-2. Schematic of 3D-ICP facet parameters

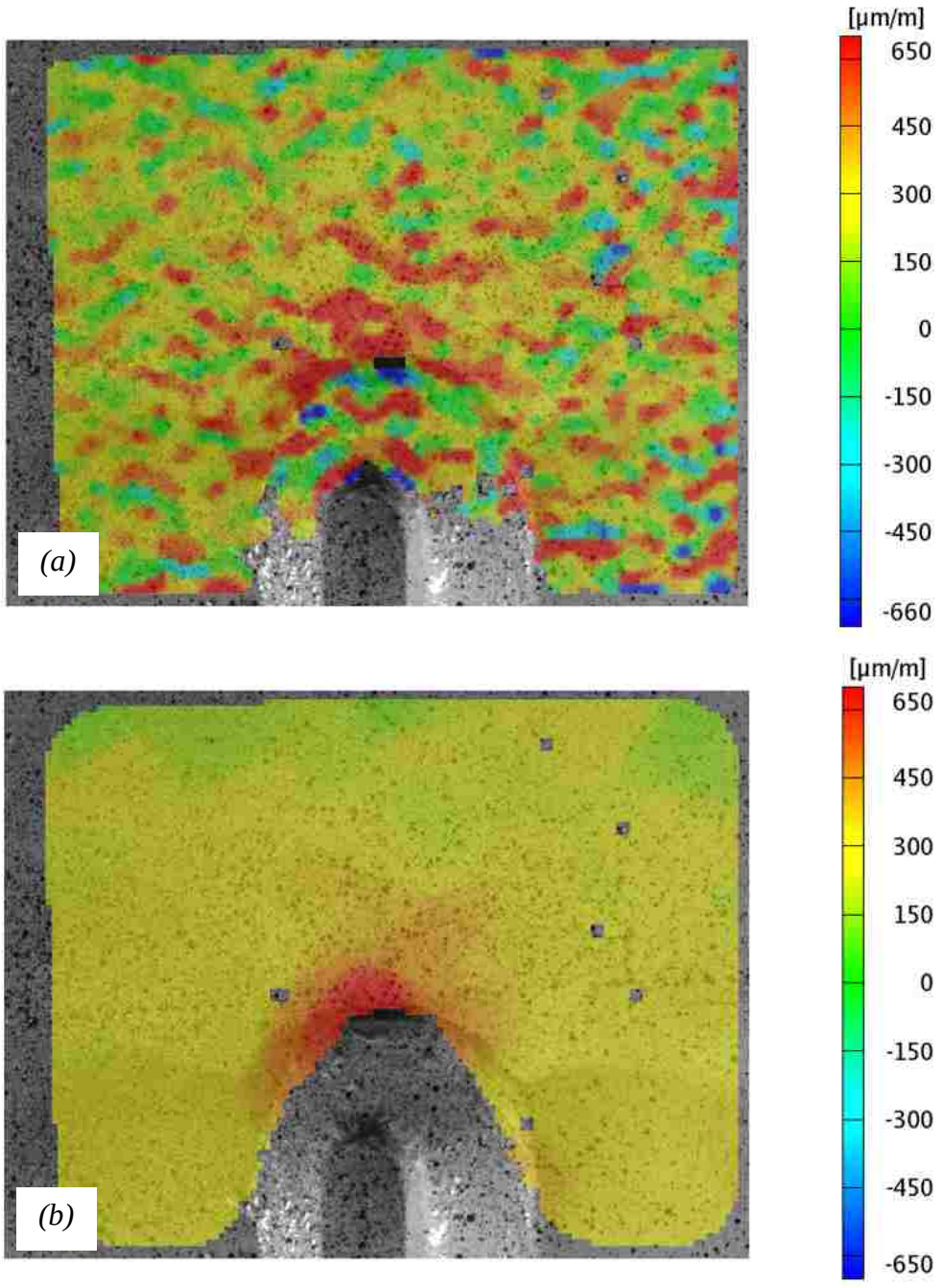

Figure B-3. Type XII stiffener termination weld 3D-ICP strain results: *a*, unfiltered results; *b*, filtered results.

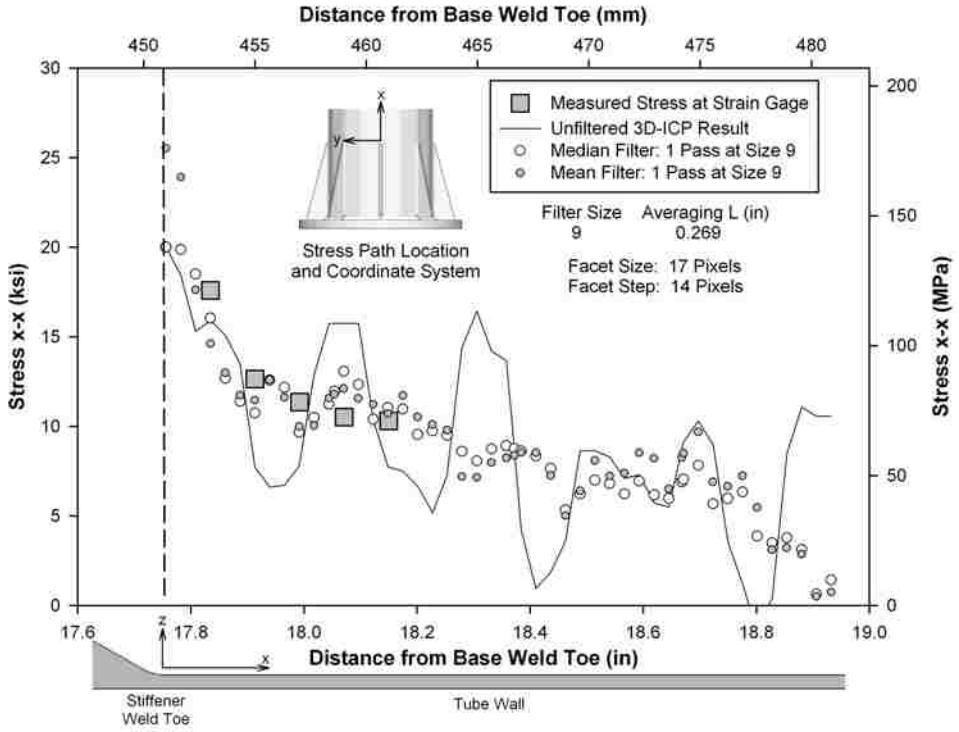

Figure B-4. 3D-ICP results after one filter pass

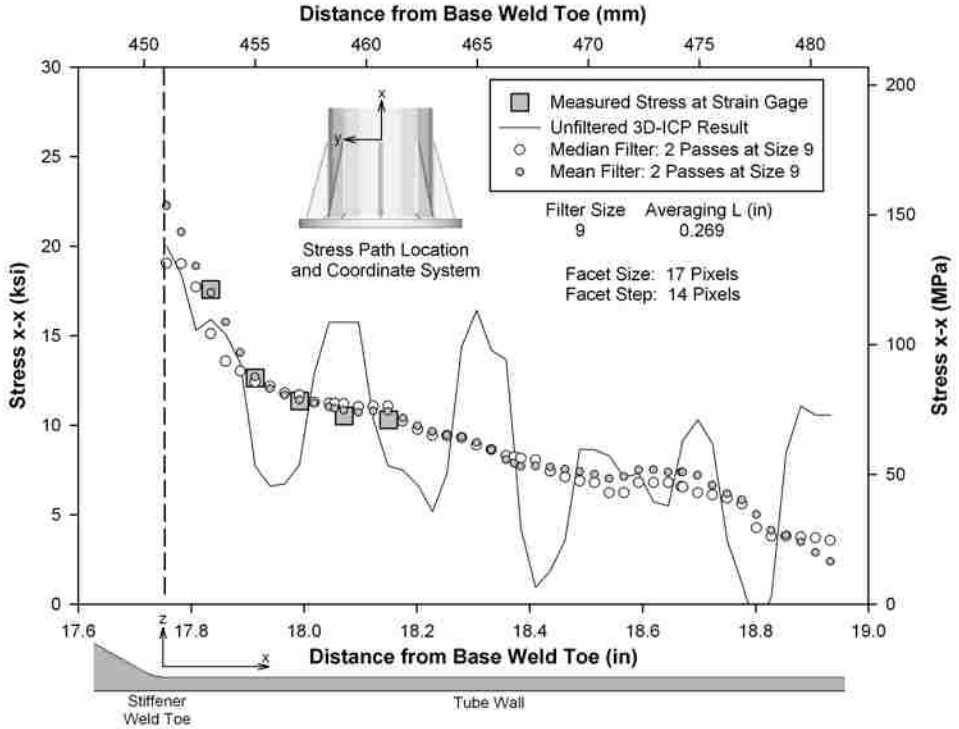

Figure B-5. 3D-ICP results after two filter passes

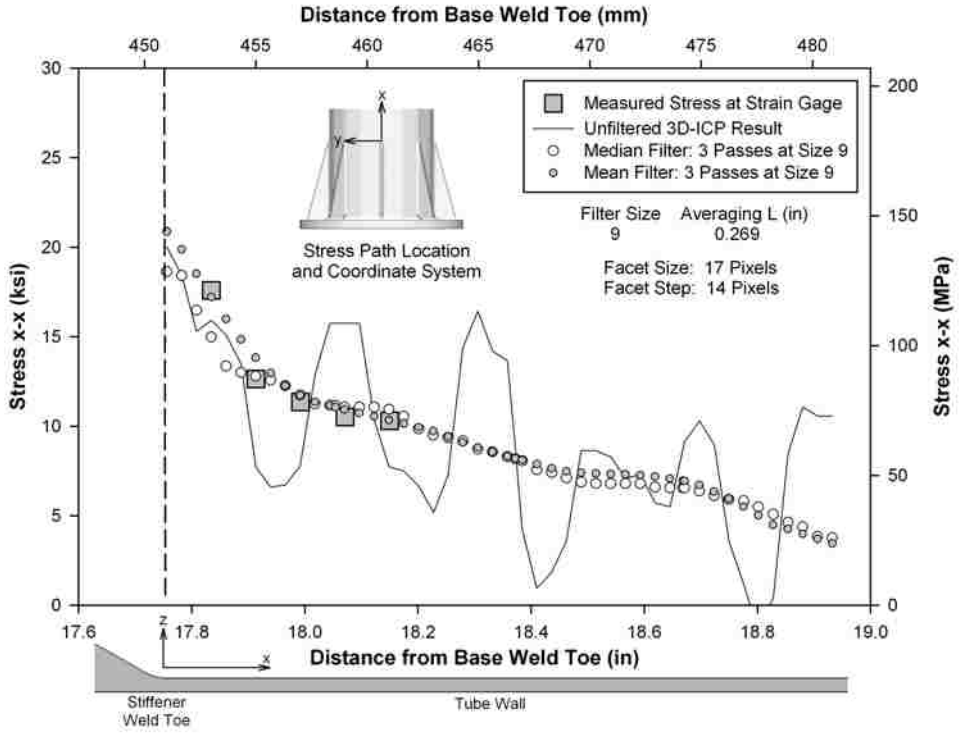

Figure B-6. 3D-ICP results after three filter passes

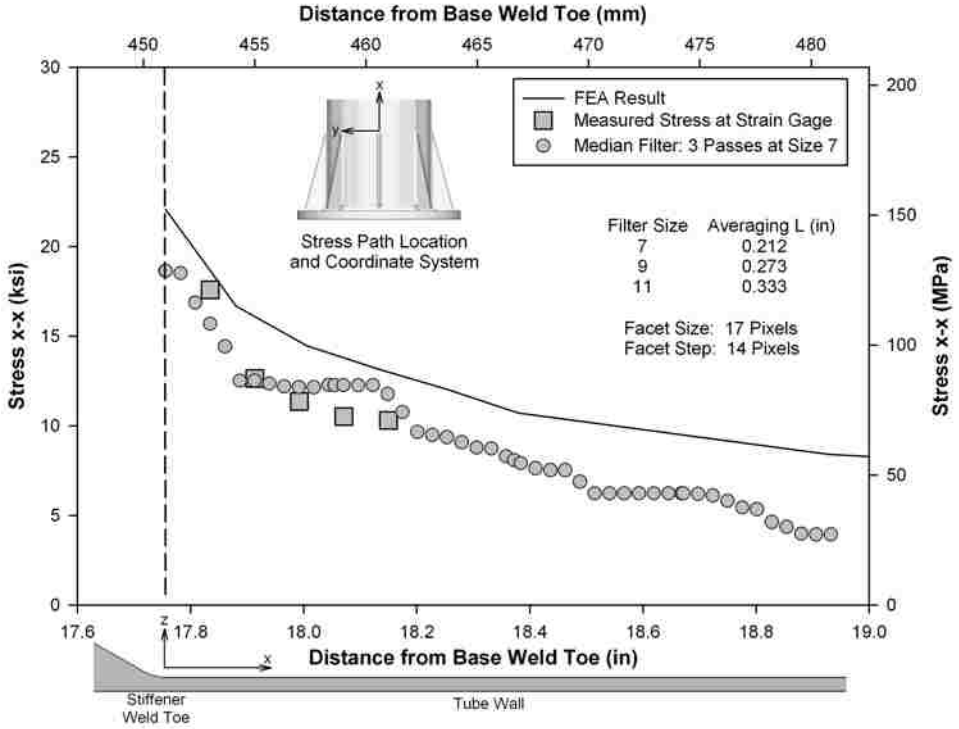

Figure B-7. 3D-ICP results using a size 7 median filter

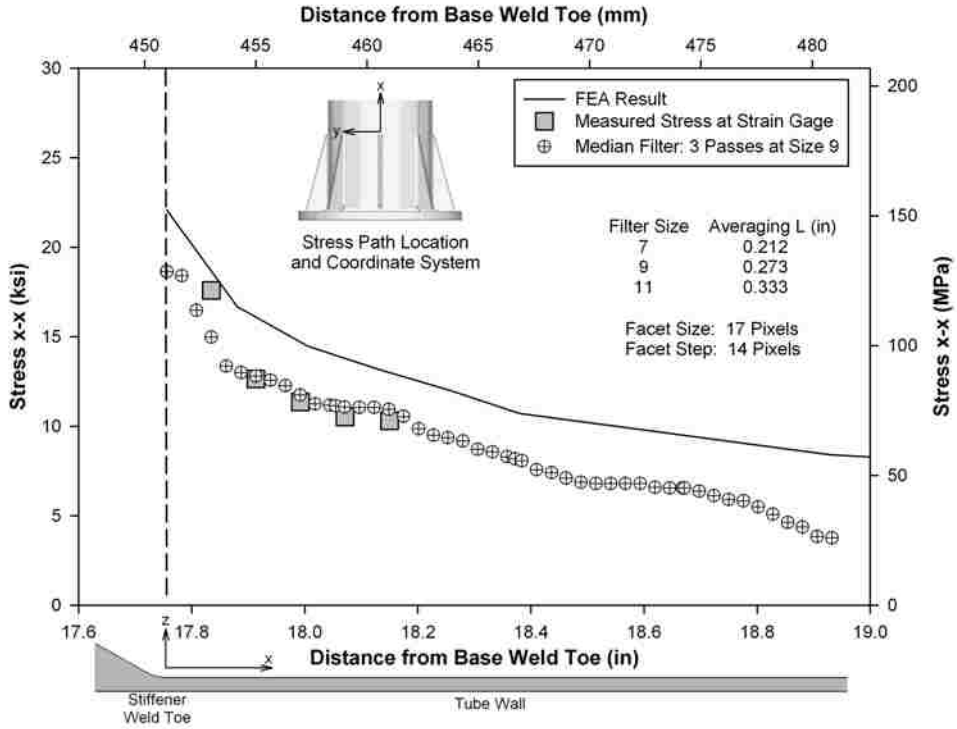

Figure B-8. 3D-ICP results using a size 9 median filter

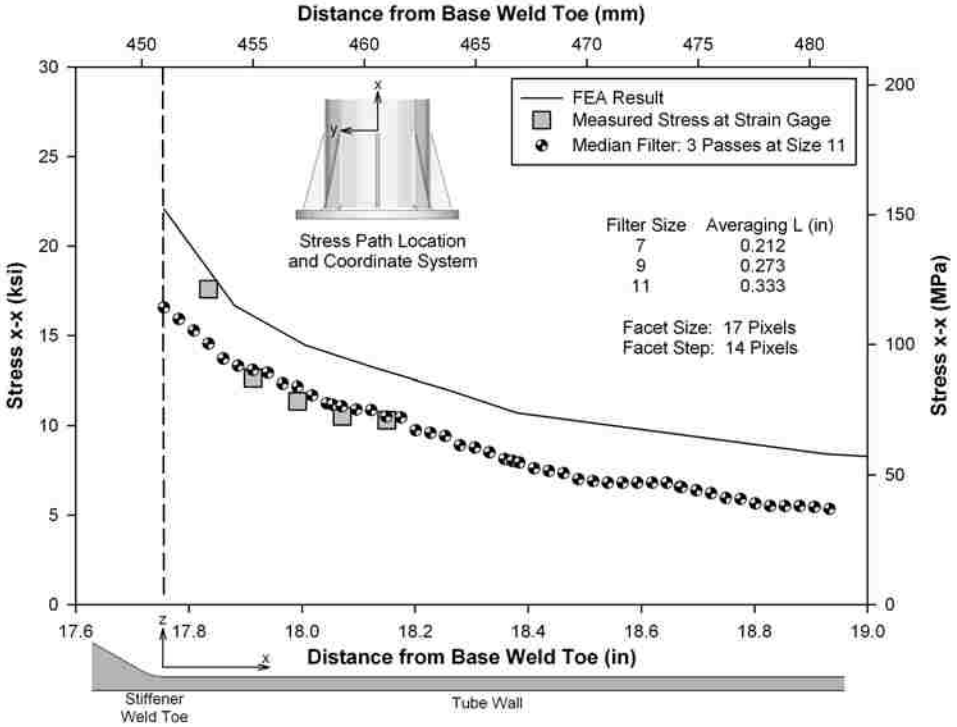

Figure B-9. 3D-ICP results using a size 11 median filter

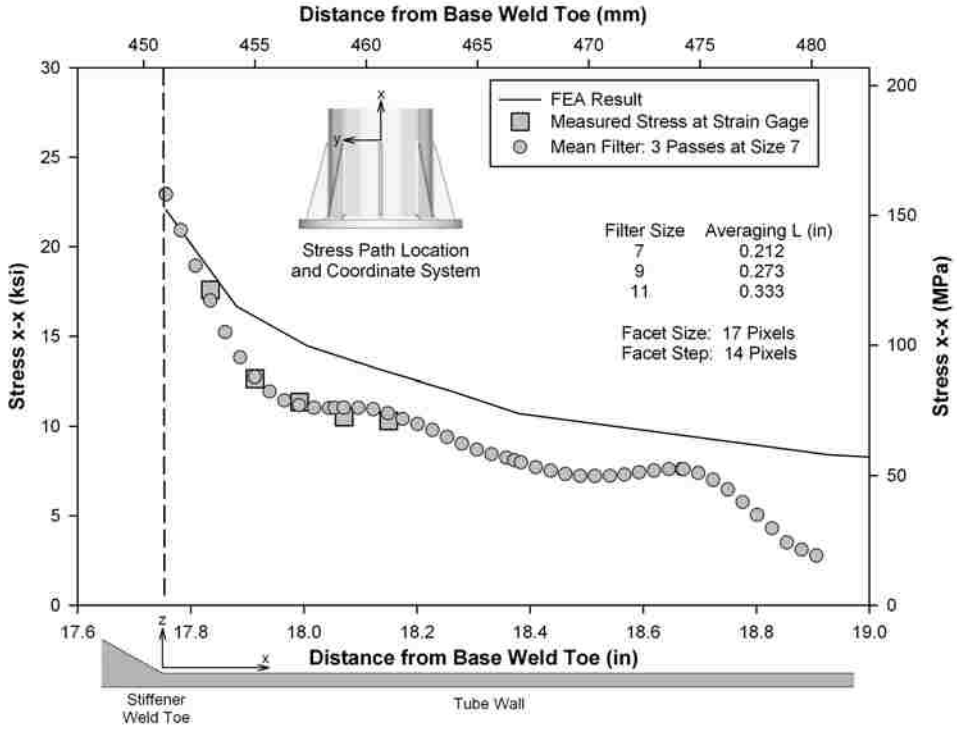

Figure B-10. 3D-ICP results using a size 7 mean filter

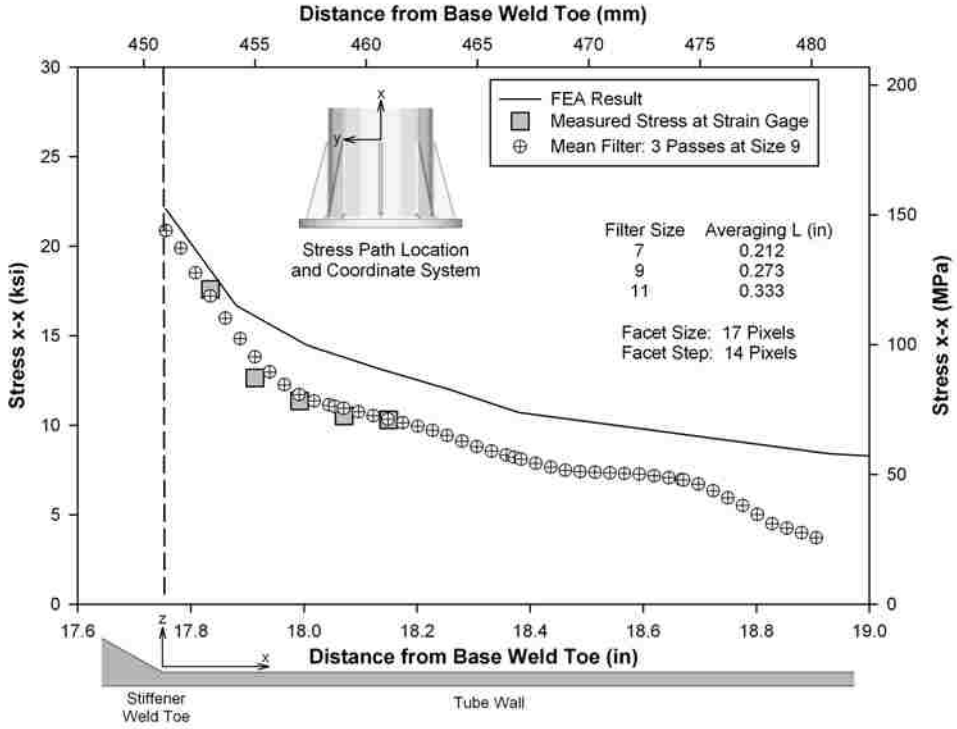

Figure B-11. 3D-ICP results using a size 9 mean filter

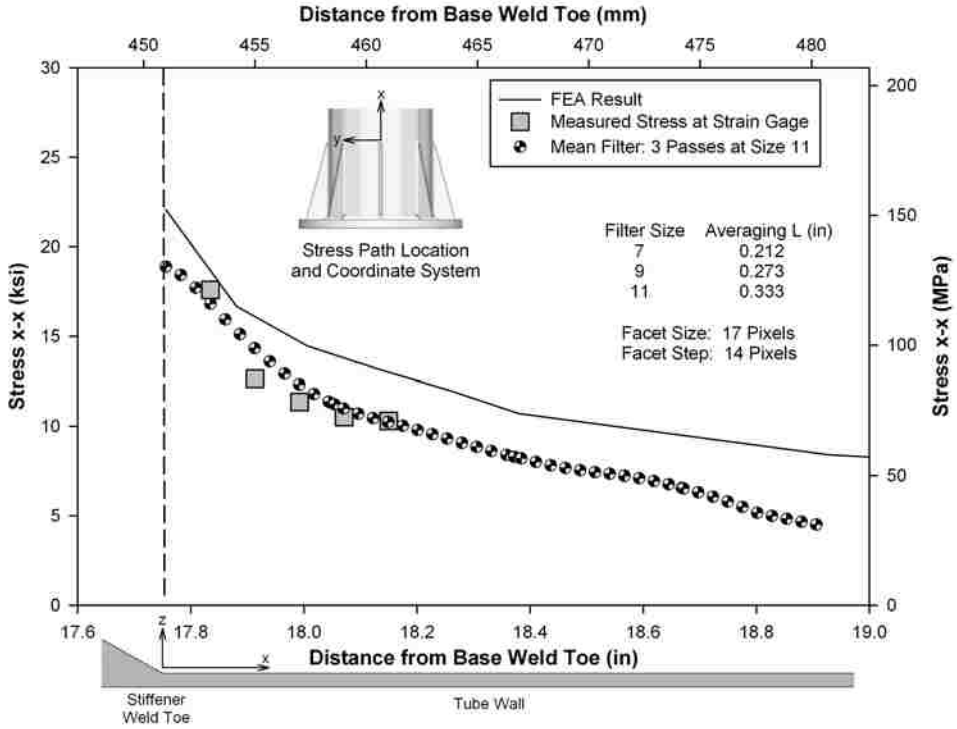

Figure B-12. 3D-ICP results using a size 11 mean filter

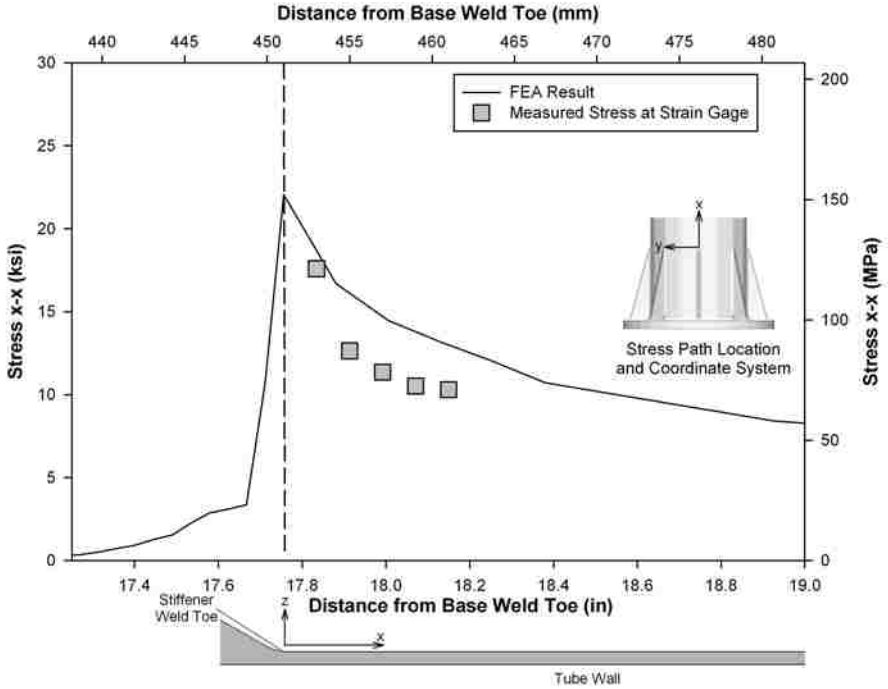

Figure B-13. Finite element analysis predicted stresses for Type XII at stiffener termination weld toe

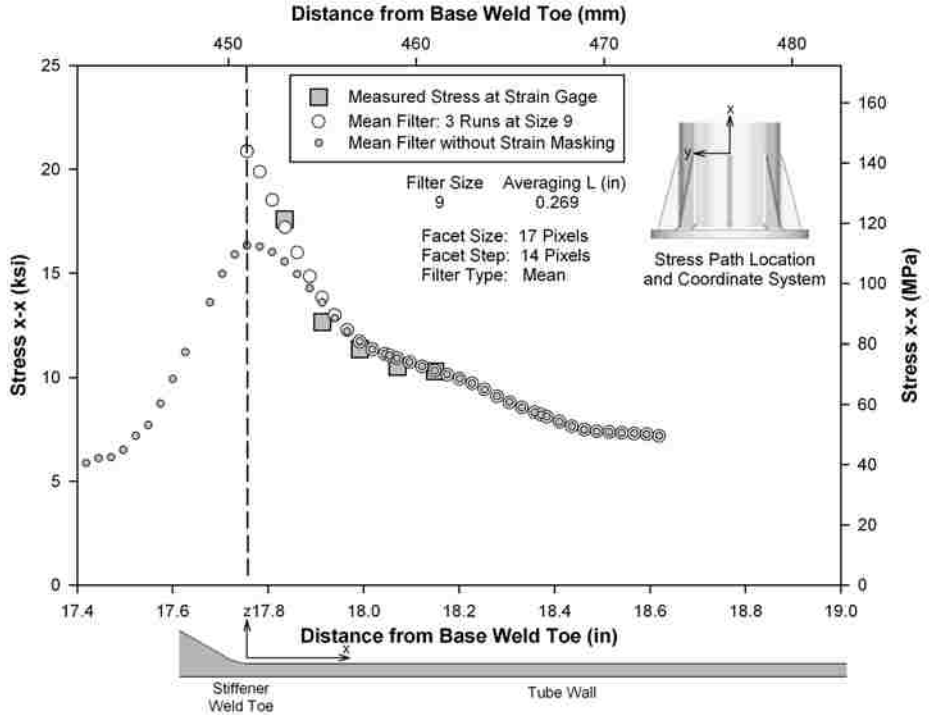

Figure B-14. Comparison of 3D-ICP data for Type XII at stiffener termination with strain masking and without strain masking of weld surface

VITA

The author received his Bachelor of Science in Engineering degree in Civil Engineering from Tulane University, New Orleans, Louisiana in May 2007. During the Hurricane Katrina evacuation in 2005, he spent the Fall Semester at Rensselaer Polytechnic Institute in Troy, New York.

The author is currently employed by Arora and Associates, P.C. in Bethlehem, Pennsylvania, as a structural engineer.